LEVEL II

②

NEW ELECTRONIC TRANSITION LASER SYSTEMS

By: D. L. Huestis, R. M. Hill, D. J. Eckstrom,
M. V. McCusker, D. C. Lorents, H. H. Nakano,
B. E. Perry, J. A. Margevicius, and N. E. Schlotter

May 1978

Technical Report No. 1, for period 17 February to 17 August 1977

D D C
RECEIVED
JUL 28 1978
E

78 07 21 013

SRI International

⑥

NEW ELECTRONIC TRANSITION LASER SYSTEMS.

⑩

By: D. L. Huestis, R. M. Hill, D. J. Eckstrom,
M. V. McCusker, D. C. Lorents, H. H. Nakano,
B. E. Perry, J. A. Margevicius, and N. E. Schlotter

⑪

May 1978

ACCESSION for

NTIS	White Section ✖
DDC	Buff Section ☐
UNANNOUNCED	☐
JUSTIFICATION	

BY

DISTRIBUTION/AVAILABILITY CODES

Dist.	AVAIL. and/or SPECIAL
A	

41¢ 281
78 07 21 013   att

The views and conclusions contained
in this document are those of the
authors and should not be interpreted
as necessarily representing the
official policies, either expressed
or implied, of the Advanced Research
Projects Agency or the U.S. Government.

SECURITY CLASSIFICATION OF THIS PAGE (When Data Entered)

REPORT DOCUMENTATION PAGE		READ INSTRUCTIONS BEFORE COMPLETING FORM
1. REPORT NUMBER	2. GOVT ACCESSION NO.	3. RECIPIENT'S CATALOG NUMBER
4. TITLE (and Subtitle) NEW ELECTRONIC TRANSITION LASER SYSTEMS		5. TYPE OF REPORT & PERIOD COVERED Technical Report No. 1 17 Feb 1977 to 17 Aug 1977
		6. PERFORMING ORG. REPORT NUMBER MP 78-07
7. AUTHOR(s) D. L. Huestis, R. M. Hill, D. J. Eckstrom, M. V. McCusker, D. C. Lorents, H. H. Nakano, B. E. Perry, J. A. Margevicius, N. E. Schlotter		8. CONTRACT OR GRANT NUMBER(s) DASG60-77-C-0028
9. PERFORMING ORGANIZATION NAME AND ADDRESS SRI International 333 Ravenswood Ave Menlo Park, California 94025		10. PROGRAM ELEMENT, PROJECT, TASK AREA & WORK UNIT NUMBERS
11. CONTROLLING OFFICE NAME AND ADDRESS Defense Advanced Research Projects Agency Washington, D.C.		12. REPORT DATE May 1978
		13. NUMBER OF PAGES 246
14. MONITORING AGENCY NAME & ADDRESS(if different from Controlling Office) Ballistic Missile Defense Advanced Technology Center Redstone Arsenal, Alabama 35809		15. SECURITY CLASS. (of this report) Unclassified
		15a. DECLASSIFICATION/DOWNGRADING SCHEDULE

16. DISTRIBUTION STATEMENT (of this Report)

Approved for public release; distribution unlimited.

17. DISTRIBUTION STATEMENT (of the abstract entered in Block 20, if different from Report)

18. SUPPLEMENTARY NOTES

19. KEY WORDS (Continue on reverse side if necessary and identify by block number)

excimer lasers
e-beam pumping
e-beam controlled-discharge pumping
rare-gas halide lasers

mercury halide lasers
electronic transition lasers
kinetics and spectroscopy of laser media

20. ABSTRACT (Continue on reverse side if necessary and identify by block number)

This report describes our research program directed toward the identification of new high-performance electronic transition lasers, and toward the detailed characterization of these laser media.

An extensive theoretical and experimental survey has been conducted, emphasizing molecules whose excited states are ionic in character. Several promising new candidates have been identified; the laser potential of some of these has been investigated in detail (ICl, RgHg, and HgCl); others should be

DD FORM 1473 EDITION OF 1 NOV 65 IS OBSOLETE
1 JAN 73

20. Abstract (continued)

the subjects of further investigation (e.g., the cadmium and zinc halides).

Perhaps the most important accomplishment reported here is the demonstration (in collaboration with Maxwell Laboratories Inc.) of an electron-beam-controlled-discharge HgCl laser. This report describes the experimental studies which led to this achievement, and points out several areas in which further research is needed.

Considerable progress has been made in characterizing the microscopic processes which dominate the performance of electron-beam pumped XeF lasers. Specific attention has been paid to identifying and measuring the rates for the most important reactions which lead to the formation of XeF_{B}^{*}. The role of the XeF_{L}^{*} state which emits the prominent 460 nm band has been partially characterized. The rate of the removal of the lower laser level by collision-induced dissociation has been calculated, and the importance of this process emphasized.

Finally, a number of experimental and theoretical studies of important processes in KrF and rare-gas halide lasers are described in this report.

CONTENTS

i

APPENDICES

   A   EXTRACTION EFFICIENCY

   B   UV ABSORPTIONS OF RARE GAS IONS IN E-BEAM PUMPED RARE GASES

   C   EQUILIBRIUM BINDING OF THE GROUND $X^2\Sigma^+_{\frac{1}{2}}$ STATE OF XeF

   D   ELECTRON BEAM CONTROLLED DISCHARGE $HgCl^*$ LASER

   E   KINETIC PROCESSES IN RARE GAS HALIDE LASERS

   F   OPTICAL EMISSIONS OF TRIATOMIC RARE GAS HALIDES

   G   DIATOMICS-IN-MOLECULES POTENTIAL SURFACES FOR THE
        TRIATOMIC RARE GAS HALIDES: Rg_2X

LIST OF ILLUSTRATIONS

iii

LIST OF TABLES

SUMMARY

The objectives of the research reported here are to:

(1) Identify new candidate molecules that could potentially lead to lasers operating in the wavelength region 325 nm < λ < 900 nm with performance comparable to or better than that of KrF, and demonstrate laser action.

(2) Characterize the critical kinetics for XeF and HgX and address the residual important issues in KrF.

Our progress has been substantial. A vital part of our program has been close and effective collaboration with Maxwell Laboratories, Inc., which has strengthened the efforts of both laboratories considerably.

New Candidates

Our theoretical characterization of laser molecules has identified several promising new candidate diatomic molecules in ionic states, specifically, ICl, IBr, ZnBr, ZnI, CdBr, CdI, HgI, Kr^+O^-, and Xe^+S^-, in addition to the previously demonstrated XeF, I_2, HgCl, and HgBr. Possible additional candidate molecules are IO, IF, AsI, ZnCl, CdCl, HgS, HgSe, and HgTe. The ionic states of all other diatomic molecules are predicted to be less promising as visible laser candidates.

Our experimental program has demonstrated the potential of some of these candidates (such as ICl and IBr), while some others (such as IO and KrO) appear to be less promising. We are now Developing rules for suggesting new candidates in weakly bound excimer levels (such as $RgHg^*$ and $CdHg^*$) and strongly bound covalent states (such as S_2^*). Some preliminary experimental work has been completed, the work on $RgHg^*$ is described below, and more work is in progress (on S_2^*, SeO^*, and others).

1

ICl and IBr

In the past, laser action has been demonstrated on ionic to covalent transitions in Br_2 and I_2 near 290 and 343 nm, respectively. The heteronuclear halogen molecules ICl and IBr have been identified in our theoretical task as having favorable electronic structure, quenching behavior, and transition wavelengths. We investigated the time and pressure behavior of the fluorescence from mixtures of argon and various halogen donors. The highest fluorescence yields obtained were 25% in the 385 nm band of IBr and in each of the two ICl bands (at 340 and 430 nm). Because ICl and IBr absorb at their emission wavelengths, we examined the production of ICl^* and IBr^* in mixtures such as argon with $HI + Cl_2$ and $HI + HBr$. The mixtures tried so far have produced substantially fewer excited states than pure Ar/ICl and Ar/IBr.

We briefly investigated the transient gain in Ar/ICl electron beam excitation at Maxwell. A value of approximately 4×10^{-3} cm^{-1} was measured, insufficient to overcome the ground state absorption. The absorption in IBr should be substantially less. Efficient extraction will probably depend on finding other alternatives.

Rare Gas/Mercury Excimers

Following our previous measurements in the Xe/Hg system, we investigated the possibility of laser action on the rare-gas/mercury excimer atom. We were encouraged by high fluorescence yields (as high as 50%) in Ar/Hg, Kr/Hg, and Xe/Hg and by preliminary indications of gain in the 2-cm path length of our Febetron Cell.

The first experiments performed on the 50-cm e-beam at Maxwell using an SRI-designed cell, flow system, and probe laser looked for gain but found only absorption in Ar/Hg and Xe/Hg. While the detailed spectroscopy and kinetics of the rare gas mercury excimers are incompletely understood, it is clear that, at least under the conditions examined, the lower laser level is removed more slowly than it is populated by fluorescence.

These disappointing results have obviously dampened our enthusiasm for the rare-gas/mercury excimers as laser candidates. Nevertheless, a substantial amount has been learned about the energy deposition and energy transfer processes in rare-gas/mercury mixtures that will be of considerable assistance in understanding the energy flow in rare gas/mercury-halide lasers.

HgCl

The molecule most studied by our experimental program has been HgCl. The work has been arduous, plagued by materials handling problems and irreproducibility. The major difficulty is reaction of the unexcited gases before they are introduced into the experimental cell.

In our studies at SRI, we have emphasized the selection of the optimum gas components for discharge pumping of HgCl and have identified $Ar/Hg/Cl_2$ as far superior to all other mixtures tried, including $Ar/Xe/Hg/CCl_4$. However, use of $Ar/Hg/Hg_2Cl_2$ may be favored for the case of materials handling and flow loop design. We have found the value of 1.5×10^{-24} cm^2 sec for the reduced stimulated emission cross section, which is substantially lower than the value found at AVCO.

Studies of e-beam pumped HgCl at Maxwell began on June 13, 1977, using the SRI cell and flow system. The gain and fluorescence yields were studied in $Ar/Xe/Hg/CCl_4$, the complexity of the energy flow was established, and the essential role of $XeCl^*$ was identified. The cell was then modified for discharge excitation.

Discharge pumping studies were initially impeded by foil failure. Corrosion-resistant Inconel foil removed this problem and allowed stable discharge excitation to be attained. Laser action was demonstrated on August 15, 1977.

Our kinetics work led to the choice of $Ar/Hg/Cl_2$ as the laser mixture. Subsequent work has suggested that under the rather slow flow conditions used in the laser demonstration, the Cl_2 was probably all consumed before

3

excitation by reaction with ground state Hg. The actual gas composition may have been Ar/Hg/HgCl$_2$ or possibly Ar/Hg/Hg$_2$Cl$_2$. Continued study of fast-flow Ar/Hg/Cl$_2$ is clearly in order.

XeF

Our work on the XeF kinetics has concentrated on three areas: the collision-induced dissociation of the ground state, the dependence of the visible and uv fluorescence yields on gas composition and excitation conditions, and characterization of the input chain by which XeF is produced.

The XeF laser operates on bound-to-bound transitions terminating on various vibrational levels of the ground state. Concern exists about the rate of removal of the lower laser level. Vibrational relaxation in the lower level is insufficient to adequately deplete the population since the low vibrational spacing (ω_e = 226 cm^{-1}) leads to the estimates that 9.6% and 4.4% of the ground state molecules will be in v'' = 2 and v'' = 3, respectively, at room temperature.

For sustained laser action, therefore, the ground state vibrational manifold must be depleted by dissociation induced by collisions with the background rare gas. We have calculated the equilibrium constant for the reaction

$$XeF(X^2\Sigma_{\frac{1}{2}}^+) + Ne \rightleftharpoons Xe + F + Ne$$
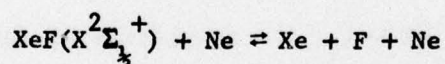
and found that if this equilibrium were established, the density of the ground state would be reduced to a negligible level. Therefore, the crucial kinetic parameter necessary to ensure against bottlenecking is the rate of collision-induced dissociation.

A crude calculation of the collision-induced dissociation rate coefficient was made using a master equation approach with the Δv dependence of the energy transfer cross sections calculated by a perturbation technique. These preliminary calculations cannot be expected to give

4

better than factor-of-two agreement with experiments. The bulk dissocia-
tion rate coefficient was calculated to be $\sim 2 \times 10^{-13}$ cm^3 sec^{-1}. The
rate coefficient for removal of $v'' = 3$ was calculated to be 4×10^{-12}
cm^3 sec^{-1}. More accurate calculations and more refined experiments to
study these important reactions are planned at SRI and Maxwell, respectively.

Our work on the fluorescence yields has emphasized the role of the
emission band near 460 nm in explaining the energy flow kinetics. Although
the results to date have been inconclusive, the important role played by
the XeF(C3/2) state, which is presumably the emitter of the 460 nm band,
and the interconversion of this state with the upper laser level XeF(B½)
by rare gas collisions, are well established.

Our studies of the XeF input chain have identified the following as
the most important energy flow pathways:

$$\text{electrons} \to \text{Ne}^+ \to \text{Ne}_2^+ \to \text{NeF}^* \to \text{F}^* \to \text{Xe}^+ \to \text{XeF}^*$$
$$\text{electrons} \to \text{Ne}^* \to \text{Xe}^+ \to \text{XeF}^*$$
$$\text{electrons} \to \text{Xe}^+ \to \text{XeF}^*$$
$$\text{electrons} \to \text{Xe}^* \to \text{XeF}^*$$
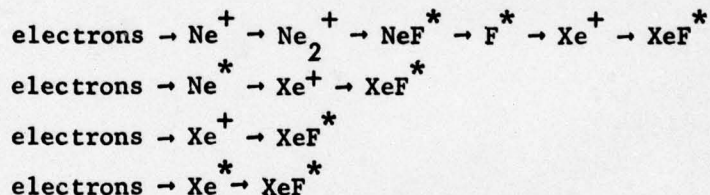
Previously, little was known about the important neon and fluorine reactions.
We have verified the role played by NeF* predissociation and F* production
and have measured the rates of reaction of F* with F$_2$, NF$_3$, and Xe. We
are now studying the reactions of Ne$_2^+$, Ne*, and Xe* by Ne** fluorescence,
Ne* absorption, and Xe$_2^*$ fluorescence, respectively.

Other Kinetics Issues

We also include here as appendices descriptions of experimental and
theoretical studies of a number of other important kinetic processes in
rare-gas halide lasers.

I. INTRODUCTION

The search for efficient high-energy visible or near-uv lasers has recently produced extremely successful results. The scalability of at least one of these systems is now demonstrated and the essential laser parameters are reasonably well understood. Soon the detailed understanding of the microscopic processes within the laser medium, together with the demonstrated laser performance characteristics, can be used to design viable large-scale laser systems.

The best understood of these lasers is KrF, which has also yielded the highest output energy, energy density, and efficiency. Unfortunately its short wavelength makes it unattractive for transmission through the atmosphere. The next most studied laser is XeF, which has produced about one-half the output energy at somewhat less than half the energy density and efficiency. The molecular iodine laser, whose discovery coincided with the rare gas halides, has received much less extensive investigation. Recent additions to the list of active candidate lasers are HgCl and HgBr. Electron-beam pumped lasers based on these molecules were first demonstrated at AVCO [Pa77]. Electron-beam controlled discharge pumping of HgCl was achieved in August of 1977 by a joint Maxwell-SRI team [THO78a]. Subsequently, discharge pumping of a HgBr laser was demonstrated at the Naval Research Laboratories [Wh78].

With several potentially efficient lasers demonstrated (or hopefully soon to be demonstrated) in the desired wavelength region, it becomes necessary to establish criteria for choosing which candidates to pursue most energetically, to establish which microscopic processes may lead to limitations on the laser performance, and to find ways of overcoming these limitations. The most difficult task facing the laser modeler is the identification of the critical rates or cross sections, those that

determine the optimum choices of the macroscopic operating conditions.
For example, the need for vibrational relaxation but avoidance of quenching
may restrict the operating gas pressure to a narrow range, transient or
ambient absorptions may limit the length of the laser cavity, or electron-
excited state collisions may limit the energy deposition density.

Eventually, one must develop a comprehensive model of all important
microscopic processes within the laser medium. To do this, an accurate
(say, $\pm$ 10%) value must be obtained for every critical rate and cross
section. In practice, only a small fraction of the conceivable processes
are important, and an even smaller fraction have been previously character-
ized. One might make the following list of priorities:

(1) Qualitative electronic structure

(2) Identification of input reaction chain

(3) Lower level removal

(4) Absorptions

(5) Upper state quenching

(6) Identification of competing reactions

(7) Upper state vibrational/rotational relaxation.

After the qualitative features have been established, the most important
process can be identified for detailed measurement or calculation.

Table 1 presents an estimate of the status of our understanding of
the kinetic processes within various candidate laser media. This report
discusses our efforts to identify promising new candidate molecule. We
begin with a theoretical description of the desirable spectroscopic
characteristics and develop rules for selecting potential candidates.
Several of these molecules were investigated experimentally. A major
portion of our effort has been directed toward a detailed understanding
of the kinetic processes for two of the most promising systems, e-beam
pumped XeF and e-beam controlled discharge pumped HgCl. Considerable

8

Table 1

KINETICS STATUS

	Rare Gas Halides	Halogens	IIB Halides	Others
Suggested Molecules			ZnX, CdX Hg_2Cl_2 (photopump)	Hg^+S^- Xe^+S^-
Fluorescence Spectroscopy		IBr, ICl	HgCl (discharge)	S_2 (e-beam) CdHg
Energy Flow Pathways			HgX (e-beam)	S_2 (photopump) RgM
Partial Kinetics	XeF	I_2		
Comprehensive Model	KrF			

9

progress has been made in both these systems. A major accomplishment
was the demonstration of laser action in e-beam controlled discharge
pumped HgCl.

II. THEORETICAL AND ANALYTICAL CHARACTERIZATION
OF LASER CANDIDATE MOLECULES

A first step in the search for new, efficient, high-energy, visible lasers is the selection of candidate molecules. The number of possible candidates is vast indeed; even if we restrict our searches to diatomic molecules, there are more than 4000 to be examined. In this section we suggest criteria for new candidate molecules, based on the implications for laser performance of the spectroscopic and kinetic properties of the molecules themselves.

Three general classes of electronic structure are identified for diatomic laser candidate molecules:

> (1) Weakly bound excimer states
>
> (2) Strongly bound covalent states
>
> (3) Ionic excited states.

At present, all demonstrated e-beam or discharge pumped lasers under active consideration are of the third class. In an attempt to identify other candidate molecules of this class, we derived semiquantitative rules from the requirements that the ionic state not be the ground state of the molecule and not be easily quenched or predissociated. Several new candidates of this class have been identified. The ionic states of all other diatomic molecules are expected to be less promising as laser candidates.

As described in the following sections, the potential of some of these new candidates has been supported experimentally (such as ICl and IBr), while some others (such as IO and KrO) appear to be less attractive. Our theoretical analysis of diatomic molecules in ionic states is essentially complete; the remaining steps are experimental characterization and laser

11

demonstration. Rules are now being developed for suggesting new candidates in weakly bound excimer levels and strongly bound covalent states. Some preliminary experimental work has been completed.

Implications of Laser Performance

A number of systems issues influence the choice of laser candidates. The most obvious of these is the laser wavelength. The scaling of the size of optical components suggests that short wavelengths would be desirable, and the limitations of atmospheric transmission (ozone and oxygen absorption and molecular scattering) favor wavelengths longer than 325 nm. These two conclusions lead to a search for electronic transition lasers in the wavelength region 325 to 900 nm.

The requirement for high optical quality dictates a suppression of density disturbances within the laser medium. This leads to the need for a sophisticated gas flow or recirculating system. There is some risk that the energy and capital costs of gas flow may dominate the other components of the laser system. Although exact values of the critical parameters are not yet known, it appears that the cost of the flow system should scale with the amount of gas that must be moved through the laser cavity between laser pulses. Hence the volume of the cavity and the specific energy density become crucial factors.

The overall laser electrical efficiency enters into the analysis in two ways. First, a higher electrical efficiency will lead to reduced size and lower capital and energy costs for the primary energy source (electron-beam and/or discharge). Second, at fixed energy deposition density (which may be set by foil heating, e-beam penetration depth, and gas pressure limitations), increased efficiency will lead to a smaller gas volume for fixed output energy and hence reduced demands on the flow loop.

In both the direct electron-beam and discharge pumping schemes, the analysis is simplified by identifying what we may call the "quantum of excitation," which is simply one atomic or molecular excited state or

12

one atomic or molecular ion. The cost per quantum in electron-beam excited rare gas hosts is

$$\frac{\text{Cost}}{\text{Quantum}} = \frac{W \, n_i}{n_i + n_{ex}}$$

where W is the energy cost per ion pair, n_i is the number of ion pairs produced per primary electron ($W n_i$ = energy of primary electrons), and n_{ex} is the number of excited states produced by the hot secondary electrons. Following the previous analysis [LO72, HZN77] of the experimental data [PHS72, THT75, THT76], we find the following costs per quantum excitation: He (31 eV), Ne (27 eV), Ar (20 eV), Kr (18 eV), and Xe (15 eV) from electron-beam deposition into the pure rare gases. In mixed gases we must also include excitation of the additives by the hot secondary electrons. For discharge pumping, the definition of the quantum of excitation is the same (one excited state or its precursor), but the cost of its production depends on the many electron collisional processes, and the calculation is not nearly so straightforward.

A major usefulness of these concepts is that, in the energy flow kinetics in electron beam and discharge excited high pressure gas mixtures, each quantum of primary excitations can result in the production of, at most, one molecule in the upper electronic laser level. We then expect the maximum internal efficiency of an electronic transition laser to be:

$$\eta \le \frac{h\nu}{(\text{quantum cost})} \, Br \, \eta_{ext} \quad ,$$

where $h\nu$ is the output quantum energy, BR is the kinetic branching ratio (the number of upper laser states produced divided by the number of primary excitations), and η_{ext} is the extraction efficiency (the number of photons extracted divided by the number of upper laser states produced).

The requirement of a high kinetic branching ratio can be restated as the demand that each energy transfer, reaction, or other collision in the

13

kinetic input chain must selectively yield the desired product. Extensive
study over the last few years [LO72, Lo76] has conclusively demonstrated
that this is the case in the electron-beam excited rare gases. The
kinetic branching ratio is essentially unity for these systems. Similarly
high kinetic branching ratios are observed (at least a low rare gas pressure)
in e-beam excited Ar/I_2 [MLH76] and $Ar/Kr/F_2$ [NHL76]. Experimentally, the
fluorescence yield (FY) is an important monitor of the kinetic branching
ratio. The observation of a high fluorescence yield necessarily means a
high kinetic branching ratio, since the fluorescence yield is always the
smaller of the two. Obviously, any rules for identifying selective energy
flow pathways will be useful in choosing promising new candidate molecules.

The exoergic chemical and energy transfer reactions that produce the
desired electronic state of the laser candidate molecule typically leave
the upper laser level in highly excited rovibronic levels. Except under
fortuitous circumstances, the gain profiles of these individual rovibronic
levels may have low overlap. To make use of all the excited state popu-
lation, it is necessary that the background gas pressure be high enough
to cause rotational and vibrational relaxation within the excited electronic
state in a time shorter than the radiative lifetime with respect to
spontaneous emission and quenching. If the desired excited state popu-
lation must then be coupled efficiently to the optical field before it
can decay by spontaneous emission or be quenched. This further implies
that the optical gain must dominate absorptions from lower molecular levels
(especially the lower rovibronic level on which the transition terminates,
absorptions by the original gas constituents, and absorptions by an
transient species produced by excitation of the laser medium).

A central parameter for describing the gain and absorption is the
stimulated emission cross section

$$\sigma_{se} = \frac{\lambda^3}{8\pi c} \frac{\lambda}{\delta\lambda} A \quad ,$$

14

where λ is the wavelength of the center of the emission profile, c is speed of light, $\delta\lambda$ is the band width, and A is the Einstein coefficient. The stimulated emission cross section may be calculated for a single rovibronic transition or for entire observed emission spectrum, provided the appropriate individual or lumped parameters are used and assuming that the rovibrational levels are collisionally coupled on a time scale shorter than the stimulated emission time, or otherwise stated, that the transition is "homogeneously broadened." The small signal gain of the laser medium is then

$$g_o = \sigma_{se}[N_u - \frac{g_u}{g_\ell} N_\ell] - g_a$$

where N_u, g_u, N_ℓ, and g_ℓ are the population densities and degeneracies for the upper and lower laser levels, respectively. The medium absorption is

$$g_a = \sum_i \sigma^i_{abs} (\lambda)N_i \quad ,$$

where the sum is over all possible absorbers (N_i) with the appropriate absorption cross sections. Obviously, to have a laser, the net gain must be positive. Indeed, Hunter et al. [HHO76] have shown that the efficiency of energy extraction is critically related to the ratio g_o/g_a,

$$\eta_{ext} \leq [1 - (g_o/g_a + 1)^{-\frac{1}{2}}]^2 \quad ,$$

and that to obtain extraction efficiencies of greater than 50% we must have $g_o/g_a > 10$. Substantial population in the lower laser level, or slow lower level removal, presents even more demanding requirements. Derivation of the corresponding equation for the extraction efficiency is given in Appendix A.

Recent experimental investigations have found that strong absorptions from the uv throughout the visible are ubiquitous in electron-beam-excited

15

rare gas mixtures [ZHL76, HZN77, HOH77]. In the pure rare gases the absorbing species include molecular rare gas ions [HOH77, WCC77] and excited atomic and molecular rare gases [ZHL76, HZN77]. The observed absorption coefficients vary (depending on pressure and energy deposition) from 1 cm^{-1} to 1 x 10^{-3} cm^{-1}. Strong absorption was observed at every wavelength examined. The ubiquity of these absorptions is not yet fully explained. They appear to persist, at least, to a comparable extent in all mixtures of rare gases with other additives. These transient absorptions have already had a substantial effect on the directions of laser development, most notably in the rare gas oxides [HZN77] and xenon fluoride [CH77].

Obviously a high gain transition is needed to overcome the anticipated absorptions. In searching for new laser candidate molecules, each of the factors in the gain equations above should be considered. Seeking new efficient lasers at all visible and uv wavelengths we will accept whatever wavelength (λ) the molecule may provide and attempt to make our choice on the other parameters. These we may summarize as (1) bandwidth, (2) Einstein coefficient versus upper state quenching, and (3) lower level removal.

Desired Spectroscopic Characteristics

The requirement of a narrow fluorescence band is simple to express in terms of the desired electronic structure. For bound-to-bound transitions, the width of individual vibronic transitions is determined by the rotational constants of the upper and lower state, while the distribution among the vibrational levels is described by the Franck-Condon principle. For bound-free transitions, the bandwidth is dominated by the slope of the lower state and the curvature of the upper state. The slope of the lower state within the Franck-Condon region of the upper state is also the dominate factor in the analysis of bound-to-bound transitions. The analysis

16

of free-to-free transitions is somewhat more complicated, but is generally dominated by the difference in slopes of the upper and lower potential surfaces. In general we find that individual vibrational bands of a bound-to-bound transition are less than an angstrom to a few tens of angstroms, while bound-to-free transitions vary from a few angstroms to a few hundred angstroms. In choosing candidate molecules, these considerations favor those with either bound lower states or lower states that are only weakly repulsive.

Once produced, the desired electronic excited state must be collected into the vibrational level of the selected transition, but must not be electronically quenched within the lifetime of the excited state with respect to spontaneous and stimulated emission. The specific value of the radiative lifetime (or Einstein coefficient) is not critical as long as it is as fast as or at least comparable to the quenching time. Assuming for the moment the unimportance of the lower level population, we can write the rate equation for the upper level (before application of the optical flux) as

$$\frac{d}{dt} N_u = pump - (A + Q) N_u \quad,$$

where pump is the rate of excited state production in $cm^{-3} sec^{-1}$ and Q is the quenching frequency (the product of the quenching rate coefficient k_q and the quencher density, N_q). In steady state, which is reached for pump times much greater than the radiative or quenching lifetimes, we find that

$$N_u = \frac{pump}{A + Q} \quad.$$

The net gain is then just

$$g_o = \frac{\lambda^4}{8\pi c \delta\lambda} \frac{A}{A + Q} pump - g_a \quad.$$

17

It is well known that quenching can be overcome by use of a large intra-cavity flux. However, in the presence of medium absorption or slow lower level removal, this recovery is incomplete (see Appendix A).

At the high buffer gas pressures necessary for rapid vibrational relaxation, the condition that the upper electronic state be kinetically isolated from lower states then establishes two requirements on the electronic structure:

(1) The upper laser level must not be predissociated by repulsive states arising from lower atomic asymptotes.

(2) The upper laser level must not be imbedded in the vibrational manifold of lower bound electronic states.

The fatality of predissociation is probably obvious since, even in the absence of collisions, the upper laser level may rapidly dissociate to lower atomic asymptotes. The disadvantages of imbedded potential curves results from the mechanism of electronic quenching by rare gas collisions. In the absence of curve crossings, binary collisions with rare gas atoms can convert only a small amount of internal energy into relative trans-lational energy. However, if one electronic potential curve lies imbedded within a lower potential curve, rare gas collisions can convert electronic energy in the upper state into vibrational energy in the lower state, with only a small net transfer of energy to the rare gas atom. The probability of such an $E \rightarrow V$ relaxation is approximately related to the Franck-Condon factors between the two electronic states. This means that, for imbedded but offset potential curves [as for $BaO(X^1\Sigma)$ and $BaO^*(A^1\Sigma^+)$], the inter-conversion can be quite rapid. For excited states whose potential curves are well removed from the lower states (as in the rare gas halides), there is poor overlap between low vibrational levels of the excited state and the very high (continuum) vibrational levels of the ground state that lie nearby in energy. Hence the electronic quenching by rare gas collisions is expected to be slow.

18

Two schemes are possible for removing the lower laser level: rapid vibrational relaxation or rapid dissociation. If the laser transition terminates on a bound lower vibrational level, effective vibrational relaxation is possible only if the lower laser level lies many kT above $v'' = 0$. Thus the lower electronic potential curve must be fairly deep and offset in internuclear distance. Collision-induced dissociation can be effective only if the lower electronic state is very shallow, so that the rate of dissociation can be fast enough. This point is discussed in some detail in the section on XeF (Section VIII). If the laser transition terminates on the repulsive portion of the lower potential curve, dissociation is automatically rapid, occurring in less than one vibrational period. However, the lower potential curve cannot be too repulsive or the gain profile will be too broad. Neither can it be extremely shallow (if it dissociates to ground state atoms) or the absorption by transient ground state molecules may become too severe.

Spectroscopic Classes

To guide the search for new laser candidates, we consider three possible classes of electronic states of diatomic molecules:

> Weakly bound excimers
>
> Strongly bound covalent states
>
> Excited states of ionic character.

Our emphasis so far has been on molecules of the third class. In the future our theoretical efforts will concentrate on the first two classes. We hope that a number of new candidates will be identified.

The class of weakly bound excimers has received considerable study, and several lasers have been demonstrated. The binding energies may vary from a few hundred cm^{-1}, as in XeO^*, to almost one electron volt in the rare-gas-excimers, such as Xe_2^*. Production of the upper laser level normally proceeds through three-body association reactions such as

19

$$O(^1S) + 2Xe \rightleftharpoons XeO^* + Xe \quad .$$
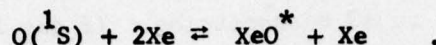
The laser transition may be between bound vibrational levels in both the upper and lower electronic states, as in XeO^*, or the lower laser level may be unbound, as in Xe_2^*.

In the search for new candidate molecules of this class, a number of potential problems must be overcome. The bandwidth may be large, and the stimulated emission cross section small, due to a steeply sloped lower laser level. The gain may be further reduced by the fact that not all the excited states may be simultaneously bound in the proposed upper laser level. In many cases the desired upper laser level is not the lowest excited state of the system. Reactive quenching may lead to a lower, more strongly bound state such as $Xe\,Na^* + Na \rightarrow Na_2^* + Xe$. Finally, if the excimer transition corresponds to an allowed transition in the excited state, atom absorption by transient lower-state molecules may be a serious impediment.
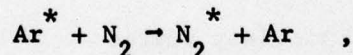
The vast majority of the electronic states of diatomic molecules are strongly bound with respect to their atomic asymptotes and are basically of covalent character. The obvious production schemes are energy transfer:

$$Ar^* + N_2 \rightarrow N_2^* + Ar \quad ,$$

chemical reactions of excited states:

$$Se^* + OCSe \rightarrow Se_2^* + CO \quad ,$$
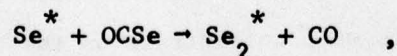
or photo excitation:

$$S_2 + h\nu \rightarrow S_2^* \quad .$$

The demonstrated or proposed laser transitions are normally dipole allowed and terminate on bound vibrational levels of the lower state.

20

The search for new candidates of this class is slowed by the typically complicated electronic level structure of the candidate molecules. Unfortunately, the energy transfer and chemical pumping reactions are not always selective in producing the desired electronic state. The rather h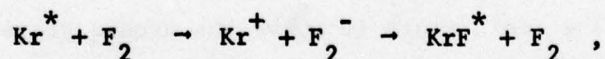igh density of electronic states often means that the proposed upper laser level may be easily quenched by collisions with the background (as was found to be the case in Ar/N_2). Finally, the lower laser level may be difficult to remove by vibrational relaxation (also found to be a problem in Ar/N_2).

Excited States of Ionic Character

Visible and uv laser development over the past few years has been dominated by the spectacular success of diatomic molecules with an isolated excited state that is predominantly of ionic character. This class of molecule includes the rare gas-halides (especially KrF, XeF, and ArF), the homonuclear halogens (I_2 and Br_2), and the mercury halides (HgCl and HgBr). It is obviously important to inspect this class of molecules in general to identify new promising laser candidate molecules.

A major advantage to these ionic states arises from the selectivity with which they can be produced, by harpooning reactions:

$$Kr^* + F_2 \rightarrow Kr^+ + F_2^- \rightarrow KrF^* + F_2 \ ,$$

by ion-ion recombination:

$$Xe_2^+ + F^- \rightarrow XeF^* + Xe \ ,$$
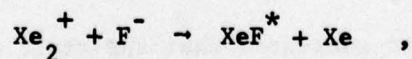
and by photodissociation:

$$HgBr + h\nu \rightarrow HgBr^* + Br \ .$$
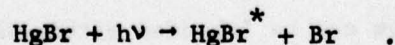
The large transition dipole moments common in these systems arise from the change from ionic character in the upper state to covalent

character in the lower state. The lower laser level may be bound (as in XeF, I$_2$, and HgCl) or unbound (as in KrF and ArF). Because of the strong coulomb binding in the upper state, it may be isolated, well below the Rydberg-type excited states of the molecule. The ionic nature of the binding and the isolation from other electronic states make the electronic structure simple to study theoretically.

Rules for Selecting Ionic Candidates

The rules we are about to suggest are illustrated on the energy level diagram shown in Figure 1. The notation used is that A is the electropositive atom (say, rare gas), and X is the electronegative atom (say, halogen). The various levels of the atom A are indicated by IP(A), ER(A), and EV(A) for the ionization potential, the energy of the lowest Rydberg-type excited state, and the energy of the highest valence-type excited state, respectively. The levels of atom X are referred to as EA(X), ER(X), and EV(X) for the electron affinity, Rydberg state energy, and valence state energy, respectively. The ionic potential curve is represented as dissociating to A$^+$ + X$^-$ at an energy of IP(A) - EA(X). The energy of the minimum in the ionic state is identified as EM, and the dissociation energy DI = IP(A) - EA(X) - EM.

Rule 1: The ionic state is above the ground state atoms.

$$EM = IP(A) - EA(X) - DI > 0 \quad \text{or}$$
$$IP(A) > EA(X) + DI$$

The intent of this rule is to guarantee that the state of predominantly ionic character is an excited state (as in the rare gas halides) and not the ground state (as in the alkali halides). Further, the requirement that the ionic potential curve not be imbedded within the ground state potential well will ensure that the minimum in the excited state will not lie vertically above the minimum in the ground state (as in the alkaline

22
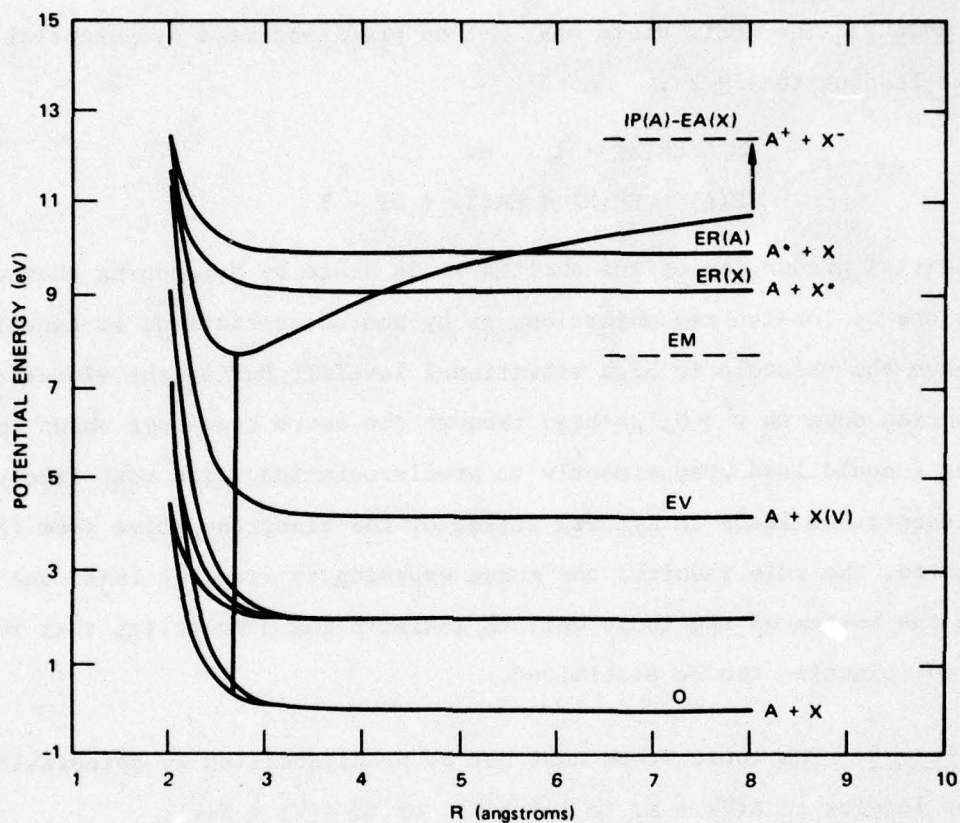
RULE 1: IONIC STATE IS ABOVE GROUND STATE

$EM = IP(A) - EA(X) - DI > 0$ OR

$IP(A) > EA(X) + DI$

RULE 2: IONIC STATE NOT PREDISSOCIATED
TO A + X*

$EM < ER(X) - 1$ OR

$IP(A) < ER(X) + EA(X) + DI - 1$

RULE 3: IONIC STATE NOT PREDISSOCIATED
TO A(V) + X, A + X(V), OR A(V) + X(V)

$EM > EV(A) + EV(X)$

$IP(A) - EV(A) > EA(X) + EV(X) + DI + 1$

RULE 4: IONIC STATE NOT PREDISSOCIATED TO
A* + X

$EM < ER(A) - 1$ OR

$IP(A) - ER(A) < EA(X) + DI - 1$

SA-6158-56

FIGURE 1   RULES FOR SELECTING MOLECULES IN IONIC STATES, ILLUSTRATED FOR
THE CASE OF KrO

earth halides) and that vibrational manifolds of the ground and excited states are not easily connected by background gas collisions (as in the alkaline earth oxides).

Rule 2: The ionic state must not be predissociated by potential curves leading to $A + X^*$.

$$EM < ER(X) - 1 \quad \text{or}$$
$$IP(A) < ER(X) + EA(X) + DI - 1$$

The initial production of the excited ionic state by harpooning chemical reactions by ion-ion recombination, or by photodissociation, is expected to leave the molecule in high vibrational levels. During the vibrational relaxation down to $v' = 0$, passage through the curve crossings shown in Figure 1 could lead predominantly to predissociation. The most likely predissociation leads to Rydberg states of the electronegative atom (X^*). As stated, the rule requires the curve crossing to occur at least one eV above the bottom of the ionic well to maximize the probability that the excited molecules can be stabilized.

Rule 3: The ionic state must not be predissociated by potential curves leading to $A(V) + X$, to $A + X(V)$, or to $A(V) + X(V)$:

$$EM > EV(A) + EV(X) + 1 \quad \text{or}$$
$$IP(A) - EV(A) > EV(X) + EA(X) + DI + 1$$

In general we seek to find the energy of the minimum of the ionic potential curve lying in the energy gap between the low-lying valance states of the atoms and the high-lying Rydberg states. To prevent easy collisional quenching or predissociation of the ionic states to the repulsive curves arising from the valance states of the atoms, we stipulate that the minimum must lie at least one eV above the highest of these asymptotes.

24

Rule 4: The ionic state must not be predissociated by potential curves leading to $A^* + X$.

$$EM < ER(A) - 1 \qquad \text{or}$$
$$IP(A) - ER(A) < EA(X) + DI + 1$$

The same arguments are used here as for Rule 2. All ionic states involving the halides and chalconides satisfy this rule.

Semiquantitative Description of Ionic Bonds

The rules described above for selecting new candidate molecules in ionic states contain only one missing parameter: the ionic bond strength DI. Following the pioneering work of Brau and Ewing [BE75a], we consider the well-studied example of the alkali halides. The goal is to establish some scaling procedure to estimate the bond strengths of other ionic bonds.

We begin by choosing a simplified Rittner potential

$$V_{AX}(R) \approx A_{AX} \exp[-\alpha_{AX}R] - e^2/R + IP(A) - EA(X) \quad .$$

The ion-dipole and higher order terms normally included [BK73] do not have a large effect within the accuracy we will need. For the short range exponential repulsion we will use the Born-Mayer representation of the Thomas-Fermi-Dirac interatomic potentials [Ab69]. Abrahamson [Ab69] has shown that we may use the combining rule

$$A_{ij}e^{-\alpha_{ij}F} - (A_iA_j)^{\frac{1}{2}} \exp\{-\tfrac{1}{2}(\alpha_i + \alpha_j)R\} \quad .$$

This formulation has been found to give a satisfactory description for the repulsions between like and unlike rare gas atoms. These atomic size parameters scale quite simply with atomic number as shown in Figures 2 and 3; namely, the α_i's vary slowly with the number of electrons, while the A_i's scale nearly as $Z^{1.5}$.

25
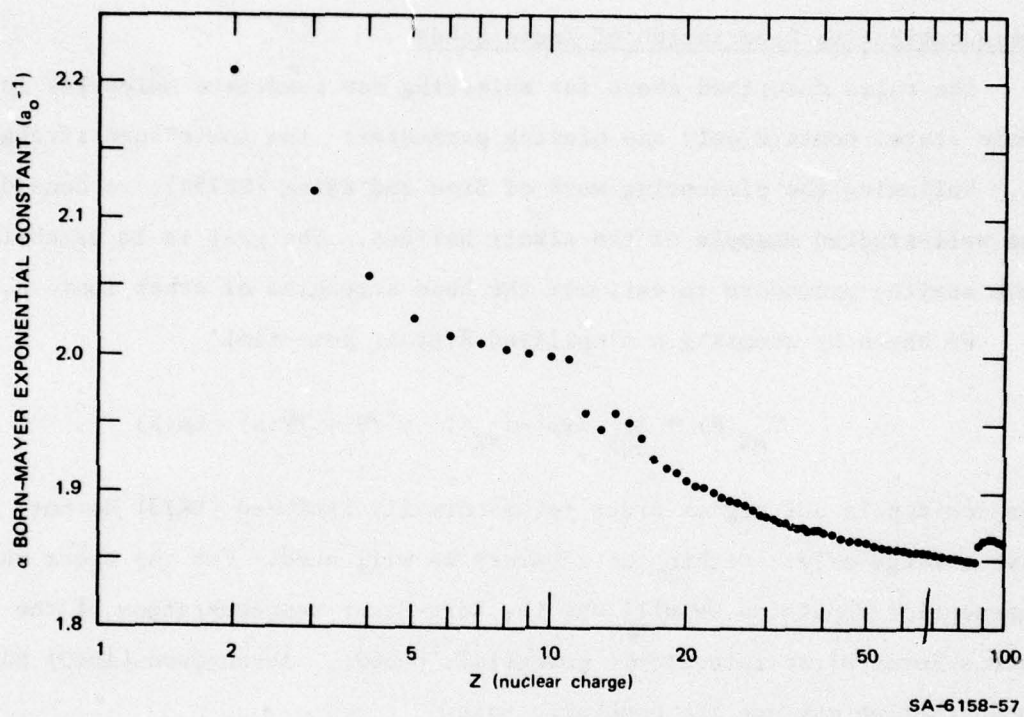
FIGURE 2   NUCLEAR CHARGE DEPENDENCE OF BORN-MAYER EXPONENTIAL
CONSTANT FROM ABRAHAMSON [Ab69]

26
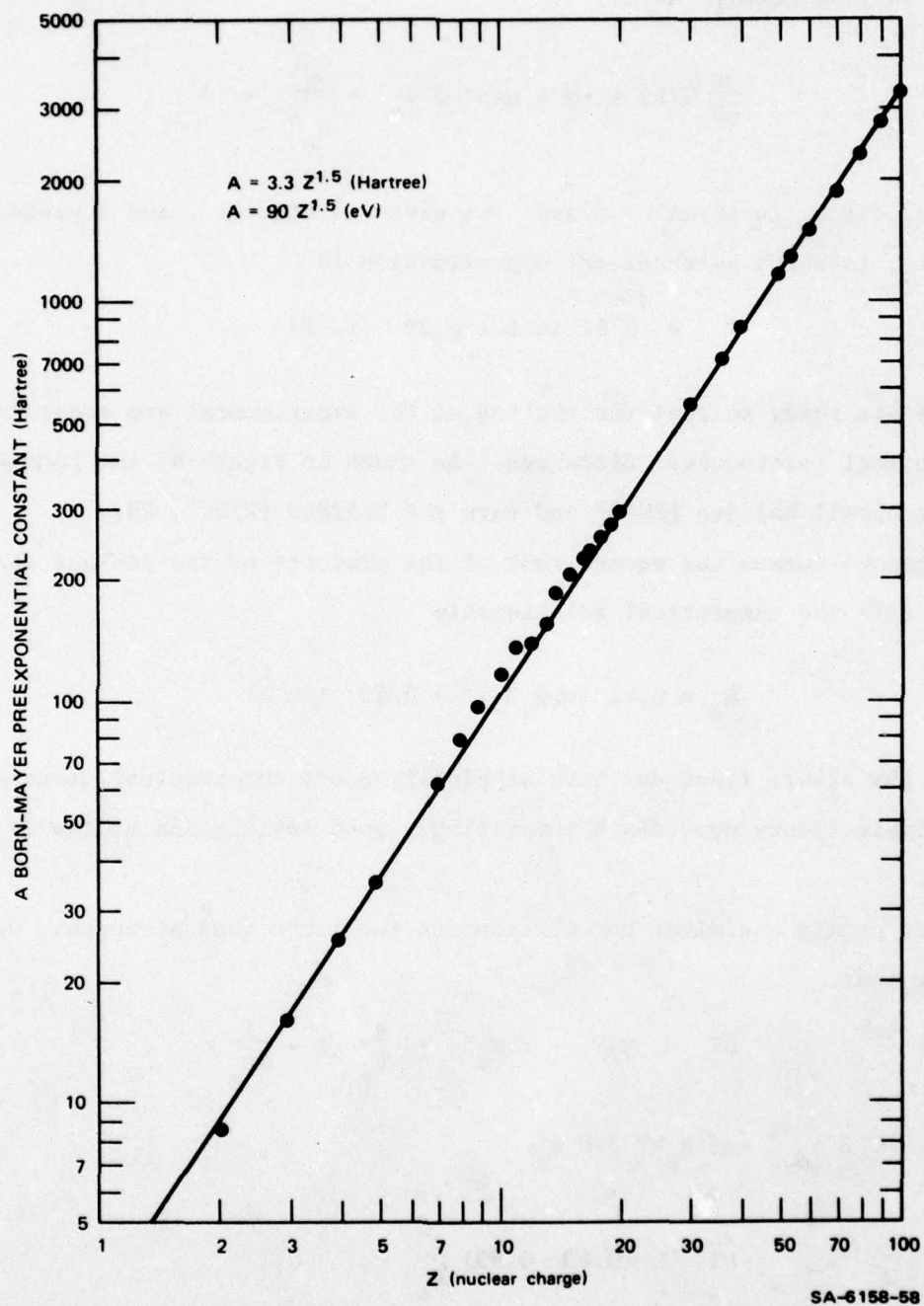
FIGURE 3   NUCLEAR CHARGE DEPENDENCE OF BORN-MAYER PREEXPONENTIAL
CONSTANT FROM ABRAHAMSON [Ab69]

27

To find the internuclear distance at the minimum in the ionic potential, we merely solve

$$\frac{d}{dR} V(R) = -\alpha\, A\, \exp(-\alpha\, R_e) + \frac{e^2}{R_e^2} = 0 \quad .$$

Solving for R_e in terms of α and A as given in Figures 2 and 3 yields results, to which an **excellent** approximation is

$$R_e = 0.61 \ln Z + 0.79 \quad (\text{in } \mathring{A}) \quad .$$

Now we are ready to test the scaling of the experimental and accurate theoretical internuclear distances. As shown in Figure 4, the bond lengths of the alkali halides [BK73] and rare gas halides [WKB77, DH77]. are graphed versus the square root of the products of the nuclear charges, along with the theoretical relationship

$$R_e = 0.61 \ln[Z_+ Z_-]^{\frac{1}{2}} + 0.79 \quad (\text{in } \mathring{A}) \quad .$$

While the alkali fluorides have atypically short internuclear distances, the simple theory provides a surprisingly good description of the major trend.

To obtain a similar correlation for the ionic bond strengths, we notice that

$$DI = V(\infty) - V(R_e) = \frac{e^2}{R_e} \left(1 - \frac{1}{\alpha R_e}\right) \quad .$$

Since $\alpha \approx 2\, a_o^{-1}$ and $R_e \approx 3\text{-}6\, a_o$

$$DI \approx (0.83 - 0.93) \frac{e^2}{R_e} \quad ,$$

then

$$\frac{1}{DI} \approx (1.1 - 1.2) \frac{R_e}{e^2} \quad ,$$

28
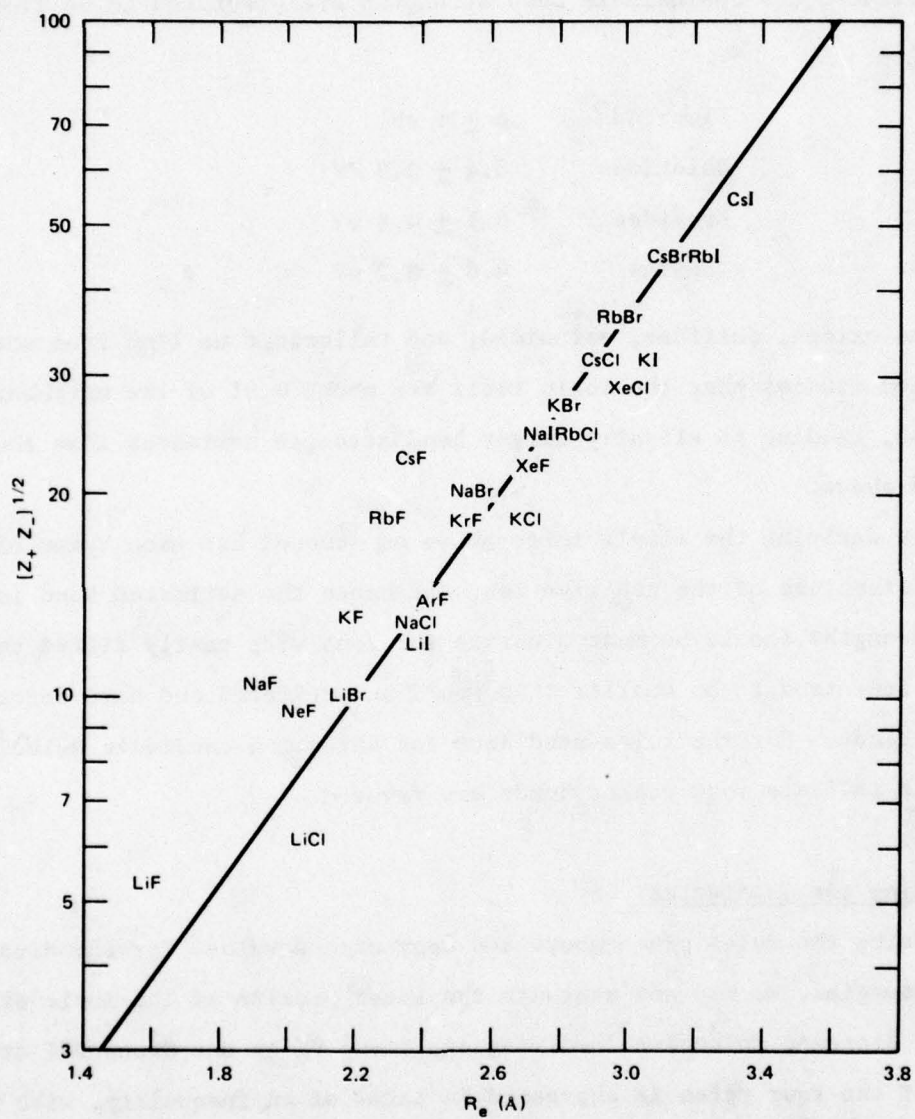
FIGURE 4   IONIC BOND LENGTH SCALING

and hence 1/DI should be approximately linear in $\ln(Z_+Z_-)^{\frac{1}{2}}$. The experimental and _ab initio_ data are shown in Figure 5. The line drawn is just an eyeball fit, but it demonstrates the nearly linear relationship. For the halides, the approximate bond strengths are predicted to be (for BX to BiX):

Fluorides	6 ± 1 eV
Chlorides	5.4 ± 0.9 eV
Bromides	5.1 ± 0.8 eV
Iodides	4.8 ± 0.7 eV .

For the oxides, sulfides, selenides, and tellurides we find from more detailed studies that the ionic radii are about 0.91 of the neighboring halides, leading to slightly larger bond strength estimates than those listed above.

In deriving the simple rules above no account has been taken of the shell structure of the positive ion, and hence the estimated bond lengths and strengths should be most accurate for ions with nearly filled shells. Other ions tend to be smaller than would be predicted and have stronger ionic bonds. But the rules used here for selecting candidate molecules tend to indicate that weaker bonds are favored.

Selecting the Candidates

Using the rules given above and approximate values for the dissociation energies, we may now evaluate the laser promise of the ionic states of all diatomic molecules involving one Group VI or one Group VII atom. Each of the four rules is expressed in terms of an inequality, with properties of the electropositive atom on the left (ionization potential, excitation energies) and properties of the electronegative atom on the right. Using the bond strength estimates above, we can numerically express the right-hand side of the inequalities as in Table 2.
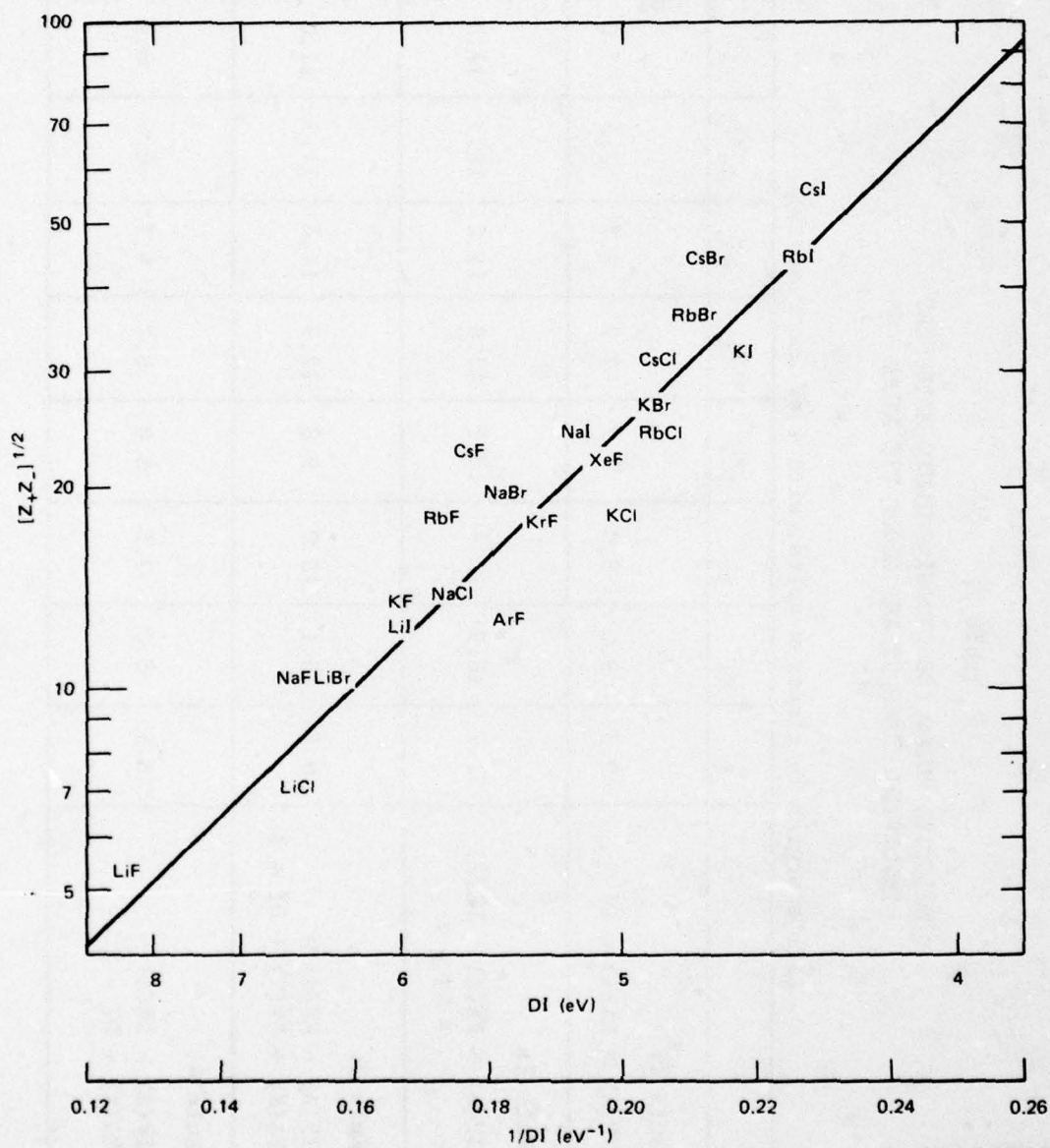
FIGURE 5   IONIC BOND STRENGTH SCALING

SA-6158-54

Table 2

SIMPLIFIED RULES FOR CHOOSING IONIC MOLECULES
INVOLVING GROUP VI AND GROUP VII ATOMS

(All energies in electron volts, with 1 eV uncertainty)

	F^-	Cl^-	Br^-	I^-	O^-	S^-	Se^-	Te^-
Rule 1: IP(A) > EA(X) + DI	9.5	9.0	8.5	7.9	7.7	7.7	7.5	7.0
Rule 2: IP(A) < EA(X) + ER(X) + DI - 1	21.2	16.9	15.4	13.7	15.8	13.2	12.5	11.5
Rule 3: IP(A) -› EV(A) > EA(X) + EV(X) + DI + 1	10.5	10.1	10.0	9.8	12.9	11.4	11.3	11.0
Rule 4: IP(A) - ER(A) < EA(X) + DI - 1	8.5	8.0	7.5	6.9	6.7	6.7	6.5	6.0

To decide how favorable the diatomic AX might be, we simply compare the ionization potential of atom A with the rule 1 and rule 2 entries in Table 2. If the candidate molecule fails the test by more than 1 eV, we reject it altogether. If it is within $\pm$ 1 eV of the criterion, we list it as a possible candidate. If the molecule passes all the tests by at least 1 eV, it is listed as a good candidate.

To apply rules 3 and 4, we must first subtract from the ionization potential of atom A, the energy of its highest valence state EV(A) or the energy of its lowest Rydberg state ER(A) and compare the result with rule 3 and rule 4 entries in the table. If there are no valence excited states, we use rule 1 instead of rule 3. In ambiguous cases, we can improve the reliability of the estimates by taking the ionic bond strength from Figure 5.

Application of rules 1 through 4 to the diatomic halides and chalconides of all elements in the periodic chart leaves very few survivors, which are listed in Table 3. Not surprisingly, several of the best candidates have already received active investigation (the rare gas halides and homonuclear halogens). The interhalogens and Group IIB metal halides are now under study in our laboratory and in a number of other laboratories. Our experimental efforts to date are described in the following sections.

Table 3

IONIC EXCITED STATES OF DIATOMIC MOLECULES

Good Candidates

($\lambda > 325$ nm) visible	($\lambda < 325$ nm) uv
XeF, ICl, IBr, I$_2$	ArF, KrF, KrCl, XeCl, XeBr
ZnBr, ZnI, CdBr, CdI	F$_2$, ClF, Cl$_2$, BrF, BrCl, Br$_2$
HgCl, HgBr, HgI	HF, HCl, HBr
KrO, XeS	KrO

Possible Candidates

($\lambda > 325$ nm) visible	($\lambda < 325$ nm) uv
IO, IF, AsI	NeF, ArCl, KrBr, XeI
ZnCl, CdCl	HI
HgS, HgSe, HgTe	NBr, PI

III. EXPERIMENTAL APPARATUS AND PROCEDURES

The experiments reported here were performed on one or more of three experimental sites: (1) the Febetron 706 facility used in the work described in the preceding series of reports [EGH73, HGH74, HGH75, GHH75, MLH76, NHL76], (2) the electron accelerator facility described in the report [MLH76], and (3) a 50-cm electron-beam (Excitron) facility at Maxwell Laboratories, Inc.

Febetron Fluorescence Studies

The experimental system, shown schematically in Figure 6, is similar to those described in our previous reports. Optical emissions, resulting from pulsed electron-beam excitation of a high pressure gas, are viewed by a spectrometer and recorded on film or digitally by an optical multichannel analyzer or transient digitizer. A Febetron 706 (Hewlett Packard) provides a 3 nsec, 2000 A cm^{-2} pulse of 500 keV electrons, which enter a stainless steel experimental cell through a 1-mil Inconel foil. The cell has windows made of MgF_2 and is designed to operate with sample gas pressures between 200 and 10,000 torr (approximately 0.25 to 15 atmospheres). By evacuating both the spectrometer and the passage between the cell window and the spectrometer entrance slits, we can study the spectral range from below 130 nm to the infrared. The cell and reservoir for nonvolatile additives can be independently cooled or heated (from about -50° to +200°C). The gases are mixed in the cell and, for the XeF studies, are replaced after every shot.

The optical emissions can be viewed through a 0.5-meter monochromator/ spectrograph (McPherson 216.5). Time integrated spectra of the emissions are taken on either Kodak Tri-X (400 ASA) or Polaroid Type 57 (3000 ASA) film. Band structures and wavelengths are then determined with the aid
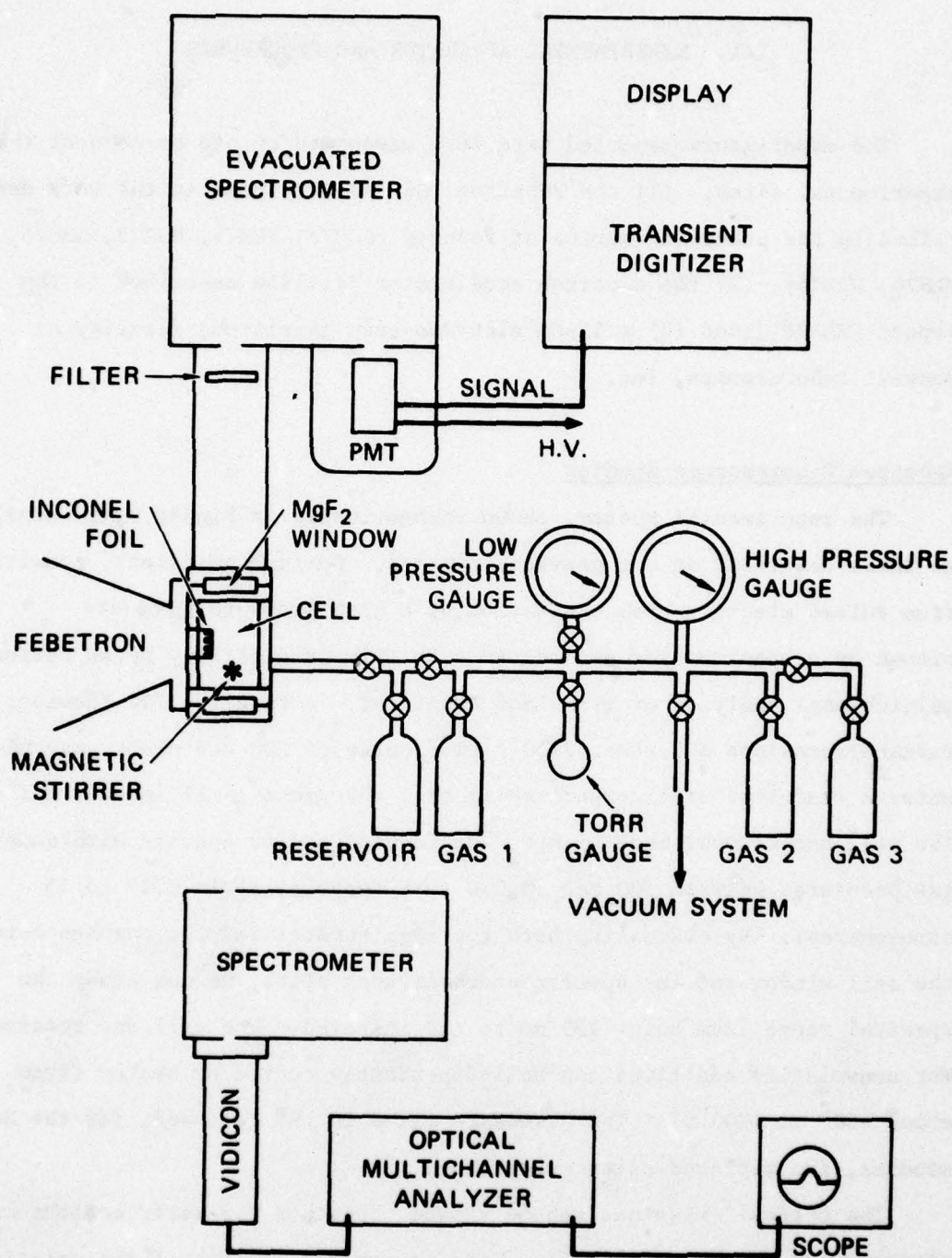
FIGURE 6   SCHEMATIC OF FEBETRON FLUORESCENCE APPARATUS

36

of either a microdensitometer or a travelling microscope. The temporal behavior of the emissions are recorded and analyzed by a Tektronix Transient Digitizer System (WP2222) from the output of a photomultiplier tube (RCA 1P28). The photomultiplier tube (PMT) is coated with sodium salicylate for detection of vuv emissions. The photon detection system, including lenses, spectrometer, and photomultiplier tube, has been calibrated so that the absolute intensity of each emission feature can be determined. The time-integrated spectrum can also be recorded using an Optical Multichannel Analyzer (Princeton Applied Research 1205A).

We have calibrated the fluorescence yield measurements in much the same way as was reported earlier [NHL76, MLH76, GHH75, HGH74]. The energy deposition from the e-beam is measured by determining the N_2 second positive (2+) band emission from Ar + 5% N_2 mixtures excited in the same experimental apparatus. The fluorescence yield for this system was determined in our previous studies to be 17.6%/P (for $P \geq 1$), where P is the argon pressure in atmospheres. Therefore, by measuring the total photon emission in the band under study and comparing it with that observed from the $N_2(2+)$ at the same argon pressure, we can determine the fluorescence yield. For the Ne/Xe/NF$_3$ studies, we have assumed that the neon excitation produced by the electron beam is one-half that of argon at the same pressure.

Febetron Absorption Studies

The substantial excited state densities produced by Febetron excitation (10^{14} to 10^{16} cm^{-3}, depending on the rare gas and pressure) are conveniently studied in absorption as well as fluorescence. For transitions with large stimulated emission cross sections, the transient gain is also subject to investigation over the 2-cm optical path. Such absorption measurements are described in some detail in a recent report [HZN77].

The layout of the apparatus for the current experiments is presented in Figure 7. The output from a flashlamp-pumped dye laser or from a cw
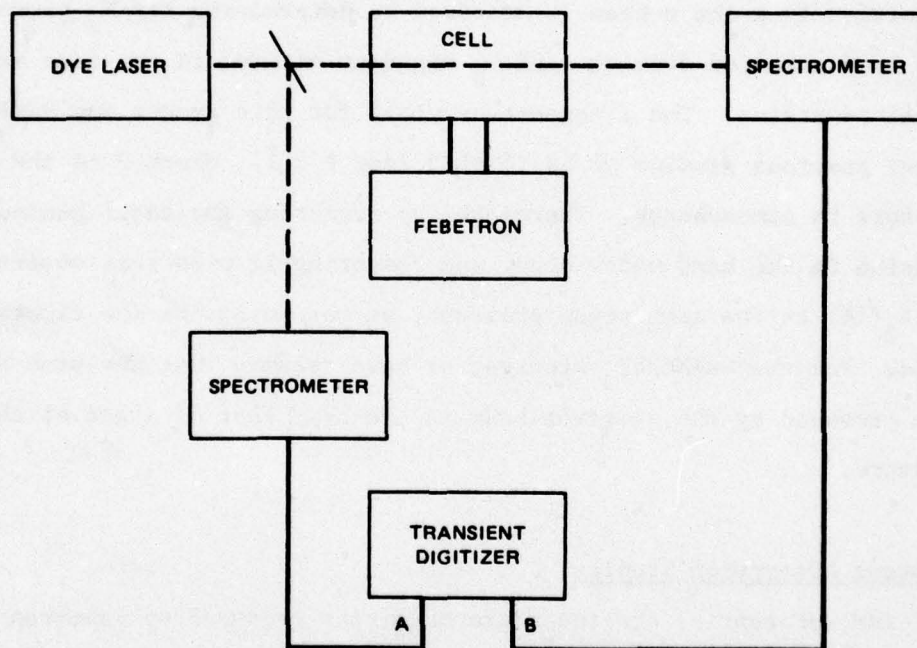
FIGURE 7   SCHEMATIC OF FEBETRON ABSORPTION APPARATUS

SA-6158-50

38

argon-ion pumped dye laser is passed through one of the Febetron cells
and detected by the standard spectrometer/photomultiplier tube/digitizer
instrumentation. In the pulsed dye laser experiments a reference beam
is split off, while in the cw dye laser experiments the reference level
is obtained from the transmitted signal before firing the Febetron.

Accelerator Fluorescence Studies

Most of our fluorescence kinetics studies of the mercury halides
were conducted on our low-current electron accelerator facility. This
device produces an electron beam current of approximately 1 μA at an energy
of 175 keV. The beam can be pulsed for kinetic studies, modulated for use
with phase sensitive detectors, or run cw. Several target cells were used
to contain the gas mixture under study. The accelerator tube terminates
in a flange that accommodates any of the cells used with the Febetron 706
excitation source (see above). To establish a reasonable vapor pressure
(few torr) of the species being studied (particularly atomic mercury and
mercuric chloride), the cells were heated to temperatures in the range
180° to 270°C.

The initial studies used static gas fills of argon, halogen-bearing
compounds, and metallic mercury. Under these conditions, HgX emissions
could be observed for a few minutes to an hour or so, depending on the
mixture. During this time the emissions decreased in intensity as the
emitting additives were apparently consumed. To avoid this limitation,
we constructed a gas-handling system that would allow the reactants to
flow through the cell; this was similar to the system later used for the
long path studies with the 50-cm long e-beam. A schematic diagram of
the system is shown in Figure 8. This system was designed to introduce
mercury vapor into the cell by saturating a stream of argon gas with
mercury vapor as the argon flows through a heated mercury reservoir. A
mixture of argon and halogen (e.g., 1% Cl_2 or 3% CCl_4) was introduced into

39
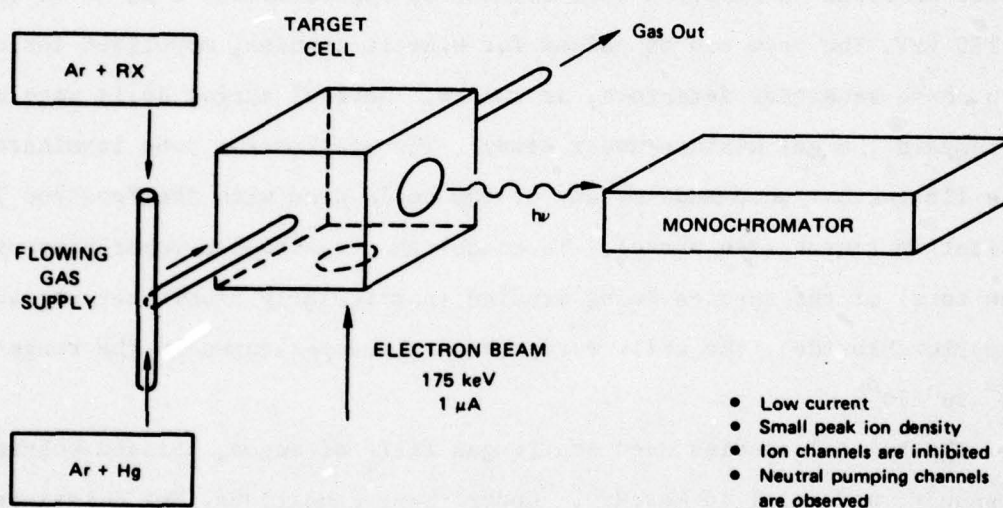
FIGURE 8   SCHEMATIC OF THE LOW-CURRENT ELECTRON-ACCELERATOR APPARATUS USED FOR MERCURY HALIDE FLUORESCENCE EXPERIMENTS

this stream near the excitation region. The mixed gases flowed 3 cm •
through a ¼-inch diameter stainless steel tube before entering the larger
volume chamber where electron excitation took place. Flow rates were
monitored with a ball type flow meter. The total flow was varied over
the range 1 to 4.5 sccm. With this arrangement we were able to make
spectral observations for an extended period of time.

Spectroscopic data were taken using a 0.2-m monochromator (Jobin-
Yvon) scanned by a stepping motor. The detector in this case was a
1P28 photomultiplier (S5 response). Signal-to-noise enhancement was
obtained by the use of a lock-in amplifier (PAR 124) or by photon counting
using a multichannel analyzer operated in the multiscaler mode and
synchronized to the stepping motor drive. For the data discussed in this
report, no extensive studies were made of the time dependence of the
emissions.

50-cm Excitron Studies

A major component of the research under this contract consists of
studies of the properties of laser candidate systems using a 50-cm
electron beam source with nominal beam conditions of $j_B = 10$ A/cm^2,
$E_b = 350$ keV, and $\tau_{pulse} = 1$ μsec. This e-beam device was ordered at
the inception of the contract period from Maxwell Laboratories, Inc. (MLI)
and was delivered on 2 August 1977. During this same time, a laboratory
with the required support equipment was prepared, and the experimental
apparatus, including a test cell and vacuum and gas handling systems, was
designed and built.

To acquire experimental results in advance of e-beam delivery, a
cooperative arrangement was made with MLI, whereby in May 1977 our test
cell and support equipment were transferred to MLI and coupled with MLI's
existing 50-cm e-beam device. From that time through August 15, experi-
ments were carried out jointly by SRI and MLI personnel--an arrangement
that proved very productive and mutually beneficial.

41

Apparatus

The e-beam device, designated an Excitron 100-10, consists of a six-stage Marx bank coupled to a single-bladed field-emitting diode of 50-cm length through a single solid feedthrough. The characteristics of the device are summarized in Table 4. It is installed and operational, and experiments have recently begun.

The laser test cell is designed for operation at 200°C and has been operated at pressures up to four atmospheres. The cell is constructed from stainless steel; outside dimensions are 7.5 x 7.5 x 58 cm; the gas chamber is 2.5 x 3.1 x 50 cm. The interface to the e-beam is through a 1-mil Ti or Inconel foil window, which has an aperture of 2 x 50 cm. Seals between cell and faceplate and between cell and foil are Viton O-rings. The cell is fitted with a pair of 1-inch diameter quartz windows viewing transverse to the cell axis and with Brewster-angle windows on the long axis of the cell. Attachments to the cell are made with Conflat flanges sealed with Viton flat gaskets (Varian). The cell is heated on three surfaces by handmade surface heaters consisting of shielded resistance wire spot-welded to formed sheet stainless steel. The cell and heaters are encased in 1-inch thick insulation held in place by an aluminum cover.

The gas-handling system was designed from the beginning to be used with continuous flow for two reasons: (1) the test gas mixture can be changed much more rapidly when species are introduced and removed by convection rather than diffusion and (2) because many candidate laser systems involve gases that react, both in their ground states and in excited states, it is essential to remove products and introduce fresh reactants as rapidly as possible. The reactivity problem, in particular, often makes it essential to mix the test gases as near as possible to the upstream end of the laser cell and to flow the gases at a high rate. For the $Ar/Xe/Hg/CCl_4$ system that produces the $HgCl^*$ laser, for example,

42

Table 4

CHARACTERISTICS OF EXCITRON 100-10 ELECTRON-BEAM SOURCE

Geometric

Marx tank dimensions:	4 ft L x 3 ft W x 4 ft H
Diode tank dimensions:	14 in. L x 39 in. W x 14 in. H
Console dimensions:	22 in. L x 22 in. W x 72 in. H
Diode length:	50 cm
Foil dimensions:	50 cm L x 2 cm H

Electrical

Type:	Marx rundown
Voltage:	$\leq$ 450 keV
Current:	1 to 30 A/cm^2 variable
Current risetime:	150 ns to 70% at 10 A/cm^2
Current uniformity:	$\pm$ 10% at 10 A/cm^2
Pulse length:	0.3 to 1 μs variable
Marx stages:	6 at 75 keV

Diagnostics

Diode voltages and total current (B-probe)

Marx charging voltage and changing current

Diode chamber pressure:
Switch gas pressures:

43

reproducible results could be obtained only by flowing at 1200 sccm (760 torr cm^3/min), which at 2 atm test pressure, constitutes a gas replacement time in the cell of 1 minute.

The flowing system was achieved by placing minor constituents in variable-temperature reservoirs and by flowing the rare-gas hosts through these reservoirs. The temperatures of the reservoirs and the rare-gas flow rates were varied to achieve the desired species mixtures. Downstream of the laser cell, two cold traps in series were used to remove both reactants and products from the exhaust flow. The test cell and gas-handling system are shown schematically in Figure 9 for the case of the Ar/Xe/Hg/CCl$_4$ system.

Diagnostics

The diagnostic measurements of interest in these experiments include absolute energy deposition, absolute sidelight fluorescence, gain or absorption, spectrometry, and laser cavity output. These will be described in turn.

Energy Deposition--Absolute energy deposition measurements are made by measuring the transient pressure rise associated with the gas heating due to electron excitation. It can readily be shown that, if ΔH is the energy deposition in joules/cm^3, then the pressure rise, Δp, in atm is

$$\Delta p = \frac{20}{3} \Delta H \quad .$$

The pressure rise is measured on millisecond time scales using a Validyne Model DP15 differential pressure transducer in conjunction with a CD12 transducer indicator. The maximum frequency response of this system is ~ 1 kHz, which is sufficient to detect the pressure and expansion waves that accompany the nonuniform, impulsive pressure rise in the cell.

In the experiments conducted at MLI, we attempted to interpret the results on the basis of these highly unsteady signals. However, more

44
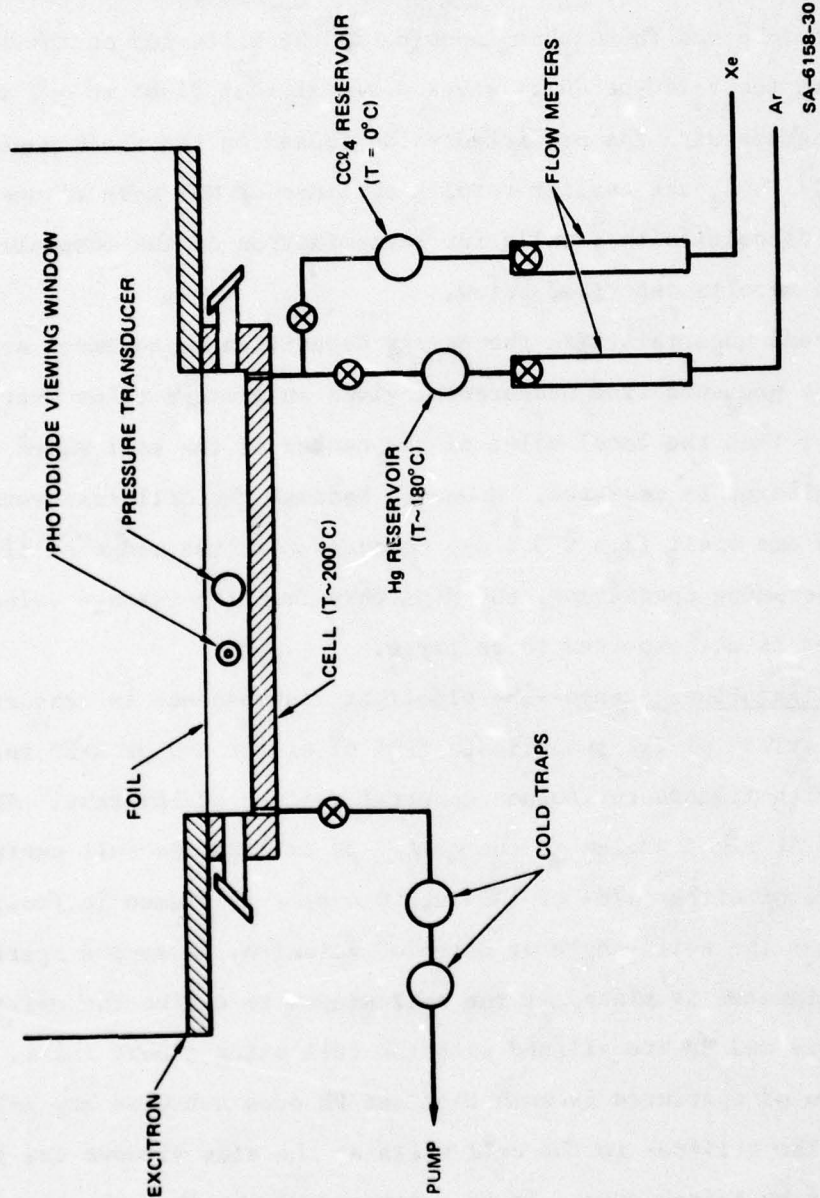
FIGURE 9   SCHEMATIC OF TEST ARRANGEMENT FOR Ar/Xe/Hg/CCl₄ STUDIES

SA-6158-30

45

recent study at SRI indicates that the initial response of the gauge to a very fast pulse is influenced by a dynamic ringing that can overshadow the true dynamic response. We carried out tests using weak pressure waves in a shock tube and found that imposing 200-Hz filtering on the signal (built into the Validyne CD12) gives a signal that rises in $\sim$ 2 msec and that agrees with the predicted value (based on the shock wave equations) within 5%. Thus, the earlier results obtained at MLI have an uncertainty in energy deposition that calls for reexamination of the absolute yields of all the results described below.

A second uncertainty in the energy deposition measurement arises because the pressure rise measurement gives an average value over the cell rather than the local value at the center of the cell where the optical emission is measured. However, because the cell transverse dimensions are small (2.5 x 3.1 cm) compared with the range of electrons at most operating conditions, the departure from the average value at the cell center is not expected to be large.

Sidelight Fluorescence--The sidelight fluorescence is measured using one of a variety of ITT photodiodes (PD) of either S-5 or S-20 response, together with filters to isolate spectral regions of interest. The PD is positioned at right angles to the cell $\sim$ 30 cm from the cell centerline. An aperture of either 1/8- or 1/4-inch diameter is placed in front of the PD to define the solid angle of detected emission. A second aperture of 1/8-inch diameter is placed at the cell window to define the emitting area. The aperture and PD are aligned with the cell using a HeNe laser. The combination of apertures is such that the PD does not view any solid surface. The orifices in the cell walls at the side windows are 1/4-inch in diameter by 1-inch deep. It is estimated [HT77] that the electrons penetrate these orifices no more than one diameter deep, and we assume that the emitting volume is 1.25 inches long (the cell width plus one orifice diameter).

With the emitting volume and solid angle known, the absolute fluorescence intensity can be determined from the PD signal if the PD is calibrated. In fact, all ITT PDs are furnished with individual calibration curves, estimated by the vendor to be accurate to $\pm$ 10% in average response over the surface, with local variations on the surface also not exceeding $\pm$ 10%. However, recent tests indicate that the S-20 PD used in the MLI phase of the experiments gives results that are lower by about a factor of 2 than at least two other PDs. This tube will be recalibrated; however, until these calibration problems are removed, there remains a uncertainty in the values of fluorescence yield reported below.

Gain/Absorption--These measurements are carried out using as a probe an NRG dye laser pumped by an NRG N_2 laser. This pump source was modified by the vendor to replace the spark gap with a thyratron so that it could be triggered externally to synchronize with the e-beam pulse. The dye laser pulse length is $\sim$ 3 nsec and the bandwidth is $\sim$ 0.3 $\overset{\circ}{A}$. The output beam is split into probe and reference channels. In the experiments at MLI, these pulses were attenuated and measured by photodiode signals on a fast oscilloscope. Before each test, several sample ratios of probe to reference signal were measured for comparison with the results during the shot. Thus, this technique measures only the transient gain or absorption. At SRI, we have available an energy ratio meter (Laser Precision Model Rk-3232 with RkP-335 probes) that we hope will allow us to measure static absorptions by gases as well as transient absorptions during the pulse.

Spectrometry--In the experiments at MLI, a Jarrell Ash 3/4-meter spectrograph was used to record both fluorescence and laser signals photographically. At SRI, the laboratory is equipped with a SPEX Model 1402 3/4-meter monochromator for either photographic or time-resolved recordings. In addition, various smaller spectrometers and monochromators are available.

<u>Laser Cavity Studies</u>--As noted above, the test cell is fitted with
Brewster windows, and it is straightforward to add external mirrors to
form an optical cavity. We can then carry out desired diagnostics on
the laser pulse, including spectroscopic detection, time histories of
laser pulses using photodiodes, and laser energy measurements.

Achievements

Work carried out during the reporting period has satisfactorily
established the equipment and the techniques for carrying out long-path
e-beam studies on laser candidate systems.   Measurement of absolute
fluorescence yields, while subject to some uncertainty in the experiments
reported here, greatly increases our ability to understand and evaluate
the systems studied. The efficiency of the gain measurement technique
has been demonstrated by successful application to several molecular
systems including Ar/Hg, Xe/Hg, $Ar/Xe/Hg/CCl_4$, Ar/ICl, and $Ar/Hg/Cl_2$.
Finally, laser demonstrations were carried out on $XeCl^*$ and $HgCl^*$ (e-beam
sustained discharge).

The design of a heatable cell and flowing gas-handling system proved
very useful, perhaps essential, in studies of $Ar/Xe/Hg/CCl_4$, $Ar/Hg/Cl_2$,
Ar/ICl, and Ar/I_2. Problems of reagent reactivity in several of these
systems suggest many experiments that require these experimental
capabilities.

Perhaps the most interesting results during the period were from
studies of the $Ar/Hg/Cl_2$ system, leading to demonstration on the e-beam
stabilized discharge laser on $HgCl^*$ at MLI in August 1977. This exciting
accomplishment suggests considerable follow-on study of this and other
Hg-halogen systems.

IV. CANDIDATE CONFIRMATION

Background

Considering the variety of molecules that have been suggested as candidates for the laser medium, some reasonable experimental criteria were needed for supporting continued studies including laser demonstration. With some molecules trivial technical constraints would provide an immediate rejection (e.g., very low vapor pressure). However, most of the new candidates suggested on the basis of theoretical analysis (see Section II) also had reasonable vapor pressures and handling characteristics.

In the initial survey we relied heavily on the demonstration of at least a modest fluorescence yield as a first criterion. The fluorescence yield (FY) is defined as the number of photons emitted per cm^3 divided by the number of primary excitations produced per cm^3. It is a convenient criterion for screening laser candidates since it provides a lower bound for the branching ratio for production of the upper laser level:

$$FY = BR \cdot \eta_{rad}$$

where η_{rad} is the radiation efficiency (Einstein coefficient divided by the sum of the Einstein coefficient plus the quenching frequency) and BR is the kinetic branching ratio for production of the excited state. Further, in the absence of absorptions, the fluorescence yield can be related to the small signal gain of the laser. As a criterion it is limited because a small fluorescence yield does not necessarily indicate a poor laser molecule. A rapid quenching reaction may reduce the fluorescence yield even though the upper state production may be large. In the absence of absorption, quenching may be circumvented by rapid stimulated emission (operating at flux levels well above the saturation flux) as discussed in detail in Appendix A.

49

The primary experimental tool used in measuring fluorescence yields was the Febetron 706. A PAR Optical Multichannel Analyzer was normally used as the detector. The versatility and ease of operation of this instrument was ideal for this work, the major limitation being rather nonlinear response below 390 nm. In all cases the standard for FY determinations is the second positive emission from N_2(C-B transition); this has been discussed in detail elsewhere [HGH74].

This experimental program has supported the potential of several of the candidates that were suggested on theoretical grounds above: ICl, IBr, and the mercury halides HgCl and HgBr. Further investigations of these systems, as well as the rare-gas/mercury system, are described in detail in subsequent sections of this report. Several other potential candidate systems were less spectacular in their light output and have not been investigated in detail. These are briefly noted here.

Ionic to Covalent Transitions in KrO

Theoretical estimation of the Kr^+O^- potential curves yielded the following suggested transition wavelength:

$$Kr^+O^- \rightarrow KrO(^1S) \qquad \sim 430 \text{ nm}$$
$$\rightarrow KrO(^1D) \qquad \sim 230 \text{ nm}$$
$$\rightarrow KrO(^3P) \qquad \sim 180 \text{ nm}$$
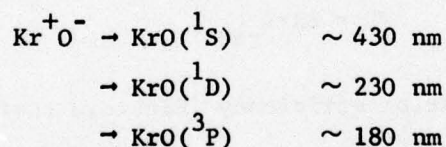
The 180 nm transition had been observed previously [GT74]. The gas mixture used was 1500 torr argon, 100 torr krypton, and 5 torr N_2O. A weak emission was seen at 180 nm, but nothing was seen at 430 and 230 nm. With 3 atm of krypton and 0.7 torr of N_2O, very weak emissions were seen at 180 and 225 nm. An unsuccessful search was made for analogous transitions in xenon, N_2O mixtures.

50

The Halogen Oxides ClO, BrO, and IO

In the gas mixture of 1 atm Ar, 5 torr N_2O, and 1 torr Cl_2 a very weak broad emission was seen in the vicinity of 400 nm, but this was partially due to window fluorescence by x rays. ClO emissions were expected near 407.6, 395.7, 384.1, 373.0, and 362.5 nm. When I_2 or Br_2 was substituted for Cl_2, no emissions were observed that could be attributed to IO or BrO.

S_2(B-X) Emissions

The recent demonstration of laser action on the B-X transition in S_2 by photon pumping [LK77] suggested that e-beam pumping is possible. The S_2(B-X) vibrational bands from 330 to 520 nm were monitored for a variety of sulfur donors. In the gas mixture of 5 atm argon and a few torr of CS_2, rather weak S_2(B-X) emissions were observed. This was also true when H_2S was used. However, when OCS was used as an additive, we measured a modest fluorescence yield of *approximately ½% from the* S_2 emissions. This yield is still quite low, but suggests that alternative S_2 sources may offer some hope for improvement.

Other Systems

Several of the candidate molecules suggested above on theoretical grounds have yet to receive experimental investigation. The most promising of these are HgI and the zinc and cadmium halides. It is anticipated that the theoretical rules now under development for selecting laser candidate molecules in weakly bound excimer states or strongly bound covalent states will suggest a number of interesting systems to be investigated.

V.   THE INTERHALOGENS ICl AND IBr

In the past, laser action has been demonstrated on ionic-to-covalent transitions in Br_2 [MST76, EJM76] and I_2 [BAB75,EB75b,HHT76] near 290 and 343 nm, respectively. The heteronuclear halogen molecules ICl and IBr have similar ionic-to-covalent transitions and were identified in our theoretical task as having favorable electronic structure, quenching behavior, and transition wavelengths. We investigated the time and pressure behavior of the fluorescence from mixtures of argon and various halogen donors. The highest fluorescence yields obtained were 25% in the 385 nm band of IBR and in each of the two ICl bands (at 340 and 430 nm). Because ground state ICL and IBr both absorb at their respective emission wavelengths, we examined the production of ICl^* and IBr^* in mixtures such as argon with HI + CO_2 and HI + HBr. The mixtures tried so far have produced substantially fewer excited states than pure Ar/ICl and Ar/IBr.

We briefly investigated the transient gain in Ar/ICl electron beam excitation at Maxwell. A value of approximately 4×10^{-3} cm^{-1} was measured, insufficient to overcome the ground state absorption. The absorption in IBr should be substantially less, and laser action should be demonstrated soon. Efficient extraction will probably depend on finding alternate halogen donors.

Fluorescence Yields and Kinetics

During the initial studies of I_2, Br_2, and Cl_2 [MLH76] when the gas under study was changed from one halogen to another, we observed some weak spectra that could not be attributed to the homonuclear halogens. It appeared possible that these spectra were due to mixed halogens, e.g. ICl, IBr, or BrCl, produced in the e-beam excitation process, and might

53

be potential laser candidates if the fluorescent yields were high. Samples of ICl and IBr were introduced into our gas cell from a cooled reservoir, excited by the Febetron in a rare gas background, and the spectra, fluorescent yields, and decay frequencies were obtained. Exact knowledge of the halogen pressures is hard to obtain as noted earlier for I_2 [MLH76] but was derived from the measured vapor pressure curves [CG65].

ICl in Ar showed two strong emission systems, peaking near 340 nm and 430.0 nm with a weaker but sharp band at 348.0 nm. IBr showed a weak, sharp band at 354.0 nm and a characteristic halogen emission system peaking at 385 nm. With krypton as the rare gas donor, the long wavelength emission systems were missing in both interhalogens. I_2 bands were present in ICl, and I_2 and Br_2 bands were present with IBr, suggesting that the excitation proceeded through reactions of excited halogen atoms:

$$Ar^* + ICl \rightarrow Ar + I^* + Cl$$
$$I^* + ICl \begin{cases} I_2^* + Cl \\ I + ICl^* \end{cases}.$$
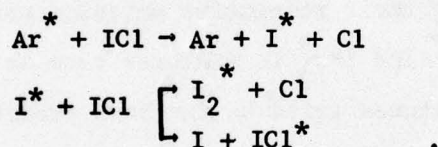
The decay frequency of the ICl emissions was found to be linear in the ICl pressure (see Figure 10) and essentially independent of the argon pressure. The rate coefficient derived from the decay data shown in Figure 10, $k = 5 \pm 10^{-10}$ cm^3 sec^{-1}, should probably be assigned to the reaction of I^* with ICl. The highest fluorescence yields observed were approximately 25% in the 385 nm band of IBr and in each of the two ICl bands (at 340 and 430 nm). The optimum additive pressure was 0.5-1 torr in both cases. The fluorescence yields dropped by about a factor of 3 at 4 torr. No evidence was observed for an argon pressure dependence of the fluorescence yield.
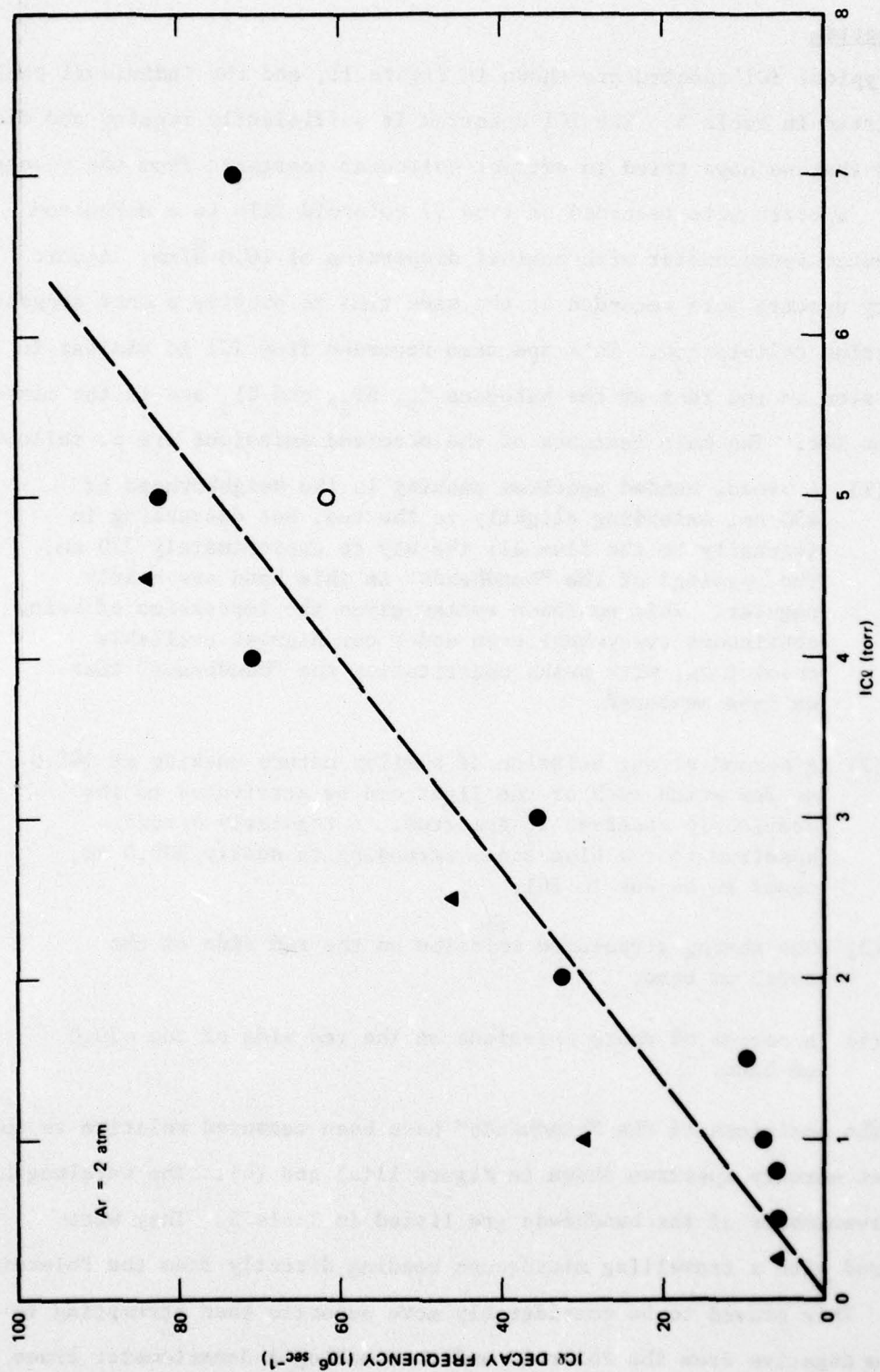
FIGURE 10 ICℓ PRESSURE DEPENDENCE OF THE ICℓ* DECAY FREQUENCY

IC1 Spectra

Typical IC1 spectra are shown in Figure 11, and the individual peaks are listed in Table 5. The IC1 spectrum is sufficiently regular and dispersed that we have tried to extract molecular constants from the spectra taken. Spectra were recorded on type 57 Polaroid film in a McPherson half-meter spectrometer with nominal dispersion of 16.8 $\overset{o}{A}$/mm. Atomic mercury spectra were recorded at the same time to provide a more accurate dispersion calibration. This spectrum recorded from IC1 is similar to those seen in the rest of the halogens I_2, Br_2, and Cl_2 and in the mixed halogen IBr. The main features of the observed emissions are as follows:

(1) A broad, banded spectrum peaking in the neighborhood of 430 nm, extending slightly to the red, but decreasing in intensity to the flux all the way to approximately 370 nm. The spacings of the "bandheads" in this band are nearly regular. This emission system gives the impression of being continuous everywhere even under our highest available resolution, with peaks constituting the "bandheads" that we have measured.

(2) A second strong emission of similar nature peaking at 342.0 nm for which much of the light can be attributed to the previously observed I_2 spectrum. A regularly banded spectrum to the blue side, extending to nearly 300.0 nm, seems to be due to IC1.

(3) One sharp, structured emission on the red side of the 342.5 nm band.

(4) A series of sharp emissions on the red side of the 430.0 nm band.

The positions of the "bandheads" have been measured relative to the off-set mercury spectrum shown in Figure 11(a) and (b). The wavelengths and wavenumbers of the bandheads are listed in Table 5. They were measured with a travelling microscope reading directly from the Polaroid film. This proved to be considerably more accurate than attempting to make a negative from the Polaroid and then making a densitometer trace

404.7 nm   Ar   435.8 nm

365.0 nm

(a)

313.1 nm   365.0 nm

I₂

(b)
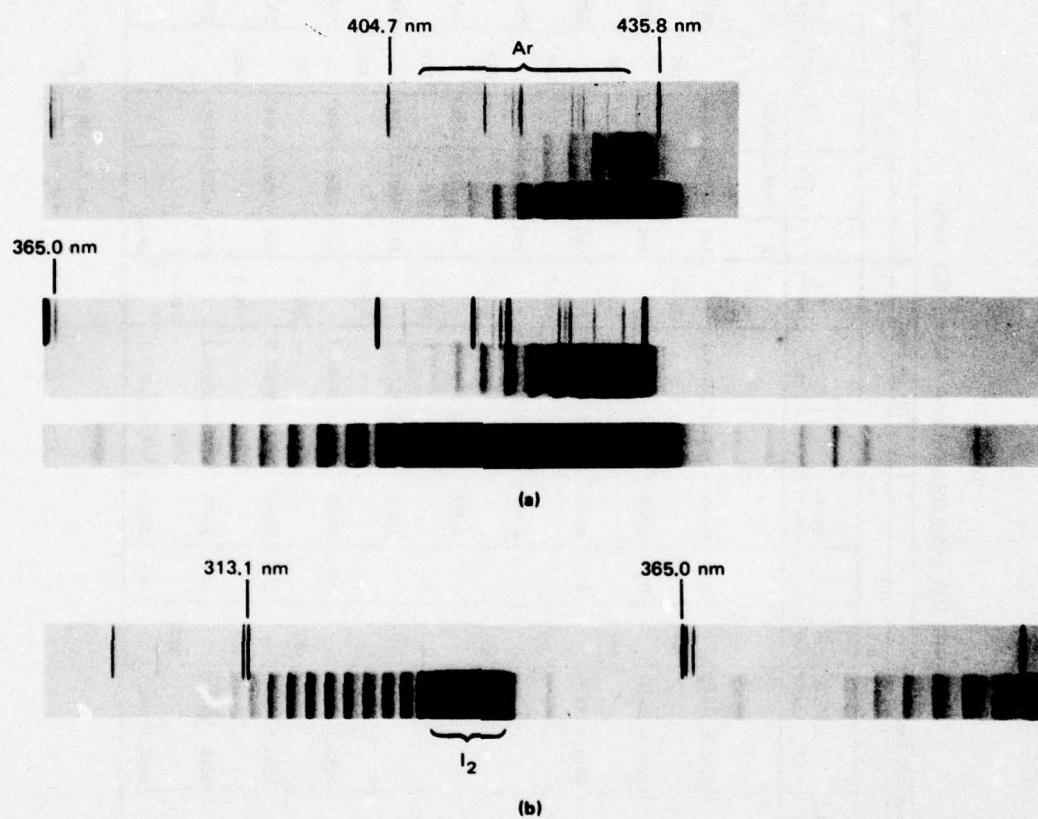
SA-6158-51

FIGURE 11   TYPICAL ICℓ SPECTRA FROM FEBETRON-EXCITED Ar/ICℓ MIXTURES

57

Table 5

ANALYSIS AND ASSIGNMENTS FOR 430-nm IC1 BAND

v′	High Frequency Band v′=0 λ(Å)	cm⁻¹	Δ (cm⁻¹)	Synthetic Spectrum	v′=1 λ(Å)	cm⁻¹	Δ (cm⁻¹)	δ (cm⁻¹)	Synth. Spect.	330 nm Band λ(Å)	cm⁻¹	Δ (cm⁻¹)
a	3735.4	26771		26771								
a+1	3769	26527	244	26526	3746.6	26691	241	164	26690	3085.4	32410.2	
a+2	3804	26288	239	26286	3780.6	26450	234	162	26450	3108.1	32164.8	239.0
a+3	3838.3	26053	235	26050	3814.5	26216		163	26214	3132.1	31927.7	237.1
a+4	3872.9	25820	227	25818			903		25982	3155.3	31692.5	235.2
a+5	3907.6	25591	229	25591					25755	3177.2	31469.8	222.7
a+6	3942.3	25366	225	25367				168	25531	3200.1	31248.7	225.6
a+7	3977.0	25145	221	25148	3950.5	25313	217	166	25312	3222.8	31023.3	219.4
a+8	4011.2	24930	215	24933	3984.7	25096	210	164	25097	3244.5	30821.5	207.7
a+9	4044.6	24724	206	24723	4018	24886	203	165	24887	3267.4	30605.2	426.9
a+10	4078.0	24518	206	24517	4051.4	24683			24681	3290.1	30394.6	210.5

v′	430 nm Low Frequency Band v′=0 λ(Å)	cm⁻¹	Δ (cm⁻¹)	Synth. Spect.	v′=1 λ(Å)	cm⁻¹	Δ (cm⁻¹)	0⁺ 0-1 (cm⁻¹)	Synth. Spect.
b	4108.8	24338		24338					24536
b+1	4137.4	24170	168	24169	4102.8	24373		203	24368
b+2	4166.0	24004	166	24003	4130.5	24210	163	206	24202
b+3	4194.7	23840	164	23839					23638
b+4	4222.8	23681	159	23678	4188.4	23875	355	194	23877
b+5	4253.0	23512	169	23520		23710	165	198	23719
b+6	4281.1	23361	151	23364		23557	153	196	23563
b+7	4308.0	23207	157	23211		23401	156	194	23410
b+8	4336.0	23057	150	23060		23255	146	198	23259
b+9	4362.5	22915	148	22913		23114	150	199	23112
b+10						22958	146		22967

Parameters for synthetic spectrum
1st Δ = 246.75 cm⁻¹
$\omega_o x_o$ = 2.13 cm⁻¹

1st Δ = 170.25 cm⁻¹
$\omega_o x_o$ = 1.32 cm⁻¹

58

from the negative. The quality of the spectra means that the absolute positions should be taken ± 20 cm^{-1} and the relative positions probably ± 5 cm^{-1}. Spectra taken under higher dispersion in different conditions might provide a better means of establishing the positions of the bandheads.

The main features of the spectrum can be fitted using three upper and two lower states. For the 430.0 nm band, we appear to see two contiguous bands, each of which is made up of $v' = 0$ and $v' = 1$ transitions from an upper state to a progression of v'' levels in the bottom state. In each case a value of energy difference between $v' = 0$ and $v' = 1$ can be derived. It is very nearly constant throughout the progression and is significantly different for the two transitions: $\Delta(v' = 0 - v' = 1)$ is 164 cm^{-1} for the higher energy transition and approximately 200 cm^{-1} for lower energy transitions. The symmetry parameter $\omega_o x_o$ is 2.13 cm^{-1} for higher energy transitions and 1.32 cm^{-1} for the lower energy transitions. A synthetic spectrum generated using 246.75 cm^{-1} for the initial ω_o for the higher energy transitions and $\omega_o = 170.25$ wavenumbers for the lower energy gives a reasonable match to the observed lines (see Table 5). ω_o cannot be determined definitely because $v' = 0 \rightarrow v'' = 0$ transitions cannot be identified.

The band on the short wavelength side of the iodine spectrum appears to show a $v' = 0 \rightarrow v''$ progression going to the same ground state as the higher frequency bands of the 430.0 nm emission system. We can derive a term separation by finding the energy differences between the levels ending on the same v''. This gives 5880 cm^{-1} between two of the upper states.

Seven states for ICl are listed in Rosen [R70] for ICl and are given in Table 5. Comparison of these molecular constants with those determined from the ICl spectra shown in Table 6 indicate that none of these states is involved in the observed emissions. No clear evidence for an isotope shift is observed.

Table 6

### MOLECULAR CONSTANTS FOR IC1

(All energies in cm^{-1})

State	T_e	ω_e	$x_e \omega_e$
D	(58168)	(431)	--
C	(53457)	(426)	--
E	37741	173.2	1.1
$B^1(0^+)$	(~ 18000)	(32)	--
$B^3\Pi_{0^+}$	(~ 17344)	(288)	13
$A^3\Pi_1$	13556.21	209.11	1.886
$X^1\Sigma^+$	0	384.293	1.501

Source: Rosen [R70]

60

Transient Gain Measurement

Experiments at SRI (described above) identified band systems of ICl with bands at $\sim$ 430 nm and 340 nm as potential laser candidates. Experiments were conducted with the 50-cm e-beam source to pursue this possibility. As with the $HgCl^*$ systems (described below), the results were quite sensitive to the flow conditions, and the experiments reported here used an Ar flow of $\sim$ 2400 sccm through an ICl reservoir held at 0^0C. If the stream is saturated, this corresponds to an ICl partial pressure of 5 torr.

Under these conditions of the two ICl^* bands, the fluorescence yield was around 4%, divided approximately equally between the 430 and 340 nm bands. Gain measurements were carried out from 430.5 to 432.7 nm; the results are shown in Figure 12. These transient gains are high enough to achieve lasing in the absence of background absorption, but ICl at 5 torr has a comparable static absorption at these wavelengths, as shown in Figure 13. Some additional work is appropriate using other sources of ICl^* to avoid this background absorption problem, and studies in IBr where the absorption is less severe.
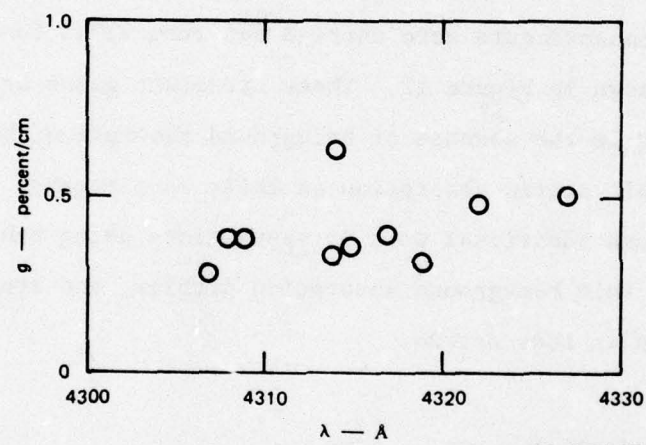
FIGURE 12   TRANSIENT GAIN VERSUS WAVELENGTH FOR ICℓ*
IN Ar/ICℓ MIXTURES

62
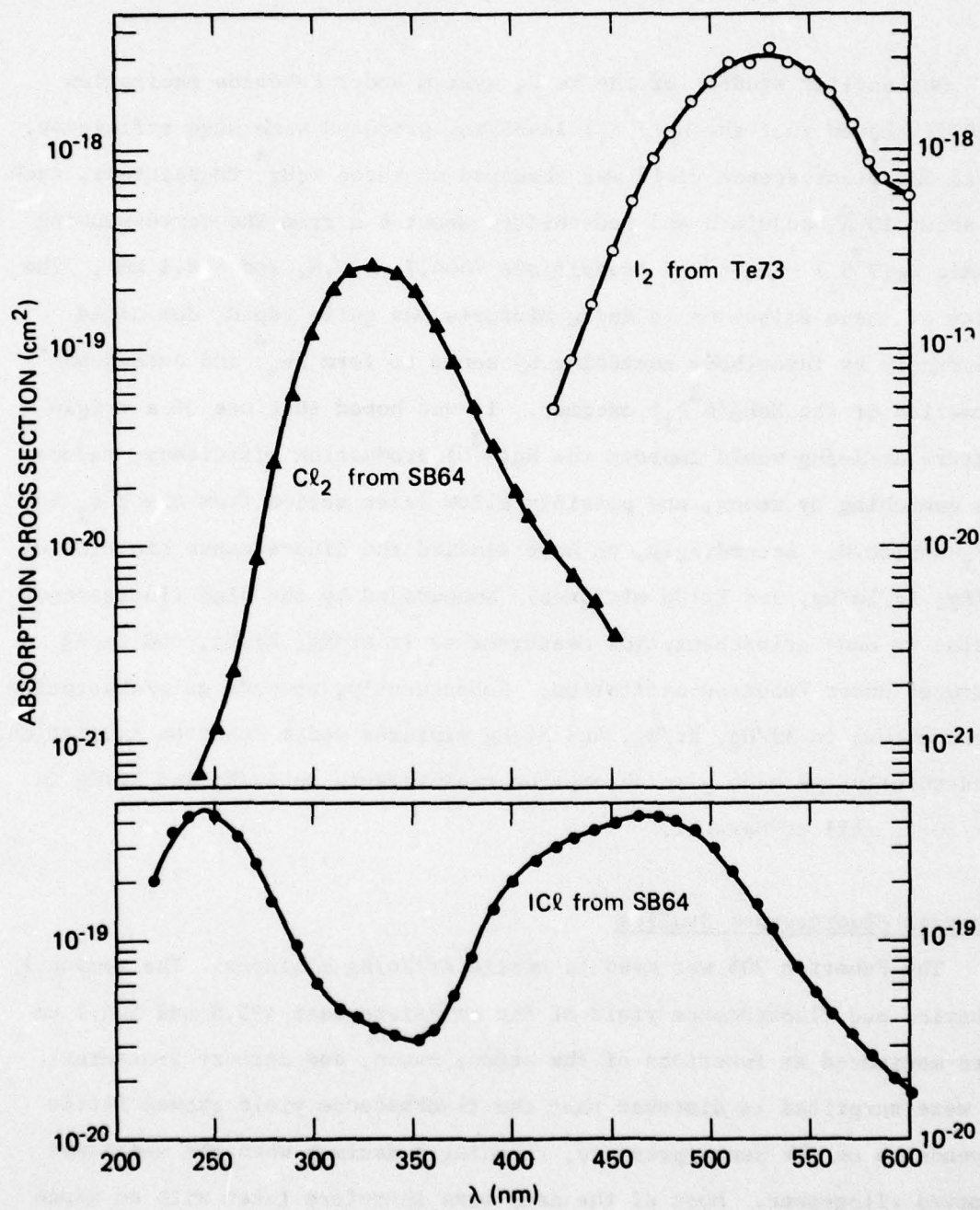
FIGURE 13 ABSORPTION SPECTRA OF I_2, Cl_2, AND ICl

SA-6158-19

63

VI. RARE-GAS/MERCURY SYSTEMS

Our earlier studies of the Xe/Hg system under Febetron excitation [GHH75] showed that the $Hg(7^3S_1)$ level was produced with high efficiency. Up to 20% fluorescence yield was observed on three $XeHg^*$ transitions, each of about 10 $\overset{o}{A}$ bandwidth and red-shifted about 6 $\overset{o}{A}$ from the corresponding atomic $Hg(7^3S_1) \rightarrow Hg(6^3P_J)$ transitions (404.7, 435.8, and 546.1 nm). The decay of these emissions in Xe/Hg mixtures was quite rapid, dominated apparently by three-body quenching by xenon to form Xe_2^* and subsequent formation of the $XeHg(6^3P_J)$ excimer. It was hoped that use of a triple mixture Ar/Xe/Hg would improve the $Hg(7^3S)$ production efficiency, reduce the quenching by xenon, and possibly allow laser action from the 7^3S_1 to 6^3P_J manifold. Accordingly, we have studied the fluorescence kinetics of Ar/Hg, Ar/Xe/Hg, and Kr/Hg mixtures. Encouraged by the high fluorescence yields we made gain/absorption measurements in Ar/Hg, Kr/Hg, and Xe/Hg mixtures under Febetron excitation. Subsequently, we made gain/absorption measurements in Ar/Hg, Kr/Hg, and Xe/Hg mixtures under Febetron excitation. Subsequently, we made gain/absorption measurements in Ar/Hg and Xe/Hg in our 50-cm cell at Maxwell.

Febetron Fluorescence Studies

The Febetron 706 was used to excite Ar/Xe/Hg mixtures. The temporal behavior and fluorescence yield of the emissions near 435.8 and 546.1 nm were monitored as functions of the argon, xenon, and mercury pressures. We were surprised to discover that the fluorescence yield showed little dependence on the xenon pressure, reaching a maximum when the xenon was removed altogether. Most of the data were therefore taken with no xenon additive.

64

Representative data are shown in Figures 14 through 16. Figure 14 shows the decay frequency for the 435.8 nm emission as a function of the Ar and Hg pressures. Figure 15 shows the integrated intensity as a function of the Ar pressure at two Hg pressures. Figure 16 shows the Hg dependence of the decay frequency.

In our previous analysis of the Xe/Hg system [GHH75], the major energy flow pathways were identified as

$$Xe^* + Hg \rightarrow Hg(7^3S) + Xe$$
$$Xe_2^* + Hg \rightarrow Hg(6^3P) + 2Xe \quad .$$
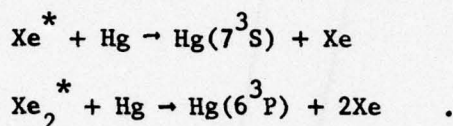
In Ar/Xe/Hg mixtures it was expected that the major pathway would be

$$Ar_2^* \rightarrow Xe^* \rightarrow Hg(7^3S) \quad .$$
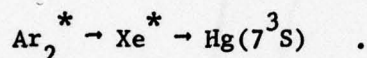
In Ar/Hg mixtures the situation should be more complicated. All the excited states of atomic argon are sufficiently energetic to Penning ionized mercury:

$$Ar^* + Hg \rightarrow Hg^+ + e + Ar \quad .$$
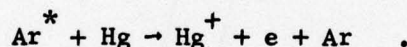
The argon excimer levels lie just below the Hg ionization limit in most of the Franck-Condon region. An unknown distribution of ions (Hg^+) and high-lying excited states (Hg^{**}) is expected to result from energy transfer. As discussed in the next subsection, the secondary electrons should also lead to substantial direct production of Hg^* in the 6^3P, 7^3S, and higher levels.

The total energy deposition in Ar/Hg mixtures should be proportional to the argon density (for Ar/Hg > 40). The resulting excited state production ($Ar^+ + Ar^* + Hg^+ + Hg^*$) should similarly be linear in Ar. For a constant fluorescence yield, the integrated intensity should therefore be a linear function of the argon density. The observed decrease of the integrated intensity above 3 atm indicates that the fluorescence yield is

65
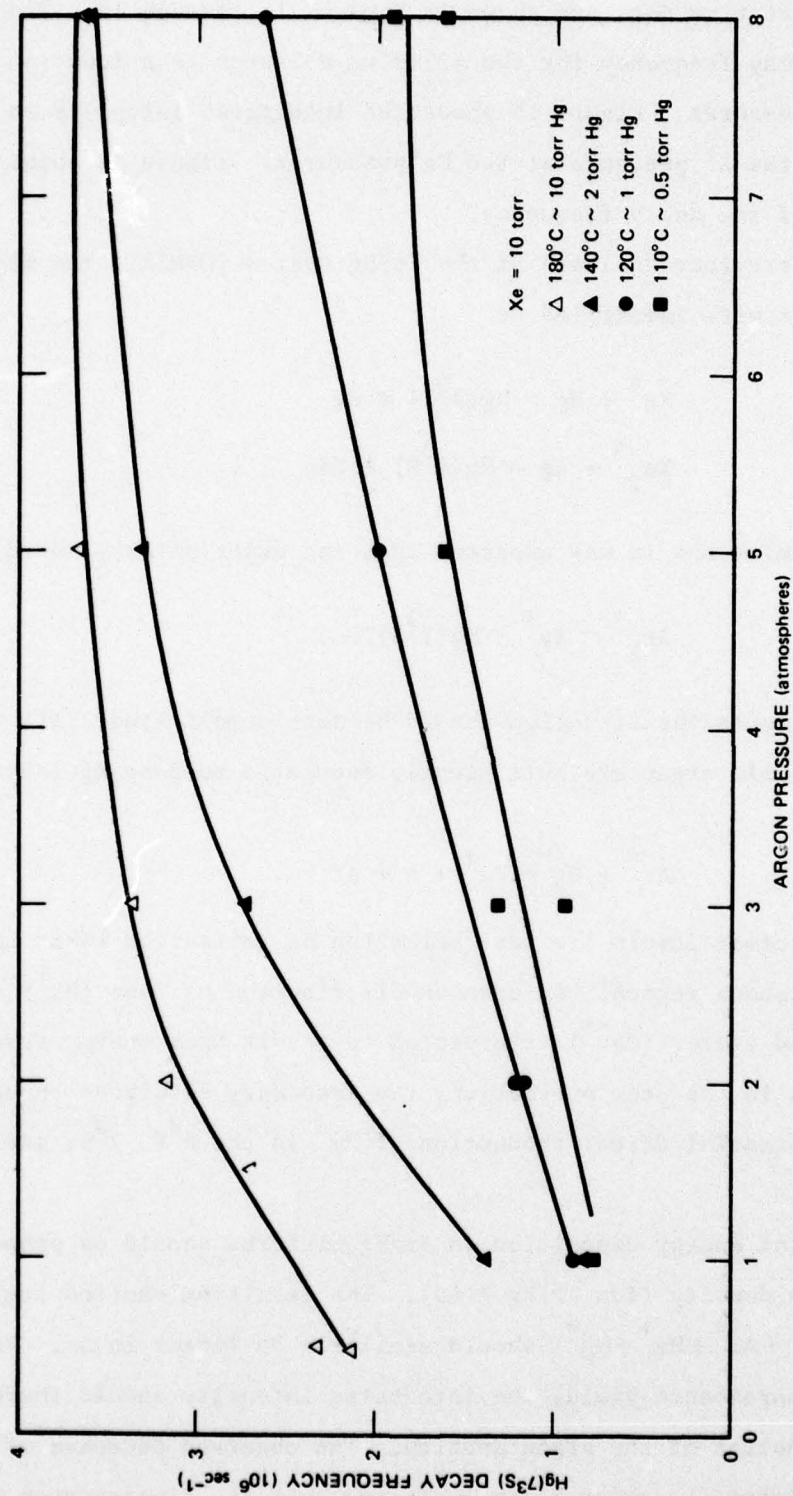
FIGURE 14 ARGON PRESSURE DEPENDENCE OF THE Hg(7³S) DECAY FREQUENCY IN Ar/Xe/Hg MIXTURES

66

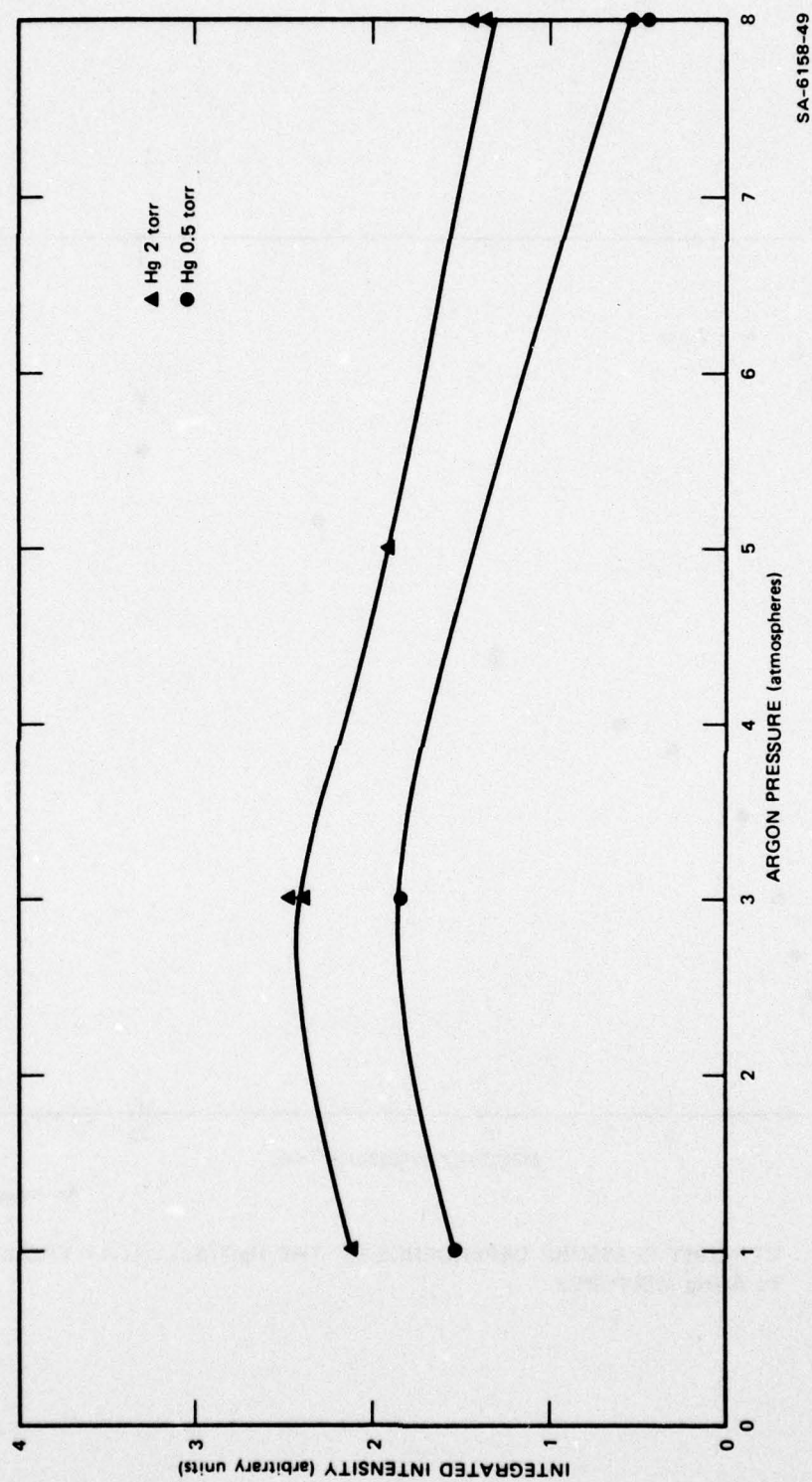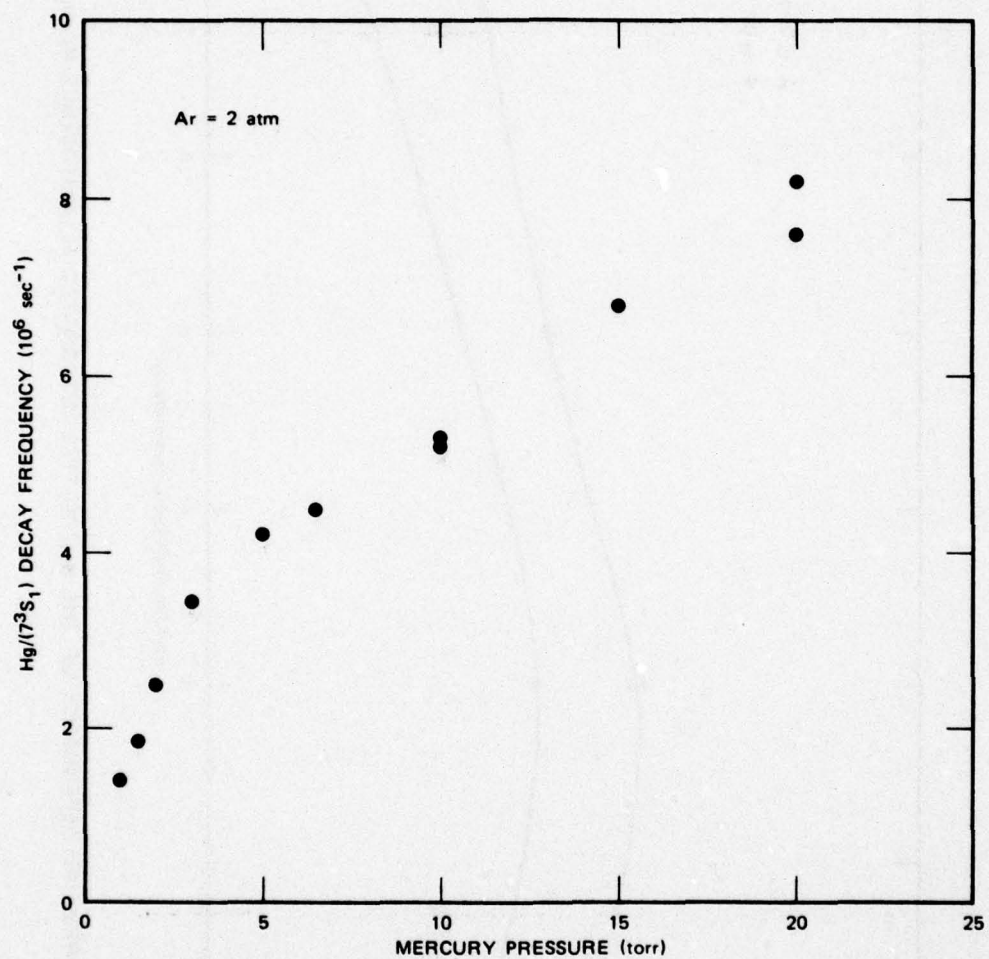FIGURE 15   ARGON PRESSURE DEPENDENCE OF THE Hg(7³S) TIME-INTEGRATED FLUORESCENCE IN Ar/Hg MIXTURES

FIGURE 16   MERCURY PRESSURE DEPENDENCE OF THE Hg(7^3S_1) DECAY FREQUENCY
IN Ar/Hg MIXTURES

SA-6158-47R

68

decreasing quite rapidly, suggesting strong quenching or a reduction in the efficiency with which $Hg(7^3S)$ is produced.

The $Hg(7^3S)$ decay frequency appears to be a strong function of Hg pressure, whereas the Ar pressure dependence is less pronounced. The dependence on both pressures is complex and nonlinear. Also note that the decay frequencies of 1×10^6 to 4×10^6 sec^{-1} are 1 to 2 orders of magnitude slower than for the Xe/Hg case [GHH75]. Originally it was hoped that the proposed lower laser level [$Hg(6^3P)$] could be removed by formation of the $XeHg(6^3P)$ excimer. However, it appears that the observed decay times are much longer than either the kinetic formation or radiative lifetime of the $Hg(7^3S)$ level, suggesting that the radiation from the $Hg(7^3S)$ level may be strongly trapped. This makes interpretation of the fluorescence yields ambiguous, but low pressure measurements indicate that the production of $Hg(7^3S)$ is at least 30-50% of the excited rare gas production.

Role of Rare Gas Subexcitation Electrons in the Excitation of Additives

In e-beam excitation of pure rare gases, the secondary electrons generated by the fast primaries contribute most of their energy to ionization and excitation of the rare gas atoms. However, as these secondaries, tertiaries, etc., lose energy, they finally fall below the threshold for excitation and can lose energy only by elastic collisions. Analysis of the energy deposition processes in rare gases shows that the average energy per electron that remains after the excitation is completed is between 5 and 6 eV in pure Ar, Kr, or Xe [Lo76]. If the electron density is low, the nascent energy distribution of these subexcitation electrons will range all the way from zero to the lowest excitation threshold. However, the elastic collisions with the rare gas atoms will rapidly cool the electrons toward an equilibrium with the gas. At high enough electron densities, where the electron-electron collisional energy exchange rate exceeds that of the electron-atom cooling rate, the electrons will approach a Boltzmann

distribution with their own temperature T_e and will cool as a gas toward equilibrium with the atomic gas. Under these conditions part of the tail of the distribution function will be above the excitation threshold, and energy will flow from the electron gas into electronic excitation. Thus, some fraction of the subexcitation energy can be recovered at high electron densities.

Under low level e-beam excitation of a host rare gas containing an additive having substantially lower energy excited states (e.g., Ar/Hg), substantial excitation of the additive may occur from the subexcitation electrons of the host. For example, in an Ar/Hg mixture the average energy of the Ar subexcitation electrons is 6.9 eV, which is well above the threshold for excitation of the ^3P_J levels of Hg. To estimate the magnitude of this effect, we can compare the excitation rate of the additive to the rate of energy loss of the electrons by elastic collisions. Obviously, a more quantitative estimate requires a detailed analysis based on all the elastic and inelastic interactions of the electrons with the gas mixture. The point of the present discussion is simply to indicate the importance of the additive excitation by the subexcitation electrons.

Consider, for example, the e-beam excitation of an Ar/Hg mixture where Ar is the major constituent. Under conditions of low excitation density where e-e energy exchange is slower than the elastic and inelastic processes, we assume that the energy distribution of the Ar subexcitation electrons is independent of energy between 0 eV and the Ar excitation threshold at 11.6 eV. In the range of energies above the Hg threshold at ~ 5.0 eV, the elastic energy loss rate to Ar is approximately equal to the energy loss due to Hg excitation at a density ratio of Hg/Ar of $\simeq 10^{-4}$. Thus for Hg/Ar $\gg 10^{-4}$, about half of the subexcitation electron energy [$\sim 5.5 N_e$ (eV)] will go toward Hg^* production. That means that $[Hg^*] \simeq \frac{1}{2} N_e \simeq \frac{3}{2} [Ar^*]$ where $[Ar^*]$ is the initially produced argon excited state density due to the e-beam deposition. Obviously this is a substantial source of Hg^* density.

70

Under high electron density conditions where e-e collisions will equilibrate the electron gas at its own temperature T_e, Hg^* production will still be substantial since kT_e is several eV and electrons removed from the tail of the distribution are continuously replenished by the e-e interactions. Thus this effect cannot be neglected in the computational codes used to predict laser performance of e-beam excited doped rare gases.

Febetron Gain/Absorption Measurements

To further explore the relative populations of the $Hg(7^3S_1)$ and $Hg(6^3P_J)$ levels, we probed the transient gain/absorption over the 2-cm path excited by the Febetron using a flashlamp-pumped dye laser (near 435.8 and 546.1 nm) and an argon-ion pumped cw dye laser (near 546.1 nm). At low mercury pressures, the time evolution of the Hg excited state density is slower than the flashlamp-pumped laser pulsewidth ($\sim$ 200 nsec). At higher pressures, the scales are comparable. Absorption is clearly observed at the atomic wavelengths, as illustrated by the time-integrated spectrum shown in Figure 17, in Ar (8 atm) + Hg (10.5 torr).

An attempt was made to follow the time dependence of the absorption/ gain using the flashlamp-pumped laser and a Tektronix R6912 transient digitizer in a split-beam experiment. Absorption was observed in the neighborhood of line center. There were very tentative indications of gain near 436.8 nm in Kr (2 atm) + Hg (100 torr). Unfortunately, signal averaging techniques could not be used to improve the signal-to-noise ratio because of the shot-to-shot variation of the amplitude of the laser and of the time--synchronization with the Febetron. The timing problems could be solved using the transient digitizer software but the shot-to-shot fluctuations in the amplitude of the flashlamp-pumped dye laser signal were significantly greater than the signal we were looking for.

A tunable cw dye laser was used briefly to investigate in the neighborhood of the 546.1 nm line. These measurements were made with a linewidth of about 0.5 Å. The results again showed clear indication of

71
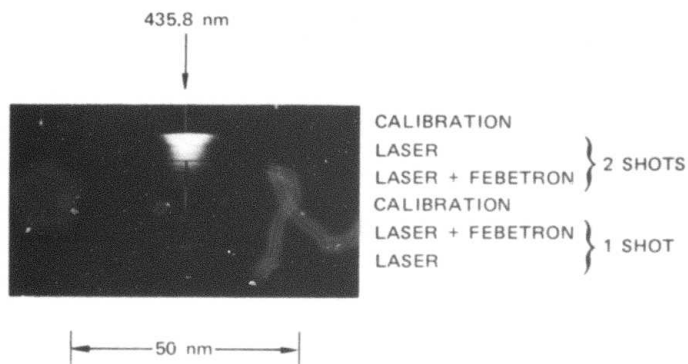
FIGURE 17   ABSORPTION NEAR 435.8 nm IN FEBETRON-EXCITED Ar(8 atm)
PLUS Hg (10.5 torr)

72

absorption at the line center and on the red side of the atomic lines. In the Kr/Hg the absorption was very narrow; in Ar/Hg the absorption was somewhat broader.

Long Path Gain/Absorption Measurements

The Febetron gain measurements described above were inconclusive in determining gain versus absorption in the red sidebands of these transitions in either Ar/Hg or Kr/Hg, although the measurements clearly showed that the atomic transitions themselves were not inverted. This diminished the prospect for gain in the sidebands as well, but it was at that time quick and straightforward to do definitive measurements using the 50-cm e-beam apparatus at Maxwell.

Using a N_2-laser-pumped tunable dye laser, we probed for gain/ absorption on the 5461 Å transition of Hg^* broadened by Ar and by Xe. The rare-gas pressure was 2 to 3 atmospheres, and the Hg pressure was $\sim$ 5 torr in both cases. We found absorption in all cases, both during and after the pulse. Results from Ar/Hg as a function of wavelength, obtained during the pulse, are shown in Figure 18. Results at λ = 5465 Å obtained during and after the trailing edge of the pulse are shown in Figure 19. Somewhat surprisingly, strong absorption is seen to persist for long times (> 1.5 μsec) after cessation of the pulse. For comparison, an Hg^* emission history is shown in Figure 20, where the termination of the e-beam pulse is indicated. This curve represents the total emission at visible from the gas, but 5461 Å emission was similar in profile. The emission also persists for an unexpectedly long time ($\tau_{decay} \simeq 550$ ns), perhaps due to radiation trapping, but not as long, apparently, as the absorption.

The absorption profile for Xe/Hg from 5459 to 5487 Å is shown in Figure 21. This profile seems to indicate a second transition originating near 5471 Å; in addition, finite absorption occurs on the blue side of the transition in contrast to the Ar/Hg case. Also, in contrast to the
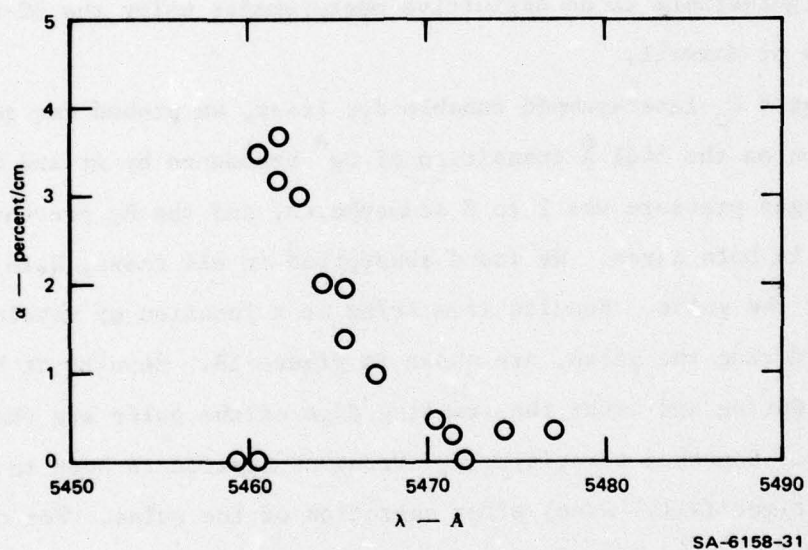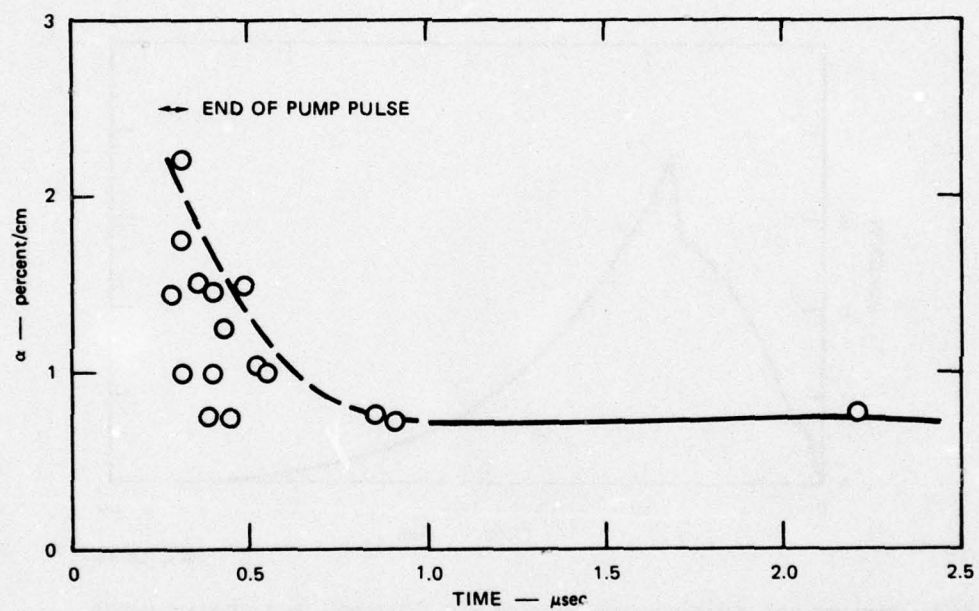
FIGURE 18   ABSORPTIONS NEAR 5461 Å IN E-BEAM PUMPED Ar/Hg
MIXTURES

74

FIGURE 19   TIME DEPENDENCE OF ABSORPTION AT 5465 Å IN E-BEAM
PUMPED Ar/Hg MIXTURES

75
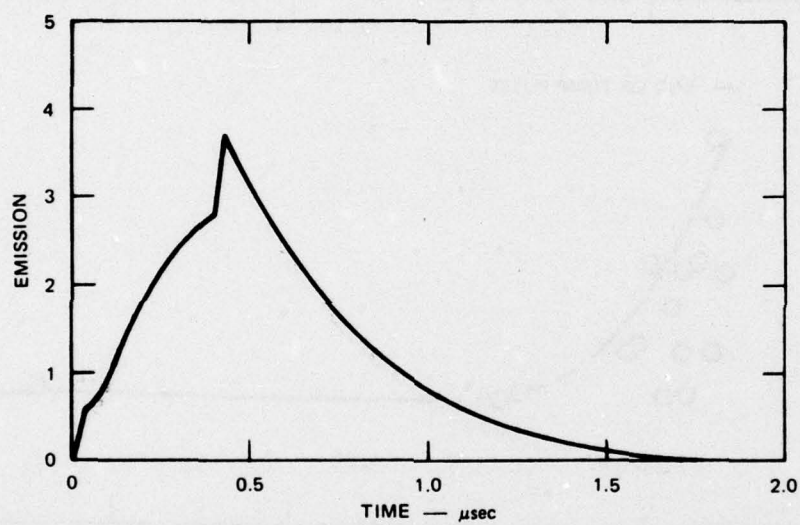
FIGURE 20   TIME DEPENDENCE OF Hg* EMISSION IN E-BEAM PUMPED
Ar/Hg MIXTURES

SA-6158-32
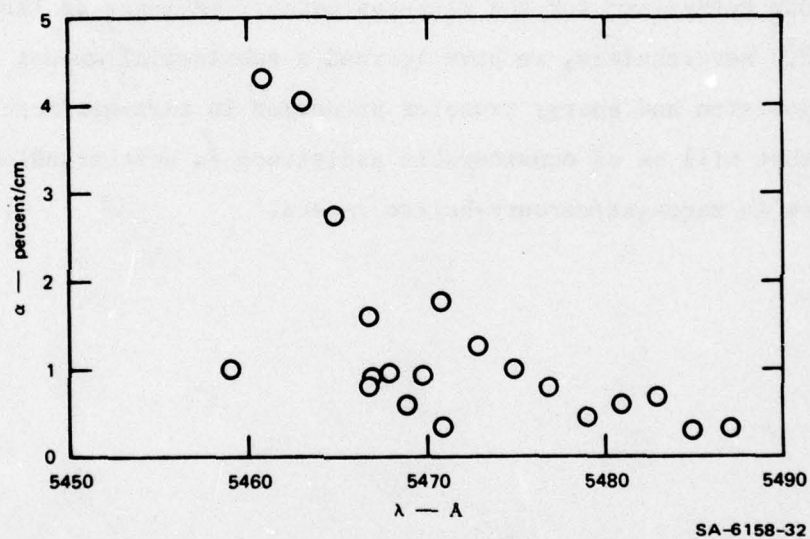
FIGURE 21   ABSORPTIONS NEAR 5461 Å IN E-BEAM PUMPED Xe/Hg
MIXTURES

Ar/Hg case, the Xe/Hg emission history follows the current history, with no afterglow. The bases of these auxiliary features are unknown, but it is clear that the $7^3S \rightarrow 6^3P_J$ transitions in these rare-gas/mercury mixtures do not constitute promising candidate laser systems.

Conclusions

While the detailed spectroscopy and kinetics of the rare-gas/mercury excimers are incompletely understood, it is clear, at least under the conditions examined, that the $Hg(6^3P_J)$ levels are removed more slowly than they are populated by fluorescence. The results obtained have obviously dampened our enthusiasm for the rare-gas/mercury excimers as laser candidates. Nevertheless, we have learned a substantial amount about the energy deposition and energy transfer processes in rare-gas/mercury mixtures that will be of considerable assistance in understanding the energy flow in rare-gas/mercury-halide lasers.

VII. MERCURY HALIDE LASER STUDIES

As laser candidates, the mercury halides have many features in common with the rare gas halides. The laser transition originates on the ionic $B^2\Sigma_{\frac{1}{2}}^+$ state (Hg^+X^-) and terminates on the weakly bound covalent ground state $X^2\Sigma_{\frac{1}{2}}^+$. The harpooning reactions

$$Hg^* + RX \rightarrow HgX^* + R$$
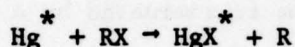
offer selective and efficient production of the upper laser level [KJD75, THO78b]. The ion recombination channels

$$Hg_2^+ + Cl^- \rightarrow HgCl^* + Hg$$
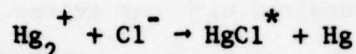
should also be important.

Laser action has been demonstrated using electron-beam pumping of $HgCl^*$ and $HgBr^*$ [Pa77]. Photolytic pumping of $HgBr^*$ has also been accomplished [Sh77]. Most promising are the recent demonstrations of electron-beam controlled discharge pumped $HgCl^*$ [THO78b, Wh78] and $HgBr^*$ [Wh78] lasers. We report here a series of preliminary experiments that led toward the demonstration of e-beam controlled discharge pumped $HgCl^*$. A reprint of the paper describing the laser demonstration is included as Appendix D.

HgX Fluorescence Studies

Spectra and fluorescence yields were investigated for a variety of halogen-bearing compounds using our electron-accelerator facility described above. This preliminary work emphasized the identification of favorable gas mixtures for laser operation, especially when discharge pumped.

79

Figure 22 shows the emission spectrum from HgBr taken with a mixture of 1000 torr Ar, $\sim$ 8 torr Hg, and 0.8 torr Br_2. The emission spectrum from HgCl is shown, in Figure 23. For this spectrum the resolution was $\sim$ 20 $\overset{o}{A}$ (note the Hg 557.0 and 579.0 nm lines on the right-hand side of the figure). The total pressure was 1000 torr Ar, with a chlorine density of approximately 1 torr and a mercury density of 3 torr. Several excited mercury atom lines are prominent in the figure, including the 253.7 nm emission in second order. This spectrum was taken using the multiscalar mode; the strong Hg 546.1 nm line is folded over in the MCA memory due to overflow. The HgCl spectrum is dominated by a regular series of vibrational bands, the strongest of which is the 0-22 band at 558.4 nm, followed by 0.21, etc., proceeding toward the blue. These assignments are based on the spectroscopic studies of Wieland [W60]. The separate peaks due to Cl^{35} and Cl^{37} are not resolved with our system. A summary of HgCl spectroscopic constants taken from Wieland's paper [W60] is given in Table 7. This spectrum should be compared with others previously discussed in the literature [Pa77]. In particular, we note that the spectrum is extremely broad, with a half width of nearly 60 nm, much broader than those reported previously. We clearly resolve more than 15 separate peaks, which appear to be from specific vibrational transitions. Since the peak emission is established as 0-22, it appears that this molecule has a rather broad Franck-Condon region. The width of the spectrum may suggest that the upper state is not fully vibrationally relaxed prior to radiation, even at 1000 torr of pressure. We would expect the spectrum arising from an unrelaxed upper state to be much less structured than was observed. However, Djeu and Mazza [DM77], in a recent study of the analogous HgBr molecule, concluded that they achieved full vibrational relaxation in the upper state with only 5 torr of helium gas (in the afterglow of a discharge).

Under our conditions, we have never seen emissions from the HgCl C or D states near 265 nm and 290, respectively [Co38]. When significantly
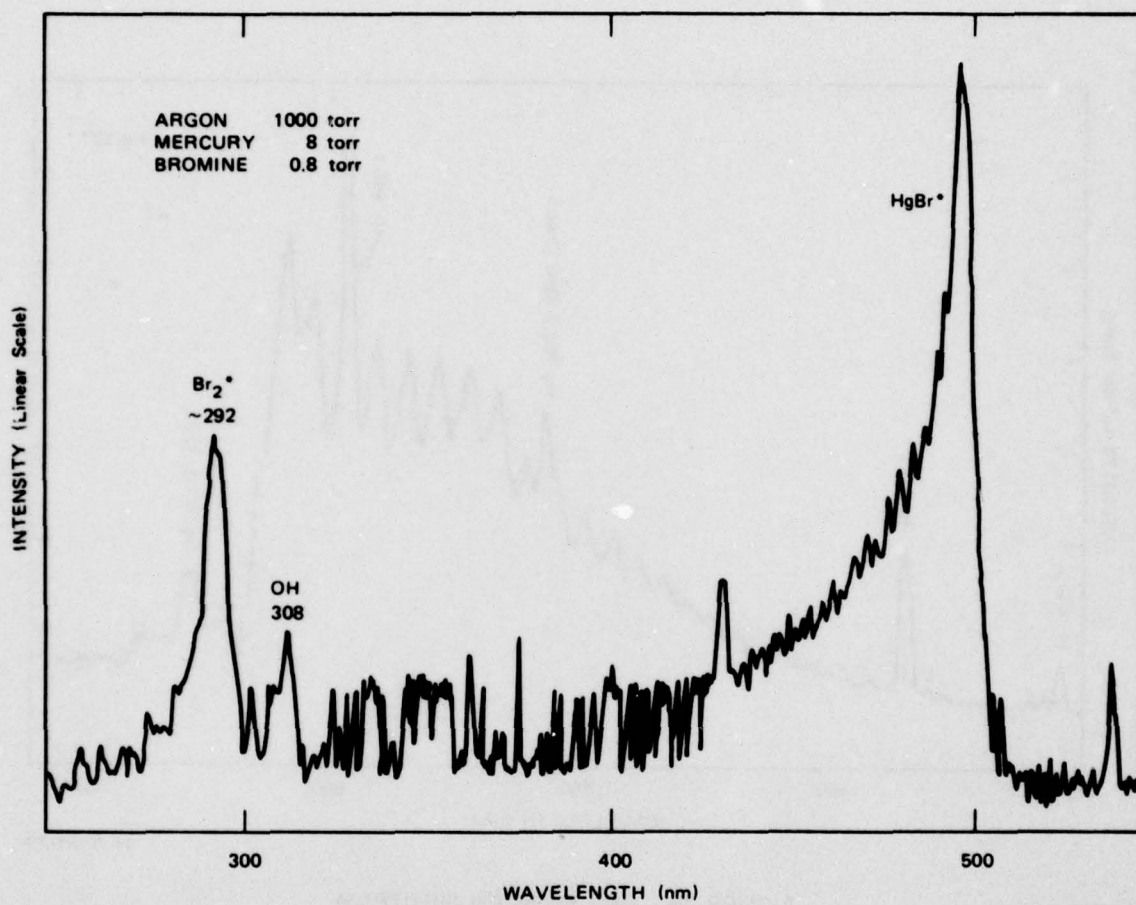
FIGURE 22 HgBr EMISSION SPECTRUM
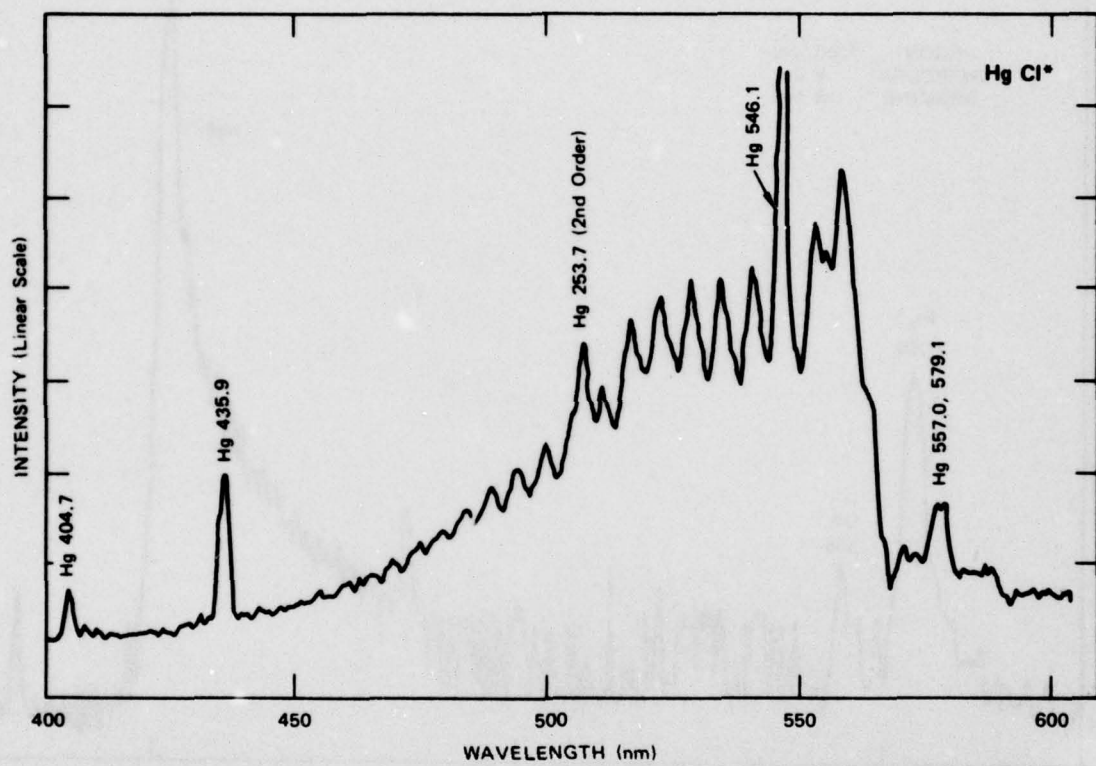
SA-6158-40

FIGURE 23   HgCl EMISSION SPECTRUM

SA-6158-39

Table 7

MOLECULAR CONSTANTS FOR HgCl

(all values in cm^{-1})

Molecule	ν_e	ω_e	$\omega_e x_e$	D_o
$HgCl^{35}(X)$	0	292.61	1.6025	8410[*]
$HgCl^{37}(X)$	0	285.80	1.529	8410
$HgCl^{35}(B)$	23421	192.0	0.50	22680
$HgCl^{37}(B)$	23421	187.53	0.477	22680

Source: K. Wieland [W60].

[*]Wilcomb and Bernstein [WB76] have reanalyzed
Wieland's data and report a dissociation energy
of 8600 cm^{-1}.

83

greater quantities of Cl_2 are introduced into the cell, we see emission from Cl_2^* at 2570, but this was not the case for the spectrum of Figure 23 where an excess of mercury was present. If we assume that all this emission is due to HgCl (and not to some other source of background) and that all the fluorescing upper state population is available for laser emission, we can compute the reduced stimulated emission cross section

$$\sigma_R = \frac{\lambda^4}{8\pi c \delta \lambda} = \tau_R \cdot \sigma(\text{peak})$$

where c is the velocity of light and λ is the wavelength of peak intensity. For this case, $\sigma_R = 1.5 \times 10^{-24}$ cm^2 sec. This is similar to the value of 1.8×10^{-24} cm^2 sec determined for the KrF laser, but much smaller than that deduced by Parks under different excitation conditions using CCl_4 as an additive [Pa77]. This discrepancy is due to the differences in the width $\Delta\lambda$ of the observed spectrum in these experiments. The spectra we observed from mixtures of $Ar/Hg/CCl_4$ and from $Ar/Hg/Xe/CCl_4$, using gas mixtures that were similar to those that Parks used, did not differ quantitatively from the spectrum just described.

By adjusting the rate at which the chlorine additive was flowing, we attempted to optimize the emission intensity for various mixtures. Following our previous practice in higher current Febetron 706 studies, we used a mixture of argon with 5% N_2 to provide a standard emission in the second positive $C(^3\Pi) \rightarrow B(^3\Pi)$ system. Several optimized mixtures were compared; the results are shown in Table 8. These data are as yet incomplete. We have not varied the total pressure, and our total pressure is substantially lower than that used by Parks [Pa77]. The range of xenon pressures explored is also limited.

Even with the flowing system, we noted a significant accumulation of a crystalline deposit in the cooler regions of the cell and related tubulation. Under ideal operating conditions, this accumulation was confined

Table 8

COMPARISON OF FLUORESCENCE INTENSITIES

	Normalized Emission Intensity	Optimum Pressures (torr) Argon = 1000 torr		
		Xenon	Hg torr	RC1
Argon/mercury/Cl_2	5-7	--	~ 5	3-5
Argon/mercury/CCl_4	1	--	~ 5	0.7 ± 0.3
Argon/xenon/mercury/CCl_4	3-4		3-10	3/4
Argon/5% nitrogen	1			

predominantly to the large volume trap downstream from the cell. With less ideal conditions, this deposit would clog needle valves and other parts of the apparatus. We concluded that this deposit contained significant fractions of Hg_2Cl_2 (calomel) and also $HgCl_2$. This suggested the study of the emissions from the vapor over heated solid Hg_2Cl_2 in an argon buffer. We placed about 1 g of Hg_2Cl_2 in the target cell near, but not on, the entrance foil for the electron beam. Argon gas was flowed through the cell at a rate comparable to that used previously. We noted an intense $HgCl^*$ emission spectrum similar to that in Figure 23, including the prominent Hg^* lines. This spectrum was observed at relatively high temperatures (above $225^{\circ}C$) and its intensity increased monotonically with increasing temperature. Due to materials limitations (Viton gaskets) we did not exceed $275^{\circ}C$. At that temperature the integrated (total) intensity was greater than that observed with the $Hg/Xe/CCl_4$ combination, but had not been optimized. Studies on this system are being continued.

For these low current studies, the peak electron and ion densities are substantially lower than for high current laser pumping conditions (10^{12} cm^{-3} versus 10^{14} to 10^{15} cm^{-3}). Because of the time necessary for neutralization, our studies discriminate against ion-ion neutralization channel and favor neutral channel processes significantly. These processes may include transfer from excited argon

$$Ar^* + Hg \rightarrow Hg^* + Ar$$
$$Hg^* + Cl_2 \rightarrow HgCl^* + Cl$$

or
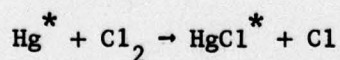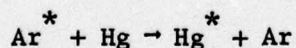
$$Ar^* + HgCl_2 \rightarrow HgCl^* + Cl + Ar$$
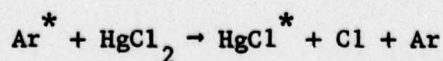
and they may also include direct electron pumping of the additive species

$$e + Hg \rightarrow Hg^* + e$$

$$Hg^* + Cl_2 \rightarrow HgCl^* + Cl$$

or

$$e + HgCl_2 \rightarrow HgCl^* + Cl + e \quad .$$
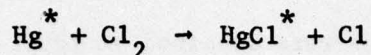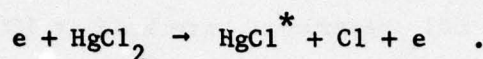
Long Path Gain and Fluorescence Measurements

The majority of the experiments performed in the SRI cell and flow system concerned the electron-beam and discharge pumping of mercury chloride lasers. The gain and fluorescence yields were studied in $Ar/Xe/Hg/CCl_4$ mixtures. The complexity of the energy flow was established and the essential role of $XeCl^*$ identified.

An extensive series of experiments was also carried out with $Ar/Hg/Cl_2$ mixtures with both pure e-beam pumping and with e-beam sustained discharge pumping. This work led to demonstration of a discharged-pumped $HgCl^*$ laser at MLI, as well as the quantitative measurements of the gain profile of the 5576 $\overset{o}{A}$ band. That work is reported separately in Appendix D.

Experiments in gas mixtures leading to $HgCl^*$ emission (e.g., Ar/Xe/Hg/RCl) are dominated by gas-phase or surface reactions between ground-state Hg and the Cl donor, either CCl_4 or Cl_2. Recent work by Dr. Ken Tang at MLI [Ta77] indicates that these reactions are rapid enough that the composition of the gas mixture can change as it flows down the test cell. This problem appeared in experiments both at SRI and at MLI, as manifested by powder deposits and by nonrepeatability of results. It was minimized insofar as possible by mixing the reactants as close to the entrance to the test cell as possible, and, in the MLI experiments, by flowing the gas through the cell as rapidly as possible. Nevertheless, we cannot be confident of the concentration or distribution of the various initial constituents or reaction products in the test cell. Thus, the results presented here must be considered as phenomenological and, in particular,

we cannot at this time describe the variation of observables with changes in test parameters.

The results presented here were obtained at total pressures between 2 and 3 atmospheres, consisting mostly of Ar. The cell temperature was $200^{\circ}C$, and the Hg and CCl_4 reservoirs were held at 180°-$200^{\circ}C$ and $0^{\circ}C$, respectively. Ar was flowed through the Hg reservoir at 400-1200 scc/m, and Xe or Ar through the CCl_4 reservoir at 10-20 sccm. If it is assumed that Hg and CCl_4 vapors saturate the rare gas streams, then their partial pressures prior to reaction would be 10-20 torr and 0.3-1.5 torr, respectively. This is probably accurate for CCl_4 but not for Hg, where a recent calibration at MLI shows some departure from saturation for the highest Ar flow rates used here, perhaps by a factor of two. Xenon partial pressures were in the range of 0 to 100 torr.

Our initial measurement was of the gain profile of the $HgCl(B \rightarrow X, \, v' = 0 \rightarrow v'' = 22)$ transition, which has its bandhead at 5576 Å for $Ar/Xe/Hg/CCl_4$ mixtures. The results, which show average gains of $\leqslant 0.3\%/cm$ from 5576 to 5595 Å, are shown in Figure 24. The dips in the gain profile at 5583 and 5588 Å may be due to Xe absorptions, since more recent measurements at MLI in $Ar/Hg/Cl_2$ mixtures do not exhibit such features. Single pass gains were 15%/cm, indicating that it would be straightforward to achieve lasing under these conditions.

Spectral studies of the fluorescence from this gas mixture showed fluorescence from Hg^*, Cl_2^*, $HgCl^*$, and $XeCl^*$ depending on conditions, with the $XeCl^*$ emission being the strongest feature under most conditions. Quantitative side light fluorescence measurements were made using filters to separate the $XeCl^*$ emission ($\sim$ 3080 Å) from the $HgCl^*$ emission ($>$ 5000 Å). Preliminary photon yields for the two emissions as a function of Hg partial pressure (assuming saturated Hg flow) are presented in Figure 25 (recalling the uncertainties of fluorescence yields described in the section on experimental procedures above). We see that the $XeCl^*$
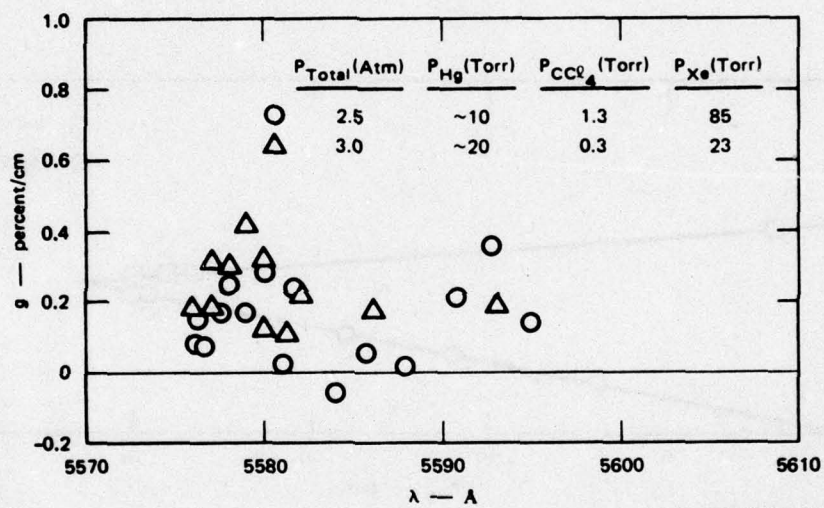
FIGURE 24   GAIN VERSUS WAVELENGTH FOR THE HgCℓ
(B $^2\Sigma^+_{1/2}$, v' = 0 → X $^2\Sigma^+_{1/2}$, v'' = 22) TRANSITION
IN E-BEAM PUMPED Ar/Xe/Hg/CCℓ$_4$ MIXTURES
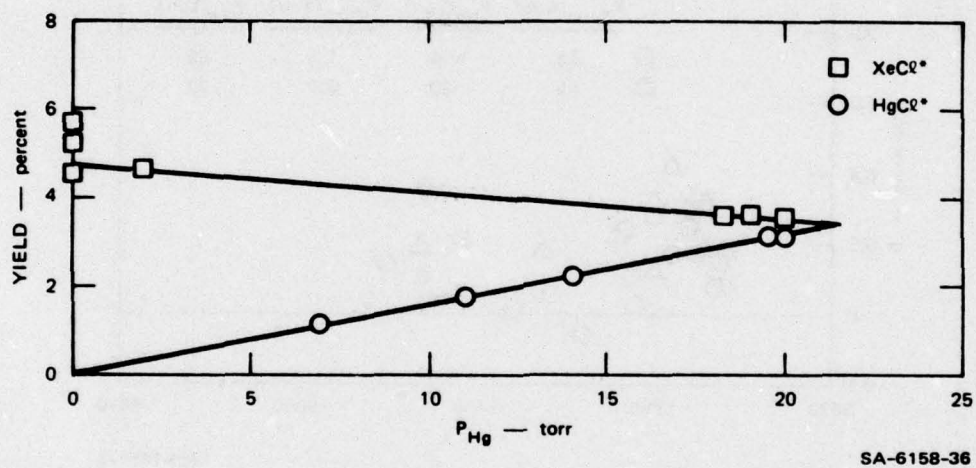
FIGURE 25 FLUORESCENCE YIELDS FOR XeCℓ* AND HgCℓ* VERSUS Hg PRESSURE FOR P_{Ar} = 3 atm, P_{Xe} = 34 torr, AND $P_{CCℓ_4}$ = 0.5 torr

90

fluorescence yield decreases by $\sim 1.5\%$ while the $HgCl^*$ increases to $\sim 3\%$ as Hg concentration increases. This suggests that $HgCl^*$ excitation may not occur solely by excitation or charge transfer from Xe^+ as suggested by Parks [Pa77]:

$$Xe^+ + Cl^- + M \rightarrow XeCl^* + M$$

$$Xe^+ + Hg \rightarrow Xe + Hg^+$$

$$Hg^+ + Cl^- + M \rightarrow HgCl^* + M \quad .$$
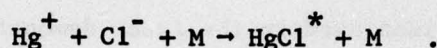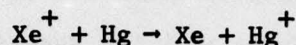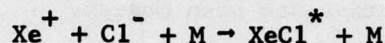
A possible alternative is direct excitation of Hg^* metastables by secondary electrons in the plasma, followed by reaction:

$$Hg + e \rightarrow Hg^* + e$$

$$Hg^* + CCl_4 \rightarrow HgCl^* + CCl_3 \quad .$$
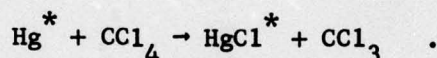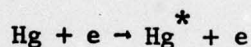
As noted, the $XeCl^*$ emission was quite bright, and we readily achieved laser action at 3080 $\overset{o}{A}$. From a careful comparison of the pump pulse shape and the laser intensity history, we deduced a laser ring-up time of 100 nsec. From the approximation $g_o c t_{ring-up} \cong 20$, we conclude that the gain was $g_o \sim 7 \times 10^{-3}/cm$. From the further approximations

$$g_o = \frac{\lambda^2}{8\pi} \frac{A}{\Delta\nu} N^*$$

and

$$FY = \frac{AN^*}{pump} \quad ,$$

we can deduce a fluorescence yield (FY) of $\sim 7\%$. This is somewhat higher than, but in reasonable agreement with, the values in Figure 25. Likewise, the gains for HgCl shown in Figure 24 give a fluorescence yield of $\sim 6\%$.

91

Conclusions

Demonstration of electron-beam controlled discharge pumping of a HgCl* laser represents a significant advance. The favorable energy level structure in atomic mercury suggests that this laser can be quite efficient. To date the laser output has been modest.

Our kinetics work described above led to the choice of Ar/Hg/Cl$_2$ as the laser mixture. Subsequent work has suggested that under the rather slow flow conditions used in the laser demonstration, the Cl$_2$ was probably all consumed before excitation by reaction with ground state Hg. The actual gas composition may have been Ar/Hg/HgCl$_2$ or possibly Ar/Hg/Hg$_2$Cl$_2$. Continued study of fast-flow Ar/Hg/Cl$_2$ is clearly in order.

VIII XeF KINETICS

The XeF laser, operating at 351 and 353 nm, has the longest wavelength of any of the rare gas halide lasers. In electron-beam pumped Ne/Xe/NF$_3$ mixtures, substantial output energies have been obtained at reasonable efficiencies [HT77]. However, the efficiencies are well below the theoretical maximum of 13% based on the ratio of the 3.5 eV XeF photon to the 27 eV primary excitation energy in neon. Before the eventual efficiency and scaling potential can be assessed, three major kinetics issues must be carefully considered: (1) characterization of the kinetic input chain, (2) quenching and the role of the 460 nm emission band, and (3) removal of the bound lower laser level. To date these issues have been only partially addressed.

Input Chain Kinetics

The original work on e-beam excited XeF was done in Ar/Xe/NF$_3$ mixtures. The advantage of Ne/Xe/NF$_3$ is apparently due to the reduction in transient absorptions, probably mostly by Ar$_2^+$. The energy flow sequence in Ar/Xe/NF$_3$ apparently resembles that of Ar/Kr/F$_2$, except that the Ar* and Ar$_2^*$ + Xe reactions are much more rapid than the corresponding Ar* or Ar$_2^*$ + Kr reactions. Previously, the chain of reactions leading to XeF* in Ne/Xe/NF$_3$ was quite poorly characterized.

Our studies of the XeF input chain have identified the following as the most important energy flow pathways:

$$\text{electrons} \rightarrow \text{Ne}^+ \rightarrow \text{Ne}_2^+ \rightarrow \text{NeF}^* \rightarrow \text{Xe}^+ \rightarrow \text{XeF}^*$$

$$\text{electrons} \rightarrow \text{Ne}^* \rightarrow \text{Xe}^+ \rightarrow \text{XeF}^*$$

$$\text{electrons} \rightarrow \text{Xe}^+ \rightarrow \text{XeF}^*$$

$$\text{electrons} \rightarrow \text{Xe}^* \rightarrow \text{XeF}^*$$
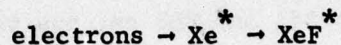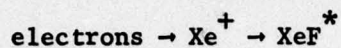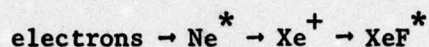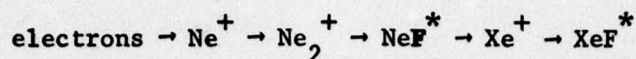
These reactions are illustrated schematically in Figure 26 and listed in Table 9.

We believe that these four input chains contribute about equally to the XeF^* production, but no quantitative assessment has been made. It appears that substantial production of Xe^+ and Xe^* should result from collisions of the hot secondary electrons with Xe (see the discussion of subexcitation electrons above). The competition is excitation and elastic electron cooling in e-Ne collisions, and inelastic e-NF_3 collisions. Preliminary calculations show that the relative direct production of Ne^+, Ne^*, Xe^+, and Xe^* is 10:3:1:4. This issue needs to be understood in detail before the maximum XeF^* production efficiency can be determined.

To characterize the important neutral reactions, we have begun time-decay studies of the Ne^* and F^* reactions studied by laser absorption and the F_2^* reactions studied by fluorescence near 158 nm. Our preliminary results on the Ne^* reactions are in good agreement with those of Setser [Se77b, BKS78]. The major unexplored neutral reactions are those of NeF^*, especially the competition of fluorescence and predissociation to F^*. We plan calculations to address this issue. The NeF^* reactions will be quite difficult to study experimentally.
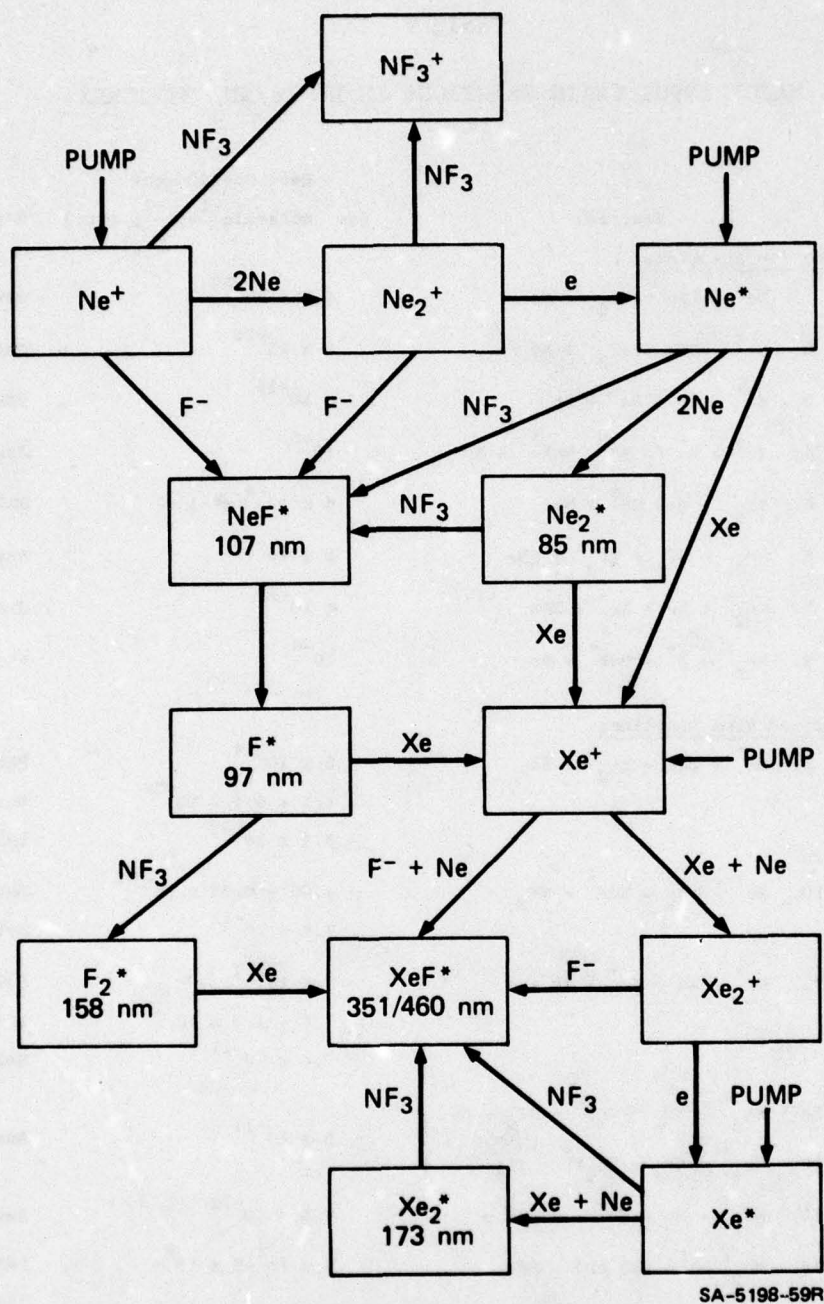
FIGURE 26   MAJOR ENERGY FLOW PATHWAYS IN E-BEAM
PUMPED Ne/Xe/NF$_3$ MIXTURES

Energy input from the electrons comes in along the
pump arrows. The specie in each box, plus the
component along the reaction arrow, yields the result
in the next box. The wavelengths of the emitting
species are indicated. They may be subject to
quenching by NF$_3$ or Xe (not shown). NeF* is
presumed to predissociate.

95

Table 9

MAJOR INPUT CHAIN REACTIONS IN Ne/Xe/NF$_3$ MIXTURES

Reaction	Rate Coefficient (cm^{-3}molecule^{-1}sec^{-1}, etc.)	Reference
Neon Ion Reactions		
1. $Ne^+ + 2Ne \rightarrow Ne_2^+ + Ne$	4.6×10^{-32}	Or73
2. $Ne^+ + NF_3 \rightarrow NF_3^+ + Ne$	5×10^{-10}	Analogy
3. $Ne^+ + Xe \rightarrow Xe^+ + Ne$	$< 10^{-14}$	JMB78
4. $Ne^+ + F^- (+ M) \rightarrow NeF^* (+ M)$	10^{-6}	Analogy
5. $Ne_2^+ + e \rightarrow Ne^* + Ne$	4×10^{-8} at 1 eV	BB70
6. $Ne_2^+ + NF_3 \rightarrow NF_3^+ + 2Ne$	5×10^{-10}	Analogy
7. $Ne_2^+ + Xe \rightarrow Xe^+ + 2Ne$	$< 10^{-13}$	JMB78
8. $Ne_2^+ + F^- \rightarrow NeF^* + Ne$	10^{-6}	Analogy
Excited Neon Reactions		
9. $Ne^* + 2Ne \rightarrow Ne_2^* + Ne$	5×10^{-34}	Ph59
	$4.1 \pm 0.4 \times 10^{-34}$	Measured
	5.4×10^{-34}	LCL76
10. $Ne^* + NF_3 \rightarrow NeF^* + NF_2$	$1.05 \pm 0.05 \times 10^{-10}$	Measured
	7.8×10^{-11}	Se77b,BKS78
11. $Ne^* + Xe \rightarrow Xe^+ + Ne + e$	7×10^{-11}	O177
	$7.5 \pm 1.0 \times 10^{-11}$	Measured
	7.4×10^{-11}	Se77b,BKS78
12a. $Ne_2^* + NF_3 \rightarrow NeF^* + NF_2 + Ne$	5×10^{-11}	Analogy
12b. $Ne_2^* + NF_3 \rightarrow Ne_2F^* + NF_2$		
13. $Ne_2^* + Xe \rightarrow Xe^+ + 2Ne + e$	7.5×10^{-11}	Analogy
14. $Ne_2^* \rightarrow h\nu$ (85 nm) $+ 2Ne$	2×10^5-3×10^8	LEH73,Lo76
Neon Fluoride Reactions		
15. $NeF^* \rightarrow h\nu$ (107 nm) $+ Ne + F$	4.2×10^8	WBR77
16. $NeF^* \rightarrow Ne + F^*$	2×10^9	Guessed
17. $NeF^* + NF_3 \rightarrow$ products	10^{-10}	Guessed
18. $NeF^* + Xe \rightarrow Xe^+ + F^- + Ne$	10^{-10}	Guessed
19. $NeF^* + 2Ne \rightarrow Ne_2F^* + Ne$	10^{-31}	Analogy

Table 9 (Continued)

Reaction	Rate Coefficient $(cm^{-3}\ molecule^{-1} sec^{-1}$, etc.$)$	Reference
Fluorine Reactions		
20. $F^* + NF_3 \to F_2^* + NF_2$	$2.5 \pm 0.1 \times 10^{-10}$	Measured
21. $F^* + Xe \to Xe^+ + F + e$	$3.1 \pm 0.1 \times 10^{-10}$	Measured
22. $F^* + 2Ne \to NeF^* + Ne$	$< 5 \times 10^{-35}$	Measured
23. $F^* \to h\nu$ (97 nm) $+ F$	$\sim 10^4$	BC76
	$< 5 \times 10^5$	Measured
24. $F_2^* \to h\nu$ (158 nm) $+ F_2$	2×10^7	Measured
25. $F_2^* + Xe \to XeF^* + F$	$1.3 \pm 0.2 \times 10^{-10}$	Measured
26. $F_2^* + NF_3 \to$ products	$3.8 \pm 0.3 \times 10^{-10}$	Measured
Xenon Ion Reactions		
27. $Xe^+ + Xe + Ne \to Xe_2^+ + Ne$	1.5×10^{-31}	Analogy
28. $Xe^+ + F^- (+ M) \to XeF^* (+ M)$	10^{-6}	Analogy
29. $Xe_2^+ + e \to Xe^* + Xe$	2×10^{-7} at 1 eV	BB70
30. $Xe_2^+ + F^- \to XeF^* + Xe$	10^{-6}	Analogy
Excited Xenon Reactions		
31. $Xe^* + Xe + Ne \to Xe_2^* + Ne$	$1.6 \pm 0.1 \times 10^{-32}$	Measured
32. $Xe^* + NF_3 \to XeF^* + NF_2$	9×10^{-11}	VKS76
33a. $Xe_2^* + NF_3 \to XeF^* + NF_2 + Xe$ 33b. $Xe_2^* + NF_3 \to 2Xe + F + NF_2$	5×10^{-11}	Analogy
34. $Xe_2^* \to h\nu$ (173 nm) $+ 2Xe$	$10^7 - 2 \times 10^8$	LEH73

Some of the important ion reactions are under study in our laboratory and in Biondi's at Pittsburgh. Johnson et al. [JMB78] have confirmed the predicted slowness of the charge exchange of Ne_2^+ with Xe. Perhaps the most important uncharacterized ion reactions are the interception reactions of Ne^+ and Ne_2^+ with NF_3. We hope to characterize some of these reactions by monitoring Ne_2^+ by absorption and by its electron recombination product Ne^{**}. It will be necessary for these reactions to be studied in a flowing afterglow such as that used by Biondi.

Neon Ion Reactions

Because the major portion of the deposited excitation begins as atomic neon ions, the rates of the reactions of neon atomic and molecular ions must be understood in some detail. In a $Ne/Xe/NF_3$ mixture the major reactions of Ne^+ are

$$Ne^+ + 2Ne \rightarrow Ne_2^+ + Ne$$

$$Ne^+ + NF_3 \rightarrow NF_3^+ + Ne$$

$$Ne^+ + Xe \rightarrow Xe^+ + Ne$$

$$Ne^+ + F^- \ (+ M) \rightarrow NeF^* \ (+M)$$
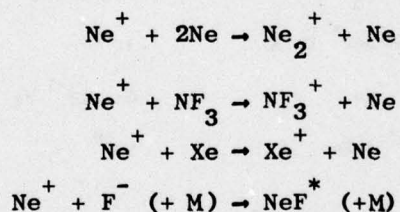
The three-body association reaction to form Ne_2^+ has been studied by Vitols and Oskam [VO72] and Orient [Or73], who found rate coefficients of $4.4 \times 10^{-32} \ cm^6 \ sec^{-1}$ and $4.6 \times 10^{-32} \ cm^6 \ sec^{-1}$, respectively. The charge transfer reaction of Ne^+ has been recently studied by Johnson et al. [JMB78] and found to be quite slow. We have been unable to find a measurement of the rate reaction of $Ne^+ + NF_3$, and we have chosen a rate coefficient of $5 \times 10^{-10} \ cm^3 \ sec^{-1}$ in analogy with the rates observed for charge transfer to other polyatomic molecules [BAM70]. For the recombination of Ne^+ with F^-, we have chosen the pressure-saturated effective two-body rate coefficient of $10^{-6} \ cm^3 \ sec^{-1}$ that is now the conventional value for all rare-gas-cation halide-anion recombinations. It is assumed

98

that the product NeF* is obtained with unit branching ratio. The subsequent predissociation to Ne + F* is described below.

The reactions of Ne$_2^+$ with a number of atoms and molecules have been studied. Unfortunately these studies have not included NF$_3$ or Xe. The dissociative recombination

$$Ne_2^+ + e \rightarrow Ne^{**} + Ne$$
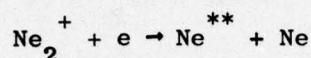
has been described in the review of Bardsley and Biondi [BB70]. The value included in Table 9 is that for an electron temperature of 1 eV. Bohme et al. [BAM70] studied the charge transfer reactions of Ne$_2^+$ with a variety of molecular species and with atomic argon and krypton. They found that charge transfer to molecules was rapid, with rate coefficients of 5×10^{-10} cm^3 sec^{-1} or larger. In analogy we have chosen this value for the reaction

$$Ne_2^+ + NF_3 \rightarrow NF_3^+ + 2Ne \qquad .$$
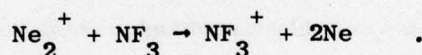
The reaction of Ne$_2^+$ with rare gas atoms appears to be unusually slow, probably impeded by the large amount of energy that must be converted into translational energy. We have chosen the value of 10^{-13} cm^3 sec^{-1} for the reaction with xenon:

$$Ne_2^+ + Xe \rightarrow Xe^+ + 2Ne \qquad ,$$
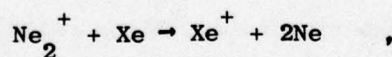
which is likely to be an upper limit considering the upper limits of 5×10^{-13} cm^3 sec^{-1} and 5×10^{-14} cm^3 sec^{-1} found for Ar and Kr, respectively [BAM70]. Recent work of Johnson et al. [JMB78] also suggests 10^{-13} cm^3 sec^{-1} as an upper limit. The ionic recombination

$$Ne_2^+ + F^- \rightarrow NeF^* + Ne$$
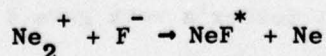
is chosen to have the conventional rate coefficient of 10^{-6} cm^3 sec^{-1}.

Excited Neon Reactions

Until recently the reactions of Ne^* were less well characterized than the corresponding reactions of the heavier rare gases. The three-body association reaction

$$Ne^* + 2Ne \rightarrow Ne_2^* + Ne$$
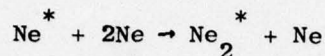
has been studied previously by Phelps [Ph59] and Leichner et al. [LCL76]. They found rate coefficients of $5 \times 10^{-34} \, cm^6 \, sec^{-1}$ and $5.4 \times 10^{-34} \, cm^6 \, sec^{-1}$, respectively, for the reactions of $Ne^*(^3P_2)$. Our laser absorption measurements give a preliminary value of $4.1 \pm 0.4 \times 10^{-34} \, cm^6 \, sec^{-1}$ for the reaction of $Ne^*(^3P_2)$, as illustrated in Figure 27. For the harpooning reaction

$$Ne^* + NF_3 \rightarrow NeF^* + NF_2 \quad ,$$
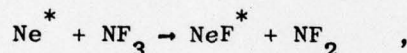
Setser [Se77b, BK78] has recently reported a rate coefficient of $7.8 \times 10^{-11} \, cm^3 \, sec^{-1}$. We have measured a value of $1.05 \pm 0.05 \times 10^{-10} \, cm^3 \, sec^{-1}$. The branching ratio to produce NeF^* is unknown. Before the Penning ionization reaction

$$Ne^* + Xe \rightarrow Xe^+ + Ne + e$$
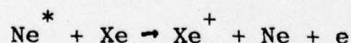
has been characterized experimentally, Olson [O177] had provided an estimate of $7 \times 10^{-11} \, cm^3 \, sec^{-1}$ using a scaling rule [BDK68] based on the polarizabilities and the rate for the analogous reaction involving He^* [LSF74]. Setser [Se77b,BKS78] has found a value of $7.4 \times 10^{-11} \, cm^3 \, sec^{-1}$, while our measurements yield $7.5 \pm 1 \times 10^{-11} \, cm^3 \, sec^{-1}$. We have also followed the reaction of $Ne^*(^3P_2)$ with F_2 and find a rate coefficient of $5.3 \pm 0.5 \times 10^{-10} \, cm^3 \, sec^{-1}$; Setser's work gave $4.14 \times 10^{-10} \, cm^3 \, sec^{-1}$.

The reaction of Ne_2^* with NF_3 could produce either NeF^* or Ne_2F^*
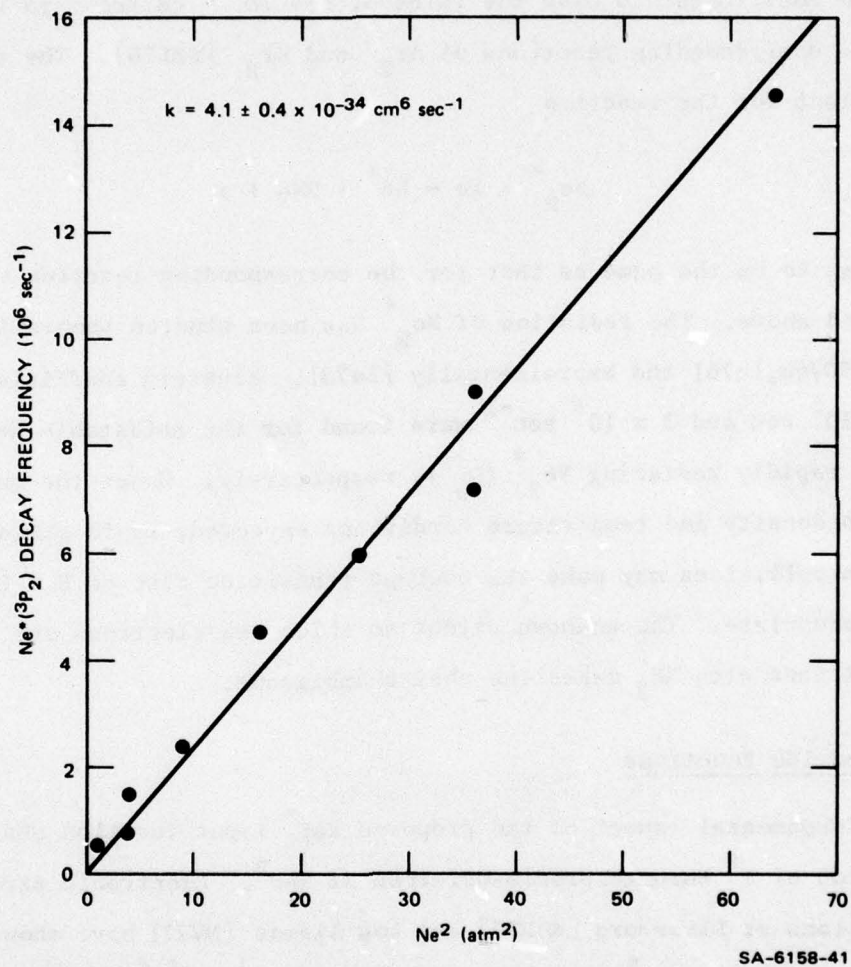
FIGURE 27   Ne*($^3P_2$) DECAY FREQUENCY VERSUS THE SQUARE OF
THE NEON PRESSURE

101

$$Ne_2^* + NF_3 \quad \begin{cases} \rightarrow NeF^* + NF_2 + Ne \\ \\ \rightarrow Ne_2F^* + NF_2 \end{cases}$$
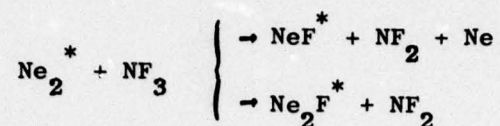
or a variety of other energetically accessible products. We have chosen the rate coefficient to have the value of 5×10^{-11} $cm^3 sec^{-1}$ in analogy with the corresponding reactions of Ar_2^* and Kr_2^* [NHL76]. The rate coefficient for the reaction

$$Ne_2^* + Xe \rightarrow Xe^+ + 2Ne + e$$
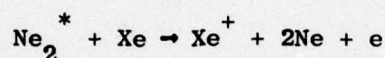
is chosen to be the same as that for the corresponding reaction of Ne^* described above. The radiation of Ne_2^* has been studied theoretically [LEH73, SC74b, Lo76] and expreimentally [Le73]. Einstein coefficients of 2×10^5 sec and 3×10^8 sec^{-1} were found for the metastable $Ne_2^* (1_u)$ and the rapidly radiating $Ne_2^* (0_u^+)$, respectively. Under the moderate electron density and temperature conditions expected, rapid mixing by electron collisions may make the average transition rate of 8×10^7 sec^{-1} more appropriate. The unknown extent to which the electrons are cooled by collisions with NF_3 makes the choice ambiguous.

Neon Fluoride Reactions

A fundamental aspect of the proposed XeF^* input reaction chain is the production of F^* through predissociation of NeF^*. Electronic structure calculations at Livermore [WBR77] and Los Alamos [DH77] have shown that the minimum in the NeF^* lies only 1.1 eV below $Ne + F^* (^4P_{5/2})$ and 1.4 eV below $Ne + F^* (^2P_{3/2})$, as illustrated schematically in Figure 28. NeF^* produced in the reactions $Ne^+ + F^- + M$, $Ne_2^+ + F^-$, or $Ne^* + NF_3$ should initially contain several electron volts of vibrational energy. During the vibrational relaxation down to $v'=0$, passage through the curve crossings shown in Figure 28 should lead predominantly to predissociation

102
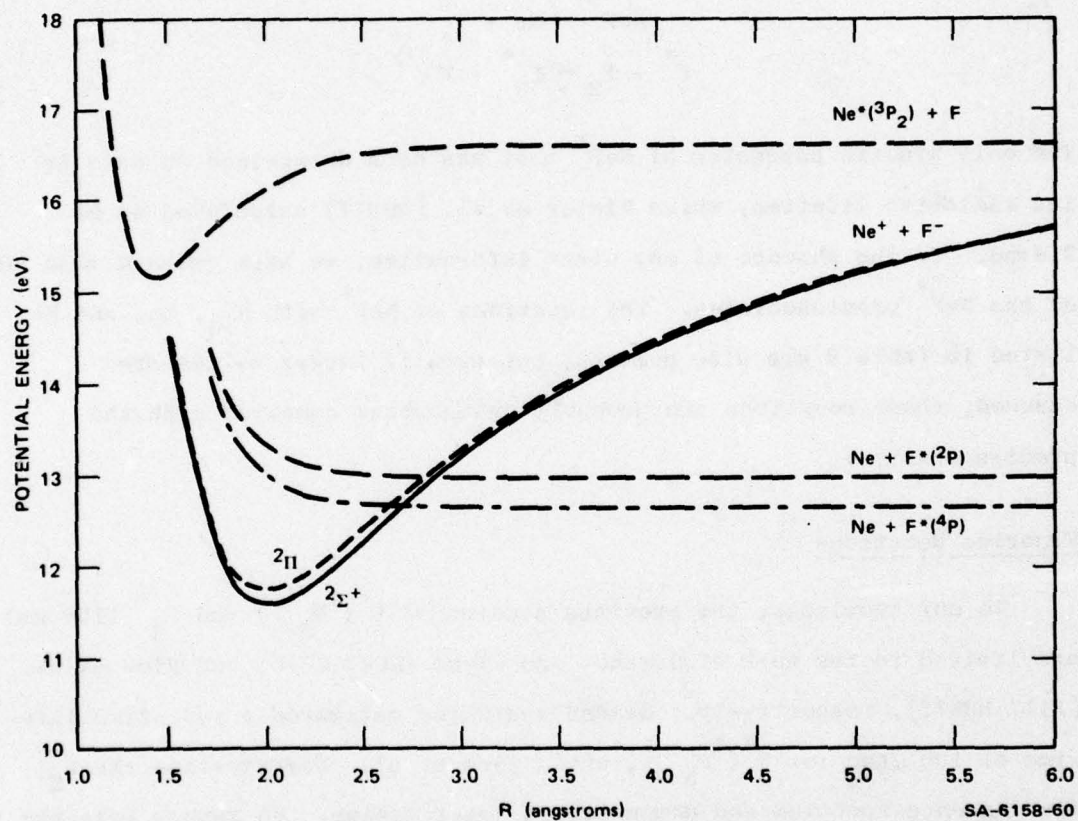
FIGURE 28   NeF* POTENTIAL CURVES

103

to $F^*(^2P)$ and $F^*(^4P)$ and to the several other $F^* + Ne$ levels that are also below the $Ne^+ + F^-$ dissociation limit. The only previous experimental study of the NeF^* fluorescence and predissociation is that of Rice et al. [Ri77,RHW77]. They found that electron beam excitation of Ne/F_2 mixtures led to some NeF^* emission near 108 nm, but that the major emitter was F_2^*. The F_2^* is presumably produced by the reaction scheme

$$NeF^* \to Ne + F^*$$
$$F^* + F_2 \to F_2^* + F \quad .$$
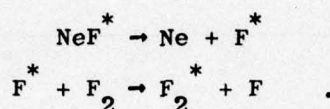
The only kinetic parameter of NeF^* that has been determined to date is its radiative lifetime, which Winter et al. [WBR77] calculated to be 2.4 ns. In the absence of any other information, we have guessed that 80% of the NeF^* predissociates. The reactions of NeF^* with NF_3, Xe, and Ne listed in Table 9 are also guesses, but even if larger values are assumed, these reactions are probably unimportant compared with the predissociation.

Fluorine Reactions

To our knowledge, the previous studies of $F^*(^4P_{5/2})$ and F_2^* (158 nm) are limited to the work of Bemand and Clyne [BC73,BC76] and Rice et al. [Ri77,RHW77], respectively. Bemand and Clyne estimated a radiative lifetime of 100 μsec for $F^*(^4P_{5/2})$, while Rice et al. characterized the F_2^* fluorescence spectrum and demonstrated laser action. We report here the preliminary results of our studies of the reactions of F^* and F_2^* with Ne, Xe, F_2, and NF_3, and the F_2^* radiative lifetime.

The decay of the lowest of the Rydberg states of atomic fluorine, $F^*(^4P_{5/2})$, was monitored by absorption of 624 nm radiation from a cw dye laser. The transition has been assigned to $F^*(^4P_{5/2}) \to F^*(^4S_{3/2})$. Some care was taken to ensure that the observed F^* decay was representative of its collisional and radiative destruction, rather than some precursor

104

reaction. The F^* population is presumed to arise in part from direct dissociative excitation of F_2 or NF_3 and in part from predissociation of NeF^*. The major precursor of NeF^* is Ne_2^+ with some contribution from Ne^*. The decay of F^* is always slower than that deduced for Ne_2^+, and pressure dependence is substantially different from that of Ne^*. Variation of the neon pressure yielded imperceptible change in the F^* decay frequency, while the decay of Ne^* increased as shown in Figure 27. The F^* decay frequency increased linearly with added NF_3 or added Xe, as shown in Figures 29 and 30, yielding the rate coefficients:

$$F^* + NF_3 \rightarrow F_2^* + NF_2 ? \qquad k = 2.5 \pm 0.1 \times 10^{-10} \ cm^3 sec^{-1}$$
$$F^* + Xe \rightarrow Xe^+ + F + e \qquad k = 3.1 \pm 0.1 \times 10^{-10} \ cm^3 sec^{-1} \quad .$$
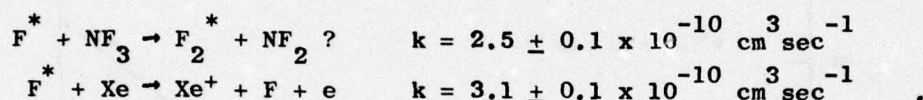
That F_2^* is the major product of the reaction with NF_3 is only a supposition. Similar variation of the F_2 pressure (not shown) gave a rate coefficient for reaction with F_2 (again presumably to give F_2^*) of $5.1 \pm 0.3 \times 10^{-10} \ cm^3 sec^{-1}$, with a zero pressure intercept less than $5 \times 10^5 sec^{-1}$. This is consistent with the estimate of 100 μsec for the radiative lifetime [BC76].

The decay of F_2^* was monitored directly by its fluorescence near 158 nm. Little change in the time dependence resulted from change in the neon pressure from 1 to 5 atm. The variation in the decay frequency with added NF_3 and Xe is shown in Figures 31 and 32, leading to rate coefficients:

$$F_2^* + NF_3 \rightarrow products \qquad k = 3.8 \pm 0.3 \times 10^{-10} \ cm^3 sec^{-1}$$
$$F_2^* + Xe \rightarrow XeF^* + F ? \qquad k = 1.3 \pm 0.2 \times 10^{-10} \ cm^3 sec^{-1} \quad .$$
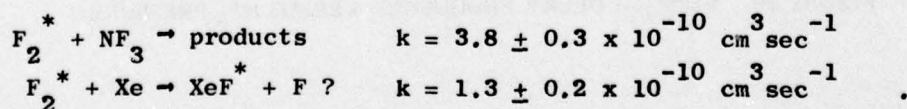
The rate coefficient for quenching by F_2 was found to be $3.5 \pm 0.2 \times 10^{-10} \ cm^3 sec^{-1}$. By extrapolation to zero F_2 or NF_3 pressure, we deduced a radiative lifetime of 40 ± 5 ns,

$k = 2.5 \pm 0.1 \times 10^{-10}$

$Ne = 2$ atm
$F_2 = 0.2$ torr

y-axis: $F^*(^4P_{5/2})$ DECAY FREQUENCY (10^6 sec^{-1})

x-axis: NF_3 (torr)
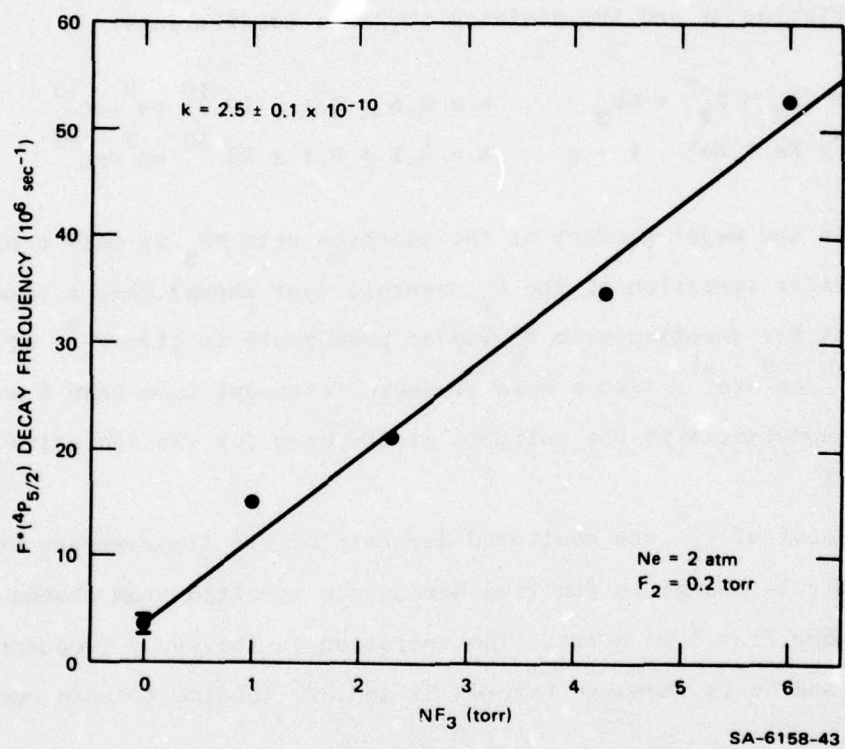
SA-6158-43

FIGURE 29 $F^*(^4P_{5/2})$ DECAY FREQUENCY VERSUS NF_3 PRESSURE
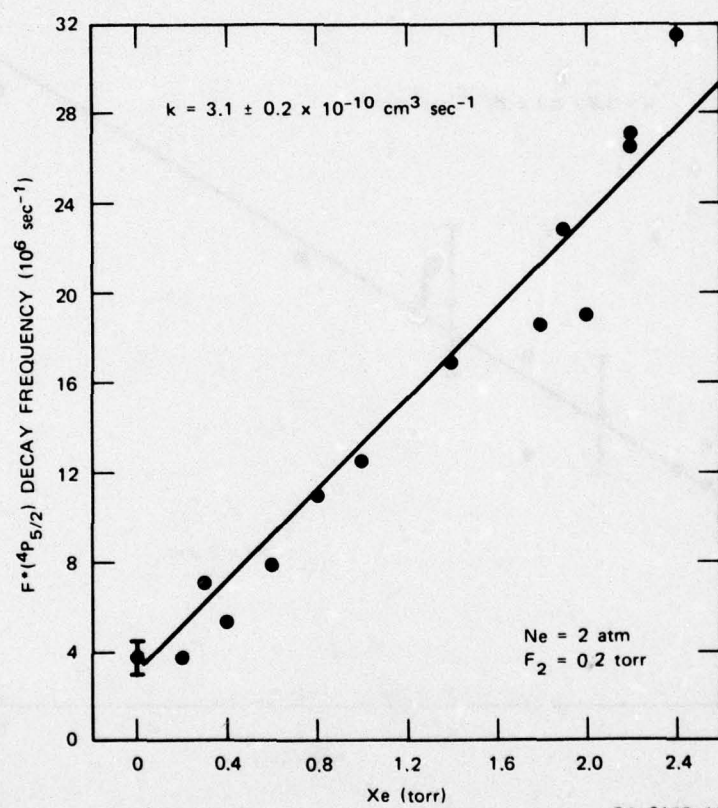
FIGURE 30   F*($^4P_{5/2}$) DECAY FREQUENCY VERSUS XENON PRESSURE

107
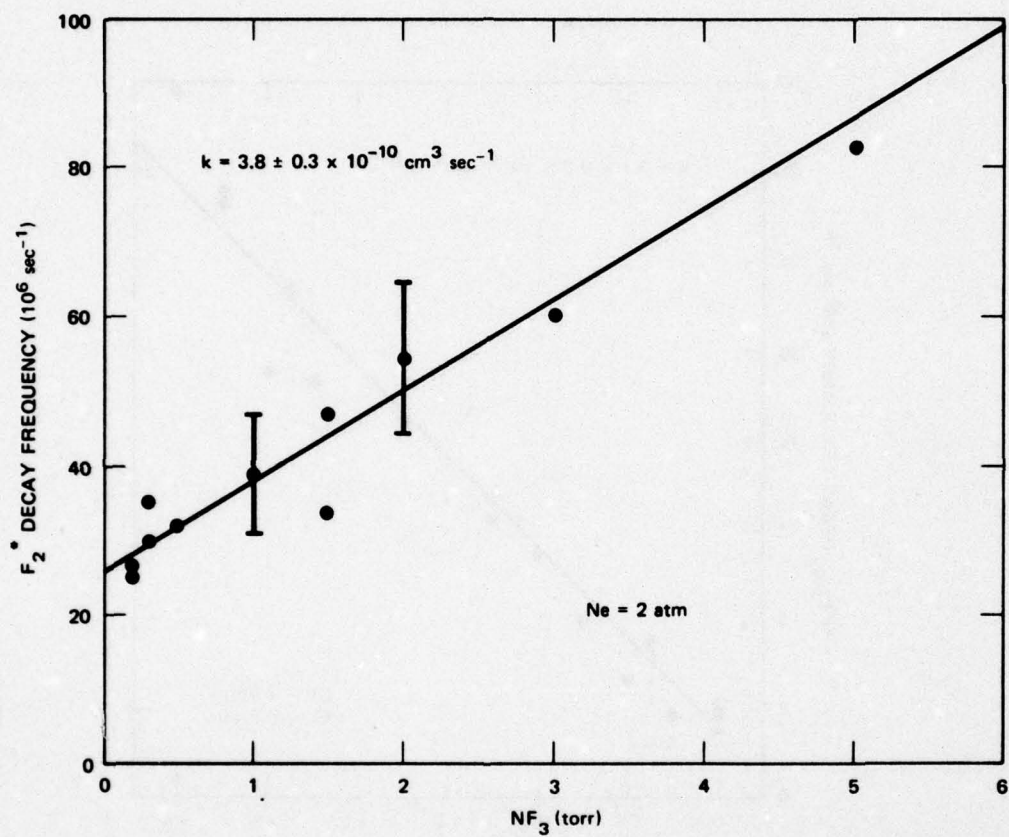
FIGURE 31 F_2^* DECAY FREQUENCY VERSUS NF_3 PRESSURE

SA–6158–28

108
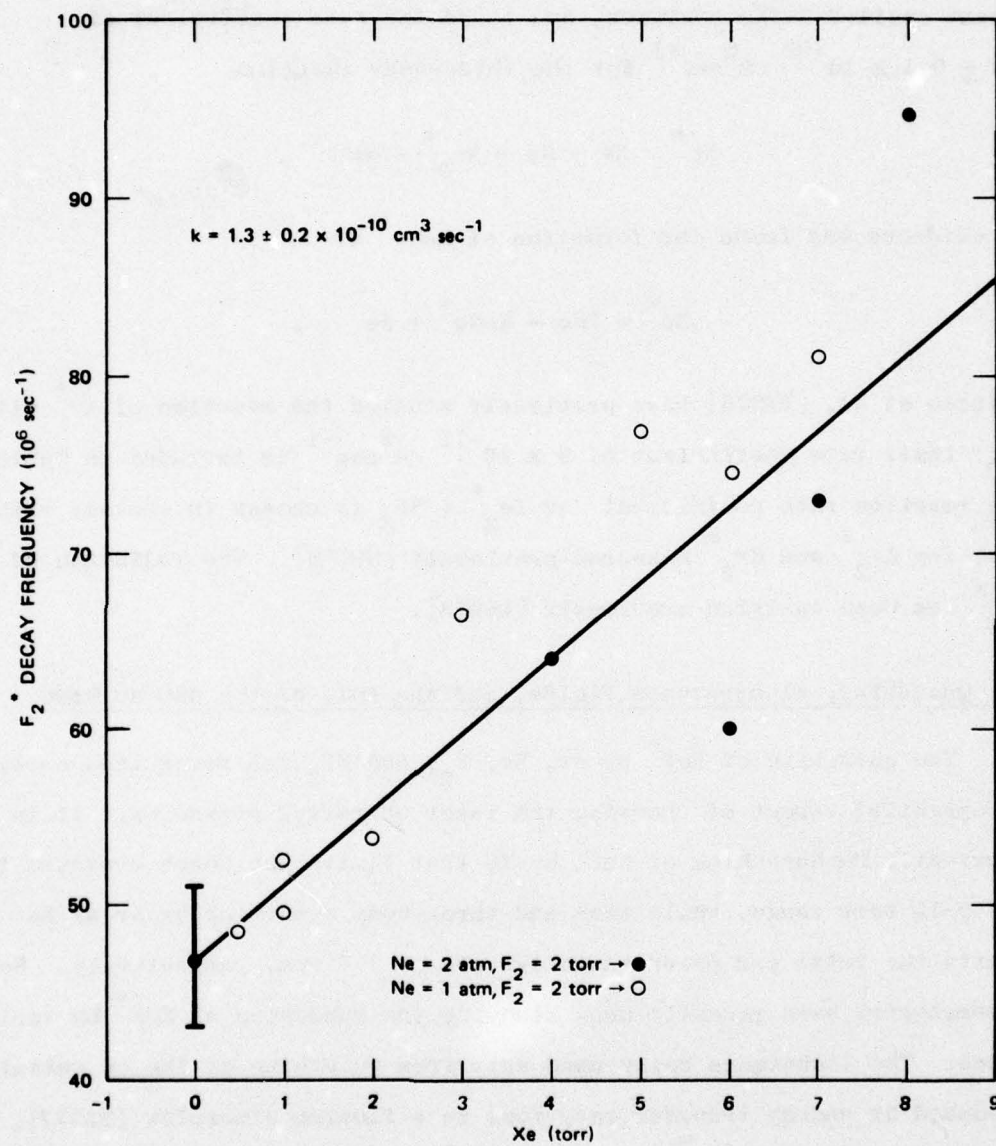
FIGURE 32 F_2^* DECAY FREQUENCY VERSUS XENON PRESSURE

SA-6158-29

109

Excited Xenon Reactions

The reaction of Xe^* to form Xe_2^* in a neon buffer had not previously been investigated. We have monitored the decay of the Xe_2^* radiation in e-beam excited Ne/Xe mixtures, and found the rate coefficient of $1.6 \pm 0.1 \times 10^{-32}$ $cm^6 sec^{-1}$ for the three-body reaction

$$Xe^* + Xe + Ne \rightarrow Xe_2^* + Ne \quad .$$
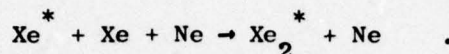
No evidence was found for formation of $XeNe^*$ by

$$Xe^* + 2Ne \rightarrow XeNe^* + Ne \quad .$$
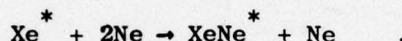
Velazco et al. [VKS76] have previously studied the reaction of Xe^* with NF_3; their rate coefficient of 9×10^{-11} $cm^3 sec^{-1}$ is included in Table 9 The reaction rate coefficient for $Xe_2^* + NF_3$ is chosen in analogy with that for Ar_2^* and Kr_2^* measured previously [NHL76]. The radiation of Xe_2^* has been analyzed previously [LEH73].

XeF Quenching, Fluorescence Yields, and the Role of the 460-nm Band

The quenching of XeF^* by Ar, Xe, F_2, and NF_3 was recognized early as an essential aspect of choosing the laser operating pressures. It is apparently the quenching of XeF^* by Xe that limits the xenon pressure to the 5-10 torr range, while two- and three-body quenching by Ar or Ne limits the total gas pressure to 1-2 atm or 3-5 atm, respectively. Several laboratories have recently been studying the quenching of XeF^* by various gases. The techniques being used vary from quenching of the cw emission produced by energy transfer reactions in a flowing afterglow [BSD77], to quenching of laser-induced fluorescence out of ground state state XeF produced by flash photolysis [FC78,CF78], to quenching of the cw emission produced by ion-ion recombination in electron-beam excited Ar/Xe/NF$_3$ mixtures [RJM77c], to quenching of the transient XeF^* produced by photo-dissociation of XeF_2 [BS77,EW77]. Our own analysis of the XeF quenching

110

is incomplete, and we will postpone a detailed discussion to a later report.

A curious and little explored aspect of the XeF* fluorescence is the broad band emission feature near 460 nm. Our early analysis in $Ar/Xe/F_2$ mixtures suggested that the feature might be due to ArXeF*. However, a similar feature also appears in $He/Xe/NF_3$ and $Ne/Xe/NF_3$. It now appears likely that the 460 nm emission arises from the XeF* $(C\frac{3}{2})$ level, which is calculated [DH77] to lie very close to the upper laser level XeF* $(B\frac{1}{2})$, radiating to the repulsive XeF$(A\frac{3}{2})$ level, in agreement with the original assignment of Brau and Ewing [BE75a]. The lifetime for the $B\frac{1}{2}$ level is 15 ± 3 nsec from an average of the various experimental and theoretical determinations. The calculated lifetime for the $C\frac{3}{2}$ level is 113 nsec [DH77], while crude experimental estimates range from 50 to 100 nsec [FC77,HHN77]. There is some evidence for a dependence of the band shape on xenon pressure, suggesting that Xe_2F may contribute as well.

The major uncertainty in our understanding of the XeF* fluorescence behavior is the relative radiative output in the 351-3 and 460 nm bands. By this we refer to the time and wavelength integrated emission intensities of the two bands. Under Febetron 706 or low-current-accelerator excitation, we observe that the ratio of the visible/uv-bands of approximately 3 ± 1 at pressures of neon or argon from 1-5 atmospheres. Under medium current (2 A cm^{-1}) long pulse (1 μsec) excitation, on the other hand, the visible/uv ratio varies from 1:5 to 1:1 under the same change of background gas pressure. Most surprisingly, the calibrated fluorescence yields are found to add up to approximately 100% under all excitation conditions at low pressure.

The most plausible explanation we have been able to find involves collisional mixing of the $B\frac{1}{2}$ and $C\frac{3}{2}$ levels by electrons. We suppose that the $C\frac{3}{2}$ is actually the lower of the two levels, lying perhaps 1000 cm^{-1} below the $B\frac{1}{2}$. The theoretical calculations to date [DH77] would not resolve this issue. We further suppose that the quenching of the $B\frac{1}{2}$ level, as studied by other workers, results in large part in production of the $C\frac{3}{2}$ level. Of course, the initial relative production of the $B\frac{1}{2}$ and $C\frac{3}{2}$ levels is unknown. Finally, we suppose that the collisional electron mixing

$$\text{XeF}^*(B\tfrac{1}{2}) + e \rightleftarrows \text{XeF}^*(C\tfrac{3}{2}) + e$$
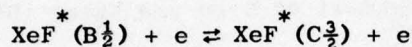
is rapid, in analogy with the rare gas excimers [Lo76].

Under the actual experimental conditions used, a major difference will be the electron density. In the Febetron case the observations were made well into the afterglow (more than 30 nsec of the 2-nsec excitation pulse) by which time most of the electrons would have been consumed by dissociative attachment. Hence under all conditions we might expect at least as much light in the 460 nm band since the $C\frac{3}{2}$ level lies lower in energy and is presumably populated statistically with respect to the $B\frac{1}{2}$ level. Under excitron excitation, however, the electron density remains high ($> 10^{14}$ cm^{-3}) throughout the 1-μsec excitation pulse. At the lowest pressures, the electrons should keep equal populations in the $B\frac{1}{2}$ and $C\frac{3}{2}$ levels. Under these conditions, the uv emissions should be favored by the ratio of the Einstein coefficients, uv/visible $\sim 3/1$ to $7/1$. At higher pressures the electron mixing must compete with the rapid collisional relaxation

$$\text{XeF}^*(B\tfrac{1}{2}) + \text{Ne} \rightarrow \text{XeF}^*(C\tfrac{3}{2}) + \text{Ne} \quad ,$$
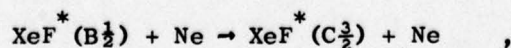
leading to a rapid decrease in the uv emission as the pressure is increased.

112

While this analysis is at present tentative, it is clear that the 460 nm band and the $C\frac{3}{2}$ state must play an important role in our understanding of the XeF^* fluorescence kinetics.

XeF Lower Level Removal

The ground state of XeF, called $X^2\Sigma_{\frac{1}{2}}$, has an attractive potential $(D_e \approx 1150 \text{ cm}^{-1})$ that supports 10 or 11 bound vibrational levels [Te76, SK77]. The XeF laser operates on bound-to-bound transitions terminating on various of the vibrational levels of the ground state. Band origins calculated from the spectroscopic constants determined by Tellinghuisen [Te76] suggest the following identifications:

XeF Laser Transitions

$$3490 \text{ Å} \qquad v' = 0 \to v'' = 1$$
$$3512 \text{ Å} \qquad v' = 0 \to v'' = 2$$
$$3513 \text{ Å} \qquad v' = 1 \to v'' = 4$$
$$3533 \text{ Å} \qquad v' = 0 \to v'' = 3$$

Concern exists about the rate of removal of the lower laser level. Vibrational relaxation in the lower level is insufficient to adequately deplete the population since the low vibrational spacing ($\omega_e = 226 \text{ cm}^{-1}$) leads to the estimates that 9.6% and 4.4% of the ground state molecules will be in $v'' = 2$ and $v'' = 3$, respectively, at room temperature.

The only hope for sustained laser action is therefore that the ground state vibrational manifold must be depleted by dissociation induced by collisions with the background rare gas. Calculation of the rates of collision-induced dissociation is a complicated task with an extensive literature.

A first step is the calcuation of the thermal equilibrium between XeF bound in vibrational levels of the ground electronic state and free xenon and fluorine atoms. It is important to establish that the free

xenon and fluorine atoms do not produce ground state XeF by three-body recombination, $Xe + F + M \rightarrow XeF + M$, faster than it is dissociated by gas collisions,

$$XeF + M \rightarrow Xe + F + M \qquad .$$
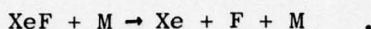
Such a calculation (see Appendix C) gives the following result. We assume that, by the end of a 1-μsec pumping pulse in $Ne/Xe/NF_3$, approximately 2×10^{16} F atoms have been produced per cm^3. If the $XeF(X^2\Sigma_{\frac{1}{2}}^+)_{v''=2}$ and $XeF(X^2\Sigma_{\frac{1}{2}}^+)_{v''=3}$ populations were in thermal equilibrium at room temperature with that density of F atoms, at 6 torr of Xe, then

$$XeF(X^2\Sigma_{\frac{1}{2}}^+)_{v''=2} = 8 \times 10^{11} \ cm^{-3}$$
$$XeF(X^2\Sigma_{\frac{1}{2}}^+)_{v''=3} = 4 \times 10^{11} \ cm^{-3} \qquad .$$

Using a $3 \times 10^{-16} \ cm^2$ absorption cross section, this leads to only $2 \times 10^{-4} \ cm^{-1}$ and $1 \times 10^{-4} \ cm^{-1}$ absorption at 351 and 353 nm, respectively, probably negligible in comparison with the other absorptions in the laser medium. One can therefore conclude that the crucial kinetic parameter for avoiding bottlenecking is the rate of collision-induced dissociation.

A crude calculation of the collision-induced dissociation rate coefficient was made using a master equation approach. The lower levels of the XeF laser ($v''=2$ for the 351 nm and $v''=3$ for the 353 nm transitions, respectively) lie so low in the ground state potential as to make improbable dissociation in a single collision with the background rare gas. While direct dissociation of the lower levels will make some contribution, the dominant process will most likely be rapid dissociation of the higher few levels within kT of the top and slower repopulation of the higher levels by "ladder climbing" from $v'' = 0, 1, 2,$ and 3.

To describe the time evaluation of the vibrational distribution, we need to estimate the vibrational excitation and deexcitation rate coefficients from each level to all the others. In addition, we must estimate

114

the direct dissociation rate coefficient for each vibrational level. The Δv dependence of the energy transfer cross sections was calculated by a perturbation technique similar to that used by Kurzel and Steinfeld [KS70] to describe vibrational excitation and deexcitation in I_2^*. The rate coefficients are taken to have the form

$$k_{fi} = Q|V_{fi}|^2 \quad \text{for} \quad f < i$$
$$= Q|V_{fi}|^2 \exp\{-\Delta E_{fi}/kT\} \quad f > i \quad ,$$

where V_{fi} is the matrix elements of the repulsive rare-gas/diatomic interaction potential between the initial and final vibrational wave functions, and Q is a constant to be chosen to give reasonable values when $f-i = \pm 1$. Following the work of Mahan [Ma70] and Kurzel and Steinfeld [KS70], we have used an exponential repulsive interaction using the combination rules of Abrahamson [Ab69]. To describe the vibrational levels, we derived Morse oscillator wave functions from the spectroscopic constants [Te76].

In common with the work of Steinfeld and colleagues [KS70,SK65], the matrix elements were well approximated by an exponential scaling with respect to the energy transferred:

$$|V_{fi}|^2 \sim \exp\{-\alpha|\Delta E_{fi}|\} \quad ,$$

where the constant α depends on the exponent in the repulsive interaction potential. Such an "exponential gap law" appears to be typical in atom-diatom inelastic scattering [He77]. Below we have used $\alpha = 0.014$ (with ΔE in cm^{-1}), $Q = 1 \times 10^{-10}$ cm^3/sec. The work of Kurzel and Steinfeld [KS70] gave $\alpha = 0.018 \pm 0.004$ and $Q \sim 5 \times 10^{-11}$ cm^3/sec for collisions of rare gases with I_2^*.

Estimation of the direct dissociation rate coefficients is somewhat more tentative. Consider a diatomic with a vibrational energy just below

115

dissociation. We suppose that the rate coefficient to acquire energy ΔE from the background gas is

$$k(\Delta E) = Ce^{-(\alpha+1/kT)\Delta E} \quad ,$$

and that the total rate coefficient for acquisition of any amount of energy is "gas-kinetic"

$$3 \times 10^{-10} \text{ cm}^3 \text{sec}^{-1} = \int_0^{\infty} k(\Delta E)d\Delta E$$

$$= C/(\alpha+1/kT) \quad .$$

Hence $C = 3 \times 10^{-10}(\alpha+1/kT)$. Now given a vibrational level with dissociation energy D_v, the rate coefficient to acquire energy $\Delta E \geq D_v$ would then be chosen as

$$k_v = \int_{D_v}^{\infty} k(\Delta E)d\Delta E = \frac{C}{(\alpha+1/kT)} \exp\{-(\alpha+1/kT)D_v\}$$

or

$$k_v = 3 \times 10^{-10} \exp\{-(\alpha+1/kT)D_v\} \quad .$$

Considering the rather crude approximations made, there preliminary calculations cannot be expected to give better than factor-of-two agreement with experiments. The dissociation rate coefficients were calculated by the steady-state vibrational distribution reached by integrating the master equation out to several hundred nanoseconds. The bulk dissociation rate coefficient

$$XeF(X^2\Sigma) + M \rightarrow Xe + F + M$$
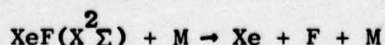
was calculated to be $\sim 2 \times 10^{-13}$, and the rate coefficient for removal of $v''=3$ was calculated to be 4×10^{-12} cm^3/sec, both at 300°K.

116

To estimate the impact of these dissociation rate coefficients, consider the case where we produce XeF^* at a rate of 2×10^{22} cm^{-3} sec^{-1} and it radiates with a 50% fluorescence yield with a 10-nsec effective kinetic decay time (spontaneous radiation plus quenching). If we suppose further that the XeF^* is all in $v'=0$, then the ambient excited state density is

$$XeF^* = N_u = 2 \times 10^{14} \; cm^{-3} \quad .$$

If the rate of production of ground state by fluorescence is 1×10^{22} $cm^{-3} sec^{-1}$ (i.e., 50% fluorescence yield), and if the background gas density is 5×10^{19} cm^{-3}, we find steady-state populations in $v'' = 2$ and 3 of

$$N_2 \approx 1.1 \times 10^{14} \; cm^{-3}$$

and

$$N_3 \approx 5 \times 10^{13} \; cm^{-3} = \frac{1 \times 10^{22}}{(4 \times 10^{-12})(5 \times 10^{19})} \quad .$$

Clearly the $v'=0$ to $v''=2$ transition at 351 nm can lase efficiently only at the beginning of the pulse. More energy can be extracted on the $v'=0$ to $v''=3$ transition at 353 nm, but the ratio $N_u/N_\ell \sim 4$ is not nearly as high as would be desirable. Increasing the background gas density above, say 1×10^{20}, would improve the N_u/N_ℓ ratio, but the increased quenching of XeF^* by the background gas is undesirable.

The laser performance [HT77] gives support to the importance of bottlenecking in the lower state. The laser begins to operate on both the 351 and 353 nm bands. After 100-200 nsec into the pulse, the 351 nm band shuts off, and laser action continues on the 353 nm, which shows an intensity time behavior typical of nearly bottlenecked lasers. Further, laser performance improves substantially as the background neon pressure is raised from 2 to 4 atmospheres.

117

Preliminary measurements [HT77] of the gain/fluorescence ratio at 353 nm show about a 30% decrease by the end of the 1-μsec pulse at 1 atmosphere of Ne. The calculations of the collision-induced dissociation referred to above would predict a 45% decrease (assuming an 18-nsec radiative lifetime [FC78]). However, the gain/fluorescence ratio near 351 nm did not show a time dependence.

It is apparent that this calculation of the collision-induced dissociation rate and the preliminary experiments, while far from complete or definitive, at least illustrate that a detailed understanding of the process is essential to optimization of the XeF laser.

IX.   OVERALL CONCLUSIONS

Candidate Selection

We have completed a detailed study of the general class of diatomic
molecules having ionic excited states that can be effective upper laser
levels. Using general theoretical arguments, we narrowed the possible
ionic candidates to a select few, most of which have already been investi-
gated (e.g., the rare gas halides). The interhalogens and Group IIB
halides are the most promising candidates that have not been investigated.
Laboratory studies at SRI and other laboratories have demonstrated the
promise of the HgCl and HgBr. Our investigations of ICl and IBr are as
yet incomplete but are sufficiently promising to justify further effort
to find appropriate donor molecules.

Other classes of laser candidate molecules, such as strongly bound
covalent states and weakly bound excimer states, have not yet been com-
pletely characterized. However, a few exemplary systems such as S_2
(covalent) and RgHg (weakly bound excimer) have received some attention.
Work on other systems in these classes is in progress.

HgCl Discharge Pumped Laser

The demonstration that an HgCl laser can, under the proper conditions,
be pumped by an electron-beam-controlled discharge was one of the most
significant contributions during this period. Its significance is
attached to the fact that the projected efficiency for discharge pumping
of this system is very high provided it can be operated under conditions
that approach optimum. Some of these conditions have already been
specified, but considerable work remains to determine the important
kinetic reaction rates that ultimately control the laser performance.

119

Certain critical problems that may limit performance such as ground-state reactions have already appeared. The success of this laser indicates that other candidates of the same class, particularly HgBr (recently demonstrated at NRL) and HgI, are strong candidates and should be given adequate investigation.

Kinetic Studies in XeF

Several developments in the understanding of important kinetic processes in the XeF laser have led to improvements in the performance of that system. The substitution of Ne for Ar as the host gas to reduce the absorption due to Ar_2^+ has necessitated understanding the input kinetic chain of the $Ne/Xe/NF_3$ mixture. The important energy flow pathways for this system have been identified and some of the rate constants determined. The kinetics of this system is complicated by the fact that several competing pathways exist and the reaction rates in each pathway must be measured.

An additional important feature of XeF that has recently been recognized is the collisional mixing of the B and C states due to electrons and host gas atoms. This mixing apparently strongly influences the relative emission intensities of the 351 and 460 nm bands of XeF. Obviously, to operate XeF efficiently at 351 nm, the mixing rate of these two states must be fast enough to permit use of the energy flowing into both states. The mechanism described above explains the experimental observations of the behavior of the two bands of XeF, but the mixing rates have not as yet been determined.

A theoretical computation of the XeF lower level removal rate was undertaken to assess the importance of bottlenecking. This problem is clearly critical to the performance of the laser and will have to be understood in considerable detail in order to attain optimum performance.

REFERENCES

Ab69   A. A. Abrahamson, Phys. Rev. <u>178</u>, 76 (1969).

BAB75   R. S. Bradford, Jr., E. R. Ault, and M. L. Bhaumik, Appl. Phys.
        Lett. <u>27</u>, 546 (1975).

BAM70   D. K. Bohme, N. G. Adams, M. Mosesman, D. B. Dunkin, and E. E.
        Ferguson, J. Chem. Phys. <u>52</u>, 5098 (1970).

BB70   J. N. Bardsley and M. A. Biondi in <u>Advances in Atomic and
        Molecular Physics</u> (Academic Press, New York, 1970), Chap. I.

BC73   P. P. Bemand and M.A.A. Clyne, Chem. Phys. Lett. <u>21</u>, 555 (1973).

BC76   P. P. Bemand and M.A.A. Clyne, J.C.S. Faraday. Trans. II <u>72</u>, 191
        (1976).

BDK68   K. L. Bell, A. Dalgarno, and A. E. Kingston, J. Phys. B <u>1</u>, 18 (1968).

BE75a   C. A. Brau and J. J. Ewing, J. Chem. Phys. <u>63</u>, 4640 (1975).

BK73   P. Brumer and M. Karplus, J. Chem. Phys. <u>58</u>, 3903 (1973).

BKS78   J. M. Brom, J. H. Kolts, and D. W. Setser, J. Chem. Phys. (to
        be published, 1978).

BS77   R. Burnham and S. K. Searles, 30th Gaseous Electronics Conference,
        Palo Alto, CA, 18-21 October 1977.

BSD77   H. C. Brashears, Jr., D. W. Setser, and D. Desmarteau, Chem. Phys.
        Lett., <u>48</u>, 84 (1977).

CF78   R. E. Center and C. H. Fisher, "Kinetic Studies for XeF and KrF
        Lasers," Final Report MSNW78-1062, Mathematical Sciences Northwest
        Inc., Bellevue, WA (January 1978).

CG65   G. V. Calder and W. F. Giauque, J. Phys. Chem. <u>69</u>, 2443 (1965).

CH77   L. F. Champagne and N. W. Harris, Fifth Conference on Chemical
        and Molecular Lasers, St. Louis, MO (18-21 April 1977).

Co38   S. D. Cornell, Phys. Rev. $\underline{54}$, 341 (1938)

DH77   T. H. Dunning, Jr. and P. J. Hay, to be published.

DM77   N. Djeu and C. Mazza, Chem. Phys. Lett. $\underline{46}$, 172 (1977).

EB75b   J. J. Ewing and C. A. Brau, Appl. Phys. Lett. $\underline{27}$, 557 (1975).

EGH73   D. J. Eckstrom, R. A. Gutcheck, R. M. Hill, D. L. Huestis, and
        D. C. Lorents, Report No. MP 73-1, Stanford Research Institute,
        Menlo Park, CA (July 1973).

EJM76   J. J. Ewing, J. H. Jacob, J. A. Mangano and H. A. Brown, Appl.
        Phys. Lett. $\underline{28}$, 656 (1976).

EW78   J. G. Eden and R. W. Waynant, Bull. Am. Phys. Soc. $\underline{23}$, 173 (1978)
        and J. Chem. Phys. $\underline{68}$, 2850 (1978).

FC78   C. H. Fisher and R. E. Center, Bull. Am. Phys. Soc. $\underline{23}$, 132 (1978).

GHH75   R. A. Gutcheck, R. M. Hill, D. L. Huestis, D. C. Lorents, and
        M. V. McCusker, Report No. MP 75-43, Stanford Research Institute,
        Menlo Park, CA (August 1975).

GT74   M. F. Golde and B. A. Thrush, Chem. Phys. Lett. $\underline{29}$, 486 (1974).

He77   D. F. Heller, Chem. Phys. Lett. $\underline{45}$, 64 (1977).

HGH74   R. M. Hill, R. A. Gutcheck, D. L. Huestis, D. Mukherjee, and
        D. C. Lorents, Report No. MP 74-39, Stanford Research Institute,
        Menlo Park, CA (July 1974).

HGH75   D. L. Huestis, R. A. Gutcheck, R. M. Hill, M. V. McCusker, and
        D. C. Lorents, Report No. MP 75-18, Stanford Research Institute,
        Menlo Park, CA (January 1975).

HHO76   R. O. Hunter, C. Howton, and J. Oldenettel, Paper 77-26, AIAA 15th
        Aerospace Sciences Meeting (1976).

HHT76   A. K. Hays, J. M. Hoffman, and C. C. Tisone, Chem. Phys. Lett.
        $\underline{39}$, 353 (1976).

HOH77   R. O. Hunter, J. Oldenettel, C. Howton, and M. V. McCusker,
        submitted for publication (1977) (included as Appendix B).

HT77   R. O. Hunter, Jr. and K. Y. Tang, private communication (1977)

122

HZN77   D. L. Huestis, E. Zamir, H. H. Nakano, R. M. Hill, and D. C. Lorents, Report No, MP 77-38, SRI International, Menlo Park, CA (May 1977).

JMB78   R. Johnson, J. Macdonald, and M. A. Biondi, J. Chem. Phys. <u>68</u>, 2991 (1978).

KJD75   H. F. Krause, S. G. Johnson, S. Datz, and F. K. Schmidt-Bleek, Chem. Phys. Lett. <u>31</u>, 577 (1975).

KS70   R. B. Kurzel and J. I. Steinfeld, J. Chem. Phys. <u>53</u>, 3293 (1970).

LCL76   P. K. Leichner, J. D. Cook, and S. J. Luerman, Phys. Rev. A <u>12</u>, 2501 (1976).

Le73   P. K. Leichner, Phys. Rev. A <u>8</u>, 815 (1973).

LEH73   D. C. Lorents, D. J. Eckstrom, and D. L. Huestis, Report No. MP 73-2, Stanford Research Institute, Menlo Park, CA (September 1973).

LK77   S. R. Leone and K. G. Kosnik, Appl. Phys. Lett. <u>30</u>, 346 (1977).

LO72   D. C. Lorents and R. E. Olson, Semiannual Technical Report No. 1, SRI Project 2018, Stanford Research Institute, Menlo Park, CA (December 1972).

Lo76   D. C. Lorents, Physica <u>82C</u>, 19 (1976).

LSF74   W. Lindinger, A. L. Schmeltekopf and G. C. Fehsenfeld, J. Chem. Phys. <u>61</u>, 2890 (1974).

Ma70   B. H. Mahan, J. Chem. Phys. <u>52</u>, 5221 (1970).

MLH76   M. V. McCusker, D. C. Lorents, D. L. Huestis, R. M. Hill, H. H. Nakano, and J. A. Margevicius, Report No. MP 76-46, Stanford Research Institute, Menlo Park, CA (May 1976).

MST76   J. R. Murray, J. C. Swingle, C. E. Turner, Jr., Appl. Phys. Lett. <u>28</u>, 530 (1976).

NHL76   H. H. Nakano, R. M. Hill, D. C. Lorents, D. L. Huestis, M. V. McCusker, and J. A. Margevicius, Report No. MP 76-99, Stanford Research Institute, Menlo Park, CA (December 1976).

Ol77   R. E. Olson, private communication (1977).

Or73   O. J. Orient, Chem. Phys. Lett. $\underline{23}$, 579 (1973).

Pa77   J. H. Parks, Appl. Phys. Lett. $\underline{31}$, 192 (1977).

Ph59   A. V. Phelps, Phys. Rev. $\underline{114}$, 1011 (1959).

PHS72 J. E. Parks, G. S. Hurst, T. E. Stewart, and H. L. Weidner,
       J. Chem. Phys. $\underline{57}$, 5467 (1972).

R70   B. Rosen, <u>Spectroscopic Data Relative to Diatomic Molecules</u>
       (Pergamon, New York, 1970).

Ri77   J. K. Rice, Seventh Winter Colloqiuim on High Power Visible Lasers,
       Park City, Utah, 16-18 February 1977.

RJM77 M. Rokni, J. H. Jacob, and J. A. Mangano, 30th Gaseous Electronics
       Conference, Palo Alto, CA, 18-21 October 1977.

RHW77 J. K. Rice, A. K. Hays, and J. R. Woodworth, Appl. Phys. Lett.
       $\underline{31}$, 31 (1977).

SC74   B. Schneider and J. S. Cohen, J. Chem. Phys. $\underline{61}$, 3240 (1972).

Se77   D. W. Setser, 30th Gaseous Electronics Conference, Palo Alto,
       CA, 18-21 October 1977.

SK66   J. I. Steinfeld and W. Klemperer, J. Chem. Phys. $\underline{42}$, 3475 (1965).

SK77   A. L. Smith and P. C. Kobrinsky, Thirty-second Symposium on
       Molecular Spectroscopy, Columbus, Ohio, 13-17 June 1977.

Ta77   K. Y. Tang, private communication, 1977.

Te76   J. B. Tellinghuisen, Report ORO-5005-8, Vanderbuilt University,
       Nashville, TN (June 1976).

THO78a K. Y. Tang, R. O. Hunter, Jr., J. Oldenettel, C. Howton, D.
       Huestis, D. Eckstrom, B. Perry, and M. McCusker, Appl. Phys.
       Lett. $\underline{32}$, 226 (1978) (included as Appendix D).

THO78b K. Y. Tang, R. O. Hunter, Jr., J. Oldenettel, and D. L. Huestis,
       submitted for publication.

THT75   C. E. Turner, Jr., P. W. Hoff, and J. Taska, "Electron Beam
         Energy Deposition and VUV Efficiency Measurements in Rare Gases,"
         UCRL-77202 preprint submitted to International Topical Con-
         ference on Electron Beam Research and Technology (November 1975).

THT76   C. E. Turner, Jr., P. W. Hoff, J. Taska and L. G. Schlitt, LLL
         Laser Program Annual Report-1975, UCRL50021-75 (March 1976),
         p. 499F.

VKS76   J. E. Velazco, J. H. Kolts, and D. W. Setser, J. Chem. Phys.
         65, 3469 (1976).

VO72   A. P. Vitols and H. J. Oskam, Phys. Rev. A 5, 2618 (1972).

W60   K. Wieland, Zeit. fur Elektrochemie 64, 761 (1960).

WB76   B. E. Wilcomb and R. B. Bernstein, J. Mol. Spec. 62, 442 (1976).

WBR77   N. W. Winter, C. F. Bender, T. N. Rescigno, J. Chem. Phys. 67,
         3122 (1977).

WCC77   W. R. Wadt, D. C. Cartwright, and J. C. Cohen, Appl. Phys. Lett.
         31, 672 (1977).

Wh78   W. T. Whitney, Appl. Phys. Lett. 32, 239 (1978).

ZHL76   E. Zamir, D. L. Huestis, D. C. Lorents, and H. H. Nakano, "Visible
         Absorptions by Electron Beam Pumped Rare Gases," 3rd Summer
         Colloquium on Electronic Transition Lasers, Snowmass-in-Aspen,
         CO, 1976; published in Electronic Transition Lasers II, L. E.
         Wilson, S. N. Suchard and J. I. Steinfeld, eds. (MIT, Cambridge,
         MA, 1977), p. 69.

Appendix A

EXTRACTION EFFICIENCY

by

D. L. Huestis
SRI International

and

R. O. Hunter, Jr.
Maxwell Laboratories, Inc.

Consider the laser medium illustrated below
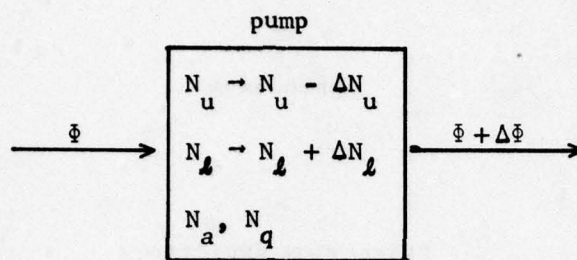
with a cw (or long time scale pump), with the optical flux also slowly varying in time. We wish to calculate the optical extraction efficiency in the amplifier mode as shown above. Only minor modifications are necessary to extend the analysis to an oscillator in steady state. The notation used is that N_u, N_{ℓ}, N_a, and N_q are the particle-densities of the upper laser level, lower laser level, absorbers and quenchers, respectively; Φ is the incoming optical flux in photons $cm^{-2} \ sec^{-1}$; $\Delta\Phi$, ΔN_u, and ΔN_{ℓ} are the changes in flux, upper, and lower laser levels, respectively. Pump refers to the rate of production of excited states (N_u) in molecules $cm^{-3} \ sec^{-1}$. Under the assumption that pump, N_a, and N_q are independent of the optical flux, the rate equations for the upper and lower laser levels are

$$0 = \frac{dN_u}{dt} = pump - k_q N_q N_u - AN_u - \sigma_{se} \Phi \left[N_u - \frac{g_u}{g_{\ell}} N_{\ell} \right] \qquad (A.1)$$

$$0 = \frac{dN_{\ell}}{dt} = AN_u + \sigma_{se} \Phi \left[N_u - \frac{g_u}{g_{\ell}} N_{\ell} \right] - RN_{\ell} \quad , \qquad (A.2)$$

where k_q is the quenching rate coefficient, A is the radiative Einstein coefficient, σ_{se} is the stimulated emission coefficient, g_u and g_{ℓ} are the degeneracies of the upper and lower laser levels, and R is the lumped

frequency of collisional removal of the lower laser level (in sec^{-1}). We have also assumed that the lower laser level is produced only by radiation from the upper laser level (not by quenching or other kinetic channels).

The number of photons extracted (in photons cm^{-3} sec^{-1}) is then

$$\Delta\Phi = \sigma_{se}\Phi\left[N_u - \frac{g_u}{g_\ell}N_\ell\right] - g_a\Phi \quad , \tag{A.3}$$

where g_a is the absorption coefficient, $\sigma_a N_a$. The extraction efficiency is then just

$$\eta_{ext} = \frac{\Delta\Phi}{pump} \quad . \tag{A.4}$$

We will assume that only the input flux Φ is under our control, all other parameters are fixed for other reasons, and choose the optical flux that maximizes the extraction efficiency.

Letting $g_u/g_\ell = \lambda$, and rearranging equation (A.2), we have (with $\sigma = \sigma_{se}$)

$$N_u = \frac{[R + \lambda\sigma\Phi]}{[A + \sigma\Phi]} N_\ell \quad , \tag{A.5}$$

and

$$(N_u - \lambda N_\ell) = \left[\frac{(R + \lambda\sigma\Phi)}{(A + \sigma\Phi)} - \lambda\right] N_\ell \tag{A.6a}$$

$$= \left[\frac{R - A}{A + \sigma\Phi}\right] N_\ell \tag{A.6b}$$

$$= \left[\frac{R - A}{R + \lambda\sigma\Phi}\right] N_u \quad . \tag{A.6c}$$

Setting $Q = k_q N_q$ and substituting in equation (A.1), we find

$$N_u = \frac{pump}{(Q + A) + \sigma\Phi \dfrac{(R - A)}{(R + \lambda\sigma\Phi)}} \quad . \tag{A.7}$$

A-3

Finally, substituting (A.6c) and (A.7) into (A.3), we have (after some rearranging)

$$\Delta \Phi = \frac{(R - A) \cdot \text{pump} \cdot \sigma \Phi}{R(Q + A) + \sigma \Phi [Q + R + (\lambda - 1)A]} - g_a \Phi \quad . \qquad (A.8)$$

Now we seek the value of the optical flux that maximizes equation (A.8). The general form

$$\Delta \Phi = \frac{\alpha \Phi}{\beta + \gamma \Phi} - \delta \Phi \qquad (A.9)$$

has a maximum at $\Phi_m = (\xi - \beta)/\gamma$, where $\xi = (\alpha \beta / \delta)^{\frac{1}{2}}$, and after some manipulation we find

$$\Delta \Phi (\Phi_m) = \frac{\alpha}{\gamma} (1 - \xi)^2 \qquad (A.10)$$

where $\xi = (\delta \beta / \alpha)^{\frac{1}{2}}$.   We then take

$$\alpha = \text{pump} \qquad (A.11a)$$

$$\beta = R(Q + A)/R - A)\sigma \qquad (A.11b)$$

$$\gamma = [Q + R + (\lambda - 1)A]/(R - A) \qquad (A.11c)$$

$$\delta = g_a \qquad (A.11d)$$

and

$$\xi = \left[\frac{g_a R(Q + A)}{(R - A)\sigma \ \text{pump}} \right]^{\frac{1}{2}} \quad . \qquad (A.11e)$$

Combining (A.6c) and (A.7) for $\Phi = 0$ we define

$$g^* = \sigma (N_u)_o = \frac{\sigma \ \text{pump}}{(Q + A)} \ , \qquad (A.12)$$

i.e., the gain one would compute from the fluorescence intensity, ignoring absorptions and lower level population. Equation (A.11e) then simplifies to

A-4

$$\xi = \left[\frac{g_a}{g^* (1 - A/R)} \right]^{\frac{1}{2}} \tag{A.11e'}$$

We note that the small signal net gain is just $g_o = g^* (1 - A/R) - g_a$. Combining equations (A.4), (A.10), and (A.11), we obtain the expression for the maximum extraction efficiency

$$\eta_{ext} = \left[\frac{1 - A/R}{1 + Q/R + (\lambda - 1)A/R} \right] \left\{ 1 - \left[\frac{g_a}{g^* (1 - A/R)} \right]^{\frac{1}{2}} \right\}^2 \quad . \tag{A.13}$$

Two special cases are of particular interest:

(1) no lower level (as in KrF), $R \rightarrow \infty$

$$\eta_{ext} = \left\{ 1 - \frac{g_a}{g^*}^{\frac{1}{2}} \right\}^2 = \left\{ 1 - \frac{1}{(g_o/g_a + 1)^{\frac{1}{2}}} \right\}^2 \tag{A.14}$$

and

(2) no absorption, $g_a \rightarrow 0$

$$\eta_{ext} = \left[\frac{1 - A/R}{1 + Q/R + (\lambda - 1)A/R} \right] \quad . \tag{A.15}$$

Figure 1 shows these results graphically for the case of no absorption ($g_a = 0$) and of modest absorption ($g^*/g_a = 11$). It is apparent that both medium absorption and insufficiently rapid lower level removal can impose serious limitations on the extraction efficiency.

$$\eta_{ext} = \left| \frac{1-A/R}{1+Q/R} \right| \left\{ 1 - \left[\frac{g_a}{g_*(1-A/R)} \right]^{1/2} \right\}^2$$

A = RADIATIVE DECAY FREQUENCY
Q = QUENCHING FREQUENCY
R = LOWER LEVEL REMOVAL FREQUENCY
g_a = ABSORPTION COEFFICIENT
g_* = GAIN COMPUTED FROM FLUORESCENCE
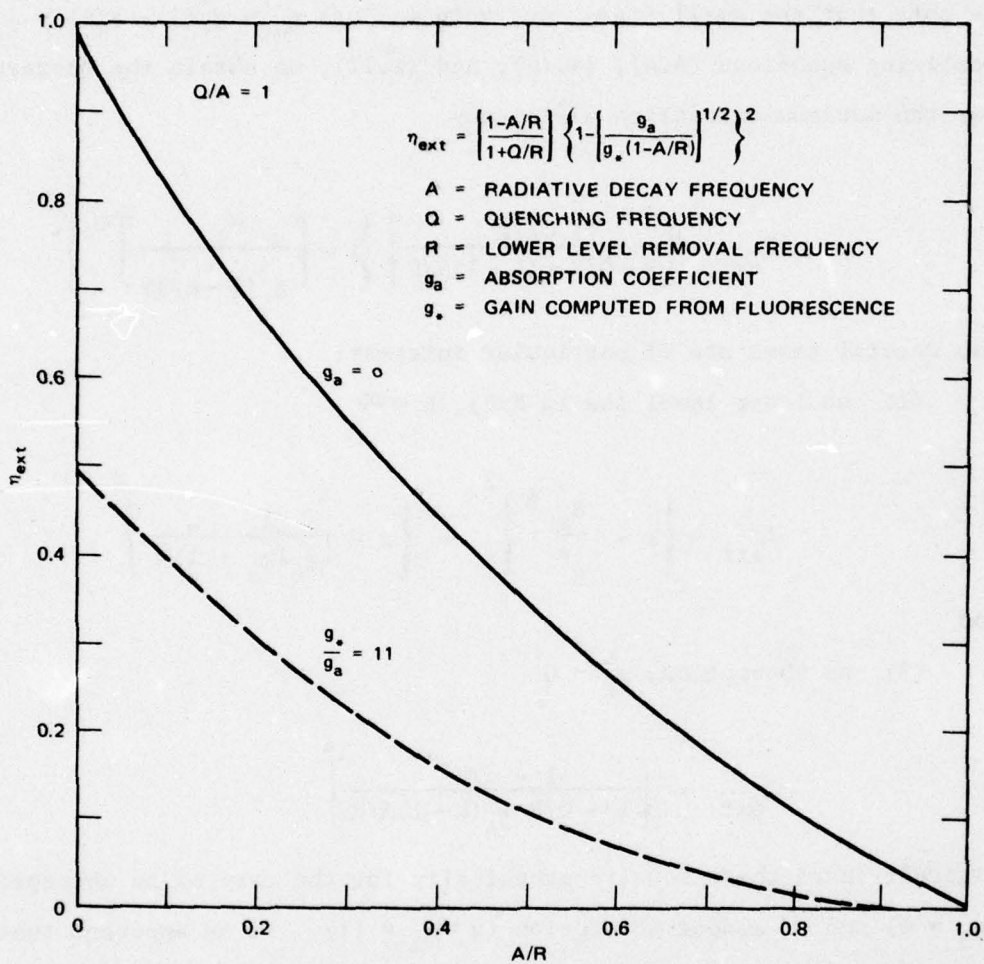
SA-6158-52

FIGURE 1   EXTRACTION EFFICIENCY VERSUS LOWER LEVEL REMOVAL

A-6

Appendix B

UV ABSORPTIONS OF RARE GAS IONS IN
E-BEAM PUMPED RARE GASES

UV ABSORPTIONS OF RARE GAS IONS IN
E-BEAM PUMPED RARE GASES

by

R. O. Hunter, J. Oldenettel and C. Howton
Maxwell Laboratories, Inc., 9244 Balboa Avenue
San Diego, California 92123

and

M. V. McCusker
Molecular Physics Center
SRI International, Menlo Park, California 94025

ABSTRACT

Absorption spectra of electron beam pumped argon and of argon/krypton mixtures have been measured in the wavelength region between 240 and 400 nm. We observe strong absorption features in both cases. With pure argon the peak absorption band is at 292 nm, has a width of 90 nm, and is identified as Ar_2^+; with the argon/krypton mixture the peak absorption is at 325 nm, has a width of 100 nm, and is apparently due to Kr_2^+. The implications for uv laser operation are discussed.

MP 77-90

INTRODUCTION

Laser action in a gas media is particularly sensitive to the presence of absorptions of the laser light by the medium itself. For electron beam pumped rare gas-halide lasers a variety of distinct absorption mcehanisms are known; these include absorption from the upper laser level to a higher level, photodetachment from negative ions (for example, F^-), photoexcitation of the non-lasing molecules, photodissociation, and photoionization. Several of these processes, such as F^- photodetachment and F_2 absorption, are reasonably well understood for many of the species believed to be found in rare gas-halide laser mixtures.[1,2] Absorptions at 441.6 nm in e-beam pumped argon/krypton/fluorine and argon/xenon/fluorine mixtures have recently been described.[3a] Absorption studies at selected wavelengths in XeF laser mixtures have also been reported recently.[3b]

Zamir et al.,[4] show that in e-beam pumped rare gas mixtures there are a variety of absorption processes in the visible regions of the spectrum. Hunter et. al.[5] demonstrated that the presence of absorptions in the laser medium can have a significant effect on the ability to efficiently extract the laser radiation. They reported that the local extraction efficiency (loosely defined as the ratio of the energy gained by the coherent radiation field to the energy contributed by the pump) can be written as

$$\eta_{extr} = \frac{1}{\frac{\varphi}{\varphi_s} + 1} - \frac{\varphi}{\varphi_s}\left(\frac{1}{g_o/g_a + 1}\right)$$

for the case where a non-saturating absorption such as photoabsorption by F_2 is the dominant absorption mechanism. In the above formula φ_s is the saturation flux, φ is the local radiation flux, g_o is the small signal gain and g_a is the absorption. This formula indicates that even when g_o/g_a is as large as 10 the optimum extraction efficiency will be less than 50% (for $\varphi/\varphi_s = 2$). Furthermore, for a given g_o/g_a value an optimum φ is obtained which sets the length scaling the laser.

It is important, therefore, to understand the dominant absorption processes that may occur in a gas laser. The work reported here is the result of an effort to explore absorptions due to the diatomic noble gas ions and other species that are present in noble gas-halide lasers. These absorptions may be present in other energy transfer lasers that utilize noble gas as well. The work presented here is an effort to systematically determine the absorption profile of noble gas mixtures appropriate to e-beam pumped lasers in the near uv. The absorption wavelength range examined was between 240 and 400 nm. This work complements the studies recently reported by Zamir et al.[4] of absorption in the visible regions of the spectrum of noble gases pumped by a Febetron 706.

THEORY AND PREVIOUS EXPERIMENTS

The absorption cross sections for molecular argon ions have been computed by Stevens et al.[6] More recent computations have been made by Wright and Michaels[7] for Ar_2^+ and Kr_2^+; the Ar_2^+ includes both CI and SCF approaches; the Kr_2^+ curves are based on extrapolation from theories for the lighter noble gases, more refined computations are now in progress. Recently Wadt et al.[8] have reported the results of a variational calculation for Ar_2^+ and Kr_2^+. In the absence of spin-orbit coupling (fine structure in the separate atom-ion state), there will be four potential curves, with the ground state $^2\Sigma_u^+$ bound by more than one electron volt. Above that lie the generally repulsive $^2\Pi_g$, $^2\Pi_u$ and $^2\Sigma_g^+$ states in increasing energy. The visible absorptions between the $^2\Sigma_u^+$ and $^2\Pi_g$ are allowed and have been observed by Miller et al.[9] using a drift tube and a cw dye laser. Absorptions on the red wings between high vibrational levels of the $^2\Sigma_u^+$ state and the $^2\Sigma_g^+$ state have recently been observed by Moseley et al.[10] in a beam experiment.

On the high pressure systems appropriate to lasers, the molecular ion is formed by three body collisions

$$Ar^+ + 2Ar \rightarrow Ar_2^+ + Ar.$$
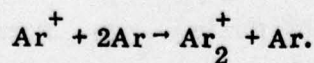
The resulting ion should be produced with significant vibrational energy. Subsequent collisions with argon can proceed via an exchange collision and cool the molecules very rapidly.[11] Cooling rates of kryption or xenon ions in an argon host gas may be less rapid since the exchange channel will not be present.

In a large e-beam pumped system, such as a krypton-fluoride laser, the ion density is estimated to be approximately 1 to 2×10^{14} cm^{-3}.[12] Free electrons are rapidly converted by dissociative attachment to F^-, so that negative ions are the dominant negatively charged species. Postive Ar^+ ions are first created by the electron beam, and then are rapidly converted to Ar_2^+. The Ar_2^+ is subsequently converted to $ArKr^+$ and then to Kr_2^+. These diatomic noble gas ions are anticipated to be the dominant positively charged species in the laser. One of the suggested production mechanisms for the KrF is through ion-ion neutralization collisions that involve these ions. In addition to these charged species there will be neutral excited atoms and molecules that will also contribute to photoabsorption.

EXPERIMENT DESIGN AND OPERATION

A schematic diagram of the experiment is shown in Figure 1. The electron gun consists of a 20 x 200 cm area planar electron beam that can provide an electron current adjustable between 1 and 10 amps/cm^2 at a voltage of 350 to 500 kilovolts. The pulse length for this work was 1 μs, and the current was nominally 1.5 amps/cm^2. The rise time of the beam current is 300 ns, and is monitored by $\dot{B}$ loops. The dye laser probe is a commercially manufactured system (Lambda Physik Model FL1000TE). The dye laser wavelength was verified by passing the laser light through a calibrated 1/4-meter monochrometer that had a resolution of 0.4 nm. At the output of the doubling crystal the dye laser pulse is approximately 3 ns in length. The detection system has a rise time of less than 3 ns. A fraction of the probe pulse is sampled with a photodiode (ITT FW114), the remainder is passed through the cell and is monitored by a second photodiode. A large fraction of the background fluorescence from the gas in the cell is suppressed by using an approximate narrow-band filter in front of the photodiode. Synchronization of the dye laser pulse is set so that the excited gas is

probed 500 ±20 ns after the initiation of the electron beam.

Data at each wavelength were taken using three to five electron beam shots.
Scatter in the data was relatively small (generally less than 0.5×10^{-3} cm^{-1} in
absorption units). The absorption is measured by determining the relative trans-
mission through the cell with unexcited gas for several dye laser pulses prior to the
e-beam excitation. Peak voltage V in the photodiodes is measured, and the absorption
signal is the ratio

$$S_{ABS} = \frac{V'_{trans}}{V'_{ref}} \cdot \frac{V_{ref}}{V_{trans}}$$

where the subscripts trans and ref refer to the transmission and reference photodiodes,
and the primes refer to the signals read while the electron beam is on. The absorp-
tion coefficient α is then computed from the relations $S = \exp(-\alpha \ell)$, where ℓ is the
effective length of the e-beam excited region. Because late time acoustic disturbances
occasionally altered the position of elements in the optical train the reference points
were taken prior to and not after the electron gun pulse excitation. With this procedure
steady state absorption processes, due for example to impurities present in the gas, are
not measured. The data describes transient absorption only. Atomic absorption lines
were noted in the regions with wavelengths longer than ~ 3200 Å. These points are not
displayed here and care was taken that the data points shown were not those that over-
lapped with these atomic transitions

The gases used were pure (99.999%) argon, krypton (99.995%), at 1470 torr
pressure and 50 torr pressure respectively. The gas was flushed from the cell and
replaced every 5 data points. It is unlikely that the effect of impurities on the results
of this measurement will be significant. Assuming an impurity concentration of 5×10^{14}
cm^{-3} and a charge transfer cross section from Ar$^+$ or Ar$_2^+$ of 3×10^{-10} cm^3/sec, and
characteristic transfer time would be 5 μs.

By comparison, the formation of Ar$_2^+$ from Ar$^+$ in a three body collision has
a rate constant of 2.3×10^{-31} cm^6/sec;[13] at 1500 torr this leads to a formation time
of approximately 2 ns. The room temperature dissociative recombination rate for
thermal electrons on Ar$_2^+$ and Kr$_2^+$ are 6.7×10^{-7} cm^3/sec and 1.2×10^{-6} cm^3/sec

respectively;[14a] at high electron temperature (~ 1 eV) the value will be less.[14b]
This process should be the dominant loss mechanism on the ions. During the
electron gun pulse the average electron energy is estimated to be on the order of
0.1-1 eV, thereby lowering the recombination rate significantly. For an electron
recombination rate of 10^{-7} cm^3/sec, the ion lifetime should be ~ 50 nanoseconds.
The density of excited neutrals (Ar^* and Ar_2^* or Kr^* and Kr_2^*) may be as large as
10^{14} to 10^{15} cm^{-3}, but because of the low concentration of impurities, Penning
ionization processes will not be significant to the ion chemistry.

From the above arguments we conclude that at the time of the probe laser
sampling, the ion populations have reached a steady state equilibrium, and that the
dominant ion in the case of pure argon is Ar_2^+. When 50 torr of krypton is added, the
transfer from Ar_2^+ to Kr_2^+ can be complicated. A block diagram of the possible
kinetic sequence is shown in Figure 2 and the relevant reactions and rate constants
are summarized in Table 1. The conclusion reached from a knowledge of the appro-
priate rates is that Ar^+ rapidly forms Ar_2^+, these ions are rapidly converted to
Kr_2^+ via an intermediate $ArKr^+$ state. The existence of such a mixed ion is well
known; the reaction chemistry has been discussed by Bohme et al.[15] and its spectro-
scopy has been discussed by Tanaka et al.[16] The kinetic lifetime of the $ArKr^+$ ion
is so short that the ion density is never large enough to be a significant absorber;
it is not likely to absorb in the wavelength region discussed here.

RESULTS

The absorption data for the case of pure argon is shown in Figure 3. Also on
that figure are the results of the theoretical computation for the absorption of Ar_2^+
by Wright and Michaels et al.[7] for both SCF and CI approaches as well as the
absorption curve of Stevens et al.[6] The results of the calculations by Wright for
absorption from the first three vibrational levels have been averaged over a Boltzman
distribution with a temperature of 300°K (ω_e = 290 cm^{-1}). The absorption at the
peak of the curve is approximately 1.7×10^{-2} cm^{-1}. This data conclusively demon-
strates that Ar_2^+ is a significant absorber. On the red side, the SCF theory clearly

is deficient, but the agreement with the other two theoretical curves is generally good. The wings of the curve are sensitive to vibrational population distribution, and therefore to temperature. We estimate that for our conditions, the instantaneous temperature rise due to heating by the electron beam is only a few degrees and that 300K temperatures is appropriate for comparison. The effect of the low energy secondary electrons on the vibrational temperature has not yet been computed.

The data for the argon/krypton mixture is shown in Figure 4. Also shown is the theory of Wright ;and Michaels thermalized to 300°K using ω_e for Kr_2^+ of 182 cm^{-1}. The peak absorption in this case is 0.9×10^{-2} cm^{-1} and the peak absorption wavelength is shifted to about 325 nm from 295 in the case of argon. We conclude that Kr_2^+ is the dominant absorber. There is, however, significant deviation from the theoretical curve on the wings of the absorption.

Dunning and Stebbings[17] have studied the photoionization of argon and krypton metastable atoms. They estimate that the upper bounds from the photoionization of $Ar \, (^3P_{0,2})$ and $Kr \, (^3P_{0,2})$ at threshold are 1.1×10^{-18} cm^2 and 4.9×10^{-19} cm^2 respectively. These values are too low for these processes to make a significant contribution under the conditions of our experiment.

CONCLUSIONS

The theories of Wright for Ar_2^+ and Kr_2^+ and of Stevens for Ar_2^+ generally show good agreement with the data at the peak of the absorption. Wadts[8] theory predicts λ_{max} for Ar_2^+ at 325 nm, and λ_{max} for Kr_2^+ at 349 nm. We conclude that over the wavelength region studied these molecular ions are the dominant photoabsorbers. While the theories are useful, they do not yet have the accuracy necessary to resolve the questions of the absorptions that will be raised by large scale laser design.

The implications of the work for laser e-beam pumped uv laser operation are serious. For lasers with an additive in an argon buffer such as argon/bromine (292 nm) and argon/iodine (343 nm), these absorptions may seriously restrict the ultimate efficiency. Other buffers such as neon or helium may be more useful. These observations also suggest that for noble gas halide lasers that operate in the wavelength region dominated by these absorptions, the gas pressures be adjusted so that atomic

ions, rather than molecular ions, are the dominant charge species. Since the Xe_2^+ absorption is expected to the centered near 350 nm, this suggestion appears to support the relatively low concentrations of xenon used in the XeF laser at 351 and 353 nm (compared with the larger concentration of krypton in KrF (248 nm) lasers).

We would like to acknowledge the cooperation of L. Wright (AFWL) for allowing access to theoretical results prior to this publication, the help of K. Tang and G. Sullivan (MLI) in taking some of the data, and D. Huestis and D. Lorents (SRI) for helpful discussions. One of us (R.O. Hunter) also benefited from conversations with Mo Krauss (NBS) and A. V. Phelps (JILA).

TABLE 1

ARGON/KRYPTON ION CHEMISTRY

(Assuming 1500 torr argon, 50 torr krypton, and an ion density of approximately 10^{14} cm^{-3}).

	Reaction	Rate	Characteristic Time	Ref.
1	$Ar^+ + 2Ar \rightarrow Ar_2^+ + Ar$	2.3×10^{-31} cm^6/sec	2 ns	A
2	$Ar_2^+ + Kr \rightarrow Kr^+ + 2Ar$	7.5×10^{-10} cm^3/sec	1 ns	B
3	$Ar^+ + Kr \rightarrow Kr^+ + Ar$	$\sim 5 \times 10^{-11}$ cm^3/sec	13 ns	C
4	$Kr^+ + 2Ar \rightarrow ArKr^+ + Ar$	2.3×10^{-31} cm^6/sec	2 ns	D
5	$Kr^+ + Kr + Ar \rightarrow ArKr^+ + Ar$	2.3×10^{-31} cm^6/sec	67 ns	D
6	$Kr^+ + Kr + Ar \rightarrow Kr_2^+ + Ar$	2.3×10^{-31} cm^6/sec	67 ns	D
7	$Ar_2^+ + Kr \rightarrow ArKr^+ + Ar$	2×10^{-10} cm^6/sec	3 ns	E
8	$ArKr^+ + Kr \rightarrow Kr_2^+ + Ar$	3.2×10^{-10} cm^3/sec	2 ns	B
9	$Ar_2^+ + e \rightarrow Ar^* + Ar$	6.7×10^{-7} cm^3/sec	15 ns	F
10	$ArKr^+ + e \rightarrow Kr^* + Ar$	10^{-6} cm^3/sec (?)	10 ns	G
11	$Kr_2^+ + e \rightarrow Kr^* + Ar$	1.2×10^{-6} cm^3/sec	9 ns	F
12	$Ar^+ + Kr + Ar \rightarrow ArKr^+ + Ar$	2.3×10^{-31} cm^6/sec	67 ns	D

References

A W. F. Liu and D. C. Conway, J. Chem. Phys. 62, 3070 (1975).

B D. K. Bohme, N. G. Adams, M. Moseman, D. B. Dunkin, and E. E. Ferguson, J. Chem. Phys. 52, 5094 (1970).

C Estimate. This is a non-resonant charge transfer and should have a small rate constant.

D Estimate based on the measured value of reference A.

E Estimate based on Kr_2^+ + Xe data of P. Kebarle, R. M. Haynes, and S. K. Searles, J. Chem. Phys. 42, 1684 (1967).

F H. J. Oskam and J. R. Mittelstadt, Phys. Rev. 132, 1445 (1963).

G Estimate based on reference F.

REFERENCES

1. R. K. Steunenberg, and R. C. Vogel, J. Am. Chem. Soc. $\underline{78}$, 901 (1956).

2. R. S. Berry and C. W. Reinmann, J. Chem. Phys. 38, 1540 (1963), see also the review article by B. Stein, "Photodetachment Cross Sections and Electron Affinities," in "Case Studies in Atomic Collision Physics II," ed. E. W. McDaniel and M. R. C. McDowell, North-Holland Publishing Co., Amsterdam, 1972.

3a. R. O. Hunter, J. Oldenettel, C. Howton and M. V. McCusker, submitted to J. Appl. Phys. 1977.

3b. L. F. Champagne and W. Watt, Quantum Electronics Conference, Park City, Utah, Feb. 1977.

4. E. Zamir, D. L. Huestis, D. C. Lorents and H. H. Nakano, "Visible Absorption by Electron-Beam Pumped Rare Gases," paper presented at the Summer Colloquium on Electronic Transition Lasers, Snowmass, Colorado, September 7-10, 1976.

5. R. O. Hunter, C. Howton, and J. Oldenettel, AIAA 15th Aerospace Sciences Meeting, Paper #77-26, Los Angeles, California, January 1977.

6. W. Stevens, M. Gardner, and A. Karo, submitted to J. Chem. Phys.

7. W. Wright and H. Michaels, private communication.

8. W. R. Wadt, "Low Lying States of Ar_2^+ and Kr_2^+: Absorption wavelengths and strengths," postdeadline paper given at the 5th Conference on Chemical and Molecular Lasers, St. Louis, Missouri, April 18-20, 1977.

9. T. M. Miller, J. H. Ling, R. P. Saxon, and J. T. Moseley, Phys, Rev. A$\underline{13}$, 2171 (1976).

10. J. T. Moseley, R. P. Saxon, B. A. Huber, P.C. Cosby, R. Abouaf, M. Tadjeddine, submitted to J. Chem. Phys. 1977.

11. D. C. Lorents and D. L. Huestis, private communication.

12. Tom Johnson, AFWL, private communication. This value is based on the results of an analysis of these systems that includes a solution of the Boltzman equation.

13. W. F. Liu and D. C. Conway, J. Chem. Phys. $\underline{62}$, 3070 (1975).

14. (a) H. J. Oskam and J. R. Mittelstadt, Phys. Rev. $\underline{132}$, 1445 (1963).
   (b) J. N. Bardsley and M. A. Biondi, Adv. Atom. Mol. Phys. $\underline{6}$, 2 (1970).

15. D. K. Bohme, N. G. Adams, M. Moseman, D. B. Dunkin and E. E. Ferguson, J. Chem. Phys. $\underline{52}$, 5094 (1970).

16. Y. Tanaka, K. Yoshino, and D. E. Freeman, J. Chem. Phys. $\underline{62}$, 4484 (1975).

17. F. B. Dunning and R. F. Stebbings, Phys. Rev. A $\underline{9}$, 2378 (1974).

FIGURE CAPTIONS

Figure 1. Schematic Block Diagram of the 2-meter long electron
           beam at Maxwell Laboratories Inc., as well as selected
           diagnostic devices.

Figure 2. Block Diagram of Argon/Krypton Ion Kinetics. The most
           rapid reactions are indicated by bold arrows. Less
           important reactions are indicated by dashed arrows. The
           relevant rate constants are listed in Table 1.

Figure 3. Ar_2^+ Ion Absorption Spectrum as a function of wavelength.
           The bold dots are the data of this experiment with typical
           error bars indicated. The curves are the thermalized
           theoretical results of Wright and Michaels[7] and
           Stevens, et al.[6]

Figure 4. Kr_2^+ Ion Absorption Spectrum as a function of wavelength.
           The curve is from the theory of Wright and Michels.[7]
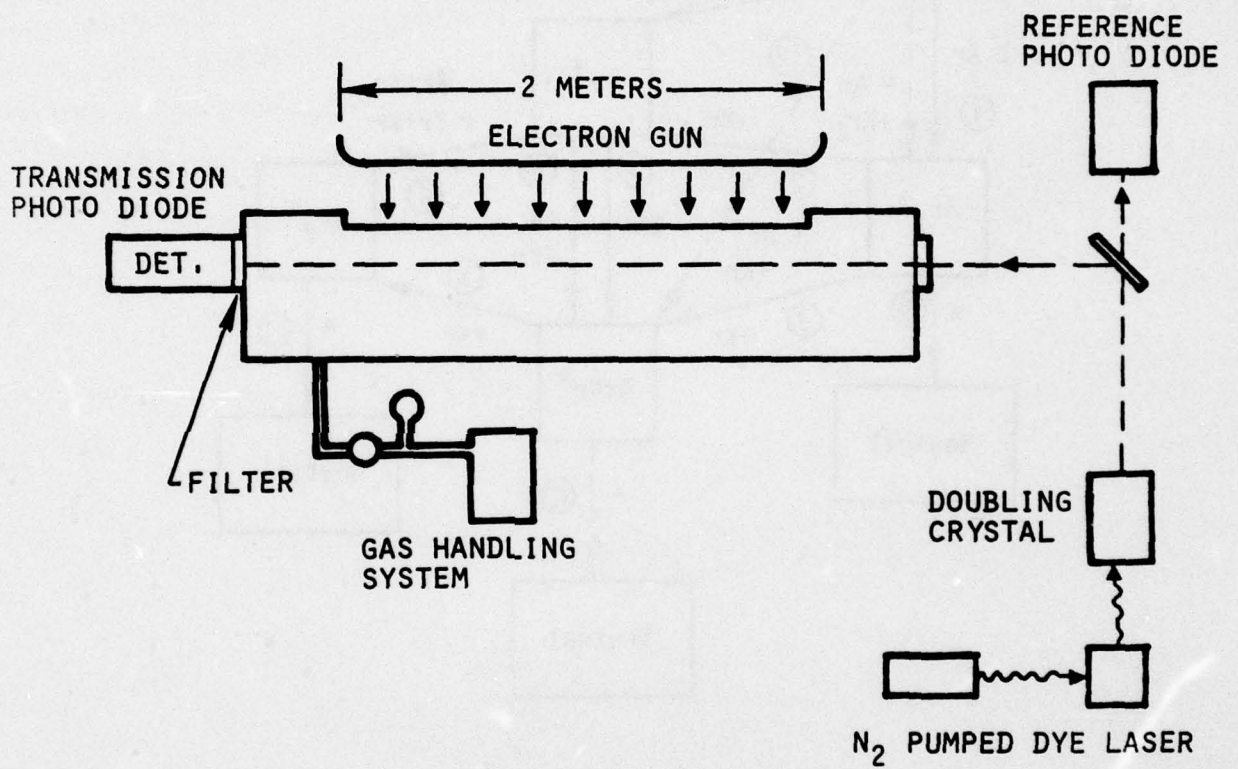
PRODUCTION BY HIGH ENERGY PRIMARY ELECTRONS
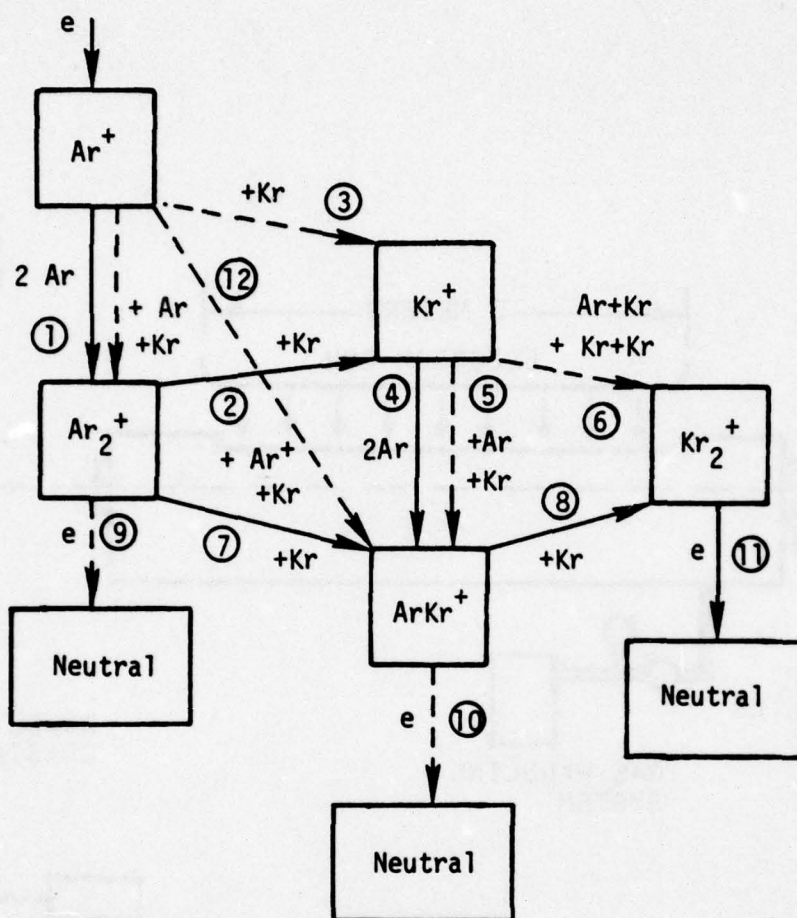
Ar_2^+ ION ABSORPTION SPECTRUM

Kr$_2^+$ ION ABSORPTION SPECTRUM

1520 TORR ARGON + 50 TORR KRYPTON
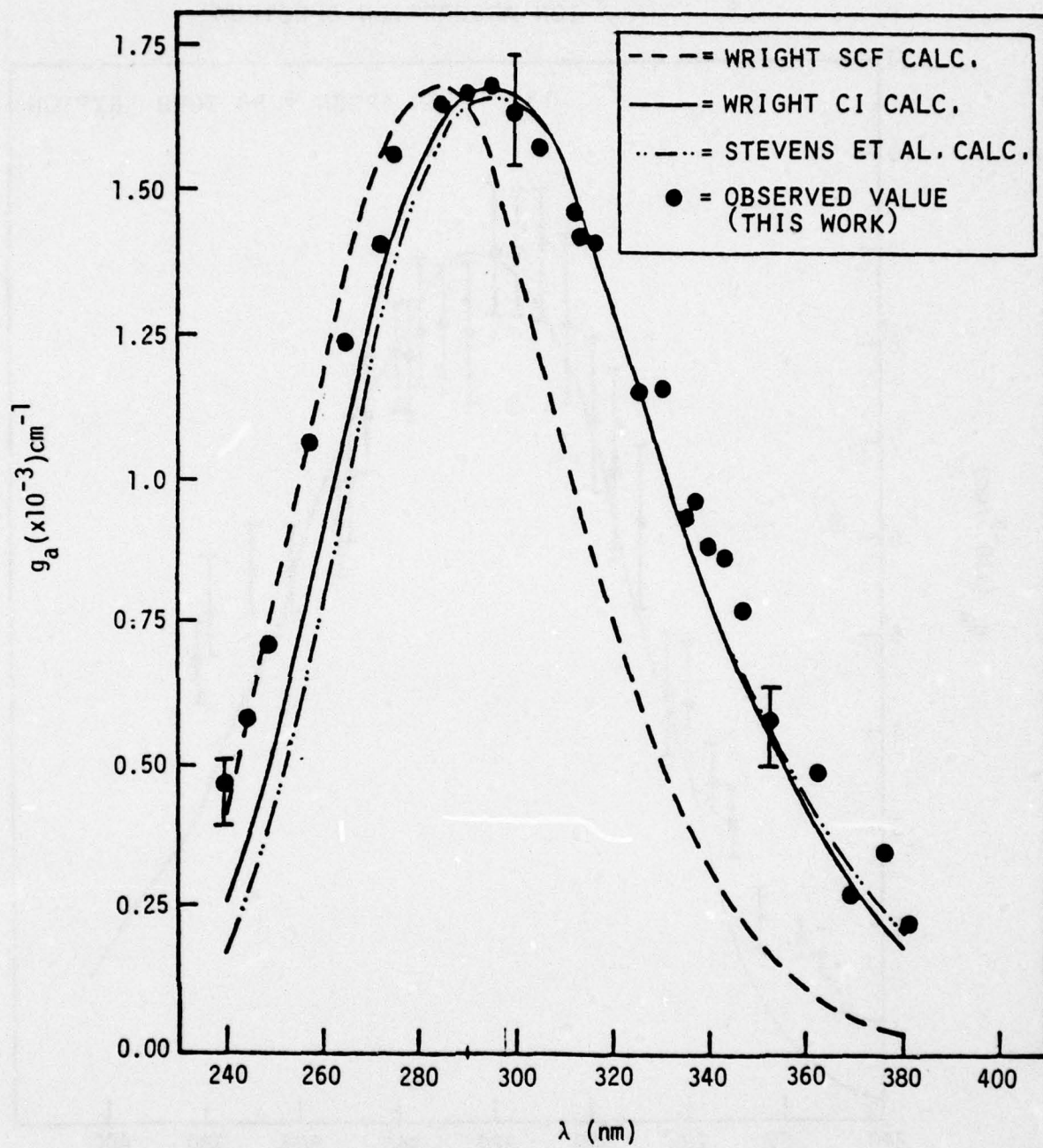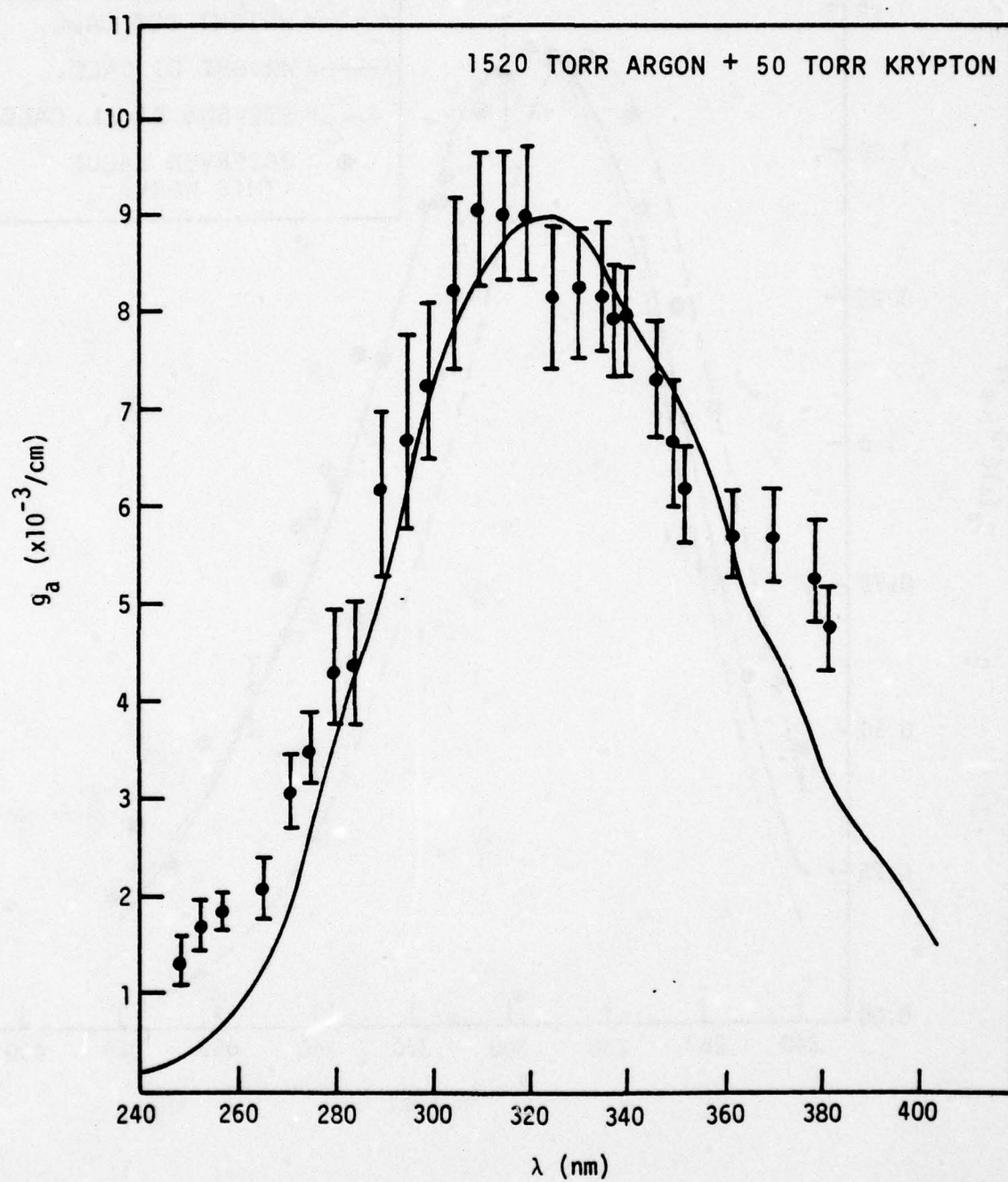
Appendix C

EQUILIBRIUM BINDING
IN THE GROUND $^2\Sigma^+_{\frac{1}{2}}$ STATE OF XeF

May 12, 1977

EQUILIBRIUM BINDING

IN THE GROUND $^2\Sigma^+_{\frac{1}{2}}$ STATE OF XeF

by

David L. Huestis

The ground state of XeF, called $X^2\Sigma_{\frac{1}{2}}$, has an attractive potential
($D_e \approx 1150$ cm^{-1}) that supports 11 bound vibrational levels [Te76]. The
XeF laser operates on bound-to-bound transitions terminating on various
of the vibrational levels of the ground state. Band origins calculated
from the spectroscopic constants determined by Tellinghuisen suggest the
following identifications:

<div align="center">

XeF laser transitions

3490 Å	$v' = 0 \to v'' = 1$
3512 Å	$v' = 0 \to v'' = 2$
3513 Å	$v' = 1 \to v'' = 4$
3533 Å	$v' = 0 \to v'' = 3$

</div>

Concern exists about the rate of removal of the lower laser level. Vibra-
tional relaxation in the lower level is insufficient to adequately deplete
the population as illustrated by the following table of vibrational energies
and equilibrium relative populations at room temperature:

Table I

XeF $X^2\Sigma_{\frac{1}{2}}^+$ Vibrational Levels[a]

v	E_v	P_v	B_v	D_v
0	0	.59	.1873	1040
1	204	.23	.1809	836
2	387	.096	.1745	653
3	549	.044	.1681	491
4	687	.022	.1617	353
5	802	.011	.1553	238
6	892	5.4×10^{-3}	.1489	148
7	957	2.5×10^{-3}	.1425	83
8	1000	9.0×10^{-4}	.1361	40
9	1025	1.4×10^{-4}	.1297	15
10	1037	8.9×10^{-5}	.1234	3

(a) All energies in cm^{-1}.

The rotational constants (B_v) and level binding energies (D_v) will be discussed below.

To illustrate the magnitude of the problem, consider the following laser conditions: We suppose that the pumping rate for production of excited states is 2×10^{22} cm^{-3} sec^{-1}, and that 20% of the excited states produced end up as $XeF^*(v' = 0)$ and that they all radiate to give $XeF(v'' = 2)$, either by spontaneous fluorescence or stimulated emission. The gain/absorption cross section is taken to be 3×10^{-16} cm^2, the effective lifetime of XeF^* as 10 ns. This gives an ambient population of $XeF^* = 4 \times 10^{13}$. The rate of population of the ground state vibrational manifold is then 4×10^{21} cm^{-3} sec^{-1}. To fill $v'' = 2$ to 4×10^{13} takes only 10 ns in the absence of vibrational relaxation. At thermal equilibrium among the vibrational levels about 9.6% are in $v'' = 2$. Hence, even including rapid vibrational relaxation the laser will bottleneck in about 100 ns.

The only hope for sustained laser action is therefore that the ground state vibrational manifold must be depleted by dissociation induced by collisions with the background rare gas. Calculation of the rates of collision-induced dissociation is a complicated task with an extensive literature. Here we shall concentrate on the calculation of the thermal equilibrium between XeF bound in vibrational levels of the ground electronic state and free xenon and fluorine atoms.

Following Davidson [Da62] we express the thermal equilibrium as

$$\frac{[XeF]_{v''}}{[Xe][F]} = K_{v''}(T) \quad ,$$

where the specific equilibrium constant for vibrational level v'' is given by

$$K_{v''}(T) = \frac{Q_e(XeF) \; Q_{v''}(XeF) \; Q_t(XeF)}{Q_t(Xe) \; Q_t(F) \; Q_e(F)}$$

where the electronic (Q_e), vibrational (Q_v) and translational (Q_t) partition functions are all computed with zero of energy as that of Xe and F atoms at rest in their ground states.

The translational partition functions are given (in terms of mass in amu, density in cm^{-3} and temperature in K) by

$$Q_t(M) = \left(\frac{2\pi MkT}{h^2}\right)^{\frac{3}{2}}$$

$$= 1.8792 \times 10^{20} \; M^{\frac{3}{2}} T^{\frac{3}{2}} \quad ,$$

which yields

$$\frac{Q_t(XeF)}{Q_t(Xe) \; Q_t(F)} = 7.87 \times 10^{-23} \; T^{-\frac{3}{2}} \quad .$$

The electronic partition functions are similarly straightforward. The ground state of XeF is of $^2\Sigma_{\frac{1}{2}}^+$ symmetry of degeneracy 2, and hence

$$Q_e(XeF) = 2 \quad .$$

The ground state of F is $^2P_{\frac{3}{2}}$, of degeneracy 4. The doubly degenerate upper fine structure level lies at 404 cm^{-1}, yielding

$$Q_e(F) = 4 + 2e^{-404/kT} \quad .$$

The vibrational-rotational partition function is somewhat more complicated:

$$Q_v = \sum_{J=0}^{J_v} (2J+1)e^{D(v,J)/kT} \quad ,$$

where J_v is the highest bound rotational level and $-D(v,J)$ is the energy of the vibration-rotation level referenced to Xe + F($^2P_{\frac{3}{2}}$). We will approximate $D(v,J)$ with an expression quadratic in $(v + \frac{1}{2})$ and linear in $J(J + 1)$:

$$-D(v,J) = -D_e + \omega_e(r + \tfrac{1}{2}) - \omega_e x_e(v + \tfrac{1}{2})^2 + B_e J(J + 1)$$

$$- \alpha_e(v + \tfrac{1}{2})J(J + 1) \quad .$$

The effective rotational constant is

$$B_v = B_e - \alpha_e(v + \tfrac{1}{2}) \quad .$$

The highest rotational level is defined through

$$D(v, J_v) = 0$$

or

$$B_v J_v(J_v + 1) = D_e - \omega_e(v + \tfrac{1}{2}) + \omega_e x_e(v + \tfrac{1}{2})^2 \equiv D_v \quad .$$

We now approximate the finite sum by an integral:

$$Q_v \approx \int_0^{D_v} \frac{e^{-x/kT}}{B_v} \, e^{D_v/kT} \, dx \quad ,$$

where $x = B_v J(J + 1)$, $dx = B_v(2J + 1)dJ$, which gives

$$Q_v \approx \frac{kT}{B_v}[e^{D_v/kT} - 1] \quad .$$

We now need to determine values for B_v and D_v. The vibrational constants for $XeF(X^2\Sigma_{\tfrac{1}{2}}^+)$ are given by Tellinghuisen [Te76] as

$$D_e'' = 1150 \text{ cm}^{-1}$$

$$\omega_e'' = 226.05$$

$$\omega_e x_e'' = 11.189$$

$$\omega_e y_e'' = 0.3166$$

$$\omega_e z_e'' = 0.07214$$

$$R_e'' \sim 2.3 \text{ \AA}$$

A Birge-Sponer plot of levels calculated from these constants is nearly linear from $v'' = 0$ to $v'' = 9$. We have chosen to represent the ground state with a Morse potential with $\omega_e = 226 \text{ cm}^{-1}$, $\omega_e x_e = 11.1 \text{ cm}^{-1}$, and $D_e = 1150 \text{ cm}^{-1}$. In the absence of a detailed rotational analysis the rotational constants must be more crudely estimated. Using the estimated value for $R_e = 2.3 \text{ \AA}$, we find $B_e = 0.19 \text{ cm}^{-1}$. Two choices for α_e seem reasonable

(1)   Morse potential [He50] implies

$$\alpha_e = \frac{6}{\omega_e} [\sqrt{\omega_e X_e B_e}^3 - B_e^2] = 0.0064 \text{ cm}^{-1}$$

(2) $B_{\bar{v}} = 0$ at the top of the well

$$D_{\bar{v}} = 0 \text{ defines } \bar{v}, \quad \alpha_e = \frac{B_e}{\bar{v} + \frac{1}{2}} = 0.019 \text{ cm}^{-1}$$

These two choices give lower and upper bounds for α_e respectively. Although this factor of 3 uncertainty might seem serious, the effect on the rotational constants is not intolerable (3% for $v'' = 0$, 18% for $v'' = 2$). We have chosen to use the value $\alpha_e = 0.0064 \text{ cm}^{-1}$ as calculated from the Morse-Potential assumption. The B_v values calculated have been listed above.

Table II and Figure 1 show the calculated values of the equilibrium constants for $v'' = 0$ to $v'' = 4$ as a function of temperature. Also shown is the total binding equilibrium constant

$$K = \frac{[XeF]}{[Xe][F]} = \sum_{v''} K_{v''} \quad .$$

The uncertainties are probably 10-30% due to inaccurate knowledge of B_e and α_e.

The impact may now be assessed of the establishment of a population of $XeF(X^2\Sigma_{\frac{1}{2}}^+)$ in thermal equilibrium with the dissociated fluorine atoms. By the end of a 1 μs pumping pulse in Ar/Xe/NF$_3$ such as that referred to above, approximately 2×10^{16} F atoms will have been produced. If the $XeF(X^2\Sigma_{\frac{1}{2}}^+)_{v''=2}$ population were in thermal equilibrium at room temperature with that density of F atoms, at 6 torr of Xe, then

XeF Equilibrium Constants

$$K_{v''} \ (10^{-22} \ cm^3)$$

T(K)	v'' 0	1	2	3	4	Total
250	35	11	4.0	1.6	0.70	53
300	11	4.4	1.9	0.85	0.42	19
350	5.1	2.2	1.1	0.53	0.28	9.4
400	2.7	1.3	0.67	0.36	0.19	5.4
450	1.6	0.84	0.46	0.26	0.15	3.5
500	1.1	0.59	0.34	0.20	0.12	2.4
550	0.75	0.43	0.26	0.16	0.095	1.8
600	0.56	0.33	0.20	0.13	0.079	1.4
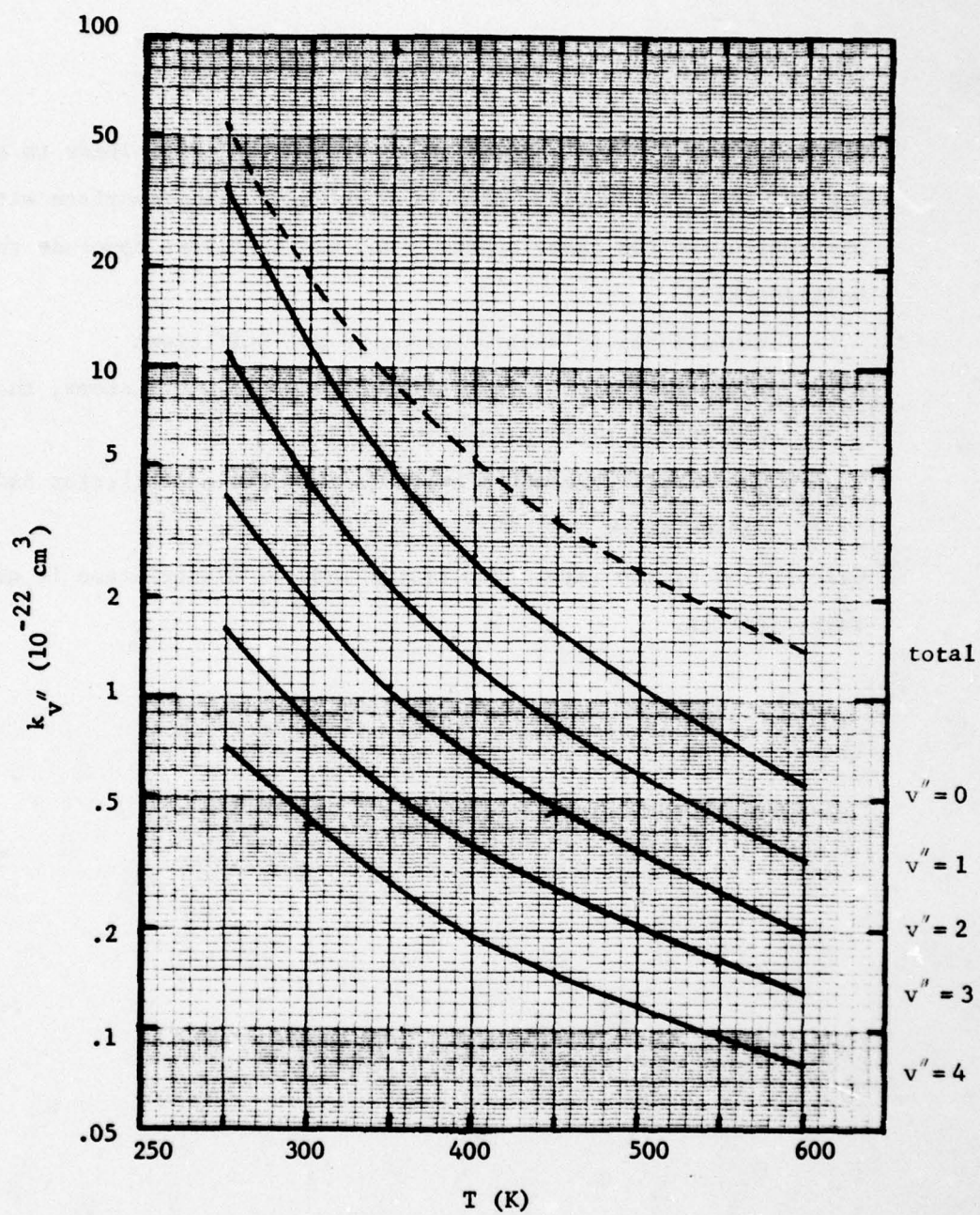
Figure 1. $XeF(X^2\Sigma_{\frac{1}{2}}^+)_{v''}$ Binding Equilibrium Constants

$$XeF\left({}^2\Sigma_{\frac{1}{2}}^+\right)_{v''=2} = 1.9 \times 10^{-22}[2 \times 10^{17}][2 \times 10^{16}]$$

$$= 7 \times 10^{11} \text{ cm}^{-3} \quad .$$

Using a 3×10^{-16} cm^2 absorption cross section, this leads to only 2×10^{-4} cm^{-1} absorption, probably negligible in comparison with the other absorptions in the laser medium. One can therefore conclude that to avoid bottlenecking

- Vibrational relaxation alone is not sufficient
- In thermal equilibrium with the free Xe and F atoms, the XeF ground state population is low
- The crucial kinetic process is the rate of collision induced dissociation

Calculation of the rate of collision induced dissociation is now under investigation.

References

Da62   N. Davidson, <u>Statistical Mechanics,</u> McGraw-Hill (New York, 1962), Chap. 7 and 8.

He50   G. Herzberg, <u>Molecular Spectra and Molecular Structure. I. Spectra of Diatomic Molecules</u>, Van Nostrand (New York, 1950), Chap. III.

Te76   J. B. Tellinghuisen, Report ORO-5005-8, Vanderbuilt University, Nashville, Tenn., June 1976.

Appendix D

ELECTRON-BEAM-CONTROLLED DISCHARGE HgCl* LASER
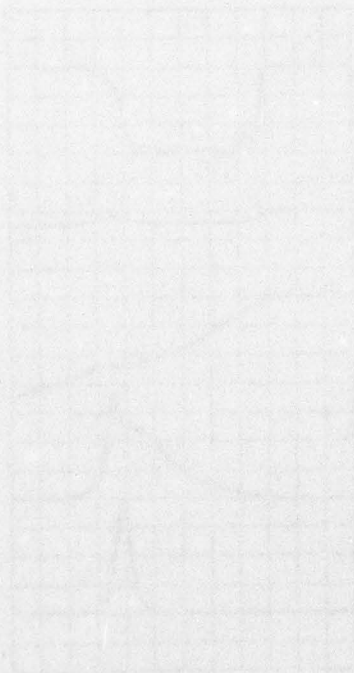
Electron-beam-controlled discharge HgCl* laser[a]

Kenneth Y. Tang,[b] R. O. Hunter, Jr.,[c] J. Oldenettel, and C. Howton

Maxwell Laboratories, Inc., 9244 Balboa Avenue, San Diego, California 92123

D. Huestis, D. Eckstrom, B. Perry, and M. McCusker

Molecular Physics Center, SRI International, Menlo Park, California 94025

Laser action of HgCl* was observed using an electron-beam-controlled discharge to pump a gas mixture of Hg/Cl_2/Ar. An order of magnitude in the fluorescence enhancement was obtained. This gives an excitation efficiency by controlled discharge to be a factor of about 2 higher than that by direct electron-beam pumping. In addition to the previously reported 5576-Å laser transition of HgCl*, a strong transition at 5584 Å was also observed.

PACS numbers: 42.55.Hq, 34.50.Hc

Laser action on the $B \rightarrow X$ transition of HgCl* at 5576 Å was recently achieved by Parks, who used a high-intensity electron beam to pump a gas mixture of Hg/Cl_4/Xe/Ar.[1] The HgCl* is believed to be formed mainly through an ionic channel by the recombination of Hg^+ and Cl^-, which are produced respectively by the charge transfer from Ar^+ or Xe^+ and by the collision with secondary electrons. Thus, the efficiency of this direct-pumped system is limited by the 26 eV required for the production of the argon ion. However, it is known that HgCl* can also be formed by a direct reaction of Hg* (^3P) with Cl_2 with large cross section.[2] Since Hg* can be efficiently produced by direct electron excitation in a discharge with an energy expenditure of only approximately 5 eV, electron-beam-controlled discharge pumping of HgCl* offers the possibility of achieving an efficient high-power visible laser. In this letter, we report first operation of the HgCl* laser using an electron-beam-controlled discharge pumping of an Hg/Cl_2/Ar mixture. In addition to the previously reported HgCl* laser line at 5576 Å, a new laser line at 5584 Å was observed.

The experiments were carried out with a stainless-steel cell which was separated from the electron gun by a 1-mil Inconel foil. The cell was heated uniformly to about 200°C. The Brewster-angle quartz windows were heated to about 300°C to avoid Hg_2Cl_2 deposition. The electron beam had an area of 2×50 cm^2 and was produced by a Maxwell Excitron machine. The characteristics of a typical pulse were 300 kV voltage, 2 A/cm^2 transmitted current density, and 400 ns pulse length, as shown in Fig. 1. The discharge electrode was a 46-cm stainless-steel rod (0.95 cm in diameter) placed about 0.5 cm away from the foil. A screen was inserted in front of the foil to keep the arc following termination of the electron beam from directly striking the foil. For a typical experiment, the discharge capacitor (3.35 μF) was charged to 3 kV. With a loss of 0.8 kV through the inductance in the circuit, a dis-

charge voltage of 2.2 kV and a current of 2.5 kA were obtained. This gives an E/N value of roughly 8.3×10^{-17} V cm^2 and a discharge current density of about 25 A/cm^2. The discharge voltage and current traces are shown in Fig. 1.

The laser cavity was formed by a 2-m radius of curvature totally reflective mirror and a partially reflective flat mirror. Three mirrors with different reflectivities have been tested. Laser action was observed with mirrors having reflectivities of 85 and 45% and not with the 20% mirror. The experiments discussed below were performed with the 85% mirror. The fluorescence signal was directly viewed through a
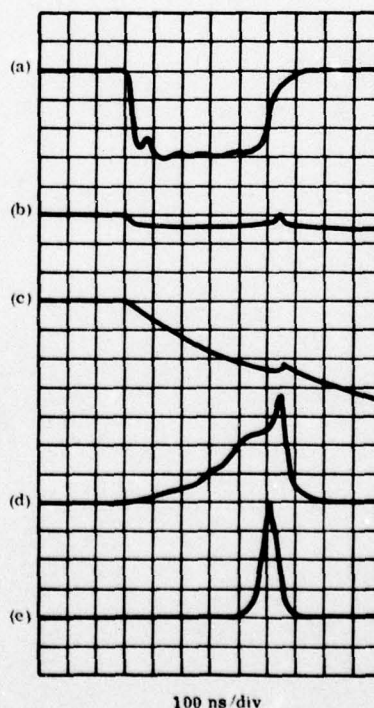

FIG. 1. Oscillogram traces showing (a) electron-beam voltage (100 kV/div), (b) discharge inductive voltage loss (2.6 kV/div), (c) discharge current (1 kA/div), (d) spontaneous fluorescence signal (10 mV/div), and (e) laser signal (2 V/div).

[b] To whom correspondence should be addressed.
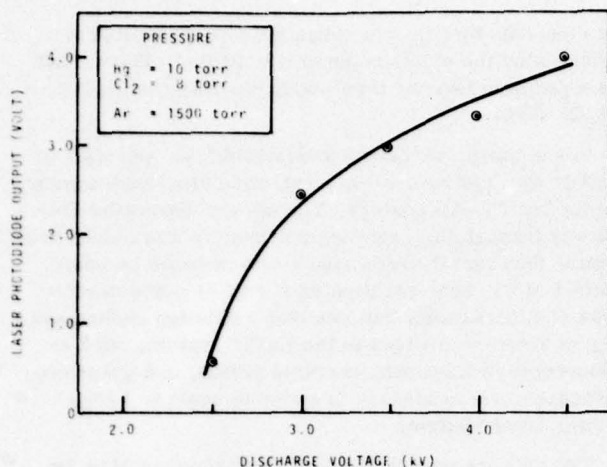[c] Fannie and John Hertz Foundation Fellow, University of California at Irvine.

FIG. 2. A plot of the HgCl* laser output versus the discharge voltage.

side window by an ITT F 4018 S-20 photodiode. The laser output was monitored either by a Jarrell-Ash 1-m spectrograph or by an ITT F4018 S-5 photodiode.

An external Hg reservoir was heated to about 180 °C giving a vapor pressure of about 10 Torr. The hot Ar gas passed through the Hg reservoir and, before entering into the cell, was mixed with Cl_2 (1% in Ar) from a separate line. Gas flows were controlled so that in the cell the mixture of Hg, Cl_2, and Ar contained partial pressures of about 10 T, 8, and 1500 Torr, respectively.[3]

A typical trace of fluorescence signal is shown in Fig. 1(d). The fluorescence enhancement due to the discharge is about a factor of 10 near the end of the pulse. Considering the relative fluorescence intensities and the relative amount of energy deposited in the gas, we

estimate that the excitation efficiency is at least a factor of 2 higher for the discharge pumping than for the electron-beam pumping.

Figure 1(e) shows a photodiode laser signal. The duration is about 50 ns (FWHM) for a 400-ns electron-beam pumping pulse used. Increasing the electron-beam pulse width was found to increase the laser pulse width. With the reproducibility within 15% from shot to shot, the laser pulse amplitude was found to increase with the increase of discharge voltage as can be seen in Fig. 2. We have observed a factor of about 8 increase when the discharge voltage was varied from 2.5 to 4.5 kV. No laser action was observed, however, at 2.0 kV or below, indicating that a direct electron-beam pumping at the test conditions does not produce lasing in this gas mixture.

We have estimated the output energy with a calibrated photodiode. Without optimizing the experimental conditions, the estimated laser output was about 0.1 mJ. This corresponds to a laser efficiency of about 0.01%. Such low extraction efficiency is believed to be due to the inductive loss in the discharge circuit, to the loss in Brewster windows, and to the gas convection in the optical path due to air heating from the hot cell. As a result, the optical flux is well below the saturation flux.

The fluorescence and laser spectra show strong line narrowing and interesting fine structure. Figure 3 shows a spectrum of the HgCl* laser output. It was taken from a microdensitometer trace of the negative of Polaroid type 55 film. At low resolution ($\Delta\lambda \approx 1.6$ Å), we see four lasing transitions. The most intense band located at 5576 Å can be assigned to $v' = 0$ ($B^2\Sigma^+_{1/2}$ to $v'' = 22$ ($X^2\Sigma^+_{1/2}$) transition and the band located at 5517 Å can be assigned to be $v' - 0$ to $v'' - 21$ transition.[4] These two transitions were observed previously by Parks using a gas mixture of $Hg/CCl_4/Xe/Ar$ pumped by electron beam only.[1] In our experiment we observed
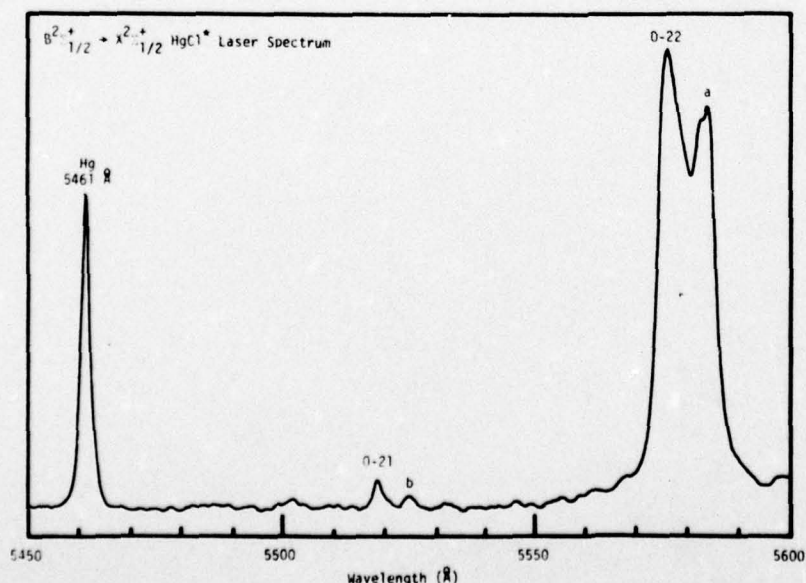

FIG. 3. Microdensitometer trace of $B \to X$ HgCl laser transitions; shown here is also the reference Hg 5461-Å line.

two additional bands (marked by a and b), each of which is about 8 Å to the red of the above transitions. The assignments for these two transitions are not certain, but they cannot be assigned to the transitions of $HgCl^{37*}$. Failure to observe the strong transition (band a) near 5584 Å in the earlier electron-beam pumped system[1] is probably due to the fact that this transition is absorbed by xenon, since its wavelength is coincident with the xenon transition line $(6p_{01} \rightarrow 9d_{00})$. In fact, such xenon absorption appears in the gain profile for the $Hg/CCl_4/Xe/Ar$ system[5] but not for the $Hg/Cl_2/Ar$ system.[6]

At higher resolution $(\Delta\lambda \approx 0.03 \text{ Å})$, fine rotational structure can be resolved. In fact, each vibronic transition consists of many rotation lines. Such characteristics have been previously observed in the bound-bound laser transitions, for example, in XeF^*,[7] S_2,[8] etc.

The role Cl_2 played in the controlled discharge system was tested. Variation of the Cl_2 concentration was found to seriously affect the performance of the laser and no laser action was observed when Cl_2 was replaced by CCl_4. Under the conditions we used (10 Torr Hg and 1500 Torr Ar), the nominal lower limit of Cl_2 concentration of 3.5 Torr was set by arcing prior to the electron-beam initiation. The nominal upper limit of about 11 Torr was set by suppression of laser action. The optimum concentration of Cl_2 was about 5.5 Torr. A similar relationship was found in fluorescence signals. For example, a reduction of about 40% in fluorescence signal was found when Cl_2 concentration was varied from 5.5 to 11 Torr. The fall-off of laser and fluorescence intensities with Cl_2 concentration may be due to either of two effects. The first is related to the capture

of electrons by Cl_2, which has the ultimate effect of decreasing the electron pump rate of Hg^*. The second is a possible two- or three-body quenching of $HgCl^*$ by Cl_2 (+ Ar).

In summary, we have demonstrated the operation of $HgCl^*$ with electron-beam-controlled discharge pumping of the $Hg/Cl_2/Ar$ mixture. The energy deposition efficiency through this pumping mechanism was shown to be better than that through pure electron-beam pumping. Effect of Cl_2 concentration on the laser performance was shown. Results indicate that a detailed understanding of kinetics involved in the $HgCl^*$ system, such as fluorescence lifetimes, quantum yields, and quenching processes, is necessary in order to scale to a high-power laser system.

[1]J.H. Parks, Appl. Phys. Lett. **31**, 192 (1977).
[2]H.F. Krause, S.G. Johnson, S. Datz, and F.K. Schmidt-Bleek, Chem. Phys. Lett. **31**, 577 (1975).
[3]The concentrations of Cl_2 and Hg quoted in this paper were the nominal concentrations. In a later experiment, we have found the reaction of Cl_2 with ground-state Hg is moderately rapid, leading to uncertainties in the values of the concentrations quoted here.
[4]K. Wieland, Helv. Phys. Acta **14**, 420 (1941).
[5]D. Ekstrom, B. Perry, K.Y. Tang, and R.O. Hunter, Jr. (unpublished).
[6]K.Y. Tang and R.O. Hunter, Jr. (unpublished).
[7]J. Tellinghuisen, G.C. Tisone, J.M. Hoffman, and A.K. Hays, J. Chem. Phys. **64**, 4796 (1976).
[8]S.R. Leone and K.G. Kosnik, Appl. Phys. Lett. **30**, 346 (1977).

Appendix E

KINETIC PROCESSES IN RARE GAS HALIDE LASERS

E-1

KINETIC PROCESSES IN RARE GAS HALIDE LASERS

Donald C. Lorents
SRI International
Molecular Physics Center
Menlo Park, California 94025

The progress that has been made in the development of high energy electronic
transition lasers operating in the vuv to visible range of the spectrum has been
truly remarkable in the last 5 years. This spurt of progress began in 1972 with
the realization and demonstration of rare gas excimer lasers such as Xe_2 and the
recognition of the importance of unbound lower states for the extraction of laser
energy [BDP70, KF72, HS73]. These advances were accelerated by the development
in electron beam and pulsed power technology that provided the means by which
high density gases could be excited with extremely high power densities [JD76].
These developments stimulated efforts to understand the kinetic processes in high
density rare gases excited with electron beams. The considerable literature and
general understanding of electronic and atomic collision processes in rare gases
led to very rapid development of detailed models of the observed fluorescence and
laser characteristics of these gases [L76, WG76].

A spin-off of these results was the realization that in general the dense
rare gases were excellent media for converting the kinetic energy of electron
beams to energy residing in the lowest excited atomic and molecular states of the
rare gases. At high densities in the pure rare gases this energy can only escape
by radiation in the excimer bands to which the gas is transparent. Efficiencies
for producing this electronic excitation were predicted to be in the 50% range
for excitation densities not exceeding a level where excited state-excited state
reactions and other excited state quenching processes lead to inefficiencies [L76].
Experimental measurements of the excimer radiation efficiency have recently
confirmed these predictions [THT76]. Thus the rare gases, because of their high
lying electronic states that can be efficiently excited, are excellent host media
from which to initiate transfer of electronic excitation energy to additive atomic
or molecular species. The range of possible electronic transitions that can be
excited by this technique is enormous and it remained only to find efficient and
selective energy transfer processes that would populate only one upper laser level
of an acceptor. Preferably that acceptor should be an excimer with a dissociating

E-2

lower level.

The key suggestion that led to the study of halogen donors in excited rare gases came almost simultaneously from Setser's group at Kansas State University [VS75] and from Golde and Thrush from Cambridge [GT74]. Setser first announced his results at a laser conference in St. Louis in 1974 and within months the first rare gas halide laser had been successfully demonstrated [SH75]. A lively race followed to discover all the possible RgX lasers and to begin to characterize their performance.

From the point of view of atomic and molecular physics, the rare gas halide lasers are rich sources of interesting collision processes that need to be understood not only because they are important to the laser operation but because they are of themselves of fundamental interest. The objective of this paper is to review the progress in understanding the basic kinetic mechanisms that determine the characteristics of these lasers.[†]

The rare gas halide lasers are indeed successful. Lasing has been demonstrated on at least 6 different rare gas halides at wavelengths ranging from 193 nm to 351 nm, pumped with e-beams, e-beam sustained discharges and avalanche discharges (see Table I for references). Pulse energies ranging from mJ to several hundred Joules have been obtained with efficiencies ranging up to 10%. Table I gives a listing of the dominant optical emissions observed from excited high density rare gas/halogen mixtures and indicates the RgX lasers that have been demonstrated. Of these lasers the rare gas fluorides ArF, KrF, and XeF have received most attention because of the ease with which they can be operated and their general high efficiency.

RARE GAS HALIDE SPECTRA AND STRUCTURE

The spectra of the diatomic rare gas halides, RgX^*, all have very similar characteristics which are exemplified by the $ArCl^*$ emission spectrum shown in Fig. 1. This spectrum was obtained by Golde and Thrush [GT74] at low pressures in a flowing afterglow by reaction of argon metastables with Cl_2 and CCl_4. The spectra are typified by a single broad emission peak ($\Delta\lambda \simeq 2\text{-}3$ nm) followed by a progression of less intense peaks toward the blue. The spectra are characteristic of transitions from a strongly bound upper state to a slightly repulsive lower state with a progression due to vibrational excitation of the upper level. Spectral measurements have been made for nearly all rare gas/halogen combinations using both e-beam excitation of high density rare gases and low pressure flowing

[†] A review article of RgX lasers by C. Brau of Los Alamos Scientific Laboratory will soon be published in Excimer Lasers, C. K. Rhodes, ed. (Springer-Verlag).

Table I

RgX Laser and Fluorescent Wavelengths

	Ne	Ar	Kr	Xe
F	Fluoresces 108 Dissociates (a)	Laser 193 (b)	Laser 248 (c)	Laser 351 (d)
Cl	Dissociates Cl_2 (254) (e)	Fluoresces 175 Dissociates (f)	Laser 222 (g)	Laser 308 (h)
Br	Dissociates Br_2 (290) (e)	Dissociates Br_2 (290) (i)	Fluoresces 206 (j)	Laser 282 (k)
I	Dissociates I_2 (342) (e)	Dissociates I_2 (342) (𝓁)	Dissociates I_2 (342) (m)	Fluoresces 254 Dissociates (n)

The wavelengths are in nm. In high density media the dominant emitters and their peak wavelength are listed.

(a) RHW77
(b) HHT76, MP77, LSS77, BD76
(c) EB75a, BBA76, HHT76b, MP76, SSG76, BD76, MJ75
(d) BE75b, MJD76, ABB75, BD76, BHD76, MJD76, WMS76
(e) Prediction
(f) MLH76, GSC76, W77a, CP76
(g) MP76, MP77, ES76
(h) EB75a, THH76a
(i) MLH76, KS77, MST76, EJM76
(j) W77b
(k) SH75
(𝓁) MLH76, MHH75, EB75c, BHB75, HHT76a
(m) MLH76
(n) EB75b, MLH76

ArCl* from Ar* + Cl_2

ArCl* from Ar* + CCl_4
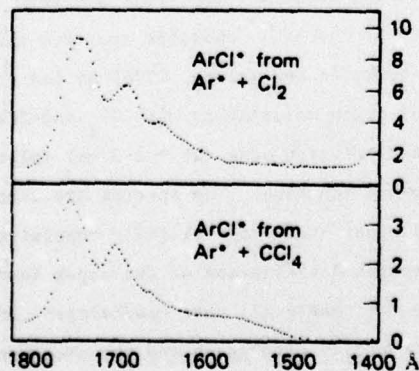
1800 1700 1600 1500 1400 Å

Fig. 1. ArCl* emission spectra from reactions of Ar* with Cl_2 and CCl_4. From GT74.

afterglows (see Table I for references). The low pressure spectra in general show more vibrational structure than data taken at high pressures where vibrational relaxation is completed by the time the molecule radiates, but otherwise the spectra are very similar. Vibrational relaxation is observed to occur even at very low pressures, indicating that the mechanism for this relaxation must be extremely efficient [GSC76].

Detailed observations of the exit channels of the $Ar^* + Cl_2$ reaction at low pressures show that about 50% of the reactions produce $ArCl^*$, 1/6 yield Cl^*, and 1/3 yield Cl_2^+ [GSC76]. This is in contrast with the reaction of Kr^* with F_2 which produces only KrF^* [VKS76]. In reactions of Ar^* with Br_2 and I_2 only the excited dissociated products Br^* and I^* are observed [MLH76, KS77]. Evidently the RgX^* is unstable in these cases and predissociates to the atomic products. Table I lists the RgX combinations that predissociate as well as those that are stable and lase. Note that the diagonal of this table is the boundary dividing the stable and unstable RgX^* molecules and those on the diagonal are observed to both fluoresce and dissociate.

The structure of the rare gas halide excited states that produce the observed optical emissions is dominated by an ionic bonding (Rg^+X^-) that is strongly analogous to the ionic bonding in the ground state alkali halides. These strongly bound states produce deep-welled potentials that become the lowest excited states for those rare gas halides that are observed to radiate optically. The diabatic ionic states dissociate to Rg^+ and X^- on potential curves that cross several covalent states that dissociate to $Rg^* + X$ or $Rg + X^*$. This is illustrated in Fig. 2 which shows the electronic states of KrF as calculated by Dunning
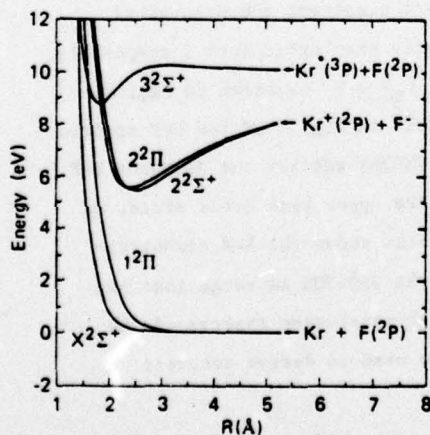

Fig. 2. **Ab initio** calculations without spin orbit coupling of the ground and lowest excited ionic and covalent states of KrF. From DH76.

and Hay [DH76, HD77]. In this case the crossings are at such large R that the states will certainly interact very weakly, allowing a predominantly diabatic dissociation. A very important aspect of an RgX* state in order that it be a good laser state is that once the energy is delivered to the ionic channel, it relax to the bottom of that state without interactions with any repulsive ground or excited states that permit that energy to be lost via spontaneous or collision induced predissociation. As indicated in Table I only those RgX combinations lying above the diagonal fall into this category and make good RgX lasers.

The analogy of the rare gas halide ionic excited states to the ground states of the corresponding alkali halides is very close and it is useful for estimating well depths and internuclear separations. The analogy was used very successfully by Brau and Ewing [EB75c] to predict the transition wavelengths of many of the rare gas halides before they were observed. The analogy is also particularly useful because the studies of the harpoon reactions among the alkali halides provide insight into the reaction mechanisms that produce the rare gas halide excimers.

The KrF states shown in Fig. 2 were calculated _ab initio_ and show the characteristic features of these molecules. The $^2\Sigma^+$ and $^2\Pi$ states formed from the ground state interaction of $Rg(^1S)$ and $X(^2P)$ are basically repulsive with the exception of XeF which is bound by about 1150 cm^{-1} in the $X^2\Sigma^+$ state. The ionic charge transfer states also consist of $^2\Sigma^+$ and $^2\Pi$ states that do not interact with the ground states or higher covalent excited states except at high energies along the repulsive wall. The predominant transition is the ionic to covalent one between the $^2\Sigma^+$-$^2\Sigma^+$ states and the other transitions ($^2\Sigma$-$^2\Pi$ and $^2\Pi$-$^2\Pi$) although observed are weak. In a more exact treatment the spin-orbit effect must be included and the Π and Σ ionic states then split into 3 components, two dissociating to $Kr^+(^2P_{\frac{3}{2}}) + F^-$ and one to $Kr^+(^2P_{\frac{1}{2}}) + F^-$ as shown in Fig. 3.

Detailed spectral studies such as the one shown in Fig. 4 of the KrF spectra observed from an e-beam excited $Ar/Kr/F_2$ mixture [MP76] exhibit the dominant B-X transition at 248 nm, a weaker D-X emission from the upper spin orbit state, as well as the broader B-A emission. This spectrum also shows the B-X transition of ArF at 193 nm and an underlying background in the 260-300 nm range that has been identified as Ar_2F. Detailed analyses of high resolution spectra of the B-X emission in XeI, XeBr, XeCl, and KrF have been used to derive accurate potential functions for these states [THH76a,b].

E-6
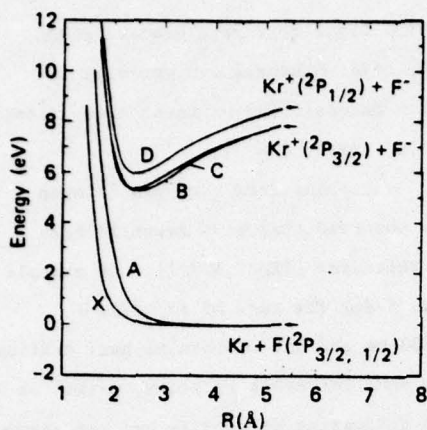
Fig. 3. _Ab initio_ calculations of the ground and ionic KrF states with spin orbit coupling. From DH76.
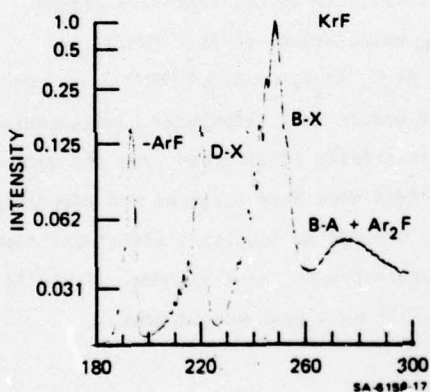
Fig. 4. Emission spectra of an e-beam excited $Ar/Kr/NF_3$ mixture at pressures of 3300/100/5 torr respectively. From MP76.

As indicated in Table I many excited rare gas halogen mixtures at high density radiate primarily from X_2^* molecules. For example, Ar/RI mixtures at 1000 T/1T radiate exclusively from the lowest ionic state, $^3\Pi_{2g}$, of I_2^* dissociating to $I^+ + I^-$, to the lowest excited covalent state, $^3\Pi_{2u}$, dissociating to $2I(^2P_3)$ [MHH75]. This emission peaks at 342 nm and is highly structured since it is a bound-to-bound transition. The ionic nature of this system allows the energy to flow almost exclusively into a single upper level by mechanisms analogous to the RgX^*. In this case it has been observed that 70% of the excited states and ions produced

E-7

initially in the Ar lead to $I_2^*(^3\pi_{2g})$ [MHH75]. Similar transitions are also observed in Ar/Br_2 [MLH76] and Ar/Cl_2 [MLH76, CP76] mixtures and recently in He/F_2 mixtures [RWH77]. Lasers have also been demonstrated on these transitions in I_2, Br_2 and F_2 [EB75c, BHB75, HHT76a, MST76, EJM76, RHW77].

In addition to the diatomic RgX^* and X_2^* emissions from rare gas halogen mixtures, broad band continuum emissions are observed that have recently been identified as transitions in triatomic Rg_2X molecules [LHH77, MJR77]. An example of these continuum emissions is shown in Fig. 5 for the case of an $Ar/Kr/F_2$ mixtures. The continuum emission peaks at 400 nm and has a width at half maximum of about 53 nm. The intensity of the 400 nm band increases relative to that of the KrF^* with increasing Ar density and with increasing Kr density and becomes the dominant emitter at high pressures. In Ar/F_2 mixtures a similar continuum band has been observed at 290 nm and identified from both experimental [LHH77] and theoretical [WH77] studies to be an ionically bound triatomic excited state, $Ar_2^+F^-$, analogous to the diatomic Ar^+F^-, that radiates to its repulsive ground state dissociating to $2Ar + F$. The ab initio calculations on Ar_2F [WH77] and diatomics in molecules computations on Ne_2F, Ar_2F, Kr_2F, and Kr_2Cl [HS77] have confirmed that these triatomic ionic states are stable in a triangular configuration where the Rg_2^+ internuclear separation is essentially undisturbed from its normal equilibrium distance. These continuum emissions have been observed and identified in several rare gas halide mixtures and they provide an important additional tool for studying and understanding the kinetic processes in these systems. Table II lists the observed [LHM77] and calculated [HS77] Rg_2X peak wavelengths.

Table II

Emission Wavelengths of Triatomic Rare Gas Halides

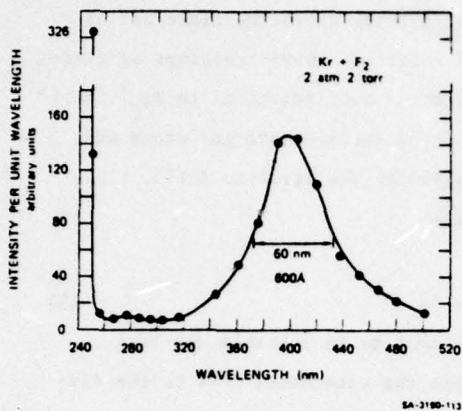| Rg_2X	Peak λ (nm)	
	Experiment	Theory
Ne_2F	-	143, 145
Ar_2F	290	268, 274
Kr_2F	400	383, 399
Ar_2Cl	246	-
Kr_2Cl	325	338, 348
Xe_2Cl	450	-

Fig. 5. Continuum emission band from e-beam excited Ar/Kr/F$_2$ mixture. The intense emission at 248 nm is from KrF*. From NHL76.

RARE GAS HALIDE REACTION KINETICS

There are two important types of reaction kinetics occurring in rare gas halide lasers, both of which need to be understood. The first of these are the reactions among the ions that are most important under conditions of low power excitation in gas mixtures where the electron attachment to the halogen donor is dominant. The principal mechanism of RgX* formation under these conditions is that of positive ion-negative ion recombination. The second occurs under conditions of high power e-beam pumping, where electron recombination with positive ions is faster than attachment, or in discharge pumped lasers where excited states are produced directly. The excited state reaction channels then become the dominant mechanisms for formation of RgX*. These two conditions are referred to as attachment dominated and recombination dominated cases, although in either case both types of reactions contribute to the excited state formation.

In discussing the kinetics of RgX lasers it must be recognized that in all cases the rare gas is the dominant gas and the halogen donor is only a minor constituent that participates in the kinetics but does not play any role in the energy deposition. In pure electron beam excitation of rare gases the ratio of the rate of production of ions to that of excited states is about 3 [L76]. The positive ions produced quickly form diatomic ions by the reaction

$$Rg^+ + 2Rg \rightarrow Rg_2^+ + Rg \quad . \tag{1}$$

These diatomic ions can then recombine with the electrons to form excited states:

$$Rg_2^+ + e \rightarrow Rg^{**} + Rg \quad , \tag{2}$$

where the Rg^{**} consists mainly of excited states lying above the first set of excited states, $Rg^{*}[np^{5}(n+1)s]$. The Rg^{**} can relax via curve crossings or electron interactions to Rg^{*} and subsequently by three-body reactions to Rg_{2}^{*} [L76].

In electron beam controlled discharge pumping excited rare gas atoms are produced mainly by the secondary electrons heated by the electric field, i.e.,

$$e + Rg \rightarrow Rg^{*} + e \quad . \tag{3}$$

However, ionization also occurs by

$$e + Rg^{*} \rightarrow Rg^{+} + 2e \tag{4}$$

and this process in rare gases will generally lead to an unstable discharge. However, if an attaching gas is added such that the attachment rate in the discharge is greater than twice the ionization rate, a stable discharge can be maintained [DMJ76]. In principle this is the most efficient method for pumping rare gas halide lasers and although this method has been demonstrated for RgX lasers, it has so far not been as successful as pure e-beam pumping. When an electron attaching gas (most halogen donors have strong electron affinities and large electron attachment coefficients) is added to the rare gas, the attachment will compete with the recombination by means of

$$e + RX \rightarrow X^{-} + R \quad , \tag{5}$$

where TX is a halogen donor. Attachment dominated conditions are attained when

$$k_{5}[RX] > k_{2}[Rg_{2}^{+}] \quad , \tag{6}$$

i.e., when the rate of electron attachment exceeds the rate of electron recombination. Since the number of Rg_{2}^{+} is dependent on the pump power and both k_{5} and k_{2} are functions of electron temperature, the condition (6) is not a simple relationship.

It is clear that the excited ionic RgX^{*} can be formed by ion-ion recombination reactions such as

$$Rg^{+} + X^{-} + M \rightarrow RgX^{*} + M \tag{7}$$

$$Rg_{2}^{+} + X^{-} + M \rightarrow RgX^{*} + M + Rg \tag{8a}$$

$$\rightarrow Rg_{2}X^{*} + M \quad . \tag{8b}$$
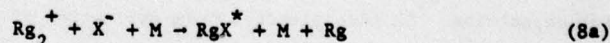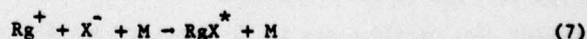
However, under recombination dominated or discharge pumped conditions where the excited state production is dominant, RgX^{*} is formed by the charge transfer (harpoon) reactions

E-10

9

$$Rg^* + RX \rightarrow RgX^* + R \tag{9}$$

$$Rg_2^* + RX \rightarrow RgX^* + Rg + R \tag{10a}$$

$$\rightarrow Rg_2X^* + R \quad . \tag{10b}$$
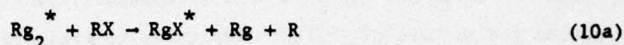
The high efficiency of the rare gas halide laser is due in large part to the ionic nature of the RgX^* upper laser state that permits both of the reactions (7) and (9) to populate that same level with very high cross sections. Thus in spite of the fact that it is not possible to create conditions in which a single formation reaction controls the flow of energy, it is funnelled into a single state by the fact that nearly all reactions lead to the same exit channel. Once the RgX^* is formed in the ionic state, it is vibrationally relaxed to the bottom of its well very rapidly by collisions with the ambient gas atoms which are occurring at a rate of the order of $10^{10}/S$.

The large cross sections for both of these formation processes are largely due to the long range ionic potential. Rate constants for the ion-ion recombination reactions (7) and (8) can be calculated by a modified Thompson Coulomb model [N60, B64, MG74]. This model gives three-body rate constants of the order of 10^{-25} cm^6/S at low pressures but as the pressure increases this rate decreases and passes through a maximum at about 10^3 torr. The effective two-body rate coefficient at the maximum is of the order of 2×10^{-6} cm^3/S. These rates have not been measured for rare gas halides nor have the branching ratios of reactions such as (8a) and (8b) been studied. Indirect evidence from studies of the KrF laser performance indicates that reaction (8b) produces mainly KrF^* [Hu77].

The harpoon reactions (9) have been studied extensively by Setser and co-workers [VKS76] and rate constants and branching ratios measured for Kr^* and Xe^* metastables reacting with a large number of halogen donor molecules. In most cases the reactions occur with cross sections typical of harpoon reactions ($\sim 10^{-14}$ cm^2) but only the simpler donor molecules yield the RgX^* with near unit efficiency. Reactions of the type (10a) and (10b) have been studied only indirectly in e-beam excited rare gas halogen mixtures. These are also harpoon reactions that have high cross sections but the branching ratio between RgX^* and Rg_2X^* formation is not known. It must be recognized that the branching in these reactions may in fact be a function of the ambient gas density, i.e., three-body stabilization of long-lived collision complexes can be very significant at these densities.

KINETIC PROCESSES IN RARE GAS HALIDE LASERS

The KrF laser has operated most successfully by e-beam pumping of a three component gas mixture of $Ar/Kr/F_2$ typically at pressures of 1500T/100T/2-3T. The kinetics of this system are very complex and difficult to model since most of the reactions have not been studied individually.

Besides the measurements of the rate coefficients and cross sections of individual reactions, information on the reaction kinetics of laser mixtures can be extracted from fluorescent yield measurements (photons radiated divided by the number of Rg excited states produced) and decay rate measurements as a function of the density of the component gases of typical laser mixtures. For example, at SRI a 3 ns electron beam pulse is used to excite the gas mixture and the intensities of the various optical emissions are monitored as a function of time [NLH76]. The excitation conditions of this pump are such that the neutral kinetics dominate the reaction chain.

The ion reaction chain is indicated in Fig. 6. The vertical ion reaction channel is quite firmly established and the reaction rates are all fast. The conversion of Kr^+ to Kr_2^+ proceeds rapidly even at low Kr densities by means of the intermediate $ArKr^+$ formed in a three-body reaction with 2Ar and a subsequent two-body reaction with Kr [BAM70]. The horizontal reactions are all with F^-. The existence of $ArKrF^+$ is postulated on the basis of the existence of $ArKr^+$ and its probable association with F^- in analogy with Ar_2F and Kr_2F. No optical emission has as yet been identified with this molecule but its emission should be broad band and to the red of KrF. Under most conditions its lifetime is probably very short due to fast reaction with Kr.
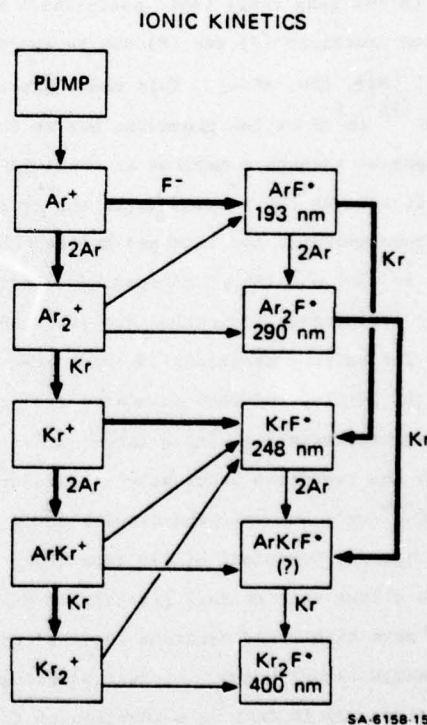
IONIC KINETICS

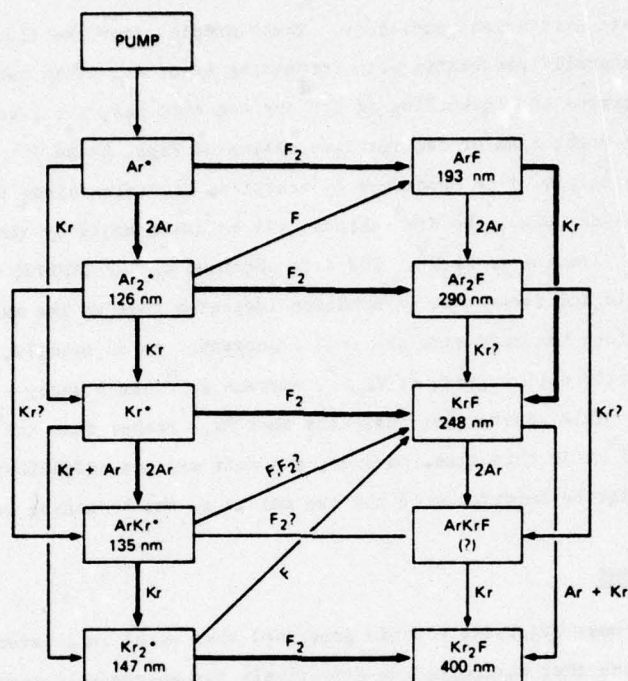Fig. 6. Ion reaction chain for an e-beam excited $Ar/Kr/F_2$ mixture.

Fig. 7. Excited neutral reaction
chain for an Ar/Kr/F$_2$ mixture.

The excited state reaction chain, Fig. 7, appears very similar to that of the ions. Indeed the vertical reaction among the rare gas excited states is exactly parallel. The molecule ArKr* is the least well characterized but its emission has been observed [VOF75] and it is required in the reaction chain to account for the rapid formation of Kr$_2^*$ in excited Ar/Kr mixtures. In this case, of course, the horizontal reactant is the fluorine donor F$_2$ or NF$_3$. As has already been discussed, a major uncerainty in these reaction schemes is the branching between RgX* and Rg$_2$X* formation in the reactions of Rg$_2^*$ with RX or Rg$_2^+$ with X$^-$. In addition, of course, many of the rate constants for these reactions are very uncertain [NHL76]. Not included in these diagrams are the quenching reactions of the excited rare gas halides with the fluorine donor molecule. These reactions are generally fast and can compete effectively with the radiative rates [MJR77, BSD77]. However, the radiative rate under lasing conditions is increased and the quenching losses are less serious.

Several laboratories [MJR77, ES76] have conducted measurements of the intensities of the various emissions as a function of component gas mixtures

E-13

under steady state excitation conditions. These studies show the fluorescence yield of KrF* generally decreasing with increasing Ar or Kr. This behavior is generally interpreted as a quenching of KrF* by the rare gas, i.e., vertical reactions on the right side of the reaction chains of Figs. 6 and 7. However, this data can equally well be described by reactions occurring along the left side of these chains, e.g., the KrF* channel may be intercepted by the more rapid formation of Kr_2^* leading to Kr_2F^*. The data obtained at SRI [NHL77] using both fluorescence yield and decay rate information indicates that in the excited state case reactions along the left side are very important. As an example, the decay rate of Kr_2^* exactly follows that of Kr_2F^*, whereas KrF* has a decay rate about 10 times faster. This observation indicates that Kr_2^* rather than KrF* is the precursor of Kr_2F^*. At this time, however, the data are not sufficiently detailed to assess the relative importance of the two chains or the branching between them.

PHOTON INTERACTIONS

Perhaps the most important kinetic processes that occur in a laser are the photon interactions that determine how effectively the energy delivered to the excited states can be extracted as laser radiation. The processes that absorb the laser photons are of particular concern.

The absorptions directly affect the efficiency of the laser by limiting the number of available photons that can be extracted in a coherent beam. This can be seen in the expression below giving the extraction efficiency of a laser operating in a cw mode.

$$\epsilon = \frac{Q_L}{A + Q_u + Q_L} \cdot \frac{T}{T + l\Sigma_a} \cdot \left[1 - \frac{P_{th}}{P}\right]$$

In this expression, which can be easily derived from the steady state operating condition of a laser, Q_L is the total removal rate of the lower laser level, Q_u is the quenching rate, and A is the spontaneous emission rate of the upper laser level. Note that for an excimer where Q_L is large compared to $A + Q_u$ the first term of the expression approaches 1. In the second term, T is the mirror trans-mission, l is laser length, and Σ_a is the total absorption coefficient due to all absorbers. Obviously an efficient laser requires $T \gg l\Sigma_a$. The third term indicates that the pump power, P, of the laser must be large compared to the power at the lasing threshold, P_{th}. This simplified expression becomes more

E-14

13

complex when the transient absorptions which are dependent on pump power are considered.

In an excited gas as complex as the mixtures used in an RgX laser many possible transient absorbing species are created. The major advantage of the excimer lasers, of which KrF is a member, is that the lower states of the lasing transitions are repulsive and do not absorb appreciably at the laser wavelength. The only exception to this is XeF which is bound sufficiently in the ground state (1150 cm^{-1}) to cause a bottlenecking problem.

Contributions to absorption in RgX lasers can be made by the following transient species:

1. Positive ions: Photodissociation of Rg_2^+
2. Negative ions: Photodetachment of X^- or photodissociation of X_2^- or X_3^-
3. Excited species: Photoionization of Rg^*, Rg^{**}, or dissociation of Rg_2^*, RgF^*, or Rg_2F^*.

In the KrF laser, for example, Ar_2^+ and Kr_2^+ are important absorbers at 248 nm because of the large broadband $^2\Sigma_u$-$^2\Sigma_g$ photodissociation cross sections [SGK76, MSH77, MH77] that peak at 295 and 320 nm respectively. The cross section at 248 nm is on the blue side of the absorption band and is quite sensitive to the amount of vibrational excitation of the Ar_2^+ or Kr_2^+ ions. The wavelength dependent absorption profiles of Ar_2^+ and Kr_2^+ have recently been measured [MH77] and for Ar_2^+ have been normalized to the cross sections calculated theoretically by Stevens et al. [SGK76]. The experimental and theoretical profiles match very well on the red side but the theory falls about a factor of two below experiment out in the blue wing. The Ar_2^+ and Kr_2^+ may be the dominant absorbers for the KrF laser operated in an $Ar/Kr/F_2$ mixture.

It is expected that the absorptions in Ar_2F and Kr_2F will be very similar to Ar_2^+ and Kr_2^+ respectively. This is reasonable on the basis of the ionic structure of $Rg_2^+X^-$ in which the Rg_2^+ retains its structure almost as if the X^- were not there. The importance of the Rg_2X absorptions is critically dependent on how they are formed, whether from KrF^* or by reactions (8b) and (10b), because in the former case the rapid removal of RgX^* by the laser flux precludes formation of Rg_2X^*. Rg_2^* and Rg^* absorptions in the visible range of the spectrum have recently been identified in excited rare gases [ZHL77] but the contribution of these species to absorption in the KrF laser is not known.

The photodetachment cross sections for the atomic negative ion have been both

measured [M71] and calculated [RG67] and reasonable agreement exists. However, neither the formation processes nor the photodissociation cross sections have been studied for the diatomic and triatomic fluorine ions. For heavier halogens these ions have been observed to form rapidly in rare gas/halogen mixtures [HM76].

CONCLUSION

The success of the rare gas halide lasers has opened up a new class of efficient near uv coherent photon sources that are already being considered for applications in photochemistry and isotope separation, as well as a multitude of scientific applications. It is obvious that these lasers will be integrated into our technology very quickly. It is therefore of some considerable importance to understand quantitatively the microscopic processes that determine the characteristics of these lasers. As I have tried to indicate in this paper, the important atomic and molecular collision processes occurring in RgX lasers are many and complex and, although rapid progress is being made to understand them, much detailed and challenging work remains to be done.

ACKNOWLEDGEMENT

REFERENCES
ABB75   E. R. Ault, R. S. Bradford, Jr., and M. L. Bhaumik, Appl. Phys. Lett. 27, 413 (1975).
B64   K. A. Bruechner, J. Chem. Phys. 40, 439 (1964).
BAB75   R. S. Bradford, Jr., E. R. Ault, and M. L. Bhaumik, Appl. Plys. Lett. 27, 546 (1975).
BAM70   D. K. Bohme, N. G. Adams, M. Moseman, D. B. Dunkin, and E. E. Ferguson, J. Chem. Phys. 52, 5094 (1970).
BBA76   M. L. Bhaumik, R. S. Bradford, Jr., and E. R. Ault, Appl. Phys. Lett. 28, 23 (1976).
BDP70   M. G. Basov, V. A. Danilychev, and Yu. M. Popov, Sov. J. Quant. Elect. 1, 18 (1971).
BE75a   C. A. Brau and J. J. Ewing, J. Chem. Phys. 63, 4640 (1975).
BE75b   C. A. Brau and J. J. Ewing, Appl. Phys. Lett. 27, 435 (1975).
BHD76   R. Burnham, D. Harris, and N. Djeu, Appl. Phys. Lett. 28, 86 (1976).
BDS77   H. C. Brashears, Jr., D. W. Setser, and D. Des Marteau, Chem. Phys. Lett., to be published.
CP76   C. H. Chen and M. G. Payne, Appl. Phys. Lett. 28, 219 (1976).

DH76   T. H. Dunning and P. J. Hay, Appl. Phys. Lett. $\underline{28}$, 649 (1976).

DMJ76   J. D. Daugherty, J.A. Mangano, and J.H. Jacob, Appl. Phys. Lett. $\underline{28}$, 581 (1976).

EB75a   J. J. Ewing and C. A. Brau, Appl. Phys. Lett. $\underline{27}$, 350 (1975).

EB75b   J. J. Ewing and C. A. Brau, Phys. Rev. A $\underline{12}$, 129 (1975).

EB75c   J. J. Ewing and C. A. Brau, Appl. Phys. Lett. $\underline{27}$, 557 (1975).

EJM76   J. J. Ewing, J. H. Jacob, J. A. Mangano, and H. A. Brown, Appl. Phys. Lett. $\underline{28}$, 565 (1976).

ES76   J. G. Eden and S. K. Searles, Appl. Phys. Lett. $\underline{29}$, 356 (1976).

GSC76   L. A. Gundel, D. W. Setser, M.A.A. Clyne, J. A. Coxon, and W. Nip, J. Chem. Phys. $\underline{64}$, 4390 (1976).

GT74   M. G. Golde and B. A. Thrush, Chem. Phys. Lett. $\underline{29}$, 486 (1974).

HD77   P. J. Hay and T. H. Dunning, J. Chem. Phys. $\underline{66}$, 1306 (1977).

HHT76a   A. K. Hays, J. M. Hoffman and G. C. Tisone, Chem. Phys. Lett. $\underline{39}$, 353 (1976).

HHT76b   J. M. Hoffman, A. K. Hayes, and G. C. Tisone, Appl. Phys. Lett. $\underline{28}$, 538 (1976).

HM76   B. A. Huber and T. M. Miller, J. Appl. Phys. $\underline{48}$, 1708 (1977).

HS73   P. W. Hoff, J. C. Swingle, and C. K. Rhodes, Optics Comm. $\underline{8}$, 128 (1973).

HS77   D. L. Huestis and N. Schlotter, private communication.

Hu77   R. Hunter, private communication.

JD76   J. D. Daugherty, "Electron Beam Ionized Plasmas," Chap. 9 of $\underline{Principles}$ $\underline{of\ Laser\ Plasmas}$, G. Bekefi, ed. (John Wiley & Sons, 1976).

KS77   J. H. Kolts and D. W. Setser, J. Appl. Phys. $\underline{48}$, 409 (1977).

KF72   H. A. Koehler, L. J. Ferderber, D. L. Redhead, and P. J. Ebert, Appl. Phys. Lett. $\underline{21}$, 198 (1972).

L76   D. C. Lorents, Physica $\underline{82C}$, 19 (1976).

LHH77   D. C. Lorents, R. M. Hill, D. L. Huestis, M. V. McCusker, and H. H. Nakano in Electronic Transition Lasers II, L. E. Wilson, S. N. Suchard, and J. I. Steinfeld, eds. (MIT Press, 1977).

LHM77   D. C. Lorents, D. L. Huestis, M. V. McCusker, H. H. Nakano, and R. M. Hill, to be published.

LSS77   T. R. Loree, P. B. Scott, and R. C. Sze in $\underline{Electronic\ Transition\ Lasers}$ $\underline{II}$, L. E. Wilson, S. N. Suchard and J. I. Steinfeld, eds. (MIT Press, 1977).

M71   A. Mandl, Phys. Rev. A $\underline{3}$, 251 (1971).

ME74   H.S.W. Massey and H. B. Gilbody, $\underline{Electronic\ and\ Ionic\ Impact\ Phenomena}$, Vol. 4 (Oxford Press, 1974) p. 2266.

MH77   M. V. McCusker and R. Hunter, private communication.

MHH75   M. V. McCusker, R. M. Hill, D. L. Huestis, D. C. Lorents, R. A. Gutcheck, and H. H. Nakano, Appl. Phys. Lett. $\underline{27}$, 363 (1975).

MJ75   J. A. Mangano and J. H. Jacob, Appl. Phys. Lett. $\underline{27}$, 495 (1975).

MJD76   J. A. Mangano, J. H. Jacob, and J. B. Dodge, Appl. Phys. Lett. $\underline{29}$, 426 (1976).

MJR77   J. T. Mangano, J. H. Jacob, M. Rokni, and A. Hawryluk, Appl. Phys. Lett. $\underline{31}$, 27 (1977).

MLH76   M. V. McCusker, D. C. Lorents, D. L. Huestis, R. M. Hill, H. H. Nakano, and J. A. Margevicius, "New Electronic Transition Laser Systems," Technical Report No. 4A, Contract DAAH01-74-C-0624, SRI MP76-46, Stanford Research Institute, May 1976.

MP76   J. R. Murray and H. T. Powell, Appl. Phys. Lett. $\underline{29}$, 252 (1976).

MP77   J. R. Murray and H. T. Powell in $\underline{Electronic\ Transition\ Lasers\ II}$, L. E. Wilson, S. N. Suchard and J. I. Steinfeld, eds. (MIT Press, 1977).

MSH77   J. T. Moseley, R. P. Saxon, B. A. Huber, P. C. Cosby, R. Abouaf, and M. Tadjeddine, Phys. Rev., to be published.

MST76   J. R. Murray, J. C. Swingle, and C. E. Turner, Jr., Appl. Phys. Lett. 28, 530 (1976).

N60   G. L. Natanson, Soviet Phys.-Tech. Phys. 4, 1263 (1960).

NHL76   H. H. Nakano, R. M. Hill, D. C. Lorents, D. L. Huestis, and M. V. McCusker, "New Electronic Transition Laser Systems," SRI Report MP76-99, Contract DAAH01-74-C-0624, Stanford Research Institute, December 1976.

RG67   E. J. Robinson and S. Geltman, Phys. Rev. 153, 4 (1967).

RHW77   J. K. Rice, A. Kay Hays, and J. R. Woodworth, Appl. Phys. Lett. 31, 31 (1977).

SGK76   W. J. Stevens, M. Gardner, and A. Karo, private communication.

SH75   S. K. Searles and G. A. Hart, Appl. Phys. Lett. 27, 243 (1975).

SSG76   D. G. Sutton, S. N. Suchard, O. L. Gibb, and C. P. Wang, Appl. Phys. Lett. 28, 522 (1976).

THH76a J. Tellinghuisen, A. K. Hays, J. M. Hoffman, and G. C. Tisone, J. Chem. Phys. 64, 2484 (1976).

THH76b J. Tellinghuisen, A. K. Hays, J. M. Hoffman, and G. C. Tisone, J. Chem. Phys. 65, 4473 (1976).

THT76   C. E. Turner, Jr., P. W. Hoff, J. Taska, and L. G. Schlitt, LLL Laser Program Annual Report-1975, UCRL 50021-75 (March 1975) p. 499F.

VKS76   J. E. Velazco, J. H. Kolts, and D. W. Setser, J. Chem. Phys. 65, 3469 (1976).

VOF75   E. T. Verkhovtseva, A. E. Ovechkin, Ya. M. Fogel, Chem. Phys. Lett. 30, 120 (1975).

VS75   J. E. Velazco and D. W. Setser, J. Chem. Phys. 62, 1990 (1975).

W77a   R. W. Waynant, Appl. Phys. Lett. 30, 234 (1977).

W77b   R. W. Waynant in NRL Memorandum Report 3482, "ARPA/NRL X-Ray Laser Program," Final Technical Report, Naval Research Laboratory, Washington, D.C.

WG76   C. W. Werner and E. V. George, "Excimer Lasers," Chap. 10 of Principles of Laser Plasmas, G. Bekefi, ed. (John Wiley & Sons, 1976).

WH77   W. Wadt and P. J. Hay, Appl. Phys. Lett. 30, 573 (1977).

WMS76   C. P. Wang, H. Mirels, D. G. Sutton, and S. N. Suchard, Appl. Phys. Lett. 28, 326 (1976).

ZLH77   E. Zamir, D. L. Huestis, D. C. Lorents, and H. H. Nakano, in Electronic Transition Lasers II, L. E. Wilson, S. N. Suchard, and J. I. Steinfeld, eds. (MIT Press, 1977).

Appendix F

OPTICAL EMISSIONS OF TRIATOMIC RARE GAS HALIDES

OPTICAL EMISSIONS OF TRIATOMIC RARE GAS HALIDES[†]

D. C. Lorents, D. L. Huestis, M. V. McCusker,
H. H. Nakano, and R. M. Hill
Molecular Physics Laboratory
SRI International, Menlo Park, California 94025

ABSTRACT

We report in this paper the observation of optical emissions from triatomic rare gas halide molecules formed in excited high density rare gas-halogen mixtures. The broadband continuum emissions are identified as transitions between ionically bonded excited states $(Rg_2^+X^-)$ and repulsive covalent lower states that dissociate to ground state atoms. These emissions become predominant at high rare gas densities.

MP 77-53R

The recent discovery of strongly bound excited diatomic rare gas halide (RgX[*]) molecules that radiate to a weakly bound or repulsive ground state has led to the development of a new class of efficient near-uv and uv lasers. The RgX[*] exciplex molecules were first observed and suggested as possible laser candidates by Velazco and Setser in 1974.[1] They observed emission from the set of the XeX[*] molecules and suggested the ionic nature of these bonds in analogy with the alkali halides.[2] Golde and Thrush independently observed the emission from ArCl[*] produced in the reaction of Ar[*] with chlorine bearing compounds.[3] By exploiting the similarity between excited rare gas halides and ground state alkali halides, Ewing and Brau[4] predicted the transition energies of a large fraction of the set of RgX molecules and compared their predictions with spectra obtained from e-beam excited high density rare gas/halogen mixtures.[5] These initial observations were rapidly followed by detailed spectral[6] and structural analysis[7] studies as well as ab initio calculations[8,9] with the result that many of these molecules are already quite well characterized.

These molecules have very desirable laser characteristics because of their repulsive ground (except for XeF and XeCl) states and their favorable reaction kinetics that leads to efficient energy flow into a single upper laser level. As a result, the development of these lasers pumped with e-beams, discharges, or e-beam controlled discharges has been rapid and successful.

A recent report summarizes the laser progress and gives a detailed

analysis of experimental studies of the energy flow kinetics for e-beam

excited $Ar/Kr/F_2$ mixtures.[10]

In this paper we report a new class of triatomic rare gas halide

exciplex molecules whose emissions were discovered in the coarse of studies

of the diatomic RgX^* molecules at high densities. The new emissions are

structureless broad band continua whose intensities increase with pressure

and in some cases become predominant over all other emissions at high

pressures. The emissions are identified as ionic to covalent transitions

in Rg_2X molecules that are ionically bound in the excited state and

repulsive in the lower state.

Experimental Measurements

Mixtures of rare gases and halogen containing compounds were excited

with a Febetron 706 that produces a 3 nsec, 5-10 joule pulse of 500 keV

electrons. The gas mixtures were contained in a stainless steel cell with

MgF_2 windows. The gas was mixed in the excitation cell with a magnetic

stirrer and the partial pressures were measured by an MKS True Torr

gauge (0.1-10 torr) and a Matheson Model 63 gauge (0.1-10 atmospheres). The

pulsed electron-beam entered the cell through a 0.001-inch foil backed by

a multi-hole "Hibachi" structure to allow high pressure operation.

Spectra were obtained with a McPherson ½-meter spectrograph (Model

216.5) using both film and an RCA 1P28 photomultiplier tube. The film

spectra were taken on Polaroid type 57 film from which negatives were made

using Kodak Tri-X. Densitometer scans of the negatives were made using a Jarrell-Ash recording microphotometer. No attempts were made to correct for the variation of sensitivity with wavelength in the film generated spectra. For the broad band emissions seen from Ar_2F (290 nm) and Kr_2F (400 nm) the spectra were generated by measuring the intensity at a number of points across the band, with the spectrograph-photomultiplier combination. This detection system had been calibrated using a tungsten filament standard lamp in the visible and the molecular branching ratio method in the near UV, so that sensitivity changes with wavelength could be accounted for. The photomultiplier output was recorded using a Tektronix 5812 transient digitizer which made determinations of decay rates and time integrated output fairly easy. Each data point, of course, represents one excitation pulse by the e-beam exciter. The e-beam intensity varies by $\pm$ 20% from pulse to pulse but a more serious problem is introduced by excitation induced changes in the gas mixtures. We were able to obtain reproducibility only by a complete change of the gas mixture in the gas cell between each excitation pulse.

The absolute photon flux in the radiating bands can be determined using the calibrated spectrograph detector system. In addition, the number of excitations produced by the e-beam can be determined using the techniques given in Reference 10. This allows a fairly accurate, $\pm$ 30%, determination of the fluorescent yield, defined as the ratio of the number of photons emitted in a given band to the number of excitations produced by the e-beam.

F-5

Spectral Emissions: Ar/F$_2$ Mixtures

The new emissions were first observed in Ar/Kr/F$_2$ mixtures in the course of studies of the formation and decay kinetics of KrF*. In addition to the already established emissions of ArF (193 nm) and KrF (248 nm) from this mixture, we observed structureless broad band emissions peaked at 290 nm and 400 nm.[11] The band shapes and widths were observed to be independent of pressure. To isolate the source of the broad band radiators the krypton was removed from this mixture with the result that only the 193 and 290 emissions remained.

A spectrometer scan of the 290 nm profile obtained from an excited Ar/F$_2$ mixture using a photomultiplier detector is shown in Fig. 1. Neither the broad bandwidth nor the energy of this transition can be explained by the accepted energy level structure of ArF.[12,13] Evidently the 290 nm emitter is a more complex molecular species composed of Ar and F atoms, Ar$_m$F$_n^*$. The dependence of the fluorescence yields of the 193 nm and 290 nm emissions in Ar/F$_2$ mixtures have been measured as a function of Ar pressure, keeping the F$_2$ at 1 torr. The fluorescence yield of ArF* decreases rapidly from about 30% at 1 atm to about 3% at 5 atm, while the 290 nm yield decreases more slowly from about 50% at one atm to about 30% at 10 atm. The ratio of the 290 nm to the 193 nm fluorescence yield increases linearly with Ar pressure and is about

12-to-1 at 7 atmospheres. These contrasting pressure dependencies confirm the suggestion that the two emissions do not originate from a common upper level. Further, the predominance of the 290 nm emitter at high pressures suggests that it lies lower in energy than ArF^* since under high density collision dominated conditions the energy flow is normally downward in energy. At high densities the rare gas kinetics favor the rapid formation of Ar_2^*,[14] which suggests that it may be the precursor of the 290 nm emitter.

From measurements of the time decay of the two emissions, we observe that the ArF^* decay rate is as much as 10 times faster than that of the 290 nm decay; e.g., 50 MHz for ArF^* and 5 MHz for 290 nm. This observation supports the suggestion of two different radiators and that the 290 nm emitter is either formed later in the kinetic chain or has a longer radiative lifetime. Finally we have also observed the 290 nm band from mixtures of Ar and NF_3 and find the decay frequency to be even slower than in Ar/F_2 mixture.

$Ar/Kr/F_2$ Mixtures

A similar set of observations has been made on the 400-nm band in $Ar/Kr/F_2$ mixtures. This band is observed together with the 248-nm band of Kr^* in Kr/F_2 mixtures containing no Ar and therefore is identified as a $Kr_m F_n^*$ molecule. Observation of this band has also been reported from other laboratories.[15-17] The emission profile of the 400-nm band is shown in Fig. 2. The Kr pressure dependence of the fluorescence yields of each of the radiators in an $Ar/Kr/F_2$ mixture has been measured and in this case, we

observe that the 400-nm band becomes the dominant emitter as the Kr

pressure is increased above about 20 torr in a mixture of 5-atm Ar and

1-torr F_2. As in the case of 290-nm emission from Ar/F_2 mixtures, the decay

time of the 400-nm emission in the $Ar/Kr/F_2$ mixtures is much longer than

that of any of the other rare gas halide emissions (about the same as that of

Kr_2^* in the same mixture). Thus, we conclude that the 400-nm emitter is the

lower-lying electronic level to which most of the energy is flowing. Since

the total fluorescence yield is not 100%, some of the emission is being

quenched, probably by F_2. As in the case of the 290 nm band in Ar/F_2 mixtures,

the 400 nm band cannot be explained in terms of the well-established

electronic structure of the KrF molecule.[5,7,8] We conclude that neither

the 290 nm nor the 400 nm bands are emitted by a diatomic molecule, and the

next simplest species to consider are triatomics.

Structure of Rare Gas Fluoride Triatomics

In analogy with the Ar^+F^- and Kr^+F^- ionic bonds, two possible ionically

bonded triatomics, $Ar_2^+F^-$ and $Ar^+F_2^-$, (similarly for Kr) can be suggested.

Either of these excited states should lie lower in energy than the

corresponding diatomic because of the energy of the additional bond; this

is the Rg_2^+ ion bond in one case (~ 1.2 eV) and the F_2^- bond (~ 1.4 eV) in

the other case. In contrast, the ground state of Ar_2F will certainly be

repulsive due to the repulsive interaction between the Ar atoms (the Ar-F

interaction is probably very weak at the expected internuclear separations).

F-8

However, ArF_2 in the ground state should have some binding (with respect to ArF + F) due to the strong F_2 bond. The validity of these arguments depends upon the geometry assumed for the ionic upper state at its minimum. However, it is difficult to imagine any geometry of ArF_2 that will be sufficiently repulsive in the ground state to explain both the energy and bandwidth of the observed transitions. Hence, we suggest that the 290-nm emitter is Ar_2F^* and that the 400-nm emitter is Kr_2F^*. This conclusion is strengthened further by the observation of the same bands in mixtures in which the F_2 is replaced by NF_3 or other fluorine donors. Recently, observations of this 400 nm band were reported in Ar/Kr/RX mixtures using several fluorine donors, RX = NF_3, N_2F_4, F_2, SF_6, and CF_4.[17] If these species are formed by harpooning reactions in analogy with the alkali halides, it is unlikely that more than one F atom is abstracted from the fluorine donor.

Strong support for the Rg_2X model of these radiators derives from the analogous ionically bonded dialkali-halides. This analogy was used effectively in the diatomic case to estimate bond strengths of RgX^* molecules from the analogous alkali halide AX bonds. Since the Rg_2^+ and alkali dimer ions, Ar_2^+, are stable and bound with energies of 0.5 to 1.0 eV, we expect the alkali analog to the Rg_2X^* excited state to be the corresponding A_2X ground state molecule.

Unfortunately, the ground-state surfaces of these A_2X molecules are not well characterized. However, the existence of bound A_2X molecules has

been established from beam-scattering studies of A_2 with X where A_2X is observed as a long-lived intermediate complex that decays into the products $AX + A$.[18-20] It is generally accepted that the intermediate complex is formed by the crossing from a covalent to a bonding ionic surface (also known as the harpoon or electron jump model). In the single-collision case in which the total energy remains positive, the collision complex usually decays via an intersection with a second covalent surface. For example, the reaction $K_2 + Cl \rightarrow K_2^+Cl^- \rightarrow K + KCl$ is observed with a cross section of 50-100 Å; the reaction also branches to $K^* + KCl$ about equally.[19]

Several groups have investigated theoretically the structure of the A_2X surfaces using pseudo-potential techniques.[21-23] These studies demonstrated that these molecules are bound ionically, with the most stable geometry being triangular. The potential energy well depths with respect to $A + AX$ dissociation are in the range from 0.5 to 1 eV. Although the triatomic analogy to Rg_2X is not as obvious as the diatomic case, the suggestion that the Rg_2X^* will have stable ionic states $(Rg_2^+X^-)$ that are formed by a harpooning reaction of Rg_2^* with X_2 is strongly supported by the observations on the A_2X molecules. On this basis, we expect the stable geometry of Rg_2X^* to be triangular. In contrast to the alkali halide beam studies, the strongly exoergic reactions

$$Rg_2^* + X_2 \rightarrow Rg_2X^* + X$$
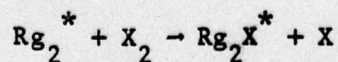
observed here are occurring in a high-density environment where multiple

collisions during the lifetime of the complex could relax it to the stable potential minimum before it radiates. We can expect that bound Rg_2X^* molecules will also be formed by the three-body reaction

$$RgX^* + 2Rg \rightarrow Rg_2X^* + Rg \quad ,$$
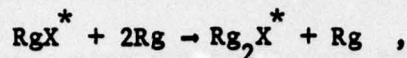
and the relative importance of these two reaction mechanisms remains to be determined. Under some excitation conditions in rare gas halogen mixtures it is expected that ion reactions such as

$$Rg_2^+ + X^- + M \rightarrow Rg_2X^* + M$$
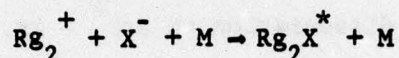
provide an alternative formation reaction.

The relevant energy levels for the ArF molecule and the postulated Ar_2F molecule are shown in Fig. 3, together with the relevant dissociation limits. This simple model assumes a triangular geometry for the excited $Ar_2^+F^-$ state with the Ar^+-Ar spacing equal to the Ar_2^+ equilibrium separation and that Ar_2F^* lies below ArF^* by just the binding energy of Ar_2. A vertical transition to the ground state ends on a repulsive state having an energy of about 1 eV due mainly to the Ar_2 repulsion at that internuclear separation (the Ar-F ground-state interaction is assumed to be small). The upper level is then determined by the 290-nm transition wavelength and lies about 1.1 eV below ArF^*. If we now assume that the slope of the ground state Ar_2F potential at R_e is equal to that of Ar_2 at the equilibrium separation of Ar_2^* and that the shape of the upper states is similar, then the bandwidth of the 290-nm band is easily scaled from the bandwidth of Ar_2^* emission at 125 nm. This scaling gives a value of 41 nm-full width at half

maximum as compared with the observed value of 52.5 nm. In the Kr_2F case, the bandwidth scaling gives 53 nm as compared with 60 nm observed. Thus both the energy levels and the bandwidth of these emissions are remarkably consistent with this simple triatomic molecular model.

The above arguments suggesting the source of the 290 nm continuum bands observed in Ar/F_2 mixtures as Ar_2F^* have recently been substantiated by a detailed ab initio calculation on the Ar_2F system.[24] This calculation confirms that Ar_2F^* is ionically bonded in a triangular geometry and is stable with respect to dissociation to $ArF^* + Ar$. The calculation also confirms that the Ar_2^+ internuclear separation in Ar_2F^* is essentially the same as its normal equilibrium distance. Thus the evidence presented here, taken together with the detailed ab initio calculations, firmly establishes the assignment of these emissions as the charge transfer transitions in Rg_2X molecules.

Other Rg_2X Molecules and Emissions

The Ar_2F and Kr_2F assignments immediately suggested the search for other members of the same class. Earlier measurements in this and other laboratories[25] on Ar/Cl_2 mixtures had yielded an unidentified background continuum upon which the $Cl_2(E-B)$ spectrum peaking at 254 nm was superimposed. That spectrum is shown at two different Cl_2 concentrations in Fig. 4. The broad continuum peaking at about 250 nm we now identify as the ionic to covalent transition from Ar_2Cl^*. The fact that the intensity of the Cl_2^* emission increases relative to the Ar_2Cl^* emission as the Cl_2 density increases suggests that Ar^* is reacting with Cl_2 before it has a

chance to form Ar_2^* or that Ar_2Cl^* reacts with Cl_2 to produce Cl_2^*. The latter reaction is exothermic by about 10^4 cm^{-1} and therefore is a reasonable possibility.

In Fig. 5 the continuum spectra obtained from excited $Ar/Kr/Cl_2$ and $Ar/Xe/Cl_2$ mixtures are shown. The Kr_2Cl^* emission is observed to peak at 325 nm and the Xe_2Cl^* emission peaks at about 450 nm. Fluorescent yield measurements have not been made on any of these triatomic rare gas chlorides, but the pressure dependence and time decay behavior is similar to that of the fluorides and there is little doubt that these identifications are correct.

In gas mixtures containing Xe and a fluorine donor, a prominent continuum band at 460 nm is observed that has characteristics very different from the emissions described above. This band has also been observed in other laboratories[5] but the identity of its emitter has remained elusive. The band is prominent and has the same wavelength and bandwidth in $Ne/Xe/NF_3$, $Ar/Xe/NF_3$ and $Kr/Xe/NF_3$ mixtures, but in Xe/NF_3 it is replaced by a much broader continuum extending from 250 nm to 600 nm. These features are unchanged when F_2 is substituted for NF_3. In the triple mixtures the 460 nm band intensity is linear with host gas density, but peaks at about 5 torr of Xe and decreases with increasing Xe above that. In contrast, the 351 nm XeF band increases with host gas density at low pressures but saturates at high pressures. The decay rate of the 460 nm band is fast but always somewhat slower than the 350 nm XeF emission. Thus the characteristics of the 460 nm band mixtures containing Xe and F_2 are distinctly different from the other triatomic

rare gas halides, which suggests that this band is not due to Xe_2F. The
rapid quenching rate of both the 351 and 460 nm emissions by Xe suggests
that Xe_2F, if it is formed, predissociates to ground state products. It is
possible that the 460 nm band is due to the $C\frac{3}{2}$-$A\frac{3}{2}$ transition in XeF (see
Ref. 9 where these states are identified for KrF). It is likely that the $B\frac{1}{2}$
and $C\frac{3}{2}$ states of XeF lie very close to each other as the calculations
of Hay and Dunning[9] indicate they do in KrF. Collisional mixing of these two
states may be important and could lead to the fast decay rate although the
C-A transition is expected to have a longer radiative lifetime than the B-X
transition.

In $Ar/Xe/I_2$ mixtures of 1500T/34T/0.3T a continuum emission band
is observed at 320 nm together with the established emissions at 342 nm
(I_2^*) and 254 nm (XeI^*). Brau and Ewing observed in a Xe/I_2 mixture a much
broader double humped continuum band with peaks at ~ 320 nm and 375 nm.
They interpreted these transitions as $XeI(^2\Sigma_{\frac{1}{2}} \rightarrow {}^2\Pi_{\frac{1}{2}}, {}^2\Pi_{\frac{3}{2}})$ but this assign-
ment now seems unlikely since under some conditions we observe the 254 and
320 nm bands without the 375 nm band. It is possible that the 375 nm band
is Xe_2I and the 320 nm emission is the red band of XeI. A more thorough
study of these emissions is needed to clarify the identifications in the
system.

The data obtained on the Rg_2X^* transitions are summarized in Table I.
The measured transition energies, $\Delta E(Rg_2X)$, listed in column 1 are used

with known energies, T_e(RgX), of the corresponding diatomic RgX* and the

dissociation energy, D_e(Rg$_2^+$), of the diatomic rare gas ion to estimate

the ground state dissociation energy, E_g, of the triatomic. This estimate

is based on the simple model discussed for Ar$_2$F in which it is assumed that

the excited level of the triatomic lies below the diatomic by just the

binding energy of the diatomic ion. This assumption is expressed most

simply in the following equation:

$$T_e(RgX) - D_e(Rg_2^+) = \Delta E(Rg_2X) + E_g(Rg_2X) \quad . \qquad (1)$$

Obviously, the model presented here is an inadequate description

of the energy levels of these triatomic molecules and serves only as

an initial means of identifying relationships. On the other hand,

ab initio calculations of these triatomics require inordinate efforts on

the fastest computers. However, Huestis et al.[26] have pointed out that

very satisfactory Rg$_2$X energy surfaces can be generated using the diatomics-

in-molecules model in which only the diatomic potentials are required

to be known accurately. Since most diatomic potentials can be accurately

generated with modern computational facilities, it appears that reasonable

triatomic surfaces can also be generated. Schlotter and Huestis[27]

have recently reported such calculations for Ne$_2$F, Ar$_2$F, Kr$_2$F and Kr$_2$Cl.

The calculated transition energies agree well with the measured values in

the three cases where comparisons are possible. These calculations indicate

that the potential minima of the ionic state of Rg$_2$X* lie higher than indicated

by equation (1), i.e. they lie below the RgX* level by about one half of the

Rg$_2^+$ binding energy.

Table I. $\Delta E(Rg_2X)$ triatomic transition energies, $T_e(RgX)$ energy level of RgX, $D_e(Rg_2^+)$ rare gas ion dissociation energy, and $E_g(Rg_2X)$ ground state energy of Rg_2X at the equilibrium coordinates of its excited state. T_e values were obtained from references given in the text. $D_e(Rg_2^+)$ values were taken from Ref. 28 and Ref. 29.

	$\Delta E(Rg_2X)$ cm^{-1}	$T_e(RgX)$ cm^{-1}	$D_e(Rg_2^+)$ cm^{-1}	$E_g(Rg_2X)$ cm^{-1}
Xe_2Cl	22200 450 nm	32470	8065	2205
Kr_2Cl	30770 325 nm	45050	9760	4520
Ar_2Cl	40650 246 nm	57140	10080	6410
Kr_2F	25000 400 nm	40320	8760	5565
Ar_2F	34246 292 nm	51815	10080	7490

REFERENCES

1. J. E. Velazco and D. W. Setser, IEEE J. of Quant. Elect. QE-11, 708 (1975).

2. J. E. Velazco and D. W. Setser, J. Chem. Phys. 62, 1990 (1975).

3. M. F. Golde and B. A. Thrush, Chem. Phys. Lett. 29, 486 (1974).

4. J. J. Ewing and C. A. Brau, Phys. Rev. A12, 129 (1975).

5. C. A. Brau and J. J. Ewing, J. Chem. Phys. 63, 4640 (1975).

6. J. Tellinghuisen, J. M. Hoffman, G. C. Tisone, and A. K. Hays, J. Chem. Phys. 64, 2484 (1976).

7. J. Tellinghuisen, A. K. Hays, J. M. Hoffman, and G. C. Tisone, J. Chem. Phys. 65, 4473 (1976).

8. T. H. Dunning and P. J. Hay, Appl. Phys. Lett. 28, 649 (1976).

9. P. J. Hay and T. H. Dunning, J. Chem. Phys. 66, 1306 (1977).

10. H. H. Nakano, R. M. Hill, D. C. Lorents, D. L. Huestis, and M. V. McCusker, Report No. MP 76-99, Stanford Research Institute, Menlo Park, California (December 1976).

11. D. C. Lorents, R. M. Hill, D. L. Huestis, M. V. McCusker, and H. H. Nakano, in Electronic Transition Lasers II, L. E. Wilson and J. I. Steinfeld, editors (MIT Press, 1977).

12. H. H. Michels and R. H. Hobbs, in Electronic Transition Lasers II, L. E. Wilson and J. I. Steinfeld, editors (MIT Press, 1977).

13. P. J. Hay and T. H. Dunning, Jr., in Electronic Transition Lasers II, L. E. Wilson and J. I. Steinfeld, editors (MIT Press, 1977).

14. D. C. Lorents, Physica 82C, 19 (1976).

15. T. N. Rescigno and N. W. Winter, in Electronic Transition Lasers II, L. E. Wilson and J. I. Steinfeld, editors (MIT Press, 1977).

16. J. A. Mangano, J. H. Jacob, M. Rokni and A. Hawryluk, Appl. Phys. Lett. 31, 27 (1977).

17. J. C. Wyss, J. B. West, C. E. Webb, and D. C. Richman, Bull. Am. Phys. Soc. 21, 1288 (1976).

18. P. B. Foreman, G. M. Kendall, and R. Grice, Mol. Phys. 23, 127 (1972).

19. W. S. Struve, J. R. Krenos, D. L. McFadden, and D. R. Herschbach, J. Chem. Phys. 65, 4473 (1976).

20. J. C. Whitehead, D. R. Hardin and R. Grice, Mol. Phys. 25, 515 (1973).

21. S. M. Lin, J. G. Wharton, and R. Grice, Mol. Phys. 26, 317 (1973).

22. A. C. Roach and M. S. Child, Mol. Phys. 14, 1 (1968).

23. W. S. Struve, Mol. Phys. 25, 777 (1973).

24. W. R. Wadt and P. J. Hay, Appl. Phys. Lett. 30, 573 (1977).

25. C. H. Chen and M. G. Payne, Appl. Phys. Lett. 28, 219 (1976).

26. D. L. Huestis, D. C. Lorents, N. E. Schlotter, R. M. Hill, M. V. McCusker and H. H. Nakano, 32nd Symposium on Molecular Spectroscopy, Columbus, OH 13-17 June 1977.

27. N. E. Schlotter and D. L. Huestis, 30th Annual Gaseous Electronics Conference, Palo Alto, CA, October 1977.

28. D. C. Lorents, R. E. Olson, and G. M. Conklin, Chem. Phys. Lett. 20, 589 (1973).

29. H. V. Mittmann and H. P. Weise, Z. Naturforsch 29a, 400 (1974).
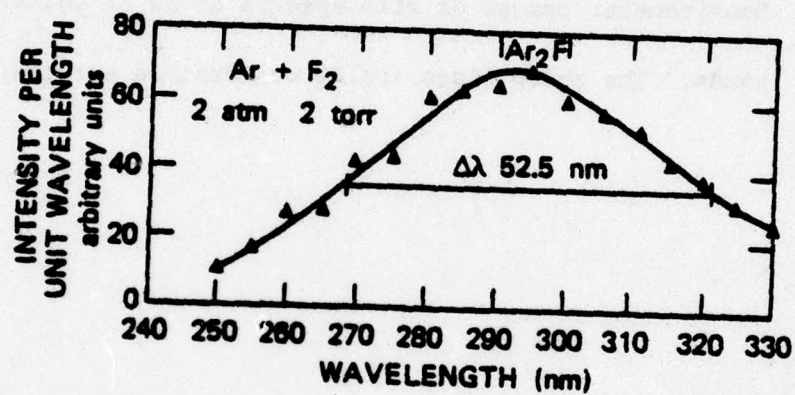
FIGURE CAPTIONS

Figure 1. A spectrometer scan of the continuum emission of an e-beam excited Ar/F_2 mixture.

Figure 2. Spectrometer scan of the continuum emission from an excited Kr/F_2 mixture.
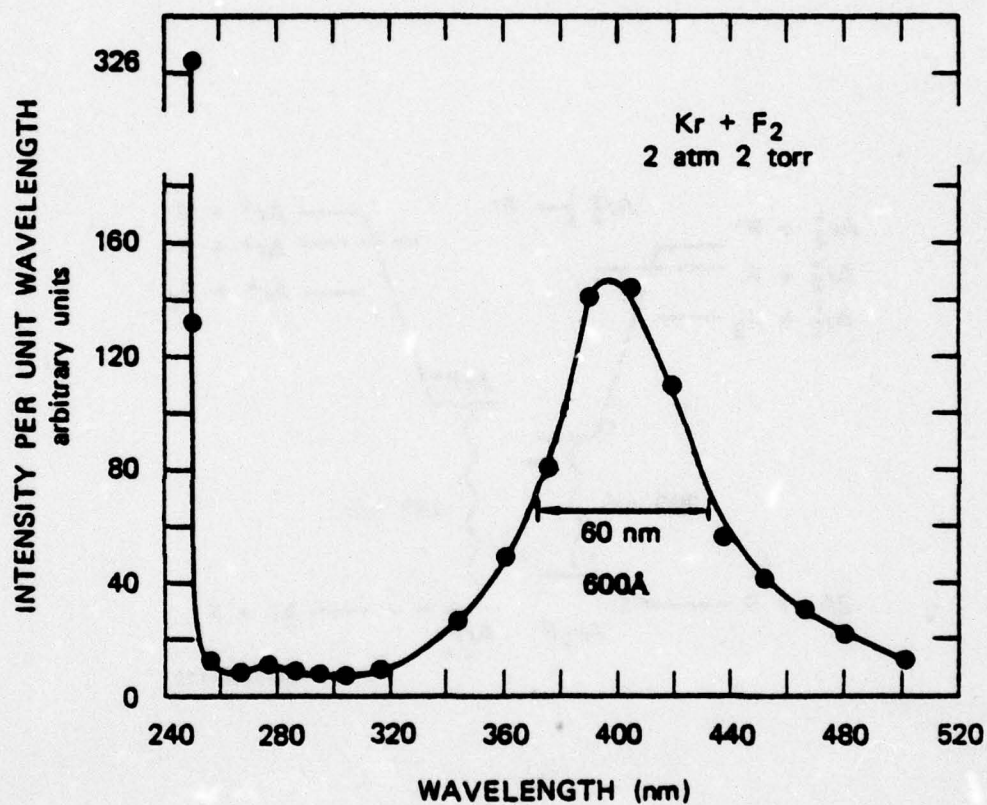
Figure 3. Relevant ArF and Ar_2F energy levels.

Figure 4. Photographic spectra observed in Ar/Cl_2 mixtures.

Figure 5. Densitometer traces of film spectra of Xe_2Cl and Kr_2Cl bands. The sharp lines are Hg calibration spectra.

Figure 1. A spectrometer scan
of the continuum emission of an
e-beam excited-Ar/F₂ mixture.

Figure 2. Spectrometer scan of the continuum emission from an excited Kr/F_2 mixture.
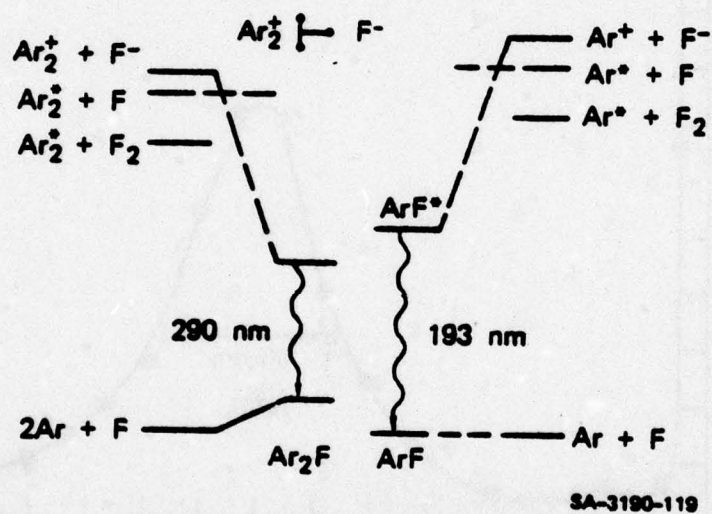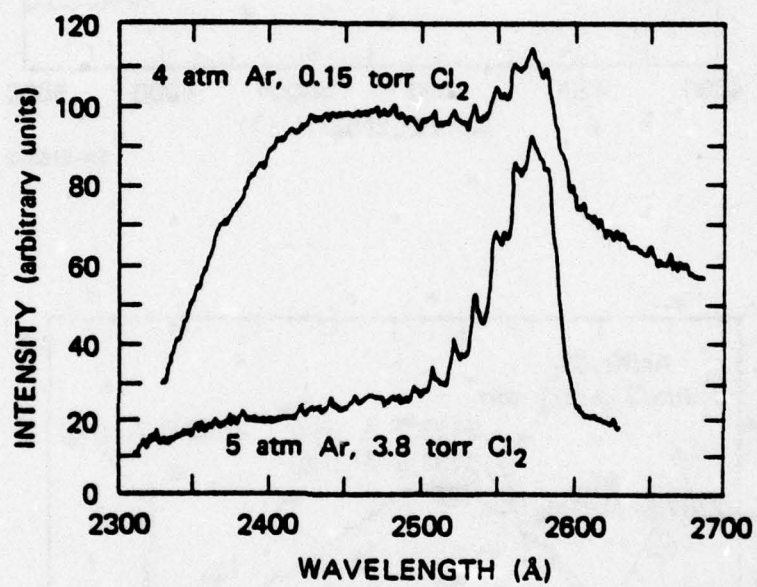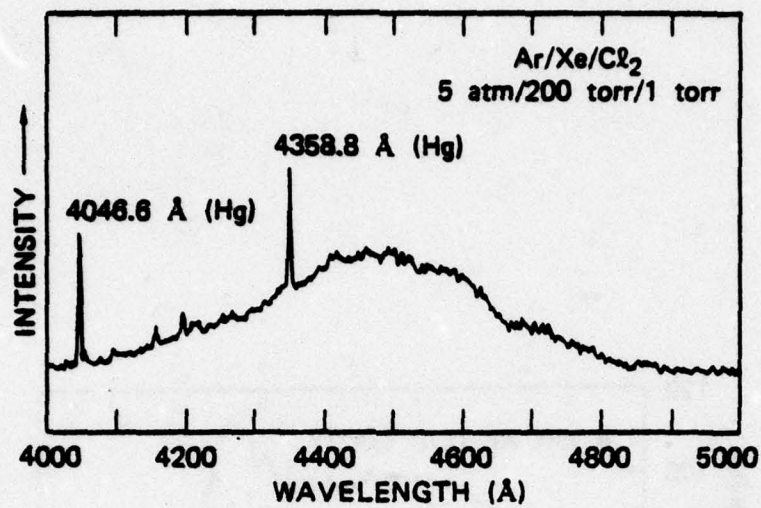
SA-3190-113

F-21

SA-3190-119

Figure 3. Relevant ArF and Ar$_2$F energy levels.

SA-3190-71

Figure 4. Photographic spectra observed in Ar/Cl$_2$ mixtures.

Ar/Xe/Cl$_2$
5 atm/200 torr/1 torr

4358.8 Å (Hg)

4046.6 Å (Hg)

INTENSITY →

4000 4200 4400 4600 4800 5000
WAVELENGTH (Å)

SA-6158-2

Ar/Kr/Cl$_2$
3 atm/3 atm/1 torr

3125.7 Å (Hg)   3650.5 Å (Hg)
3131.5 Å (Hg)

2967.5 Å (Hg)

INTENSITY →

2800 3000 3200 3400 3600 3800
WAVELENGTH (Å)
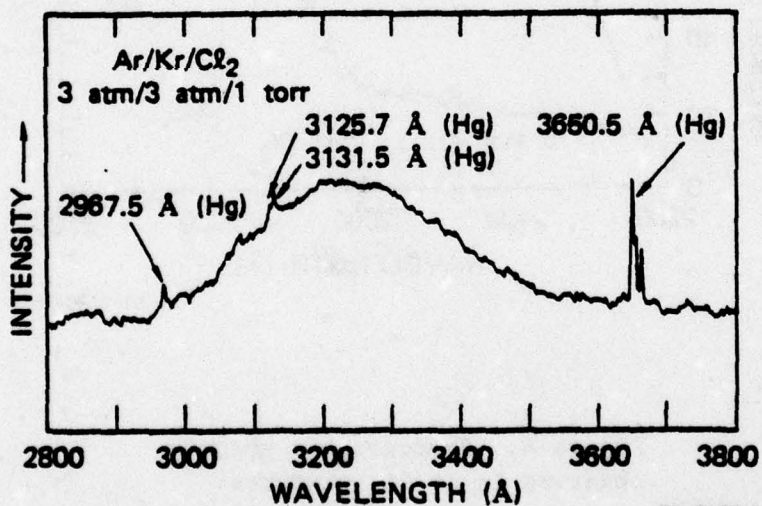
SA-6158-1

Figure 5. Densitometer traces of
film spectra of Xe$_2$Cl and Kr$_2$Cl
bands. The sharp lines are Hg
calibration spectra.

F-24

Appendix G

DIATOMICS-IN-MOLECULES POTENTIAL SURFACES
FOR THE TRIATOMIC RARE GAS HALIDES: Rg_2X

DIATOMICS-IN-MOLECULES POTENTIAL SURFACES

FOR THE TRIATOMIC RARE GAS HALIDES: Rg_2X [†]

D. L. Huestis and N. E. Schlotter
Molecular Physics Laboratory
SRI International
Menlo Park, CA 94025

and

Department of Chemistry
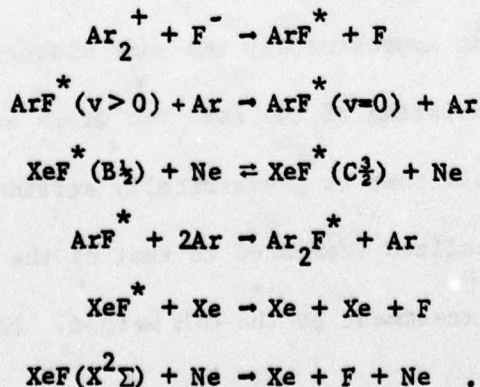Stanford University
Stanford, CA 94305

ABSTRACT

Potential energy surfaces have been calculated for the lowest nine

electronic states of Ne_2F, Ar_2F, Kr_2F, and Kr_2Cl, including spin orbit

coupling. The Diatomics-In-Molecules (DIM) method used takes advantage of the

accurate _ab initio_ potential curves now becoming available for the

constituent diatomics. In the case of Ar_2F, the DIM results are in close

agreement with more elaborate calculations. DIM calculations, for a

minimum of effort, supply the potential energy surfaces needed for

calculating absorption and emission spectra as well as molecular

dynamics.

MP 77-121

INTRODUCTION

In the course of detailed spectroscopic and kinetic investigations of the rare gas halide lasers (e.g., KrF), the triatomic rare gas halide excimers (Ar_2F, Kr_2Cl, etc.) were identified[1-6] and their important kinetic roles were characterized.[1,4-7] Recently, sophisticated calculations have been reported of a few of the potential surfaces at several geometries for Ne_2F,[8] Ar_2F,[9-11] and Kr_2F.[11] We have adapted the Diatomics-in-Molecules (DIM) method and used it to calculate the potential energy surfaces for the lowest nine electronic states of Ne_2F, Ar_2F, Kr_2F, and Kr_2Cl including spin-orbit coupling. This work will be extended to the whole class of triatomic rare gas halides using the accurate diatomic potential curves that are becoming available. Some preliminary results have been reported previously.[12,13]

The DIM calculations are inexpensive and should be of sufficient accuracy to calculate emission and absorption spectra along with radiative lifetimes and absorption cross sections (using the diatomic transition moments). In addition, these surfaces are needed for chemical dynamics calculations of many important reactions, such as

$$Ar_2^+ + F^- \rightarrow ArF^* + F$$

$$ArF^*(v > 0) + Ar \rightarrow ArF^*(v=0) + Ar$$

$$XeF^*(B\tfrac{1}{2}) + Ne \rightleftharpoons XeF^*(C\tfrac{3}{2}) + Ne$$

$$ArF^* + 2Ar \rightarrow Ar_2F^* + Ar$$

$$XeF^* + Xe \rightarrow Xe + Xe + F$$

$$XeF(X^2\Sigma) + Ne \rightarrow Xe + F + Ne \quad .$$

THE DIM WAVEFUNCTION AND HAMILTONIAN

Diatomics-in-Molecules (DIM) is a method developed by Ellison[14] for

obtaining potential surfaces of the ground and excited states of polyatomic

systems from diatomic potentials. The increasing availability of accurate

diatomic potentials has led to wide application of DIM.[15] In spite of

substantial recent progress that has been made, sophisticated ab initio

calculation of polyatomic potential surfaces is discouraged by the necessarily

substantial investment of computer time required. DIM potential surfaces are

now being used to study the dynamics of a variety of chemical systems.[15]

DIM calculations are based on the concept of partitioning the polyatomic

molecule into the possible diatomic fragments. This procedure is familiar

to organic chemists as the electron pair bond. The binding in methane would

be expressed in terms of four C-H bonds and six H-H repulsions. The quantita-

tive usefulness of DIM arises from assumptions about the extent to which the

atomic electron distributions are distorted by molecule formation. The

essential argument is that the distortions arise mostly from nearest neighbor

interactions, and that approximately the same distortion would occur in the

diatomic molecule consisting of the same two atoms at the same internuclear

separation. A molecule that is geometrically strained or whose electron

density is very delocalized (compared to that of the isolated atoms) may be

a poor candidate for treatment by the DIM method. In the triatomic rare gas

halides these problems should not be serious. The binding interactions are coulombic in origin, while the repulsions arise from simple electron cloud overlap. In particular, Kim and Gordon[17] have noted that closed shell systems show little atomic distortion.

In application of the DIM method, the polyatomic wavefunction is written as a linear combination of valence-bond (VB) wavefunctions (also called VB structures). Each of these VB structures is analyzed separately in terms of atomic and diatomic wavefunctions. A hamiltonian matrix is constructed over the VB basis using the atomic energies and diatomic potential curves, and is diagonalized to yield the polyatomic potential surfaces.

To describe the VB structures in Ar_2F, we consider the states that arise from bringing together two argon atoms and one fluorine atom, all in their ground electronic states, as shown in Fig. 1. Each of the argon atoms has the closed shell configuration $1s^2 2s^2 sp^6 3s^2 3p^6$. The fluorine atom has the configuration $1s^2 2s^2 2p^5$, where the half-filled p-orbital may point along the x-, y-, or z-axis. Consider the valence bound wavefunction for the case where the fluorine $2p_x$ orbital is half-filled. We call this wavefunction Ψ_{xc}. It can be written in the three equivalent forms shown below.

$$\Psi_{xc} = \Psi_1 = \left| \left| Ar_b \right| \left| Ar_a F_c(x) \right| \right| \rightarrow$$

$$= \Psi_2 = \left| \left| Ar_a \right| \left| Ar_b F_c(x) \right| \right| \rightarrow$$

$$= \Psi_3 = \left| \left| Ar_a Ar_b \right| \left| F_c(x) \right| \right| \rightarrow$$

The connecting lines illustrate pictorially the various diatomic bonds that are emphasized in each representation of the valance bond structure. Corresponding to the bonds, an additional antisymmetrization of the product of the

G-5

atomic wavefunctions emphasizes the diatomic fragment under consideration (Ar_2 in the case of Ψ_3). The fact that the three representations (Ψ_1, Ψ_2 Ψ_3) are mathematically identical allows one to choose the representation that is most convenient for evaluating matrix elements.

A similar exact partitioning applies to the polyatomic hamiltonian (in the Born-Oppenheimer approximation). The standard representation of the hamiltonian is (in atomic units)

$$H = \sum_i -\tfrac{1}{2} \nabla_i^2 + \sum_{i,q} - \frac{Z_q}{r_{iq}} + \sum_{i<j} \frac{1}{r_{ij}} + \sum_{p<q} \frac{Z_p Z_q}{R_{pq}}$$

where i and j refer to electrons and p and q refer to the nuclei. Such a hamiltonian can be written in the general form

$$H = \sum_p H_p + \sum_{p<q} V_{pq}$$

where H_p contains the kinetic energy operators and all potential energy terms depending exclusively on the coordinates of atom p and its associated electrons. Similarly, V_{pq} contains all two-body interactions of nucleus p and its associated electrons with nucleus q and its associated electrons. Alternately, the hamiltonian can be written in the form[14]

$$H = \sum_{p<q} H_{pq} - (N-2) \sum_p H_p \quad ,$$

where H_{pq} is the diatomic hamiltonian

$$H_{pq} = H_p + H_q + V_{pq} \quad ,$$

and N is the number of atoms in the polyatomic.

If we arbitrarily assign electrons 1-18 to Ar_a, electrons 19-36 to

Ar_b, and electrons 37-45 to F_c (as suggested by representation Ψ_3 above), then we can write the diatomic hamiltonian for the Ar_2 diatomic fragment as:

$$H_{ab} = H_{Ar_2} = \sum_{i=1}^{36} \left\{ -\tfrac{1}{2} \nabla_i^2 - \frac{Z_a}{r_{ia}} - \frac{Z_b}{r_{ib}} + \sum_{j=i+1}^{36} \frac{1}{r_{ij}} \right\} + \frac{Z_a Z_b}{R_{ab}} \quad .$$

Similar reasoning and a change of indices can be used to obtain the ArF diatomic fragment hamiltonians.

The DIM wavefunctions for the three covalent potential surfaces for Ar_2F are to be written as a linear combination of the VB structures:

$$\Psi_{DIM}^i = \alpha_x^i \Psi_{xc} + \alpha_y^i \Psi_{yc} + \alpha_z^i \Psi_{zc} \quad .$$

One needs then to evaluate matrix elements of the form

$$< \Psi_{ic} |H| \Psi_{jc} > \qquad i,j = x,y,z$$

which requires that we operate the pieces of the partitioned hamiltonian on Ψ_{xc}; for example,

$$H\Psi_{xc} = H_{ab}\Psi_3 + H_{bc}\Psi_2 + H_{ac}\Psi_1 - H_a\Psi_2 - H_b\Psi_1 - H_c\Psi_3.$$

For $H_{ab}\Psi_3$ we recognize the Ar_2 wavefunction ($\varphi^{ab} = |Ar_a Ar_b|$) as an eigenfunction of the Ar_2 hamiltonian, with eigenvalue $E^{ab}(^1\Sigma_g^+)R_3$. To operate H_{ac} on Ψ_1, we must project the fluorine $2p_x$ wavefunction onto the R_1 axis, which yields

$$\varphi_x^{ac} = - \sin\theta_{13} \varphi_1{}^{ac}{}_2{}_{1\Sigma^+} + - \cos\theta_{13} \varphi_1{}^{ac}{}_2{}_{1\Pi} \quad .$$

Correspondingly, Ψ_2 must be projected onto the R_2 axis. Taking the energies of the atomic states as zero (they are in their ground states), we obtain

$$\langle \Psi_{xc} | H | \Psi_{xc} \rangle = \langle \Psi_3 | H_{ab} | \Psi_3 \rangle + \langle \Psi_2 | H_{bc} | \Psi_2 \rangle + \langle \Psi_1 | H_{ac} | \Psi_1 \langle$$

$$= [E^{ab}(^1\Sigma_g{}^+)]_{R_3} + [\sin^2\theta_{23} E^{bc}(1\,^2\Sigma^+) + \cos^2\theta_{23} E^{bc}(1\,^2\Pi)]_{R_2}$$

$$+ [\sin^2\theta_{13} E^{ac}(1\,^2\Sigma^+) + \cos^2\theta_{13} E^{ac}(1\,^2\Pi)]_{R_1}$$

All the other diagonal and off-diagonal matrix elements between Ψ_{xc}, Ψ_{yc}, and Ψ_{zc} can similarly be evaluated in terms of diatomic energies and trigonometric factors. These are shown in Table 1.

We have glossed over the conceptual difficulties imposed by the polyatomic antisymmetrizers and the nonsymmetrized diatomic hamiltonian (i.e., only electrons 1-36 appear in H_{ab}). However, Ellison[14] and Tully[16] have dealt with the problems at some length. In Ar_2F and $Ar_2^+F^-$, with only one open shell, it can be shown, by laborious manipulations, that electron numbering and antisymmetrization need not be considered.

The ionic states of Ar_2F are slightly more complicated. There are 6 VB basis functions. These are $Ar_a^+Ar_bF_c^-$ and $Ar_aAr_b^+F_c^-$, with the wave function for the open shell argon ion having three possible orientations: x, y, and z. The constituent diatomic molecules are Ar_2^+, Ar^+F^-, and ArF^-. Evaluation of the matrix elements is complicated by the fact that the Ar_2^+ molecular ion wavefunction must be expressed in terms of linear combinations of the atomic ion wavefunctions, or conversely:

$$\varphi_{za}^{ab} = \sqrt{\tfrac{1}{2}}\, \varphi_{2\Sigma_u^+}^{ab} + \sqrt{\tfrac{1}{2}}\, \varphi_{2\Sigma_g^+}^{ab} \ .$$

The partitioning of the hamiltonian is also more complicated, since there are two equivalent partitionings:

$$H = H_{(ab)^+} + H_{a^+c^-} + H_{bc^-} - H_{a^+} - H_b - H_{c^-}$$

$$= H_{(ab)^+} + H_{ac^-} + H_{b^+c^-} - H_a - H_{b^+} - H_{c^-} \; .$$

These two partitionings   correspond to two schemes of numbering the electrons and assigning them to atoms, depending upon which of the two argon atoms is chosen to be ionized. The matrix elements obtained are shown in Table 2.

INCLUSION OF SPIN-ORBIT COUPLING

Although inclusion of the spin-orbit interaction is not crucial to the understanding of the electronic structure of Ne_2F and Ar_2F, the spin-orbit effects become substantial for the heavier triatomic rare gas halides. Recently, it has become common to take high quality ab initio potential curves for diatomics and include spin-orbit interactions in a semiempirical fashion.[18-20] For nonlinear polyatomic molecules, this should not be possible without ambiguity, since the x, y, and z components of the wavefunction are inextricably mixed by the electro-static interactions. The DIM method, on the other hand, deals explicitly only with the atomic and diatomic fragments. Hence, the polyatomic spin-orbit matrix elements can be expressed in terms of those of the constituent atoms and diatoms.

Tully[21]   has treated the DIM spin-orbit matrix elements in a general formalism based on angular momentum coupling. It will be useful here to consider the specific case of a planar molecule. It is a

particularly interesting feature (already known from double-point group theory) that even in C_{2v} geometries, for doublet states, all electrostatic symmetry is broken and all states interact with each other; therefore, the states cannot be distinguished by symmetry type.

Consider the coordinate system in which atom A is at the origin and atoms B and C (and any others) are in the x-z plane. A singly occupied p-orbital on atom A has an electrostatic energy E_x, E_y, and E_z if it points in the x, y, or z directions, respectively, with an off-diagonal matrix element E_{xz}. We could choose to use the complex basis functions instead:

$$p_+ = \sqrt{\tfrac{1}{2}}(x + iy), \quad p_- = \sqrt{\tfrac{1}{2}}(-x + iy), \quad \text{and} \quad p_o = z \, ,$$

but we can easily transform from one basis to the other. Our choice of coordinate systems allows us to select iy as the out-of-plane basis function with no change in the electrostatic matrix elements. Our basis set is therefore $x\alpha$, $x\beta$, $iy\alpha$, $iy\beta$, $z\alpha$, and $z\beta$. The spin orbit coupling matrix elements are calculated in the standard fashion;[22] for example,

$$< iy\alpha \left| H_{so} \right| z\beta > = \zeta < iy\alpha \left| L \cdot S \right| z\beta > = -\zeta/2$$

using for ζ the value obtained from fitting the spin-orbit splittings in the separated atoms.

The 6 x 6 real hamiltonian matrix so obtained is given in Table 3. Note that matrix elements connect all six basis functions. In an attempt to find some residual manifestation of the planar symmetry of the molecule, we are lead to examine the behavior of each basis function with respect to reflection

in the xz plane. Using the relation $\sigma_{xz} = C_2(y) \cdot i$ we find that
$\sigma_{xz} \cdot \alpha = \beta$ and $\sigma_{xz} \cdot \beta = -\alpha$. This leads to a partitioning of the basis
functions into two classes:

$$\sigma_{xz} \cdot \varphi = +i\varphi : \varphi = \sqrt{\tfrac{1}{2}}x(\alpha-i\beta), \ \sqrt{\tfrac{1}{2}}y(i\alpha-\beta), \ \sqrt{\tfrac{1}{2}}z(\alpha-i\beta)$$

$$\sigma_{xz} \cdot \varphi = -i\varphi : \varphi = \sqrt{\tfrac{1}{2}}x(\alpha+i\beta), \ \sqrt{\tfrac{1}{2}}y(i\alpha+\beta), \ \sqrt{\tfrac{1}{2}}z(\alpha-i\beta)$$

If the electrostatic and spin-orbit matrix elements are expressed in this
new basis, we obtain two identical 3 x 3 matrices, which are shown in
Table 4. The identical form of the two complex (but hermitian) hamiltonians
proves that each root of the 6 x 6 spin-orbit matrix must be repeated (as
we know to be the case to be for diatomics), and that a reflection plane
can be used to divide the states into two degenerate classes. We will use the
real 6 x 6 matrix for programming simplicity.

In the ionic states of the Rg_2X triatomics, either of the rare gas
atoms can be chosen to be ionized. This means that we must construct
a spin-orbit hamiltonian for each independently, and then evaluate the
interatom electrostatic matrix elements (as shown in Table 2). These are
combined to yield a 12 x 12 real matrix or a 6 x 6 complex matrix.

RESULTS

The diatomic potentials were obtained from the references indicated
in Table 5. We did not make an exhaustive comparison of the various
potentials when they were available from more than one source. We note,
however, that the unmodified electron-gas calculations tend to underestimate
the repulsion, whereas the Thomas-Fermi-Dirac method overestimates it. For

use in construction of the DIM hamiltonian, these potential curves were interpolated using cubic splines in reciprocal powers of the internuclear distance. The calculations were performed on a PDP 11/40,[†] and took approximately 5 seconds per point; the majority of this time was used to diagonalize the 12 x 12 hamiltonian matrix for the ionic excited states with spin-orbit coupling.

Figure 2 shows a comparison of our DIM calculations and the ab initio (POL-CI) calculations of Wadt and Hay[9] for the ionic states of Ar_2F in the C_{2v} geometry without spin-orbit coupling. The two methods agree to better than 0.15 eV at each point, or within the accuracy claimed for these extensive ab initio calculations. No calibrations or ad hoc corrections have been used in the DIM calculations. Our calculations confirm the previous characterizations[2,3,9] of the excited states of the triatomic rare gas halides as coulombic complexes of the rare gas molecular ion (Rg_2^+) with the halide atomic ion (X^-).

Figure 3 shows a contour plot of the lowest ionic potential surface $2\,^2B_2$ of Ar_2F. In this case, the one ArF internuclear distance is kept constant. and the second argon is moved in the xz plane. The essentially equilateral triangular nature of the molecule is revealed, and there is some evidence for a secondary minimum in the linear configuration corresponding to $ArAr^+F^-$.

Inclusion of spin-orbit coupling in the calculation gives the Ar_2F potential surfaces shown in Figs. 4 and 5. Because the spin-orbit coupling in Ar^+ is small, the surfaces with and without spin orbit are similar in appearance. For

example, compare the $4^2\Gamma$ curve shown in Fig. 5 with a cut at $Z = -2$ through the contour graph shown in Fig. 3. The spin-orbit interaction does contribute, however, to the avoided crossing of the $4^2\Gamma$ and $5^2\Gamma$ potential surfaces, which is barely visible in Fig. 5 near $R = 6\ a_o$.

Somewhat larger spin-orbit effects are shown in Kr_2F (Fig. 6) and Kr_2Cl (Fig. 7). Also evident is the substantially smaller size of F^- compared to Cl^-, leading to a deeper binding and a longer predicted emission wavelength in Kr_2F.

Table 6 summarizes our DIM potential surface calculations. In each case, the Rg_2 distance is quite close to the bond length calculated for the isolated molecular ion Rg_2^+. Note especially the comparison of Kr_2F with Kr_2Cl. Similarly, the RgX distances are close to the values for the isolated diatomic. These observations tend to confirm the assumption that distortion of the electron density is not severe, and support the appropriateness of DIM as a calculational technique. The trend in the binding energies of Rg_2X^* relative to RgX^* is probably not significant and is within the differences in the calculational techniques used to calculate the diatomic potentials. We note, however, that these binding energies are all substantially less than the Rg_2^+ bond strength, which might have been associated with the formation of $Rg_2^+X^-$ from $Rg + Rg^+X^-$. The transition wavelengths listed correspond to vertical transitions from the minimum in the $4^2\Gamma$ excited potential surface. All three transitions are allowed by spin-orbit coupling, but their relative strengths are yet to be calculated. The vibrational bandwidths should be substantial due to the repulsive nature of the lower surface. The agreement of the wavelengths with the available experimental values is gratifying.

G-13

FUTURE APPLICATIONS

We are now in the process of evaluating the transition moments between the various DIM potential surfaces, using the diatomic transition moments. The dipole transition operator can be partitioned in a fashion similar to that used for the hamiltonian,[16] although special care must be used to treat consistently the relative phases of the diatomic wavefunctions. The economy of the DIM calculations should allow a complete treatment of the integration over nuclear coordinates that would be intolerably expensive on ab initio potential surfaces. We are especially interested in the UV absorption cross sections, corresponding to transitions $4^2\Gamma \rightarrow 9^2\Gamma$ potential surfaces shown in Figs. 4-7. These absorptions may play an important role in the rare gas halide lasers.

Emissions attributable to Xe_2F are yet to be observed.[3] There is a strong possibility that the lowest ionic state of Xe_2F is unstable and that the quenching of XeF^* by Xe proceeds through a potential surface crossing to the highest of the repulsive covalent potential surfaces. The two potential surfaces involved are the $3^2\Gamma$ covalent and $4^2\Gamma$ ionic states shown in Fig. 6 for Kr_2F. In Xe_2F, the $4^2\Gamma$ potential surface should lie more than 1 eV lower than in Kr_2F, due to the lower ionization potential of xenon. Calculations of the Xe_2F potential surfaces, now in progress, should help to clarify this issue.

One of the most curious aspects of the spectroscopy and kinetics of the XeF laser is the role played by the state emitting the broad band near 460 nm. It now appears likely that the 460 nm emission arises from the $XeF^*(C\frac{3}{2})$ level, which is calculated[24] to lie very close to the upper laser level $XeF^*(B\frac{1}{2})$, radiating to the repulsive $XeF(A\frac{3}{2})$ level. The

strength of the 460-nm emissions suggest that collisional mixing

$$XeF^*(B\tfrac{1}{2}) + Ne \rightleftharpoons XeF^*(C\tfrac{3}{2}) + Ne$$
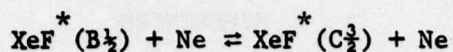
must be important. We plan to construct potential surfaces for the mixed

triatomic rare gas halides such as NeXeF to address this and other

important issues.

In conclusion, we emphasize that the Diatomics-in-Molecules method offers a

convenient, economical, and accurate method of calculating potential

surfaces for use in understanding a variety of kinetic and radiative

processes.

REFERENCES

1. D. C. Lorents, R. M. Hill, D. L. Huestis, M. V. McCusker, and H. H. Nakano, Third Summer Colloquium on Electronic Transition Lasers, Snowmass-in-Aspen, CO, September, 1976. Published in _Electronic Transition Lasers II_, L. F. Wilson, S. Suchard, and J. I. Steinfeld, Eds., MIT Press, Cambridge 1977.

2. H. H. Nakano, R. M. Hill, D. C. Lorents, D. L. Huestis, and M. V. McCusker, Report No. MP 76-99, Stanford Research Institute, Menlo Park, California (December 1976).

3. D. C. Lorents, D. L. Huestis, M. V. McCusker, H. H. Nakano and R. M. Hill, J. Chem. Phys., in press.

4. J. A. Mangano, J. H. Jacob, M. Rokni and A. Hawryluk, Appl. Phys. Lett. $\underline{31}$, 26 (1977).

5. M. Rokni, J. H. Jacob, J. A. Mangano, and R. Brochu, Appl. Phys. Lett. $\underline{30}$, 458 (1977).

6. N. G. Basov, V. A. Danilychev, V. A. Dolgikh, O. M. Kerimov, V. S. Lebedev and A. G. Molchanov, Pis'ma Zh. Eksp. Teor. Fix. $\underline{26}$, 20 (1977).

7. A. M. Hawryluk, J. A. Mangano and J. H. Jacob, Appl. Phys. Lett. $\underline{31}$, 164 (1977).

8. C. F. Bender and N. W. Winter, 32nd Symposium on Molecular Spectroscopy, Columbus, Ohio, June 1977.

9. W. R. Wadt and P. J. Hay, Appl. Phys. Lett. $\underline{30}$, 573 (1977).

10. H. H. Michels, R. H. Hobbs, and L. A. Wright, Chem. Phys. Lett. $\underline{48}$, 158 (1977).

11. W. R. Wadt and P. J. Hay, submitted for publication.

12. D. L. Huestis, D. C. Lorents, N. E. Schlotter, R. M. Hill, M. V. McCusker, and H. H. Nakano, 32nd Symposium on Molecular Spectroscopy, Columbus, OH, June 1977.

13. N. E. Schlotter and D. L. Huestis, 30th Annual Gaseous Electronics Conference, Palo Alto, CA, October 1977.

14. F. O. Ellison, J. Am. Chem. Soc. 69, 3540 (1963).

15. See, for example, Reference 16 and the references cited therein.

16. J. C. Tully, Modern Theoretical Chemistry, Vol. 7, Semiempirical Methods of Electronic Structure Calculation Part A: Techniques, ed. G. A. Segal (Plenum, New York, 1977).

17. Y. S. Kim and R. G. Gordon, J. Chem. Phys. 61, 1 (1974).

18. J. S. Cohen and B. Schneider, J. Chem. Phys. 61, 3230 (1974).

19. P. J. Hay and T. H. Dunning, Jr., J. Chem. Phys. 66, 1306 (1977).

20. W. J. Stevens, M. Gardner, and A. Karo, submitted for publication.

21. J. C. Tully, J. Chem. Phys. 59, 5122 (1973).

22. E. U. Condon and G. H. Shortley, The Theory of Atomic Spectra (Cambridge University Press, 1935).

23. N. W. Winter, C. F. Bender, and T. N. Rescigno, J. Chem. Phys., 67, 3122 (1977).

24. T. H. Dunning, Jr., and P. J. Hay, submitted for publication 1977.

25. N. W. Winter, private communication (1977).

26. W. R. Wadt, submitted for publication, 1977.

27. R. G. Gordon and Y. S. Kim, J. Chem. Phys. 56, 3122 (1972).

28. J. S. Cohen and R. T. Pack, J. Chem. Phys. 61, 2372 (1974).

29. A.I.M. Rae, Mol. Phys. 29, 467 (1975).

30. P. K. Rol, private communication (1974).

31. T. L. Gilbert and A. C. Wahl, J. Chem. Phys. 47, 3425 (1967).

32. A. A. Abrahamson, Phys. Rev. 178, 76 (1969).

33. Y. S. Kim and R. G. Gordon, J. Chem. Phys. 60, 4323 (1974).

Table 1

DIATOMICS-IN-MOLECULES HAMILTONIAN

Covalent States (without spin orbit)

$$\langle \psi_{zc} | H | \psi_{zc} \rangle = \left[\cos^2\theta_{13} E^{ac}(1^2\Sigma^+) + \sin^2\theta_{13} E^{ac}(1^2\Pi) \right]_{R_1}$$

$$+ \left[\cos^2\theta_{23} E^{bc}(1^2\Sigma^+) + \sin^2\theta_{23} E^{bc}(1^2\Pi) \right]_{R_2}$$

$$+ \left[E^{ab}(Ar_2) \right]_{R_3}$$

$$\langle \psi_{xc} | H | \psi_{xc} \rangle = \left[\sin^2\theta_{13} E^{ac}(1^2\Sigma^+) + \cos^2\theta_{13} E^{ac}(1^2\Pi) \right]_{R_1}$$

$$+ \left[\sin^2\theta_{23} E^{bc}(1^2\Sigma^+) + \cos^2\theta_{23} E^{bc}(1^2\Pi) \right]_{R_2}$$

$$+ \left[E^{ab}(Ar_2) \right]_{R_3}$$

$$\langle \psi_{yc} | H | \psi_{yc} \rangle = \left[E^{ac}(1^2\Pi)_{R_1} + E^{bc}(1^2\Pi) \right]_{R_2}$$

$$+ \left[E^{ab}(Ar_2) \right]_{R_3}$$

$$\langle \psi_{zc} | H | \psi_{xc} \rangle = \cos\theta_{13}\sin\theta_{13} \left[E^{ac}(1^2\Sigma^+) - E^{ac}(1^2\Pi) \right]_{R_1}$$

$$- \cos\theta_{23}\sin\theta_{23} \left[E^{bc}(1^2\Sigma^+) - E^{bc}(1^2\Pi) \right]_{R_2}$$

$$\langle \psi_{zc} | H | \psi_{yc} \rangle = \langle \psi_{xc} | H | \psi_{yc} \rangle = 0$$

Table 2

DIATOMICS-IN-MOLECULES HAMILTONIAN

Ionic States (without spin-orbit)

$$\langle\psi_{za}|H|\psi_{za}\rangle = \tfrac{1}{2}\left[E^{ab}(^2\Sigma_u^+) + E^{ab}(^2\Sigma_g^+)\right]_{R_3} + \left[E^{bc}(ArF^-)\right]_{R_2}$$
$$+ \left[\cos^2\theta_{13}\, E^{ac}(2^2\Sigma^+) + \sin^2\theta_{13}\, \overset{ac}{E}(2^2\Pi)\right]_{R_1}$$

$$\langle\psi_{zb}|H|\psi_{zb}\rangle = \tfrac{1}{2}\left[E^{ab}(^2\Sigma_u^+) + E^{ab}(^2\Sigma_g^+)\right]_{R_3} + \left[E^{ac}(ArF^-)\right]_{R_1}$$
$$+ \left[\cos^2\theta_{23}\, E^{bc}(2^2\Sigma^+) + \sin^2\theta_{23}\, \overset{bc}{E}(2^2\Pi)\right]_{R_2}$$

$$\langle\psi_{za}|H|\psi_{zb}\rangle = \tfrac{1}{2}\left[E^{ab}(^2\Sigma_u^+) - E^{ab}(^2\Sigma_g^+)\right]_{R_3}$$

$$\langle\psi_{xa}|H|\psi_{xa}\rangle = \tfrac{1}{2}\left[E^{ab}(^2\Pi_g) + E^{ab}(^2\Pi_u)\right]_{R_3} + \left[E^{bc}(ArF^-)\right]_{R_2}$$
$$+ \left[\sin^2\theta_{13}\, E^{ac}(2^2\Sigma^+) + \cos^2\theta_{13}\, \overset{ac}{E}(2^2\Pi)\right]_{R_1}$$

$$\langle\psi_{xb}|H|\psi_{xb}\rangle = \tfrac{1}{2}\left[E^{ab}(^2\Pi_g) + E^{ab}(^2\Pi_u)\right]_{R_3} + \left[E^{ac}(ArF^-)\right]_{R_1}$$
$$+ \left[\sin^2\theta_{23}\, E^{bc}(2^2\Sigma^+) + \cos^2\theta_{23}\, E^{bc}(2^2\Pi)\right]_{R_2}$$

$$\langle\psi_{xb}|H|\psi_{xa}\rangle = \tfrac{1}{2}\left[E^{ab}(^2\Pi_u) - E^{ab}(^2\Pi_g)\right]_{R_3}$$

$$\langle\psi_{za}|H|\psi_{xa}\rangle = \sin\theta_{13}\cos\theta_{13}\left[E^{ac}(2^2\Sigma^+) - E^{ac}(2^2\Pi)\right]_{R_1}$$

$$\langle\psi_{zb}|H|\psi_{xb}\rangle = -\sin\theta_{23}\cos\theta_{23}\left[E^{bc}(2^2\Sigma^+) - E^{bc}(2^2\Pi)\right]_{R_2}$$

$$\langle\psi_{ya}|H|\psi_{ya}\rangle = \tfrac{1}{2}\left[E^{ab}(^2\Pi_g) + E^{ab}(^2\Pi_u)\right]_{R_3} + \left[E^{ac}(2^2\Pi)\right]_{R_1} + \left[E^{bc}(ArF^-)\right]_{R_2}$$

$$\langle\psi_{yb}|H|\psi_{yb}\rangle = \tfrac{1}{2}\left[E^{ab}(^2\Pi_g) + E^{ab}(^2\Pi_u)\right]_{R_3} + \left[E^{bc}(2^2\Pi)\right]_{R_2} + \left[E^{ac}(ArF^-)\right]_{R_1}$$

$$\langle\psi_{ya}|H|\psi_{yb}\rangle = \tfrac{1}{2}\left[E^{ab}(^2\Pi_u) - E^{ab}(^2\Pi_g)\right]_{R_3}$$

Table 3

SPIN-ORBIT HAMILTONIAN MATRIX
FOR A ^{2}P ATOM IN A TRIATOMIC MOLECULE

	xα	xβ	iyα	iyβ	zα	zβ
xα	E_x	0	$\zeta/2$	0	E_{xz}	$\zeta/2$
xβ	0	E_x	0	$-\zeta/2$	$-\zeta/2$	E_{xz}
iyα	$\zeta/2$	0	E_y	0	0	$-\zeta/2$
iyβ	0	$-\zeta/2$	0	E_y	$-\zeta/2$	0
zα	E_{xz}	$-\zeta/2$	0	$-\zeta/2$	E_z	0
zβ	$\zeta/2$	E_{xz}	$-\zeta/2$	0	0	E_z

Table 4

SYMMETRY REDUCED SPIN-ORBIT HAMILTONIAN MATRIX

FOR A ^{2}P ATOM IN A TRIATOMIC MOLECULE

	$\sqrt{\tfrac{1}{2}}x(\alpha+i\beta)$	$\sqrt{\tfrac{1}{2}}y(i\alpha+\beta)$	$\sqrt{\tfrac{1}{2}}z(\alpha+i\beta)$
$\sqrt{\tfrac{1}{2}}x(\alpha + i\beta)$	E_x	$\zeta/2$	$E_{xz} - i\zeta/2$
$\sqrt{\tfrac{1}{2}}y(i\alpha + \beta)$	$\zeta/2$	E_y	$-i\zeta/2$
$\sqrt{\tfrac{1}{2}}z(\alpha + i\beta)$	$E_{xz} + i\zeta/2$	$i\zeta/2$	E_z

Table 5

DIATOMICS POTENTIALS

FOR DIM POTENTIAL SURFACES FOR Rg_2X

Molecule	States		Method	Reference
NeF	$1^2\Sigma^+,\ 1^2\Pi,\ 2^2\Sigma^+,\ 2^2\Pi$		CI	23
ArF	"	"	POL-CI	24
KrF	"	"	POL-CI	19
KrCl	"	"	CI	25
Ne_2^+	$^2\Sigma_u^+,\ ^2\Pi_g,\ ^2\Pi_u,\ ^2\Sigma_g^+$		CI	18
Ar_2^+	"	"	SCF	20
			POL-CI	26
Kr_2^+	"	"	POL-CI	26
Rg_2	$1^1\Sigma_g^+$		Electron Gas	17, 27-29
			Scattering	30
			SCF	31
			Thomas-Fermi	32
RgX^-	$1^1\Sigma^+$		Electron Gas	17,33
			POL-CI	34

Table 6

IONIC STATES OF THE

TRIATOMIC RARE GAS HALIDES Rg_2X^*

Diatomics-In-Molecules Method
with Spin-Orbit Coupling

|	$\underline{Ne_2F}$	$\underline{Ar_2F}$	$\underline{Kr_2F}$	$\underline{Kr_2Cl}$
Rg_2 distance (Å)	1.71	2.47	2.79	2.78
RgX distance (Å)	2.18	2.54	2.67	3.14
Binding Energy (eV) Relative to RgX^*	0.60	0.73	0.66	0.88
Wavelengths (nm)				
$4^2\Gamma \rightarrow 1^2\Gamma$	140	266	359	318
$4^2\Gamma \rightarrow 2^2\Gamma$	143	280	382	338
$4^2\Gamma \rightarrow 3^2\Gamma$	145	287	399	348
Experimental	-	290 ± 27	400 ± 30	325 ± 15

FIGURE CAPTIONS

Figure 1 Coordinate system for the covalent states of Ar_2F.

Figure 2 Diatomics-in-Molecules Potential Surfaces for the Ionic States of Ar_2F without Spin-Orbit

Figure 3 Diatomics-in-Molecules Potential Surface for Ar_2F^* without Spin-Orbit [Contour Energies in eV Relative to $ArF^*(2^2\Sigma^+)$]

Figure 4 Diatomics-in-Molecules Potential Surfaces for Ar_2F with Spin-Orbit

Figure 5 Diatomics-in-Molecules Potential Surfaces for the Ionic States of Ar_2F with Spin-Orbit

Figure 6 Diatomics-in-Molecules Potential Surfaces for Kr_2F with Spin-Orbit

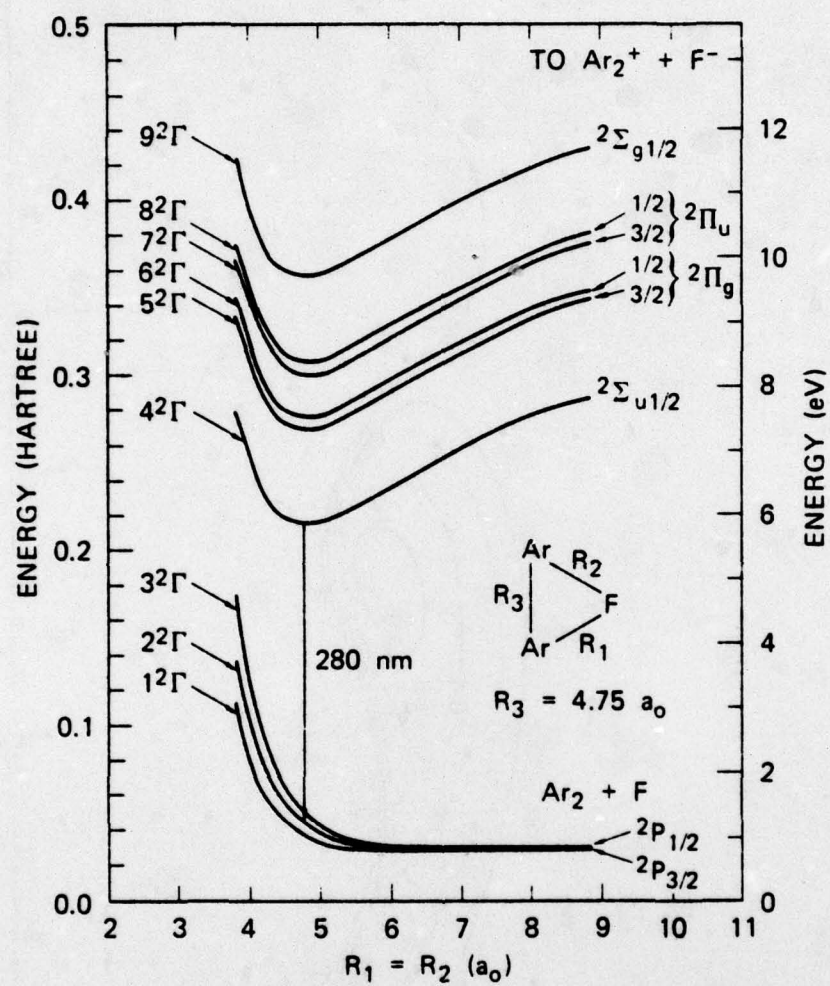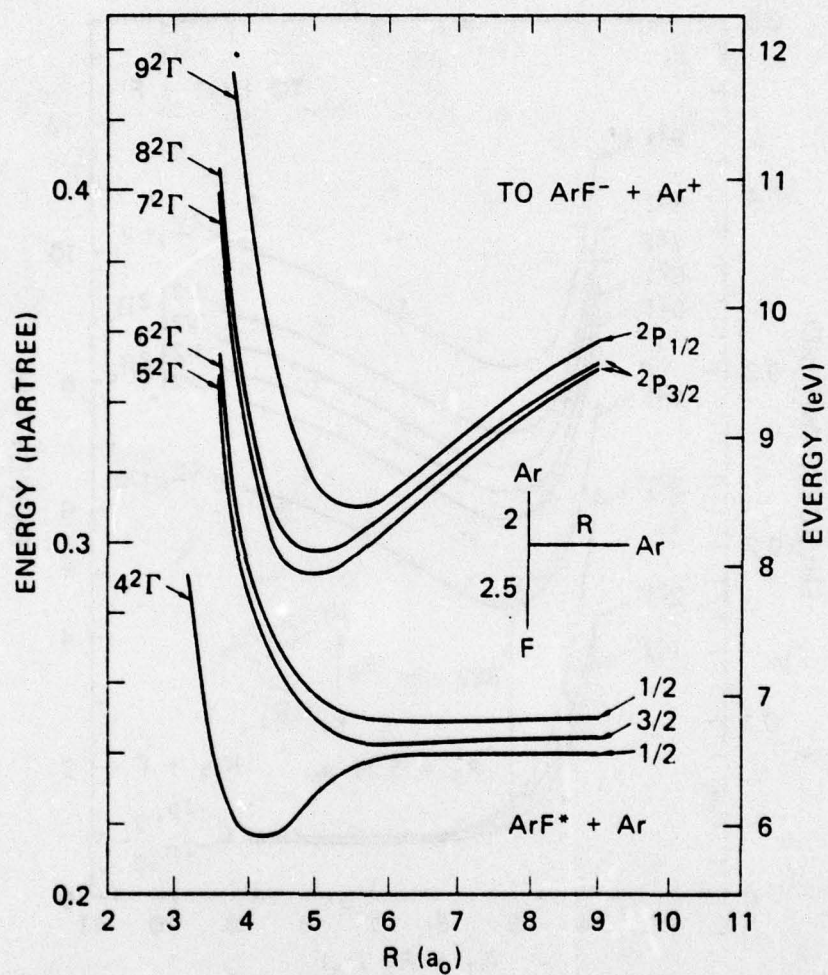Figure 7 Diatomics-in-Molecules Potential Surfaces for Kr_2Cl with Spin-Orbit

SA-6158-5

G-25

Figure 1

Huestis and Schlotter
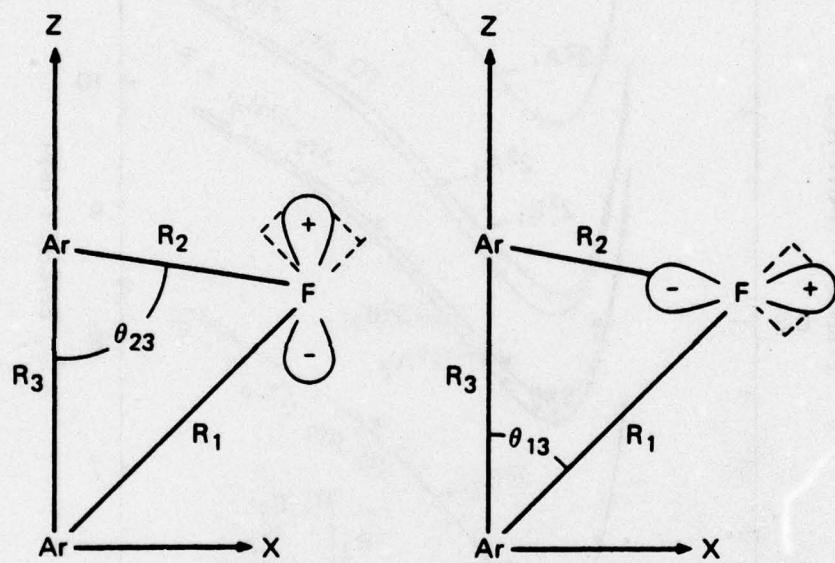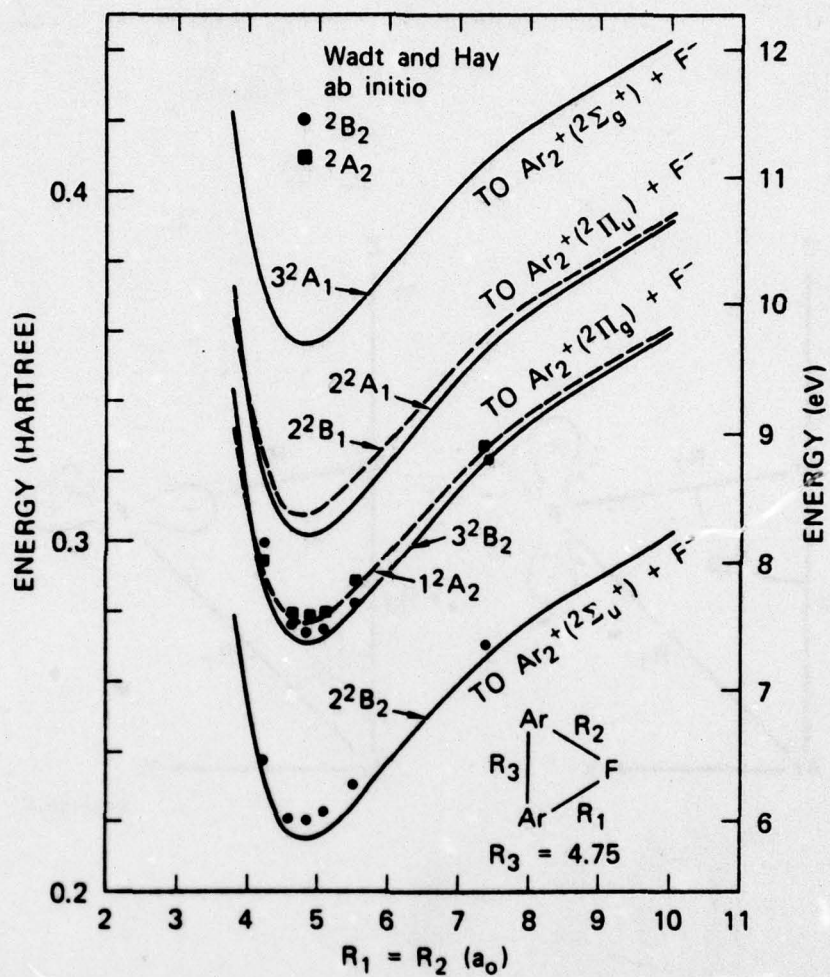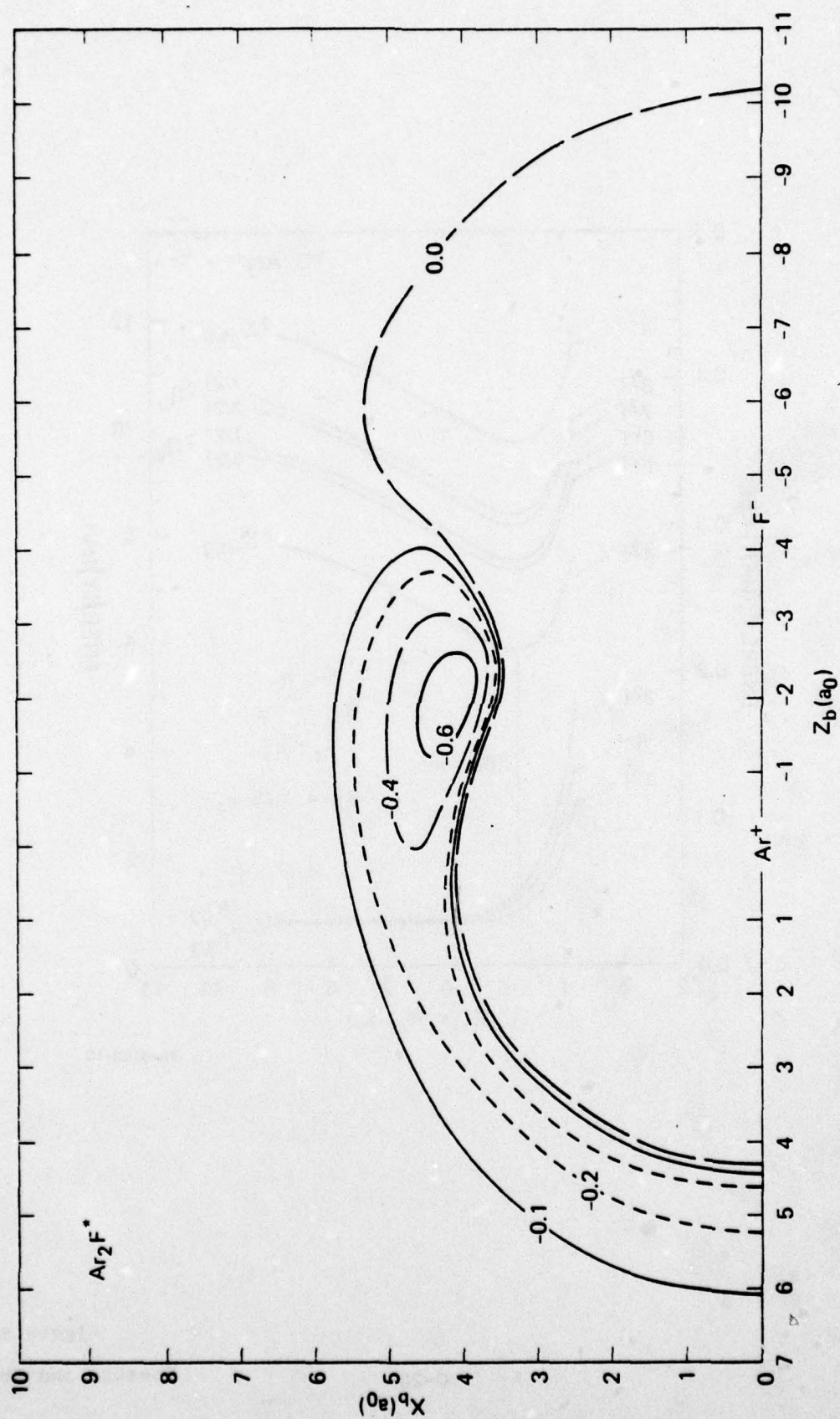
SA-6158-9

Figure 2
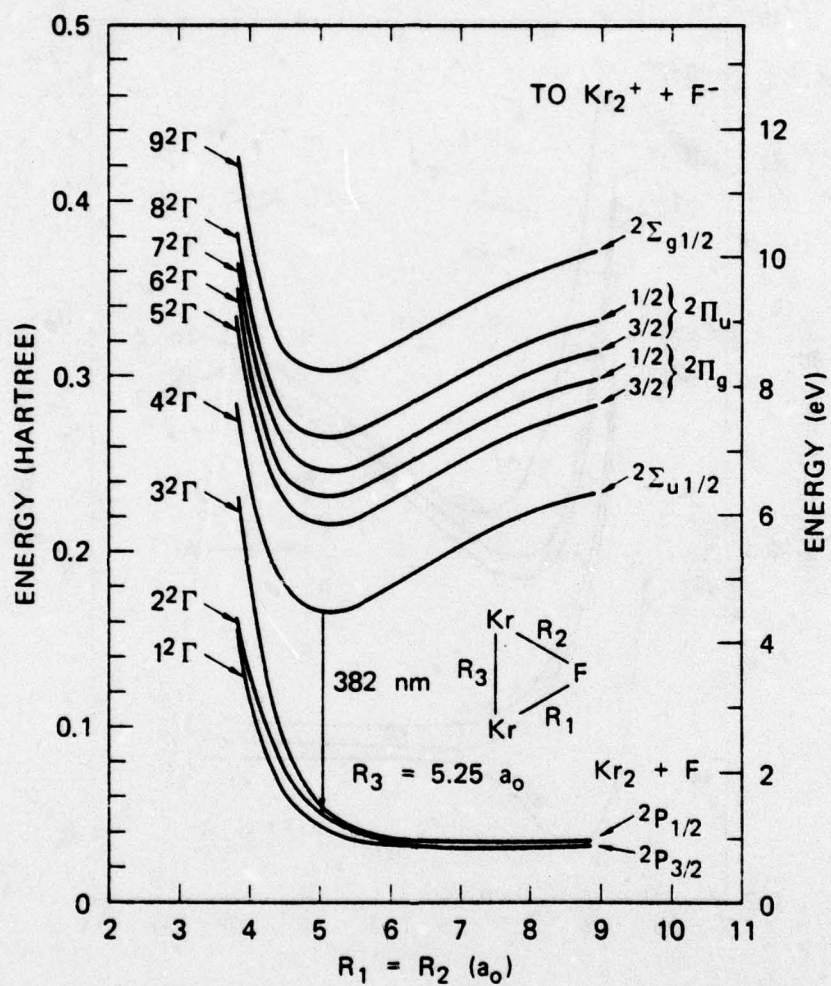
Figure 3

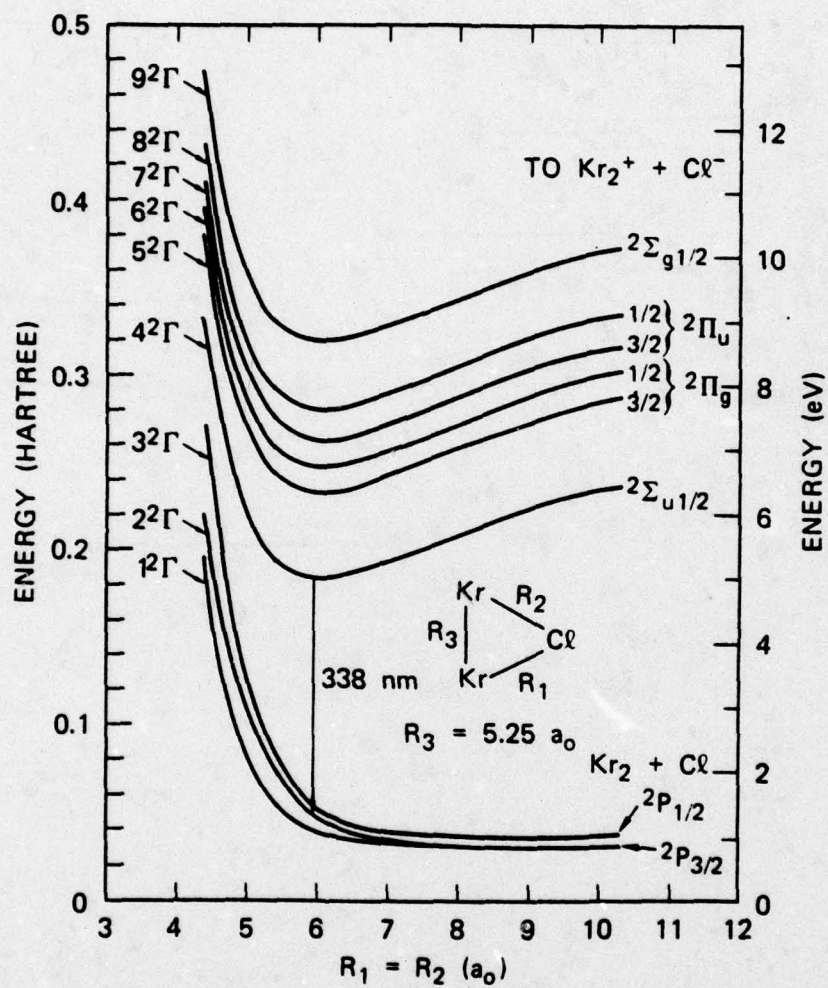Huestis and Schlotter

SA-6158-4

Figure 4

Huestis and Schlotter

SA-6158-10

Figure 5

Huestis and Schlotter

Figure 6

Huestis and Schlotter

SA-6158-12

338 nm

$R_3 = 5.25\ a_o$

SA-6158-13

Figure 7

Huestis and Schlotter